SPECTROSCOPY AND KINETIC STUDIES OF ELECTRON-HOLE RECOMBINATION IN CdSe NANOPARTICLES: EFFECT OF SIZE, SHAPE, AND LATTICE STRUCTURE

THÈSE N° 3767 (2007)

PRÉSENTÉE LE 18 MAI 2007

À LA FACULTÉ DES SCIENCES DE BASE

Laboratoire de spectroscopie ultrarapide

SECTION DE PHYSIQUE

ÉCOLE POLYTECHNIQUE FÉDÉRALE DE LAUSANNE

POUR L'OBTENTION DU GRADE DE DOCTEUR ÈS SCIENCES

PAR

Awos AL SALMAN

licence, Syrie

et de nationalité syrienne

acceptée sur proposition du jury:

Prof. M. Chergui , directeur de thèse

Prof. C. Comninellis, rapporteur

Dr M. Hamoud, rapporteur

Prof. U. Woggon, rapporteur

ÉCOLE POLYTECHNIQUE
FÉDÉRALE DE LAUSANNE

Lausanne, EPFL

2007

إلى أبي وأمي ...
وإلى إياس وأنس ...
والأحبة كلير ، قيصر وسما ...
أُهدي عملي هذا .

To my Parents …
To Iyas and Anas …
And to Claire, Kaiser, and Sama …
I dedicate this work.

Contents

Spectroscopy and Kinetics of Electron-Hole Recombination in CdSe Nanoparticles: Effect of Size, Shape, and Lattice Structure

Ph.D Thesis
AWOS AL SALMAN

Laboratoire de Spectroscopie Ultrarapide
Institut des Sciences et Ingénierie Chimiques
Faculté des Sciences de Base – EPFL /BSP / CH-1015 Lausanne

Abstract

This thesis presents an experimental study of the energy and time-resolved optical response of chemically prepared CdSe nanoparticles with different sizes, shapes (dots, rods, and tetrapods), and lattice structures (wurtzite and zinc blende).

The first part of the thesis concerns a model system: spherical CdSe quantum dots with a wurtzite lattice structure. We have investigated their fluorescence spectra and decay kinetics as a function of size, laser excitation power, detection energy, and temperature. The experiments were performed using a nanosecond time-correlated single photon counting technique and have revealed kinetics from different short and long-lived states. In contrast to comparable literature studies, we covered a wide temporal window (up to 1 μs). The study shows at least four order of magnitude of signal to background ratio
Generally, at low excitation power, we always find four independent decay components covering a range of lifetimes between one nanosecond up to hundreds of nanoseconds. The first component is < 2 ns and probably corresponds to fast relaxation and trapping processes. A second component of 3-8 ns can be attributed to the lifetime of charged excitons, while the third one is in the range of 20-30 ns is due to the radiative electron-hole recombination. Finally, a longer decay time of 80-100 ns with low amplitude (< 10 %) appears for all sizes and experimental condition. This component is related to trap states. At high power (corresponding to more than one exciton per particle), an additional fast component, in the same range as the first one (< 2 ns), appears and is due to the multiexciton effect.

The second part of the thesis concerns CdSe semiconductor nanocrystals from a slightly different point of view focusing on the crystal structure, by investigating quantum dots with a cubic lattice structure, synthesized in our group. We performed low- and high-resolution luminescence and excitation spectroscopy, and time-resolved spectroscopy as a function of size and temperature from room temperature down to 4K. These measurements reveal the optical properties and relaxation processes, and

finally infer the amount of the structure-dependent field effect on the band edge exciton structure. Overall, we observe no difference in all these properties compared to wurtzite dots. We conclude that the crystal field is much less important than shape asymmetries and exchange interaction. The appearance of a permanent dipole moment, in a cubic lattice structure of spherical quantum dots, can explain the similar response of the two different lattice structure dots in our experiments.

The third part of this work concerns the investigation of the shape effect on the spectroscopic and kinetic properties of CdSe nanocrystals. New fabrication methods have enabled the synthesis of high-quality CdSe nanorods and tetrapods. We investigated the temperature dependence of the absorption and fluorescence spectra of the different shapes of CdSe nanocrystals in the range of 4 to 300 K. We find that, while the shift of the fluorescence maximum indicates a little dependence on the shape, the broadening of the emission spectrum behaves very differently for dots and rods, indicating major differences in the broadening mechanisms for different shapes. Tetrapods behave more similar to dots, which suggest that the lowest exciton state is centered at the core. This is confirmed by the decay kinetics, which is again identical between dot and tetrapod nanocrystals, while an opposite temperature dependence decay was recorded for the kinetics of nanorods. We attribute this behaviour in tetrapods to the dot like centre. Nanorods show very different kinetics, because the lowest exciton state becomes allowed.

Keywords

CdSe Nanoparticles, Spectroscopy, kinetics, Dots, Rods, Tetrapods, Shape effect, Lattice structure effect.

Spectroscopie et cinétique de la recombinaison electron-trou dans des nanoparticules de CdSe: Effets dus à la taille, à la forme et à la structure de maille

Thèse de doctorat
AWOS AL SALMAN

Laboratoire de Spectroscopie Ultrarapide
Institut des Sciences et Ingénierie Chimiques

Faculté des Sciences de Base – EPFL /BSP / CH-1015 Lausanne

Résumé

Cette thèse présente une étude expérimentale, résolue temporellement et en énergie, de la réponse optique de nanoparticules de CdSe préparées par méthode chimique, et ayant différentes tailles, formes (boîtes, bâtonnets et tétrapodes) et structures de maille (wurtzite et zinc-blende).

La première partie de la thèse traite de l'étude d'un sytème-modèle : des boîtes quantiques de CdSe shpériques ayant une structure de maille wurtzite. Nous avons étudié leurs spectres de fluorescence et leur cinétique de décroissance en fonction de leurs tailles, de la puissance d'excitation du laser, de l'énergie de détection et de la température. Ces expériences sont réalisées à l'aide d'une technique de comptage de photons uniques corrélés temporellement, à l'échelle de la nanoseconde, des cinétiques d'états à temps de vie courts ou longs ont pu être mises en évidence. Contrairement aux études du même type que nous avons trouvées dans la littérature, nous avons couvert une large gamme temporelle (jusqu'à 1 μs). Nous obtenons un rapport signal sur bruit de plus de quatre ordres de grandeurs. De manière générale, à faible puissance d'excitation, nous obtenons toujours quatre composantes dans la décroissance ayant des temps de vie allant de la nanoseconde à plusieurs centaines de nanosecondes. La première composante est < 2 ns et correspond probablement à un processus rapide de relaxation et de piégeage. Une deuxième composante de 3-8 ns peut être considérée comme le temps de vie des excitons chargés, alors que la troisième est de l'ordre de 20-30 ns et est due à la recombinaison radiative électron-trou. Un temps de décroissance plus long de 80-100 ns apparaît enfin avec une faible amplitude (< 10%) quelles que soient la taille et les conditions expérimentales. Cette composante est liée aux états pièges. A haute puissance (plus d'un exciton par particule), une composante rapide supplémentaire du même ordre que la première (< 2 ns) apparaît et est due à l'effet multiexciton.

La deuxième partie de cette thèse étudie des nanocristaux de CdSe semiconducteurs d'un point de vue légèrement différent, se focalisant sur la structure cristalline, en étudiant des boîtes quantiques ayant une structure de maille cubique, synthétisées dans notre groupe. Nous avons effectué une étude spectroscopique à haute et basse résolutions de la luminescence et de l'excitation, ainsi qu'une spectroscopie en temps résolu en fonction de la taille et de la température, de la température ambiante à 4K. Ces mesures montrent les propriétés optiques ainsi que les processus de relaxation, et nous permettent finalement de déduire l'importance de l'effet du champ dépendant de la structure sur la structure de l'exciton de fond de bande. De manière générale, nous n'observons pas, pour toutes ces propriétés, de différence avec les boîtes wurtzites. Nous en concluons que l'effet du champ cristallin est beaucoup moins important que les asymétries de forme et l'interaction d'échange. L'apparition d'un moment dipolaire permanent dans une structure de maille cubique d'une boîte quantique sphérique, peut expliquer la similarité des réponses que nous avons obtenues dans nos expériences, des boîtes ayant les deux structures de mailles différentes.

La troisième partie de ce travaille concerne l'étude de l'effet de forme sur les propriétés cinétiques et spectroscopiques de nanocristaux de CdSe. De nouvelles méthodes de fabrication ont permis la synthèse de nanobâtonnets et tétrapodes de CdSe de hautes qualités. Nous avons étudié la dépendance en température de spectres d'absorption et de fluorescence de nanocristaux de CdSe de différentes formes, entre 4 et 300K. Alors que le décalage du pic de fluorescence indique une faible dépendance à la forme, l'élargissement du spectre d'émission est très différent pour les boîtes et les bâtonnets, ce qui indique une différence importante dans les mécanismes d'élargissements pour les différentes formes. Les tétrapodes se comportent de manière simiilaire aux boîtes, ce qui suggère que l'état d'exciton le plus bas est centré au cœur. Ceci est confirmé par la cinétique de décroissance, qui est encore une fois identique pour les boîtes et tétrapodes, alors qu'une dépendance en température contraire a été enregistrée pour la cintétique des nanobâtonnets. Nous attribuons ce comportement en tétrapode au centre qui est de type boîte. Les nanobâtonnets montrent quant à eux une cinétique très différente, car les etats d'excitons les plus bas sont alors permis.

Mots-Clés

Nanoparticules de CdSe, spectroscopie, cinétique, boîtes, bâtonnets, tétrapodes, effet de forme, effet de structure de maille.

Chapter 1

Introduction

1.1 Nano world

The research described in this thesis focuses on the characterization of the optical properties, chemical structure, and the decay kinetics of CdSe semiconductor nanocrystals as a function of size and shape.
The nano world is a particular domain where the dimensions of the materials reach the nanometer regime, which causes a dramatic change of their behaviour, characteristics and physical-chemical properties with respect to those of bulk materials[1, 2].
Nanomaterials include all materials within a large distribution of sizes, ranging from a nanometer to as large as hundreds of nanometres. We can classify them into nanostructured materials and nanoparticulate materials.
The term "nanotechnology" has evolved over the years via a terminology drift to describe "anything smaller than microtechnology," such as nano powders, and other objects that are nanoscale in size, but not referring to mechanisms that have been purposefully built from nanoscale components. This evolved version of the term is more properly labelled "nanoscale bulk technology," while the original meaning is now more properly labelled "molecular nanotechnology" (MNT), or "nanoscale engineering," or "molecular mechanics," or "molecular machine systems," or "molecular manufacturing". Nanotechnology is considered as the technology of the 21st century, following the microtechnology development and now, even if we do not realize it yet, these materials are already taken a remarkable part in our everyday life.
The interesting properties of these materials make them attractive in a variety of applications like light-emitting diode [3-5] photovoltaic devices [6], lasers [7], optical memory [8, 9] , miniaturized devices, and as fluorescent probes in biology [10-14].

Nanoparticles (NP) can be considered as single crystals with a typical size of a few nanometres. They still contain hundreds to thousands of atoms. Due to the size quantization effect, these nanoparticles preserve some bulk materiel properties but, in addition, they exhibit more interesting properties. From the technological point of view, the main reason for studying nanostructured materials is the ease of tuning the optical and the electronic properties gradually by varying the particle size and shape.
Nanoparticles can be prepared by different methods, and occur in various forms, including powder state materials, solid state, thin films and solutions. Nanoparticles possess a varity of properties depending on the chemical composition and size. The chemical structure of the nanoparticles can be very different and common materials include:
Oxides: TiO^{2-}[15], CoO [16], ZnO[17], ….
Metals: gold[18], silver[19], palladium (Pd) [20] .
Semiconductors: Silicon [21], II-V [22] compounds (CdSe, CdS, CdTe, ZnSe, ZNS) [23-25] , III-V [26, 27] compounds (GaAs, GaP, InAs, InP) [28-30] and finally the IV-VI compounds(PbS, PBSe, PbTe) [31]
In this theises, we are mainly concerned with CdSe semiconductor nanoparticles (NPs) synthesized by colloidal methods in solution, have in common that the surface of the particles is covered by organic molecules such as polymers or a surfactant attached to the surface to prevent aggregation and to control the size and shape of the particles [32-35].These surface molecules are called capping material. The advantages of the chemical synthesis are listed below:
Large quantities of the material can be easily fabricated.
The fabricated NPs have a very narrow size distribution (near monodispersity) and high photostability.
They are highly soluble in most non-polar solvents, such as toluene, hexane, and chloroform.
Attractive optical properties such as intense fluorescence and a wide absorption band in the visible region, whose wavelength can be controlled by on the NCs size (figure1.1).

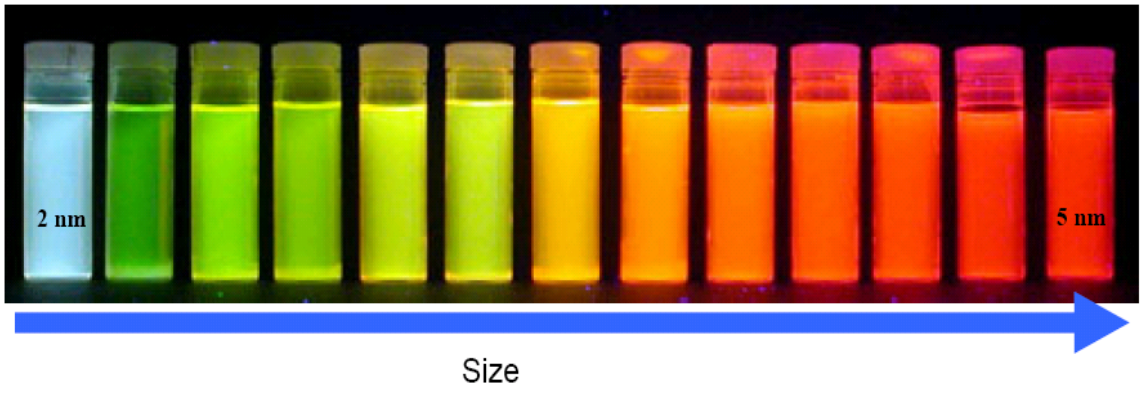

Figure 1.1: CdSe nanocrystal solutions with different particles exhibit fluorescence varying. Blue for the smallest (2.0 nm) to red for the biggest sized crystals (6.5 nm). This image is taken from www.research.northwestern.edu/research/img

The CdSe nanodot (ND) synthesis by the chemical molecular precursor method, which has been described by Murray, Norris and Bawendi [36] is considered to be the most powerful method for the preparation of semiconductor nanocrystals. The interesting properties of these nanoparticles motivated much research on their application in various fields. This work focuses on the optical properties of CdSe nanocrystals (NCs) and their dependence on size, shape (dot, rod, and tetrapod), and lattice structure (wurtzite (WZ), zinc blende (ZB)).

1. 2 Optical Properties and Electronic Structure of Semiconductor Nanoparticles:

The most pronounced property of semiconductor nanoparticles is the large changes observed in their optical spectra with changing size.

1.2.1 Quantum Size effect

The quantum size effect can be explained using a hybrid between molecular and semiconductor formalisms [37]. Since, as a function of size, the electronic properties must transforms from molecular to bulk material-like nature; the linear combination of atomic–molecular orbitals approach provides a natural framework to understand the quantum size effect.

In bulk semiconductors, the Effective Mass Model [38] [39] (EMM) is one of the methods, which has been successfully applied to understanding bulk semiconductor optical phenomena. The (EMM) is a quasi-particle theory, which treats the electron, excited to the conduction band, and hole created in the valence band as free particles, whose effective masses are determined by a quadratic fit to the curvature at the band minima (maxima) of the conduction (valence band) (figure1.2).

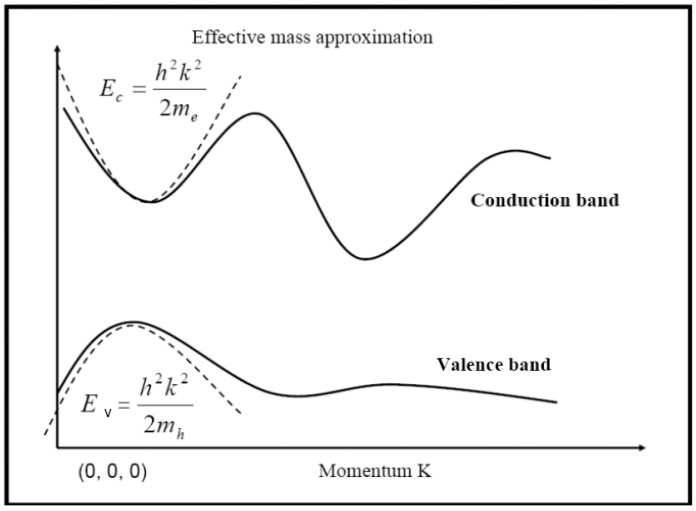

Figure 1.2: The effective mass approximation consists of a quadratic fit to the valence band maximum and conduction band minimum. The curvature gives the effective mass m_h and electron mass m_e.

If we add the culombic attraction of an electron and hole to this picture, we have a theoretically simple manifestation of an exciton. The electron and hole are bound together by a screened coulomb interaction to form a so-called Mott-Wannier exciton[40]. This exciton presents an energy spectrum analogous to a hydrogen atom (i.e. with radial and angular quantum numbers) but it is further complicated by the fact that it is coupled to a thermal bath of phonons and that the "mass" of an exciton is energy dependent. Excitons eventually decay however, by electron-hole annihilation, which can be accompanied by the emission of a photon (Luminescence), with or without phonon absorption/emission or the acceleration of a free charge (Auger process). Bulk model predictions break down when the size of the crystal is smaller than the exciton's Bohr radius (i.e. radius of the lowest energy Bohr orbital). The Bohr radius of the exciton is given by [41]:

$$a_B = \frac{\hbar^2 \varepsilon}{e^2 \mu_{\varepsilon,\hbar}} \tag{1.1}$$

Where ε is the dielectric constant, $\mu_{\varepsilon,\hbar}$ is the reduced effective mass of the electron and hole, e and $\hbar$ are the electron charges and the Planck constant respectively. The Bohr radius is 5.6 nm in CdSe QDs. The exciton energy for small clusters is different with respect to the bulk band gap. In spherical nanocrystals surrounded by an infinite potential barrier, the energy of the electron and hole quantum size levels can be written in effective mass approximation as [42]:

$$E^{e,h}_{l,n\ confinement} = \frac{\hbar^2 \varphi^2_{l,n}}{2\mu_{e,h} a^2} \tag{1.2}$$

Where l is the angular momentum quantum number, a is the nanocrystal radius, and $\varphi_{l,n}$ is the n^{th} root of the spherical Bessel function. The four lowest roots are $\varphi_{0,0} = \pi$, $\varphi_{1,0} \approx 4.49$, $\varphi_{2,0} \approx 5.76$, $\varphi_{0,1} \approx 2\pi$. It is clear from equation (1.2) that the quantization energy levels increase with decreasing nanocrystal size as $1/a^2$, and hence the total energy of the band gap transition increases with decreasing size and causes a blue shift in the band gap energy as shown in figure 1.3. The other consequence is that the quantum confinement increases the probability of overlap between the electron and hole (i.e. its optical matrix element is larger), which thus increases the radiative recombination rate. The blue shift can be understood as an extra-discretized energy due to confinement that must be overcome to promote an electron to the conduction band.

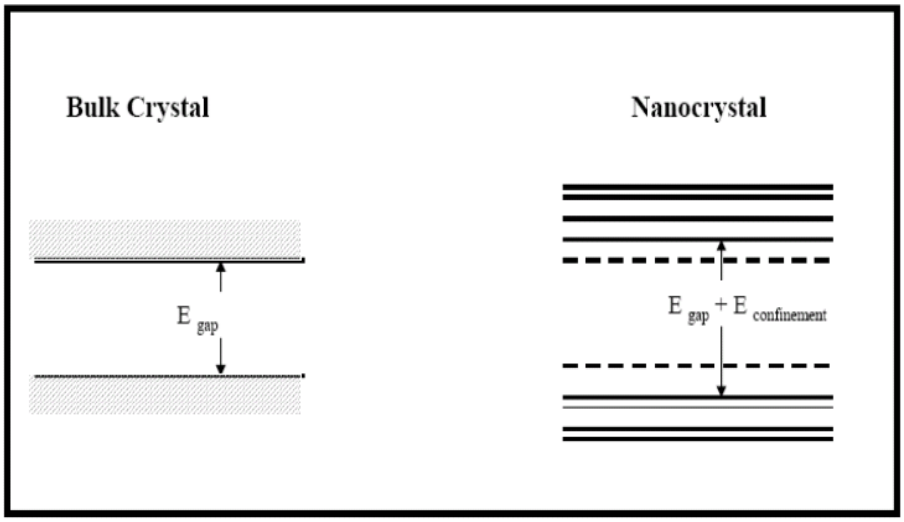

Figure 1.3: Confinement within nm-sized geometries causes a significant blue shift in the band energy, with respect to the bulk crystal.

The increase in the radiative recombination rate may be understood as a consequence of Fermi's Golden Rule:

$$\frac{1}{\tau} \propto E_0 \left| \langle f | \vec{p} | i \rangle \right|^2 \tag{1.3}$$

Where τ is the radiative lifetime, i is the initial state, f is the final state, and E_0 is the energy of the transition. Spatial confinement implies a widely spread representation in momentum space according to Heisenberg's uncertainty principle, which increases the magnitude of the optical matrix element of the transition and thus decreases the lifetime.

In the case of CdSe nanocrystals, the band gap energy could be changed from its bulk value of 1.8 eV up to 3 eV, covering the entire visible range of the optical spectrum. And because the electron and hole are confined in the same crystal volume, we have to take into account the columbic interaction between them, which is on the order of e^2/ka, where k is the dielectric constant of the semiconductor. This means that due to confinement, the kinetic energy changes the band gap energy as $1/a^2$, while the potential energy changes as $1/a$.

Because of the different size dependence, in small crystals the Coulomb energy can be considered a small correction to the energy of electron and hole, and the energy spectrum is mainly determined by confinement effects. Conversely, in large nanoparticles, Coulomb interaction strongly affects the energies of valence and conduction band states. Theoretical analysis shows that the optical properties of semiconductor nanocrystals depend strongly on the ratio of the nanocrystal radius to the Bohr exciton radius of the bulk [41, 42]. According to this ratio, the confinement of the nanocrystals is classified to three different regimes, which we treat now:

i)- Weak confinment regime:

In this regime, the particle radius is larger than the Bohr exciton ($a >> a_B$) [42-44]. Thus, the exciton binding energy is larger than the quantization energy of the electron and the hole $E_{ex.}$ The lowest exciton energy is given by:

$$\Delta E = E_g - E_{ex} + \frac{\pi^2 \hbar^2}{2\mu_{e,h}} \cdot \frac{1}{a^2} \qquad (1.4)$$

where E_g is the band gap energy of the bulk. In this size regime, the electron and hole states originate from quantum confinement of the exciton centre of mass. For example, this treatment has found successful applications in CuCl QDs.

ii)- Intermediate confinement regime:

In the case of the intermediate confinement regime, the particle radius $a \approx a_B$. That is the case for large particles of CdS or CuBr, for which a_B = 2.8 and 1.8 nm, respectively. The large difference between the electron and hole effective masses ($m_e < m_h$) permits adiabatic separation of their movement. The electron wave function is size quantized; whereas the hole moves in the coulomb potential caused by the fast electron and is pushed to the center of the particle [45].

iii)- Strong confinement regime:

For small nanocrystal ($a << a_B$), the electron and hole can be treated independently, and the optical spectra can be considered as transitions between the electron and hole quantized levels [42]. In this regime, the band gap state is given by [41-44, 46] :

$$\Delta E = E_g + \frac{\pi^2 \hbar^2}{2\mu_{e,h}} \cdot \frac{1}{a^2} - \frac{1.8 \cdot e^2}{\varepsilon} \cdot \frac{1}{a} \qquad (1.5)$$

Where ($E_{coulomb} = \frac{1.8 \cdot e^2}{\varepsilon} \cdot \frac{1}{a}$) is the Coulomb energy correction for electrons in the $1S_e$ level.

The intraband transition between quantum size levels of parabolic conduction and valence bands is simply explained by the fact that the transition is only allowed between levels with the same quantum numbers. However, the real picture is not that simple. In cubic or hexagonal lattice structure semiconductor materials, the conduction band is only parabolic at the bottom of the band. The top of the valence band consists of a 4-fold degenerate sub-band [42]. Figure 1.4 represents the bulk band structure of a typical direct band gap semiconductor for both cases, cubic and hexagonal lattice structur

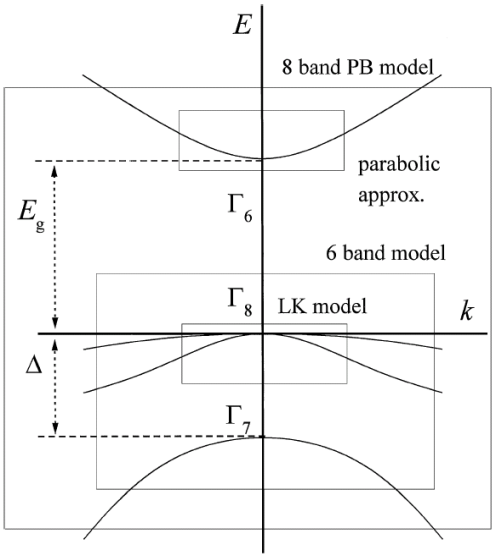

Figure 1.4: The bulk band structure of a typical direct band gap semiconductor of cubic and hexagonal lattice structure. This figure were taken from the work of A. L. Efros et al [42]

The optical properties of small semiconductor nanocrystals arises from the allowed optical transitions between the quantum size levels of electron and holes as shown in Figure 1.5. The absorption features can be explained by the effective mass model, taking into account confinement induced mixing of three valence sub-bands. In this model, the electronic states are labeled using the letter (l) to denote the angular momentum of the envelope wave function for S ($l=0$), P ($l=1$), and D ($l=2$).

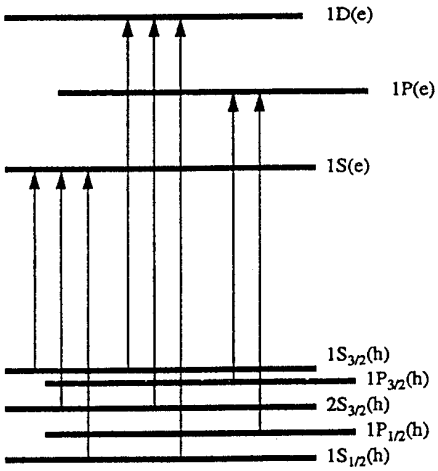

Figure 1.5: Allowed optical transitions between the quantized energy levels of the electron and the hole in small semiconductor particles.

The electron states are 2 ($2l+1$) fold degenerate. The three lowest electron states are 1S, 1P and 1D. The first three hole states are $1S_{3/2}$, $1P_{3/2}$ and $2S_{3/2}$. The subscript denotes the total hole angular momentum (F), which is the sum of the valence band Bloch-function momentum and the momentum of the hole envelope function)[44,

47]. The hole states are (2F+1) fold degenerate. To calculate the energies of these levels, the real band structure of these semiconductor materials has to be taken into consideration.
Figure 1.6A shows the absorption spectra of different sizes of CdSe nanocrystals ranging from 2.1 nm up to 4.5 nm diameter developed by a chemical method (see chapter 2) to produce very high quality CdSe quantum dots (QDs) of different sizes. This size range is in the strong confinement regime since the exciton Bohr radius of CdSe is ~ 5.6 nm. The spacing between the two lowest electron states is more than 200 meV, which is much greater than both the binding energy of the exciton and the energy of the longitudinal optical phonon (26 meV). Because of the narrow size distribution of these samples, their spectra show well resolved features corresponding to interband optical transitions coupling to different electron and hole quantized states.
The absorption spectra are sensitive to various physical and chemical effects, as listed here:

The absorption spectra can be influenced by the crystal structure of the NCs (hexagonal Wurtzite or Cubic Zinc-blend structure [48]).
The polydispersity of the ensemble of NCs which causes inhomogeneus line broadening in the spectra and thus the absorption spectra do not show discrete lines at different maxima as in the case of single nanocrystal [49].
Changes in the dielectric environment of the NCs cause a solvatochromic shift of colloidal CdSe absorption spectra [50].
The type of surface covering with organic or inorganic shells can change the absorption spectra.

The broadening of the optical transition observed in the absorption spectra of CdSe colloidal solution (figure 1.6 A) is due to inhomogeneity arising from size dispersion. The band gap emission of these samples is red shifted with respect sizes as we shown in figure 1.6B.

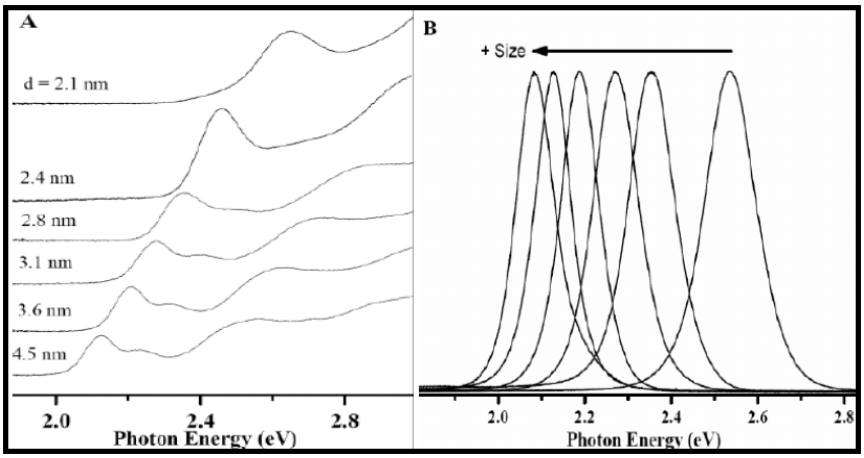

Figure 1. 6: Absorption (A) and emission (B) spectra of CdSe nanodots of different diameters.

1.3 Band-edge exciton in Quantum dots of semiconductors.

1.3. 1 Intrensic excitons.

Previous works [51-54] show unusual long radiative lifetime $\tau_R \sim 1$ μs at 10 K compared to the bulk exciton recombination time $\tau_R \sim 1$ ns. Simple calculation using the parabolic effective mass approximation could not explain these data. These experimental results encouraged many scientists to do further theoretical and experimental investigations to understand the nature of the emitting state in CdSe nanoparticles and the fine structure of the lowest excited state (band edge exciton).
For quantum dots, the fine structure of the lower pair states has been theoretically treated by Efros and co-workers [42, 55, 56];, Takagahara *et al* [57] ,Romestain *et al* and Fishman *et al* [58], Nirmal *et al.*[59], and Woggon *et al* [41]. They modelled the CdSe band edge exciton using the parabolic effective mass approximation taking into consideration the asymmetry of the nanocrystal. This asymmetry arises from the nonspherical shape of the dot together with the intrinsic asymmetry of the hexagonal lattice structure of the nanocrystal. For spherical symmetric crystals of cubic lattice structure, the first electronic quantum level is a $1S_e$ state, which is doubly degenerate with respect to its spin projection ($S = \pm ½$). The first hole quantum size level is $1S_{3/2}$ state, which is 4-fold degenerate with respect to the projection of its total angular momentum ($M = 3/2, 1/2,-1/2,-3/2$). Thus, for the spherical dots, the exciton ground state ($1S_{3/2}\ 1S_e$) is 8-fold degenerate. The degeneracy is lifted because of the shape of the particle and the internal crystal structure anisotropy together with the electron hole exchange interaction. The splitting of these states and their absorption oscillator strength are very sensitive to the crystal size and shape.
The intrinsic asymmetry of the hexagonal lattice structure of the nanocrystal splits the 4-fold degenerate hole state into 2-fold degenerate states (Kramer's doublet) having $|M| = 1/2$ and $3/2$ respectively. The splitting energy Δ_{int} does not depend on the crystal size but only on β, which is the ratio between the light and the heavy holes effective masses [42].

$$\Delta_{int} = \Delta_{CF}\ \nu(\beta) \qquad (1.6)$$

Δ_{int} is the splitting due to the intrinsic hexagonal lattice structure, and Δ_{CF} is the crystal field splitting. This splitting is equal to the energy difference between the A and B exciton states in the bulk semiconductors that having hexagonal lattice structure. $\nu(\beta)$ is a dimensionless function [55] which describes the dependence of hole level splitting due to hexagonal lattice structure (see figure 1.7. b). In the case of CdSe, the lattice structure is wurtzite and the splitting due to the crystal field of the hexagonal lattice (A-B splitting) = 25 meV [42]. In this case, $M = 3/2$ is the ground state.

The asymmetry (nonspherical shape of the nanocrystal (prolate, oblate)) introduces another factor that affects the splitting of the $1S_{3/2}$ hole degenerate state. The splitting arising from this calculated first order perturbation theory is given by [42]:

$$\Delta_{sh} = 2\,\mu\, u(\beta)\, E_{3/2}(\beta) \tag{1.7}$$

Where $E_{3/2}$ is the $1S_{3/2}$ hole state energy, has a^{-2} dependence, where a is the nanocrystals radius (in case of ellipsoid $a = (b^2C)^{1/3}$ and $c/b = 1+\mu$). $u(\beta)$ is a function [56] changes its sign at $\beta = 0.14$ and goes to zero at $\beta = 1$ (see figure 1.7.c). The shape splitting is size dependent. The net splitting of the hole states $\Delta(a,\beta, M)$ is the sum of the crystal field splitting and shape splitting:

$$\Delta(a,\beta, M) = \Delta_{sh} + \Delta_{int} \tag{1.8}$$

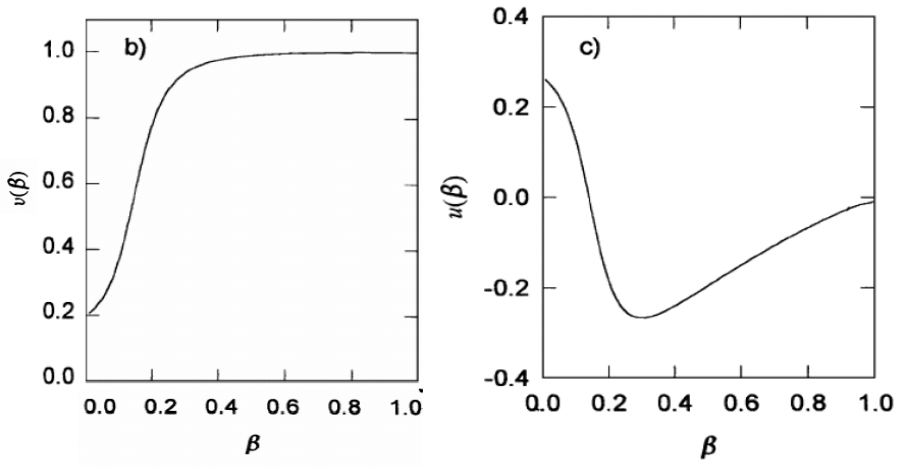

Figure 1.7: (b) The ν(β) function as a function of the hexagonal structure; (c) The dimensionless function u(β) associated with hole level splitting due to crystal shape asymmetry. This figure were taken from the work of A. L. Efros et al [42].

For CdSe nanocrystals, the net splitting increases with decreasing size and the states maintain their original order.

The other important factor, which breaks the 8-fold degeneracy of the band edge exciton state and mixes the different electron and hole spin states, is the electron-hole exchange interaction [41, 60]:

$$\Delta_{exch} = -(2/3)\, \varepsilon_{exch}\, (a_o)^3\, \delta(r_e - r_n)\, \sigma\, \mathbf{J} \tag{1.9}$$

Where σ is the electron Pauli spin –1/2, **J** is the hole spin, $\mathbf{a_o}$ is the lattice constant and ε_{exch} is the exchange strength constant (~ 450 meV in CdSe [61]). The exchange interaction splitting is proportional to the overlap of the electron and hole wave functions. Therefore, it is strongly enhanced by the spatial confinement, following an

$\mathbf{a^{-3}}$ dependence. Thus, the exchange interaction overwhelms the A-B splitting effect in small nanocrystals.

Using this treatment of the first excited state ($1S_{3/2}$ $1S_e$) of CdSe nanocrystals, the 8-fold degeneracy is split into five sub-levels as a result of the effect of the hexagonal lattice, the nonspherical shape and the exchange interaction between the electron and the hole. For the exchange interaction, the important quantum number is $N= F_h + F_e$, where F_h (F_e) is the hole (electron) total angular momentum quantum number. The five sub-levels are described by $|N_m|$. One sub-level is described by $|N_m|=2$, two with $|N_m|=1$ and two with $|N_m|= 0$. Levels with $|N_m| > 0$ are two fold degenerate. The five states are 2, 1^L, and $0^{U, L}$, 1^U, where the superscript denotes the upper (U) or the lower (L) states with the same $|N_m|$. Both the $|N_m|=2$ and 0^L sub-levels are optically forbidden within the electric dipole approximation. This leads to the existence of the so-called dark exciton state. Therefore, this dark state 2 cannot be excited by a photon and cannot directly recombine radiatively because emitted and absorbed photons cannot have an angular momentum 2. Figure 1.8 shows the splitting of the band edge exciton state as a result of the crystal field of the hexagonal lattice, shape and the exchange interaction of electron and the hole. While in figure 1.9 (a, b, and c) we present the size and shape dependence of the exciton band edge structure in ellipsoidal CdSe quantum dots. Figure 1.9d shows the effect of crystal structure in cubic CdTe quantum dots.

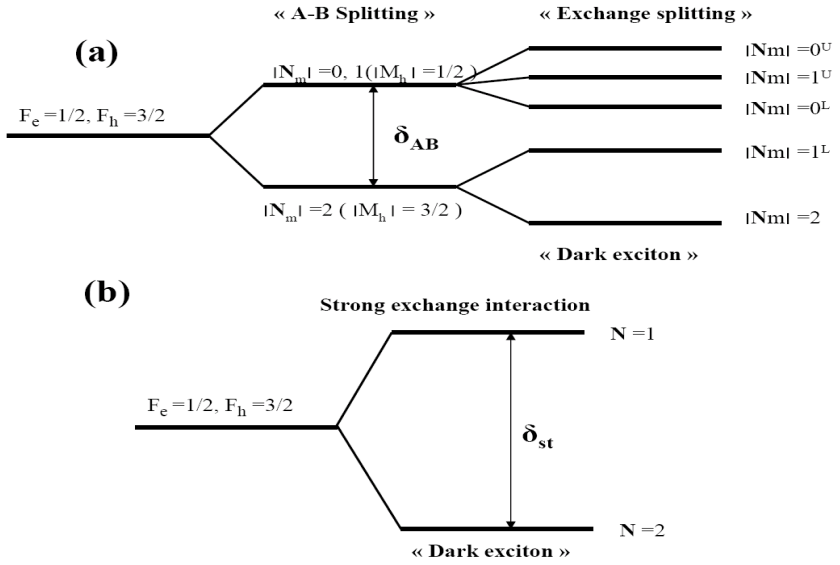

Figure 1.8: Shows the splitting of the band edge exciton state as a result of the crystal field of the hexagonal lattice, shape, and the exchange interaction of electron and the hole. (a) In normal exchange interaction. (b) strong exchange intraction (small dots).

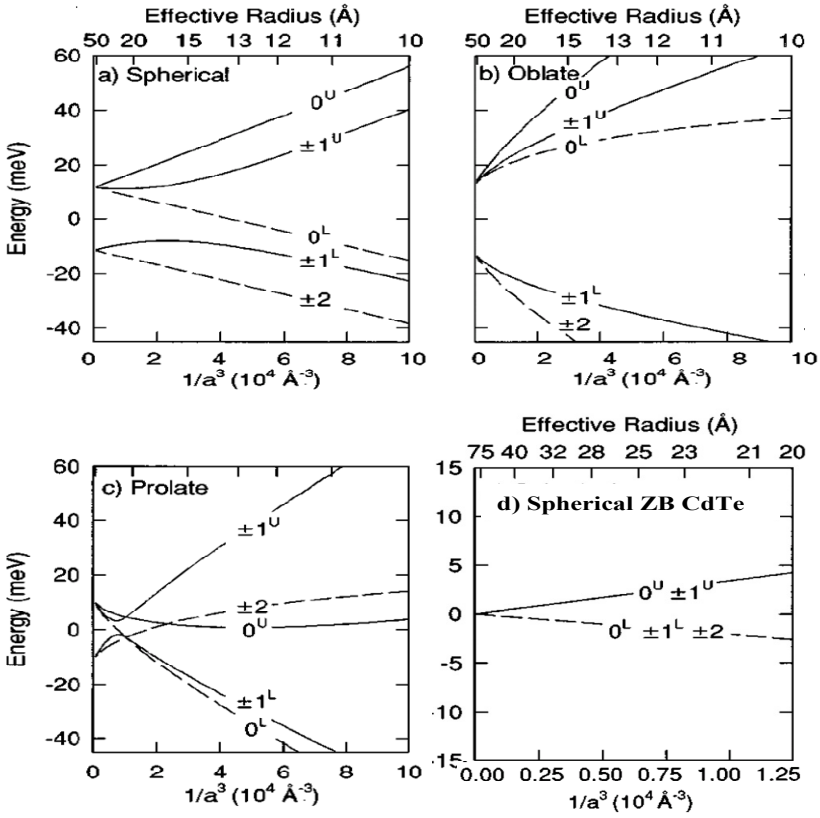

Figure 1.9: Size and shape dependence of the exciton band edge structure in hexagonal CdSe QDs (a, b, and c) and the effect of structure in cubic CdTe (d). This figure were taken from the work of A. L. Efros et al [42].

In figure 1.9C (oblate crystal), the order of the exciton level is the same as in spherical ones. The splitting between states increases with decreasing size. The case of the prolate CdSe shape presents transformation in the band edge structure, and different order of the exciton levels. The structure of the lowest exciton state was studied experimentally using Photoluminescence Excitation (PLE) and Fluorescence Line Narrowing (FLN) techniques [59, 62-64]. Low temperature PLE spectra of CdSe colloidal nanocrystals shows the fine structure in the band edge absorption in which three features appear. The lowest of these features was assigned to the $|N_m|=1^L$ exciton. The other two were attributed to a state with $|N_m|=1^U$ and 0^U. The FLN studies of CdSe nanocrystals show clearly that the emitting state is different than the absorbing one [48]. This fact is also confirmed with the PL polarization studies, which indicates that the polarization of the resonant excited PL state is different from that of the absorbed light [64]. These experimental results agree with the predicted exchange-interaction induced splitting of the lowest exciton (A) into the optical active state with $|N_m|=1^L$, which is the absorbing state, and optically passive dark exciton state with $|N_m|=2$, which is the emitting state. Moreover, by studying the effect of the magnetic field on the dynamics [42], it has been found that the decay rate increases with increasing magnetic field strength. This supports the assignment of the emitting state to the $|N_m| = 2$ dark exciton state.

In a cubic structure, the electron-hole exchange interaction splits the eightfold degenerate band-edge exciton into fivefold degenerate exciton with total angular momentum 2 and a threefold degenerate exciton with total angular momentum 1 as shown for spherical CdTe QDs in figure 1.9 (d). The crystal shape asymmetry in a cubic structure lifts the degeneracy of these states, but completely determines the relative order of the exciton states [61].

Controlling the shape of semiconductor nanocrystals affords an opportunity to test the theories of the quantum confinement [36], [59]. By elongation of the unique c-axis in CdSe nanorods, the near degeneracy in spherical quantum dot breaks as we discussed above. Preliminary studies comparing the optical properties of CdSe nanodots and that of CdSe nanorods of a width comparable to the diameter of the dots shows that the band gap absorption of CdSe NRs depends primarily on the width and slightly on the length[63]. The most unique characteristics of CdSe nanorods is the highly linearly polarized emission along their long axis from even slightly elongated nanorods, and the non-monotonic change of the global Stokes shift (splitting between the band gap emission and absorption peaks) with aspect ratio [65], [66]. The large global Stokes shift in CdSe nanorods could be very helpful in opto-electronics application such as LEDs, and quantum dot lasers where re-absorption could be a problem.
Recently, Hu *et al* [65] used the semiempirical pseudopotential method to calculate the electronic states of CdSe quantum rods with increasing aspect ratio. They started from a spherical dot with a certain diameter and inserted a cylindrical segment along the c-axis. In CdSe nanocrystals, the HOMOs originate from Se 4P atomic orbitals and the LUMO from Cd 5S atomic orbitals. Excited electronic states arise by exciting an electron from an occupied Se 4P orbital to Cd 5S orbital. These electronic states are strongly dependent on the size (the degree of confinement). Since increasing the aspect ratio only reduces confinement along the Z-direction, some energy levels are sensitive to the length of the rod much more than others, and level crossing occurs. For HOMO levels, the levels consisting of more Se $4P_Z$ component are more dependent on the length than those consisting of Se $4P_{x,y}$. By increasing the rod length, the energy levels converge into several energy levels. This is a transition from zero-dimensional confinement (0D) to one-dimensional confinement (1D), where a continuous band forms along the Z-axis. For this reason, more versatile nanoelectronic and optical devices, which combine the advantage of 0D and 1D confinement, can potentially be made using quantum nanorods as building blocks [67].

1.3.2 Surface and shallow traps.

The other mechanism, which has been used to explain the unusually long radiative lifetime, is the surface trapping since the fluorescence from quantum dots is very sensitive to the surface modification. The long life-time could be attributed to the

recombination of weakly overlapping surface-localized states [49]. Brus *et al.* [49] explained surface defects by two different types of traps: shallow traps and deep traps. Deep traps are essentially localized in space at a lattice site defect and lie in the middle of the band gap, while the other traps (shallow) lie within a few milli-electronvolts of the band edge, the energy levels of surface traps depend on the size of the NDs. Decreasing the size induces more predominant splitting of the energy levels for the shallow than the deep traps, thus no distinguish between the two types of traps in the small crystals have a strong confined regime. The energy range between traps and the delocalized states from the cluster is shown in figure 1.9.

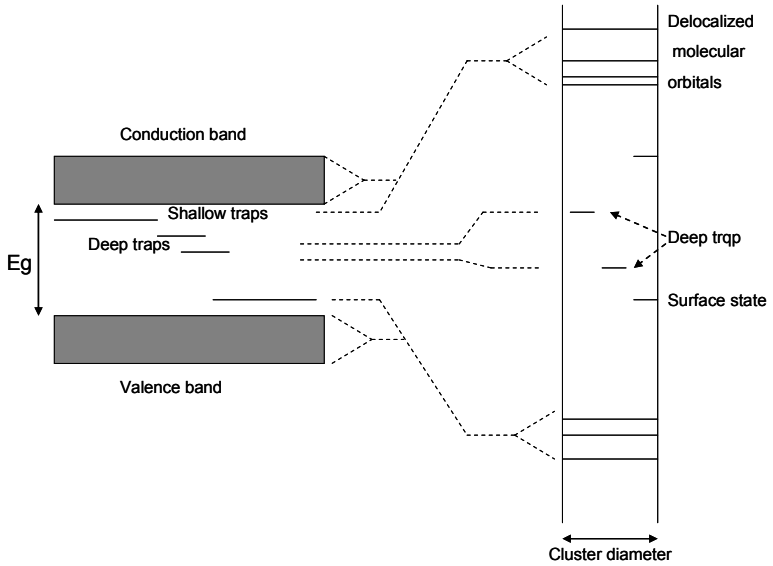

Figure 1.9: Schematic correlation diagram of traps relating bulk states (left) to nanocrystal states (right)

1.4 Phonons in nanocrystals and exciton-phonon interactions.

A phonon is a quantized mode of vibration occurring in a rigid crystal lattice. The lattice properties of nanocrystal do not differ much from those of the bulk crystal as the electron properties do because in the majority of cases nanocrystal size is considerably larger than the lattice period. In a crystal consisting of N elementary cells with n atoms in each, (3*n*N-6) elementary oscillation exist, which are called *normal modes*. All 3nN modes can be classified in term of 3n different group containing N oscillations each. Three of them are called *acoustic branches* and (3n-3) modes are referred to as *optical branches*. In other words, every vibrational state of a lattice can be described in terms of particles called phonons. In addition, two types of phonons: "acoustic" phonons and "optical" phonons appear. Acoustic phonons, which have frequencies that become small at the long wavelengths, and correspond to sound waves in the lattice. Optical phonons, which arise in crystals that have more than one atom in the unit cell, always have some minimum frequency of vibration, even when their wavelength is large. They are called optical because in ionic crystals (like sodium chloride) they are excited very easily by light (in fact, infrared radiation).

This is because they correspond to a mode of vibration where positive and negative ions at adjacent lattice sites swing against each other, creating a time-varying electrical dipole moment. Optical phonons that interact in this way with light are called *infrared active*. Optical phonons, which are Raman active, can also interact indirectly with light, through Raman scattering. Optical phonons are often abbreviated as LO and TO phonons, for the longitudinal and transverse varieties respectively. In terms of quantum mechanics the total energy of the lattice using the general Schrödinger equation is:

$$E = \frac{1}{2}\sum_i \hbar\omega_i + \sum_i n_i \hbar\omega_i \tag{1.10}$$

The first term is the harmonic oscillator zero-energy, which is a finite constant value, whereas the second term is a variable describing the excitation of the system. Various excited states are characterised by different sets of n_i numbers. Each phonon (number) in every state can take any value. The total number of phonons in crystals does not conserve because it is the sum of all n_i numbers. Thus, an ensemble of phonons has the zero chemical potential and the phonon distribution function is the Plank's formula

$$n_i = (\exp\frac{\hbar\omega_i}{KT} - 1)^{-1} \tag{1.11}$$

In the case of CdSe nanocrystal, the longitudinal (LO) optical phonon characteristic energy is 26 meV.

Exciton-phonon interaction is important in the semiconductor nanocrystal. The shape absorption and emission spectra determine by the previous interaction. At low temperature (KT<< R_y The exciton Rydberg energy ($Ry = \frac{\mu}{m_0}\frac{1}{\varepsilon^2} \times 13.6eV$)), the exciton-photon coupling dominates over exciton-phonon scattering; an exciton-photon excitation (polariton) propagates throughout a crystal. The absorption coefficient in this case describe the light-crystal interaction [68]. At high temperature (KT<R_y), exciton-phonon interaction results in noticeable absorption at photon energy than the band gap energy and the 1S- exciton resonance [69].

In nanocrystals, the phonons remain to control the intrinsic dephasing and energy relaxation and therefore determain the absorption and emission linewidths and luminescence Stokes shift. In nanocrystal have ($a << a_B$), the exciton-phonon interaction is a special interest, because smaller crystals exhibit strong confinement to be novel artificial species with controllable discreet spectra.

1.5 Carrier dynamics in semiconductor.

Electrical, thermal, or optical sources generate carrier distributions that differ from the thermal equilibrium, after removal of the excitation source; relaxation processes will force the system back into the equilibrium state. This can take anywhere from few hundred of femtosecond to a few microseconds. Even though the discrete levels

in the quantum dots increase the complexity of the carrier dynamics, the underlying physical processes are the same as for bulk case.

1.5.1 Carrier dynamics in bulk semiconductor

The carrier excitations followed by relaxation are the two dynamic processes after a short optical pulse, which detect in semiconductor.

- **Carrier generation:**

Exciting a semiconductor with any light source causes interband transition, excitonic transition or below-band gap transitions, these processes are shown in figure 1.10 for direct bad gap materials (i.e. the conduction band minimum occurs at the same position as the valence band maximum in *k*-space).

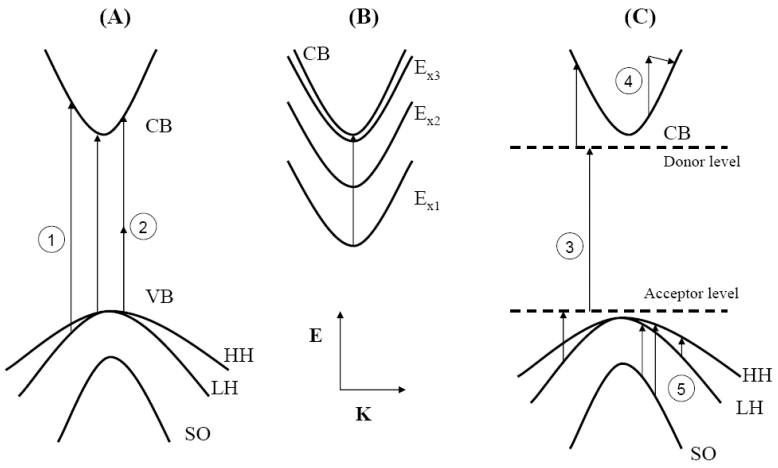

Figure 1.10: The electronic excitation in semiconductors due to interaction with photons. (A) Band to band excitation: transitions *1*. Single photon absorption. *2*. multi-photon absorption.. (B) Excitonic transition. (C) Below-band gap transitions. *3*. Impurity related transitions. *4*. interband transition. *5*. Inter-valence band transitions.

If the photon energy is larger than the band gap, interband transitions dominate, exciting electron from the valence band into the conduction band. Following Einstein's description of stimulated absorption, electron-hole pairs are created with a rate.

$$G = B_{12} P_1 (1 - P_2) \rho(h\nu) \tag{1.12}$$

Where, 1 denotes initial state (valence band) and 2 the final state (conduction band). B_{12} is the Einstein coefficient for stimulated absorption, $P_{1,2}$ the occupation probability for electrons in both states (conduction and valence bands) and $\rho(h\nu)$ density of phonons with an energy $\rho(h\nu)$

- **Relaxation:**

Coherent regime. The electromagnetic field of an ultrashort optical pulse generates a macroscopic polarization in a semiconductor. Carriers have well-defined relationship with each other and with the external field. This coherence is lost due to various efficient scattering mechanism, e.g. momentum, carrier-carrier and hole-phonon scattering[70]. Phase of the individual carriers are changed randomly within a time range of only a few tens to hundreds femtoseconds, which is referred to as dephasing. Because of the discrete energy levels in QDs, these scattering mechanisms are suppressed. Consequently, dephasing times of several hundreds of picoseconds are found at low temperatures [71].

Non-thermal regime. Due to the carrier-carrier and carrier-phonon scattering, electrons and holes are redistributed throughout the conduction and valence bands. The energy distribution of the carrier population immediately after excitation cannot be described by Fermi-Dirak or Maxwell-Boltezmann distributions. After a few hundred of femtoseconds a Fermi-Dirak distribution is reached. Since the energy exchange via scattering processes is more efficient between carriers of the same type, the characteristic temperatures for electrons and holes are different.

Hot-carrier regime. As the temperatures that describe the carrier distributions is higher than the one for the lattice, the carrier called "hot". Thermalisations set in when carriers transfer their energies to the crystal lattice through interactions with phonons. Large populations of non-equilibrium (hot) phonons are created and the carriers are cooled to the lattice temperature.
The emission rate of longitudinal optical or acoustic phonons with energy is given by[70]:

$$C_q(=\tfrac{1}{\tau}) = \frac{2\pi}{\hbar}\cdot\sum_q \left|M_q\right|^2\cdot(n_q+1)\cdot\delta(\Delta-\hbar\omega_q) \qquad (1.13)$$

Here Δ is the carrier energy difference in energy of initial and final state and n_q the Bose-Einstein distribution function $n_q = (\exp(\hbar\omega/k_BT)-1)^{-1}$. The matrix M_q is given by the particlularr interaction process. The times of the thermalization process are about 100 ps, and depend on the carrier concentration and lattice temperature.

After all of the previous processes, carriers, phonons, and lattice are now equilibrium. And can be described by one temperature. Compared to the thermal equilibrium there are still excess carriers, which are removed both via radiative and nonradiative recombination processes as e shown in figure 1. 11.

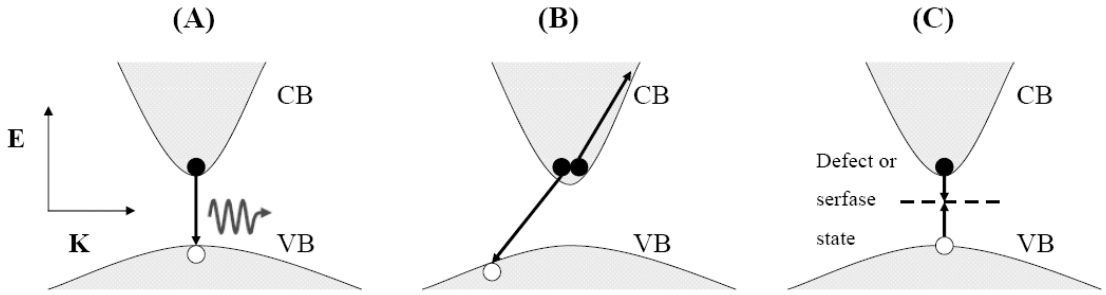

Figure 1.11: Carrier recombination mechanisms in semiconductor : (A) Radiative recombination, (B) Auger recombination , (C) recombination at defect or surface states.

- **Radiative recombination**

When an electron relaxes from the conduction band into the valence band to recombine with a hole, energy is released in form of photon. Two methods appear to have this transition: either spontaneously with a recombination rate

$$R_{spon} = A_{21} P_2 (1 - P_1) \tag{1.14}$$

Or due to stimulation by phonons

$$R_{stim} = B_{21} P_2 (1 - P_1) \rho(h\nu) \tag{1.15}$$

1 and 2 again denote valence/conduction band, $p_{1,2}$ the electron occupation probabilities and ρ the photon density. A_{21} and B_{21} are the Einstein coefficients for spontaneous and stimulated emission. In Semiconductor the occupation probability can be expressed through electron and hole concentrations, i.e.

$$p_2 \propto n \text{ and } \quad 1 - p_1 \propto p \tag{1.16}$$

A21 is proportional to the third power of the frequency of the emitted photons ν [72]

$$A_{21} = B_{21} \cdot \frac{8\pi h}{c^3} \cdot \nu^3 \tag{1.17}$$

This makes it is obvious that radiative recombination is only efficient if the transition energies involved are large.

In an indirect band gap semiconductor the, the additional interaction with a phonon, which carry the extra momentum, is required. Radiative recombination, which otherwise occurs on nanosecond timescales, is therefore slowed down drastically and can reach of several hundred of microseconds.

- **Nonradiative recombination.**

Creating photons is not the only way of realizing energy when electrons and holes recombine. Other processes are called nonradiative, since no photons are emitted.

They can be categorized into Auger recombination and recombination at defect or surface states. As we shown in the above figure 1.11.
The Auger recombination is a process in which the electron-hole is not emitted as a photon but it is transferred to third particles (an electron or a hole) that is reexcited to a higher energy state. The recombination rate is proportional to

$$R_{Auger} \propto n^2 p$$
$$R_{Auger} \propto n\ p^2 \qquad (1.18)$$

It is hence obvious that Auger processes will be important for high carrier densities. They are furthermore band gap dependent and increase exponentially as the band gap is decreased.
Deviation from a perfectly periodic structure in a crystal lattice result in localized defect in the bulk (point defect, dislocations, stacking faults) or by a surface itself (surface states . Depending on their energy levels the defects are categorized as either traps or recombination centers. When the energy difference between defect level and conduction (valence) band is small, an electron (hole) can be captured quickly. The probability of recombination with a carrier of the opposite type is rather small, though, as the energy difference to the corresponding band is large. Consequently, electrons and holes stay at the carrier traps for finite times and can return to conduction or valence bands through thermal excitation.
The other case of defects is the case of defects with energy levels deep within the forbidden gap. The situation is quite different in this case. Thermal emission of trapped carriers is significantly reduced. These levels called then recombination centre, and instead of carrier recombination at these centers, nonradiative effect via emission of phonons [73]

- **Rate equation and carrier lifetimes**

The change of the electron concentration in the band gap is given by generation rate *G*. capture rate to the defects R_n, and thermal emission rate from the defect into the conduction band G_n. In form of a rate equation we can write:

$$\frac{dn}{dt} = G - R_n - G_n \qquad (1.19)$$

The capture rate is proportional to the concentration of both the defects and the carriers.

$$R_n = C_n.N.n$$

Ignoring thermal generation, which is good approximation for deep levels, we find the following equation for the decrease of electron concentration in the conduction band after removing the generation source at t = 0

$$\frac{dn}{dt} = -R_n = -C_n \cdot N \cdot n \qquad (1.20)$$

Integration yields

$$n(t) \propto \exp(-C_n \cdot N \cdot n) = \exp(-t/\tau_n) \tag{1.21}$$

τ_n presents the an average time before an electron stays in the conduction band before it is captured by a defect.

Similar consideration for holes in the valence band lead to expressions for the hole capture rate and lifetime. At steady state, *dn/dt=dp/dt=0* then we can define an effective recombination rate if the electron and the hole are captured to the same defects:

$$R_{def} = R_n\text{-}G_n = R_p\text{-}G_p \tag{1.22}$$

$$R_{def} = \frac{C_n C_p N(n_p - n_i^{\,2})}{C_n(n+n_i) + C_p(p+p_1)} \tag{1.23}$$

Where $n_i=n_1p_1$ is the intrinsic carrier concentration and n1 and p1 are the equilibrium concentration of the electrons and holes, which will be realized if the Fermi level would coincide with the energy level of the traps.

As we assumed before, $n= p << n_1, p_1$. Then under these conditions:

$$R_{def} = \frac{C_n C_p N}{C_n + C_p} n = \frac{n}{\tau_n + \tau_p} = \frac{n}{\tau_{recomb}} \tag{1.24}$$

By combining the last result for the nonradiative (defect, Auger) and radiative (spontaneous and stimulated emission) recombination fixed above we find the relation:

$$R = R_{def} + R_{spon} + R_{stim} = A. \cdot n + B \cdot n_2 + C \cdot n_3 + R_{stim} \tag{1.25}$$

Which can be expressed in term of the carrier lifetimes τ

$$R = R_{nonrad} + R_{rad} \Rightarrow \frac{1}{\tau} = \frac{1}{\tau_{nonrad}} + \frac{1}{\tau_{rad}} \tag{1.26}$$

The nonradiative processes are much faster than the radiative ones, thus for high energy excitation, the nonradiative processes dominate the recombination statistics.

The light pulse incident on a semiconductor create initial carrier concentrations n (0) and p(0), and for low excitation energy disregard the Auger processes. One then fid the material response from the (1.21) and (1.26) to determined the radiative recombination and capture to defects as

$$n(t) = n(0) \cdot \exp\left(-t \cdot \left(\frac{1}{\tau_{rad}} + \frac{1}{\tau_n}\right)\right)$$

$$p(t) = p(0) \cdot \exp\left(-t \cdot \left(\frac{1}{\tau_{rad}} + \frac{1}{\tau_p}\right)\right) \tag{1.27}$$

This can be expressed in terms of photoluminescence intensity, the light emitted by the material due to radiative recombination is proportional to the product of the electron and hole concentrations.

$$I(t) = I(0) \cdot \exp\left(-t \cdot \left(\frac{2}{\tau_{rad}} + \frac{1}{\tau_{capt}} \right) \right) = I(0) \cdot \exp(-t / \tau_{PL}) \tag{1.28}$$

Where $I(0) \propto n(0) \cdot p(0)$, $\frac{1}{\tau_{capt}} \equiv \frac{1}{\tau_n} + \frac{1}{\tau_p}$, and $\frac{1}{\tau_{PL}} \equiv \frac{2}{\tau_{rad}} + \frac{1}{\tau_{capt}}$

τ_{PL} in the previous relations is the decay time. Thus it is possible to extract the capture rates from PL transients if the radiative recombination rate is known or much smaller than the capture rate. It is not possible to distinguish between the electrons and holes capture influences.

1.5.2 Carrier dynamics in Quantum dots.

As we indicate before, carrier dynamics in quantum dots are more complex than in bulk semiconductor. Figure 1.12 presents a sample band diagram of a QD structure after excitation from valence band to conduction bands. The excitation is assumed in the barrier.

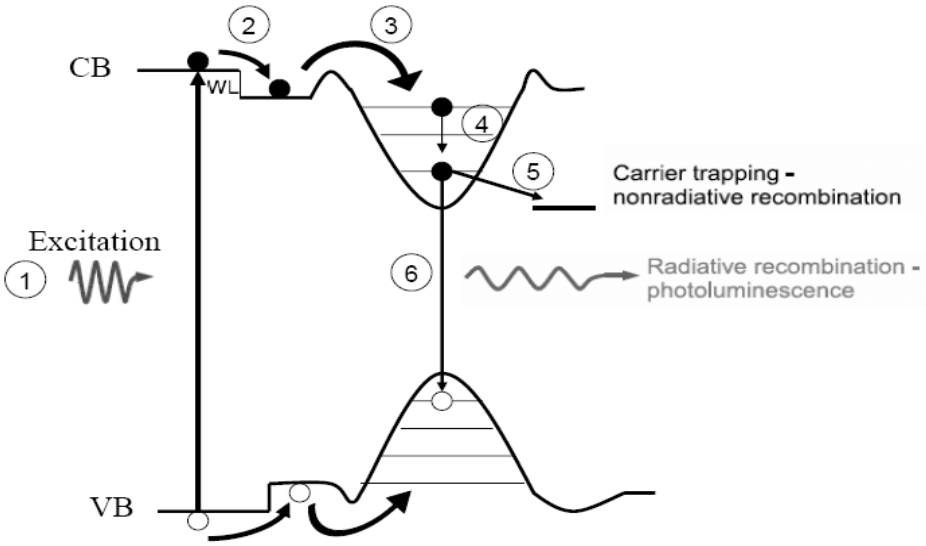

Figure 1.12: Schematic representation of possible carrier dynamics in QD structures for nonresonant excitation in the barrier. The quantized level in the wetting layer (WL) is not shown for simplicity.

The dynamics carrier processes include the following effects:
Excitation of electrons from the barrier valence band into the conduction band creates free electrons in the conduction band and free holes in the valence band, while relaxation from the barrier to the wetting layer. Capture the carrier into the

quantum dots. The capture can occur either to the ground state or to higher energy states with subsequent relaxation. Capture from the barrier state is also possible.
Carrier relaxation via carrier-carrier interaction (Auger effect) or carrier phonon interaction.
Carrier transfer from the quantum dots to a nearby deep level leading to carrier trapping or nonradiative recombination.
Radiative recombination between an electron and hole. The energy released in the process is emitted via creation of photon.
Other possible processes are radiative and nonradiative recombination of carriers in wetting layer (WL) and barrier conduction/valence band and (thermal) escape of electrons and holes from the quantum dots. For simplicity, these processes are not included in the above figure.
Photoluminescence is very important to study carrier dynamics in quantum dot structures. Carriers are ether-excited nonresonantly as it shown in the previous figure or resonantly in the QDs (from the valence band QD to the conduction band level)
In the nonresonant excitation case, electron and holes, which are created throughout certain volume determined by the focal spot diameter and absorption length, need to be transported to the quantum dot layer before they can be captured. Typical capture times are of the order of few to tens picoseconds [74]. As it shows in the figure1.13, deep level closer to the QDs can provide additional pathway for carrier capture [74]. First a carrier is captured by the deep level from the WL or barrier state. From there it can be tunnel into a quantum dot.

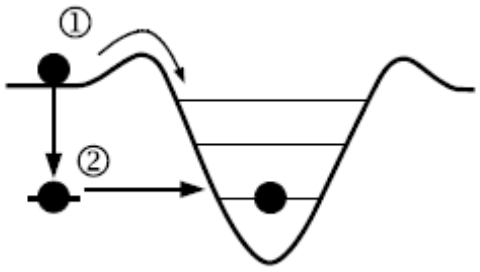

Figure 1.13: Capture channels in quantum dots: 1 direct capture over the barrier. 2 capture via deep level and following tunneling into the dot.

After being capture and confined to quantum dots, the carriers, which are typically in higher energy states, will start to relax and recombine similar as the do in bulk semiconductor. One fundamental difference in the case of quantum dot, since the level structure is discrete, interaction with LO phonons (dominate relaxation process in bulk) can only be efficient if level separation closely matches the energy of one or several phonons. The other possibility to explain the intraband relaxation is via LA phonon emission [75]. With typical very slow process (several nanosecond) [75] makes this process is special for some QDs cases.
Another possibility to relax in the discrete levels of the QD is the carrier relaxation via emission and/or absorption of more than one phonon [76, 77].

The third possibility to relax is through defect states, where the real structure are never free of defects, and some defect are situated close to the QDs, these states provide a relaxation pathway and similar to the deep levels in bulk. First, an electron is captured to the defect, and then relaxes and can be transfer back into the dot at lower energy [78].

Auger processes. Another mechanism due to the interaction between carriers provides another mechanism for relaxation by means of Auger process [70]. Same of which are illustrated in figure 1.14. At high excitation, when several (or charged) excitons are generated in the QD, an additional non-radiative relaxation pathway for electron-hole pair recombination involves a third carrier present in the nanoparticle for energy conservation. The efficiency of these Auger-like processes has been predicted to be strongly dependent on the ratio between electron and hole effective masses, as well as on the density of hole states [79].

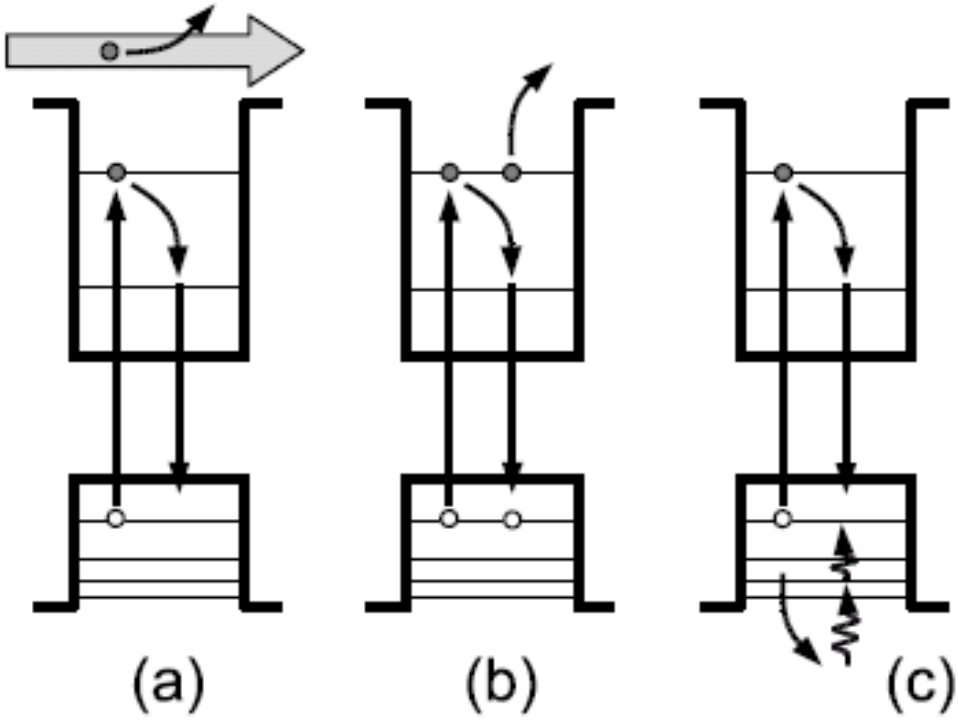

Figure 1.14: Different Auger processes in QDs: (a) Scattering of confined electron with continuum electron-hole plasma, (b) electron-electron scattering, and (c) electron-hole scattering.

1.5.3 Radiative recombination

Excited electrons and hole pairs can recombine radiatively, with transition probability *P* given by the square of the overlap integral:

$$P \propto \left| \langle \psi_{ek} | e \cdot p | 0 \rangle^2 \right| \tag{1.29}$$

Here e·p represents the dipole operator, $\langle \psi_{eh} |$ is the electron hole pair wave function and $|0\rangle$ is the ground state. The linear absorption spectrum α (ω) is proportional to *P*, which indicates the dipole allowed one-photon transitions.

In bulk semiconductors, the radiative recombination rate C_R is proportional to the density of electrons (*n*) and holes (*p*): $C_R \div np$. In QDs, due to discretization of energy levels, the decay rates mainly depend on particle size. The homogenous linewidth Γ_h of a given excited state configuration is given by the radiative lifetime τ_r:

$$\Gamma_h \approx \frac{\hbar}{\tau_r} \tag{1.30}$$

In a the great majority of QD ensemble, inhomogeneous broadening dominates the width of transitions peaks, as typical radiative lifetimes for the lowest interband excitonic transition range from hundreds of ps to ~ 1 microsecond (which corresponds to homogeneous linewidths in the order of 10^{-2}-10^{-7} meV).

Chapter 2

Description of the experimental set-ups

2.1 Overview

This chapter collects the technical details of the related but yet diverse experiments contributing to this work: Absorption, photoluminescence, and photoluminescence-excitation set-ups, time-resolved spectroscopy, and time correlated single photon counting techniques. Finally, we will describe the different shapes and structures CdSe Nanocrystals (NCs) we studied, chemical methods preparations, and their characterisation.

2.2 Steady state Absorption and fluorescence.

2.2.1 Absorption measurements.

We recorded the absorption spectra using two standard spectrometers; a Perkin-Elmer Lambda 35 and a SHIMADZU UV-3600. In solution, the sample was dispersed in 10 mm fluorescence cuvettes filled with the toluene, while in the case of film samples, a CdSe samples dispersed in a thin (1 mm) film (butyl methacrylate comethyl methecrylate) is placed perpendicularly between the light source and the detector.

To characterize the absorption of a sample we use the optical density OD or the absorbance A which is obtained by using the decadic logarithm:

$$OD = A = -Log_{10}(\frac{S}{R}) = -Log_{10}(T) \qquad (2.1)$$

Where the transmission T is the ratio of the transmitted light S (Signal) and the incident light R[80].

2.2.2 Fluorescence and low resolution excitation measurements.

We recorded the fluorescence and the excitation spectra of our samples CdSe nanoparticle solutions using a SPEX Fluorolog 2 system. Two different light sources were used: (A) a 150 W quartz-tungsten-halogen lamp (Oriel 6333 lamp in an Oriel 66881 housing with an Oriel F/0.85 pyrex Condenser and an Oriel 68938 constant power supply) in the visible region, (B) a high pressure 500W Xe-arc lamp in the near ultraviolet region. The higher power of the Xe lamp compared to the halogen lamp makes it particularly suitable for fluorescence measurements, where intense light is an advantage. However, the light intensity of the Xe lamp fluctuates with time at fixed wavelength and its spectrum contains some intense and very narrow peaks (see figure 2.1). The latter make it unsuitable for excitation measurements. Light was dispersed through a 0.22 m pathlength monochromator (Spex 1681). Bandwidth and light intensity were controlled with two slits. Parabolic mirrors focussed the beam on the sample. A resolution of 2 nm was used for the excitation monochromator.

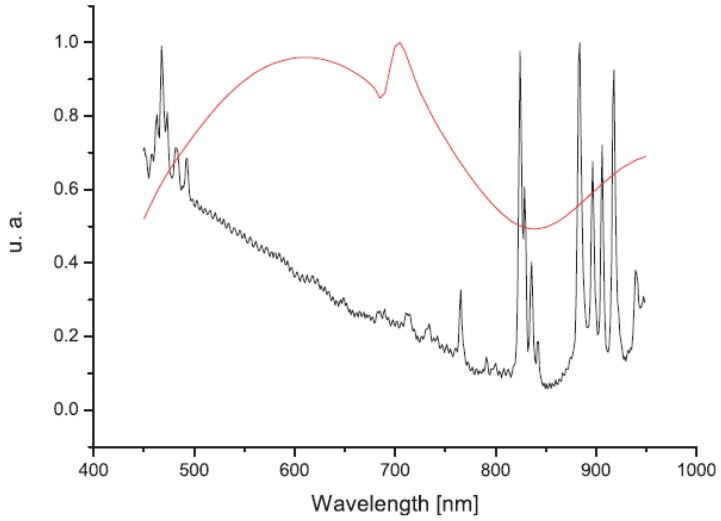

Figure 2.1: Lamp spectra: Xe lamp (black) and Quartz-Tungsten-Halogen lamp (red).

Photoluminescence spectra were collected at an angle of 90° relative to the excitation beam through another 0.22 m pathlength monochromator (Spex 1681), with a resolution of 4 nm during emission scans, and 2 nm during excitation scans. The solution spectra were taken with an optical density below 0.05 at excitation wavelengths. This low absorption value should keep at a negligible level reabsorption of the emitted light by the sample. A Hamamatsu R 928 photomultiplier tube was used to measure the luminescence photons.

In an excitation spectrum, the intensity of an emission band is recorded as a function of the excitation wavelength. Excitation spectra provide a link between the absorption and emission spectra, and can be used to distinguish between emission

bands due to different species. Since the intensity of the emitted light depends on the number of absorbed photons (in some cases the samples have a very weak absorption or are strongly scattering), excitation spectra can also substitute the very difficult absorption measurements, as the detection of fluorescence is background free and is made very efficient by the use of intense laser light for excitation.
For the scans of the PLE spectra, the incident beam was mechanically chopped at a frequency of 250 Hz, and all signals were measured using lock-in amplifiers (SR830 from Stanford Research System). The use of a lock-in amplifier improves considerably the signal /noise ratio. Fluctuations in the excitation intensity were monitored by a Hamamatsu photodiode placed behind a beam splitter after the chopper. The correction factor used was the ratio of the photodiode (PHD) signal measured without and with the sample (figure 2.2)

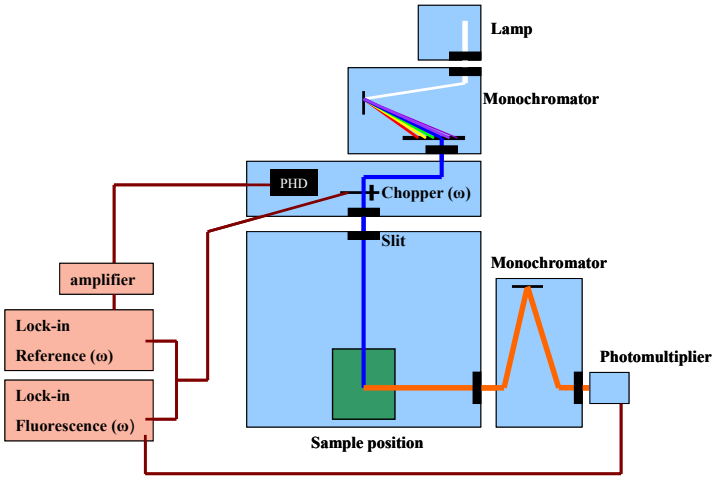

Figure 2.2: Fluorescence and photoluminescence excitation spectra set-up (see text for explanation).

Another measurements were recorded using the above set-up is the room temperature Fluorescence quantum yield (QY), which determines by comparing the integrated emission band of the NC solution to the integrated emission band of reference dye measured under identical conditions. The concentration in two cuvettes containing respectively the sample solution and Rhodamine 6G in ethanol were adjusted to values such that the absorption at the excitation wavelength (usually 480 nm) was 0.05 OD. The ratio between the integrated emission, multiplied by 95% (the QY of Rhodamine 6G[81]) gives the QY of the sample. Generally the used equation is:

$$QY_{NC} = \frac{I_{NC}}{I_{Dye}} \times \frac{OD_{Dye}}{OD_{NC}} QY_{Dye} \qquad (2.2)$$

QY_{NC} and QY_{Dye} for the quantum yield of the NC and the dye respectively. I_{NC} and I_{Dye} are the integrated emission band, and OD_{NC} and OD_{Dye} the optical densities at the excitation wavelength of the NC and the Dye respectively.

2.3 High resolution fluorescence line-narrowing and photoluminescence excitation spectra at low temperature.

The second photoluminescence excitation set-up were used later to record the high resolution photoluminescence excitation (PLE) and the fluorescence line narrowing (FLN) spectra of CdSe dispersed in a thin film of poly (butyl methacrylate comethyl methacrylate) at low temperature (4 K). The aim of this work is resolving the band-edge exciton at this range of temperatures using the techniques presented above. FLN and PLE spectroscopes can provide higher resolution and reveal band-edge structure [63]. In FLN, a subset of the sample distribution is optically excited, revealing a significantly narrowed and structured spectrum, which can be used to extract a model "single dot" emission line shape. PLE can be used similarly to extract "single dot" absorption information by monitoring a narrow spectral band of the full luminescence while scanning the excitation energy [63, 82].

The major experimental difficulty in the recording the PLE spectrum was to account for changes in laser power while the laser wavelength was scanned. This was particularly important when broad, unstructured features are present in the spectrum. In addition to the variation in power, the output of the frequency-doubled, tuneable nanosecond laser (Optical parametric oscillator MOPO) also showed changes in beam profile and beam direction as a function of wavelength. In order to eliminate these sources of error, our direct observable was the FLN, which observed with a CCD, at all range of laser excitation wavelengths and for different times of collection which depends on the variation in power. At each excitation wavelength, the emission signal was normalized to the peak of the scattered excitation light. For this, it was important to reduce the scatter as much as possible to avoid saturation of the CCD camera. This was possible for high quality clear film and the use of crossed polarisers between excitation source and the CCD.

The laser spot on the sample was imaged onto a 1mm thick fibre bundle. The fibre bundle output was matched to the entrance slit of a Jobin-Yvon monochromator equipped with 1200 l/mm grating and the spectra were recorded with a CCD camera at a resolution of ~0.08 nm. CCD cameras are integrating detectors of exceptional sensitivity in the spectral range from 200 nm to 900 nm, and reach quantum efficiencies as high as 50% at 500nm.

For the excitation, we use a nanosecond laser pulses (MOPO) with a repetition rate of 10 Hz tuneable between 450 nm and 800 nm. These pulses were produced by a Nd:YAG-laser-pumped optical parametric oscillator (MOPO, Spectra physics). These could be frequency doubled to obtain ultraviolet light.

The (MOPO) works in two stages. The first stage (Master oscillator) consists of a BBO-crystal, inside a wavelength-selective laser cavity for visible light. The intense

335nm pulses (~ 20% or 80 mJ of the third harmonic output of the YAG-laser) generate visible (signal) and infrared (idler) photons in the non-linear crystal. Its angle is adjusted such as that the signal photons are in resonance with the laser cavity and are amplified. Crystal orientation and grating angle can be adjusted in parallel, which allows to scan the laser wavelength. This is controlled by a computer.
An identical BBO crystal is mounted inside the second laser cavity (Power Oscillator), on the same axis as the crystal of the Master Oscillator. There are no special wavelength selective elements inside this resonator. Instead, the signal beam from the Master Oscillator acts as a seed for parametric amplification of signal and idler pulses, generated from the remaining output (320mJ/pulse) of the YAG-laser. This greatly enhances the efficiency of the parametric process and limits the bandwidth of the amplified pulses to below 1 cm^{-1}.
Near 500nm where our work has been done, the MOPO produced pulses of ~3 ns duration, with an energy of ~ 60 mJ/pulse. Towards the limiting value of operation at 450nm and 700nm this energy drops to approximately one third of the maximum value.
The main vacuum chamber consisted of a six-side cross-made of stainless steel. It was pumped by a 180 l/min turbo-pump, attached from below. The cooling finger of the cryostat was descending from the top of the chamber, the four side windows were closed by a UV–grade quartz windows. The pressure inside the chamber was typically in the range of 10^{-6} mbar when the cryostat was warm. It dropped below to 10^{-7} mbar upon cooling to liquid helium temperatures.
The sample holder at the lower end of the cooling finger consisted of a 5cm long block of highly pure copper, the film of CdSe were fixed between two pieces of glass on the surface of the copper finger. Thermal contacts between cooling finger and sample holder and windows were established using indium foil. Fluorescence detection was perpendicular to laser excitation. The sample holder could be moved in three directions.

2.4 Time resolved emission spectroscopy.

Prior to discus the decay time measurements, it is important to have a firm understanding of the meaning of the lifetime τ. If we excite a sample with an infinitely sharp (δ- function) pulse of light, the result will be an initial population *n(0)* in the excited state. The excited state population with decay rate $\Gamma + k_{nr}$ according to:

$$\frac{dn(t)}{dt} = -(\Gamma + k_{nr})n(t) \qquad (2.3)$$

Where n(t) is the number of excited molecules at time t after excitation, Γ is the radiative decay rate , and k_{nr} is the nonradiative decay rate. The result will be an exponential decay of the excited state population:

$$n(t) = n_0 \exp(-t/\tau). \qquad (2.4)$$

Note that the lifetime is the inverse of the total decay rate $\tau = (\Gamma + k_{nr})^{-1}$. As the fluorescence intensity is proportional to n (t), the Equation (2.4) can be written in term of the intensity of fluorescence.

$$(t) = I_0 \exp(-t/\tau) \tag{2.5}$$

Where I_0 is the intesity at time zero. Fluorescence lifetimes can be obtained in two ways. (1) from the time at which the intensity decrease to 1/e of its initial value, the lifetime is determined from the slope of a plot of log I(t) versus. (2) The lifetime is also the average amount of time of fluorophore remains in the excited state following excitation. This can be seen by calculating the average time <t>, which is obtained by averaging t over the intensity decay of the fluorophore:

$$< t >= \frac{\int_0^\infty tI(t)dt}{\int_0^\infty I(t)dt} = \frac{\int_0^\infty t\exp(-t/\tau)dt}{\int_0^\infty \exp(-t/\tau)dt} \tag{2.6}$$

The denominator is equal to τ. Following integration by parts, one finds that the numerator is equal to τ^2 . Hence, for a single-exponential decay the average time a fluorophore remains in the excited state is equal to the lifetime,

$$<t> = \tau \tag{2.7}$$

Equation (2.6) is not true for decay that is more complex. Such as the multi-exponential or the non-exponential decays. The average lifetime can always be calculated using equation (2.5). The average lifetime can be complex function of the parameters describing the intensity decay.

2.4.1 Time-correlated single photon counting (TCSPC) and fitting procedures.

In the following, we describe the set-up and the fit functions that used to fit the lifetime measurements.

Time-correlated single photon Time–correlated single photon counting (TCSPT) was used to retrieve the nanosecond fluorescence dynamics. Figure 2.3 summarizes the relevant elements of TCSPT (An extensive description can be found in Ref. [83]). This technique can only be used when the probability of collecting a fluorescence photon per excitation pulse is much less than one (typically < 1/100), otherwise the statistics get distorted. This condition is easily fulfilled when using high repetition rate, low pulse power, laser systems.

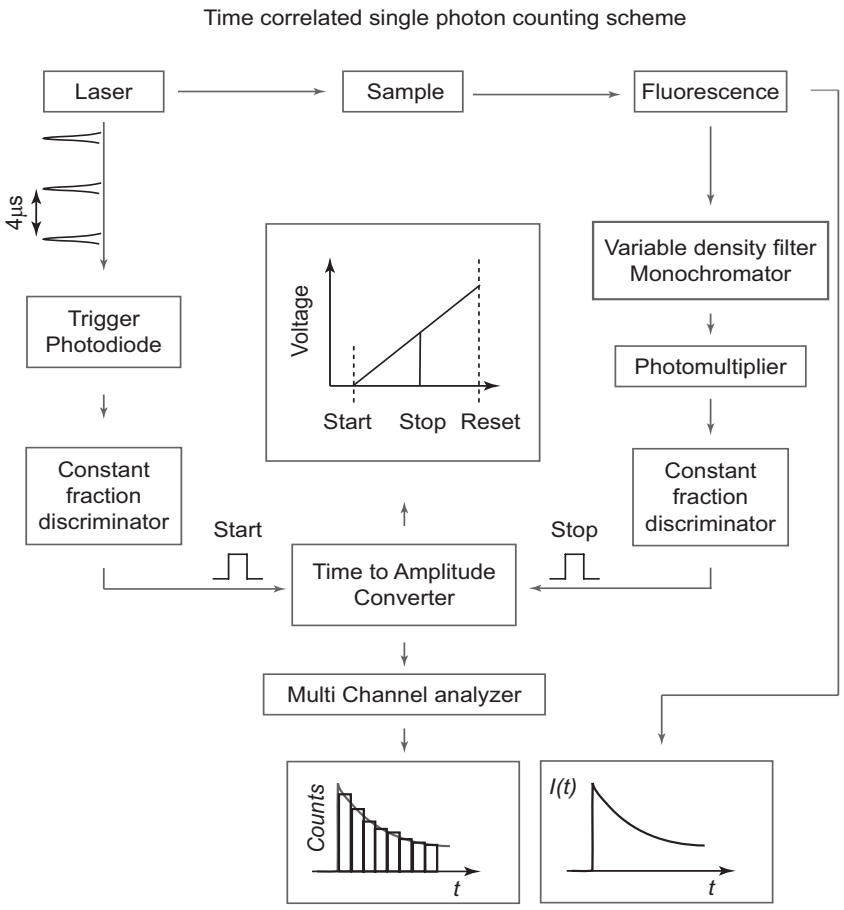

Figure 2.3: Scheme of time-correlated single photon counting prenciple.

A fraction of the amplified laser pulse was detected with a fast photo-diode, and used as start (or stop) pulse for the time to amplitude converter (TAC). The TAC receives electronic start and stops pulses, and produces a voltage that is proportional to the time between the two events. This voltage is then digitized, and a histogram of these values is kept in a multi-channel analyser. In the normal sequence, the laser gives the start pulse and the fluorescence signal produces the stop pulses. However, the order can also be inverted: since the laser produces a jitter-free pulse train, the fluorescence photon can be used as start pulse, and the next laser pulse then acts as stop pulse. This inverted scheme is useful when the repetition rate of the laser is too high, i.e. when the TAC is not capable of triggering on every laser shot. The number of detected photons must be at least 1-2 orders of magnitude lower than the number of pulses, to prevent distortion of the statistics, which brings the frequency of the start pulses within the range acceptable by the TAC.
In both cases, the result is a histogram of the arrival time of fluorescence photons, which is correlated to the fluorescence decay.
When a fluorescence photon arrives on the photomultiplier, a photoelectron is produced at the photocathode, and subsequently multiplied by a factor 10^6 to create a burst of electrons. Photomultipliers designed for TCSPC have a minimized spread of

the transit time of the electrons, and can produce sub-nanosecond electronic output pulses of ~10 mV. In order to minimize jitter[xiv], constant fraction discriminators (CFD) are employed. The CFD triggers on the zero crossing of the sum of the input pulse and a delayed and inverted replica of the pulse. With the best available detectors, this approach will typically yield an instrument response function with a width of 30 ps. In our measurements, Becker & Hickl SPC 300TCSPC was used to detect the decay kinetics, commercial photodiode (PHD) was used as a "start" signal for the TCSPC card, and a microchannel plate photomultiplier (Hamamatsu Ru551) (MCP) was used to record the decay kinetics for all samples. The instrument response function of the MCP detector is shown in figure 2.5

Laser system. Ultrashort laser pulses (~ 60 fs), at 250 kHZ repetition rate with 1 W average output power, were provided by a commercial Coherent system (figure 2.4). A 5 W diode pumped, frequency doubled laser (Verdi V5) pumps a Ti: Sapphire oscillator (Mira), which delivers ~50 fs pulses at 82 MHZ repetition rate, and 250 mW output power. The central output wavelength can be tuned from 790 to 850 nm, using a BRF crystal.
The fs pulses from the oscillator are going to the grating stretcher where they are stretched to several tens of ps and seed a regenerative amplifier (Rega 9050). This is pumped by a 10 W Verdi and provide output pulses of ~60 fs after compression, at 250 kHZ repletion rate and with 4μJ energy per pulse. The temporal and spectral profile of the pulses were characterised using a commercial autocorrelator and spectrometer (APE Pulsescope). The 400 nm laser wavelength was generated by frequency-doubling (BBO crystal 500 μm thickness) the 800 nm output of the laser. A schematic representation of the experiment is shown in figure 2.4.

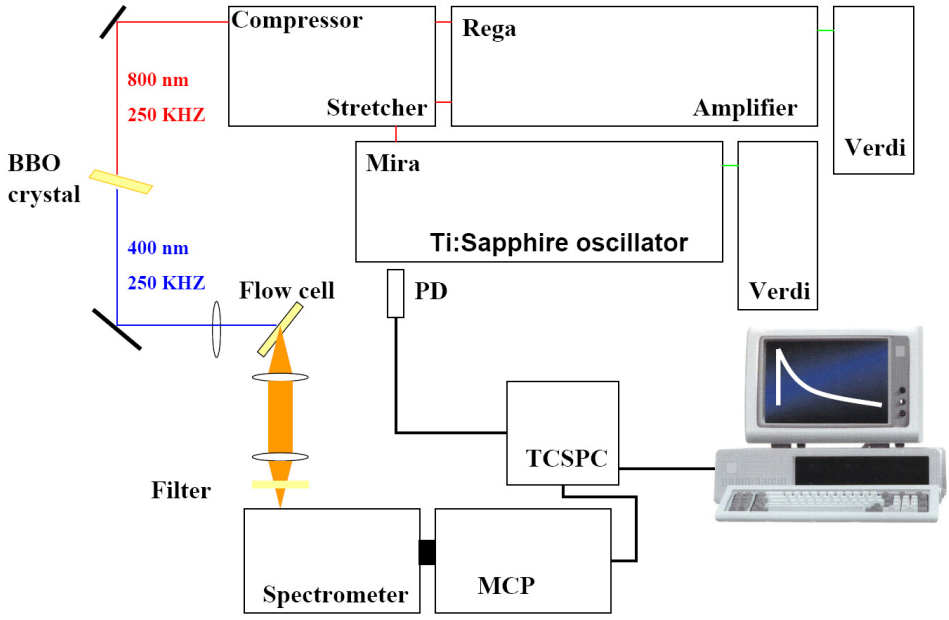

Figure 2.4: Single photon counting experimental set-up.

Sample handling and Instrument response function. The optical density of all samples was adjusted to be identical at 400 nm to ensure that the number of the absorbed
photon in each sample is the same. The solution was circulated inside a 0.5 mm thick quartz flow cell at a speed of 1 m/s to ensure constant renewal of the sample. The focal spot size was determined to be 60 μm using a beam profiler; the power range for this spot size was between (350 nW and 20 mW). The excitation power was controlled by means of variable density filters before the sample. Fluorescence was collected from the sample at 90^{o}, the fluorescence of the sample was imaged onto a monochromator (CVI-DIGIKROM- CM110) with a resolution of 1 nm in all scans. A filter GG420 was used to attenuate the remaining 400 nm light from the pump laser beam.
At low temperatures, and instead of the flow cell, small cryostat (MicrostateHE Oxford cryostat) was used. The sample (film) is mounted in vacuum on a heat exchanger, and optical access to the sample is available through the windows. The sample space and radiation shields are thermally insulated from the room temperatures surrounding by the outer vacuum chamber. This space is pumped to a high vacuum before the cryostat is cooled down. With two windows in this type of cryostat, the sample was mounted as close as possible to the inside surface of the window.
Instrument response function (IRF) is the response of the instrument (MCP) to a zero lifetime sample. This curve is typically collected using a dilute scattering solution (toluene). This decay represents the shortest time profile that can be measured by the instrument.
In our case, the IRF of the MCP shows a sharp response with a FWHM of 65 ps for 5 ns as a temporal window (chapter 4), this IRF increases to 400 ps FWHM for wide temporal window (1μs). Figure 2.5 presents an example of IRF (134 ps FWHM) for 300 ns as a temporal window. The use of logarithmic intensity scale exaggerates the low-intensity regions of the profile. One notices an after-pulse 3.8 ns after the main peak (see the inset of the figure 2.5), another peaks appears later (~ 40 ns), and finally wide background after 80ns. However, even in this case (figure 2.5) the number of photons in the peaks of the after–pulse is only about 0.04% of the counts in the peak channel. The Form and the FWHM are in good agreement with the specifications of the photomultiplier model.

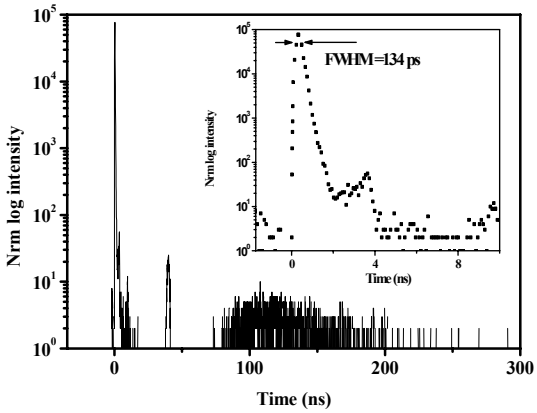

Figure 2.5: IRF of Hamamatsu Ru551MCP for 300 ns as a temporal window. The inset shows a zoom for the first 10 ns.

Fitting procedures. We used a multi-exponential fit (figure 2.6A) for all of the variations of our samples (sizes, shape, excitation powers, detection energies, temperatures, QY, and latter structures. In general, four-exponential function form of

$$I(t) = A_1 \exp(\frac{-t}{\tau_1}) + A_2 \exp(\frac{-t}{\tau_2}) + A_3 \exp(\frac{-t}{\tau_3}) + A_4 \exp(\frac{-t}{\tau_4}) \qquad (2.8)$$

τ_1, τ_2, τ_3, and τ_4 are the lifetimes constants of the fit function, while $\mathbf{A_1}$, $\mathbf{A_2}$, $\mathbf{A_3}$, and $\mathbf{A_4}$ are the pre-exponential factors. The number of components in the fit function is based on less variation residual, and on the smallest value for χ^2 (The square of the differences between the sit and the experimental points). All fit values that presented in this work have 10 % errors fit as a maximum error.

We also tried to fit the decay curves to different target functions like a stretched exponential (figure 2.6B), which has a form of $I(t)=I_0 . \exp-(t/\tau)^{\beta}$ as applied by Fisher et al.[84] and Schlegel et al.[85]. This function describes the decaying florescence intensity I(t), which drops to 1/e of its initial value I_0 after the decay time $\tau_{1/e}$ for any value of the stretching exponent β ($0<\beta \leq 1$). Small β means a broader rate of lifetime distribution, while $\beta \sim 1$ indicates a single exponential. The stretched exponential relates the lifetime to the quality of a single dot. High QY dots have a high fluorescence rate, and therefore can be easily fitted by a single exponential, while small β is related to a low fluorescence rate of bad quality dots. This fit function was tested in our work and it has two disadvantages: (i) It showed smaller (χ^2) than the normal multi-exponential fit. (ii) The residual has higher variation value. (iii) For long times, the fit does not describe the decay at all. We used these last two quality factors to accept the results of fitting in all of our relaxation processes for all parameters presented in this thesis. Figure 2.6A, B shows a typical example of the fit quality of the two functions (multi-exponential and stretched). Other fit functions like a combination of stretched and mono- or bi-exponential, with all possible orders, where tested to describe the decay kinetics of CdSe QDs, especially at low

temperatures. All of these fit functions must ignore the first 2-5 ns of the relaxation decay to be expectable. In addition, they show less quality fit than the multi-exponential. As a conclusion, all the possible fit functions point four different lifetimes to describe the whole relaxation processes in CdSe QDs.

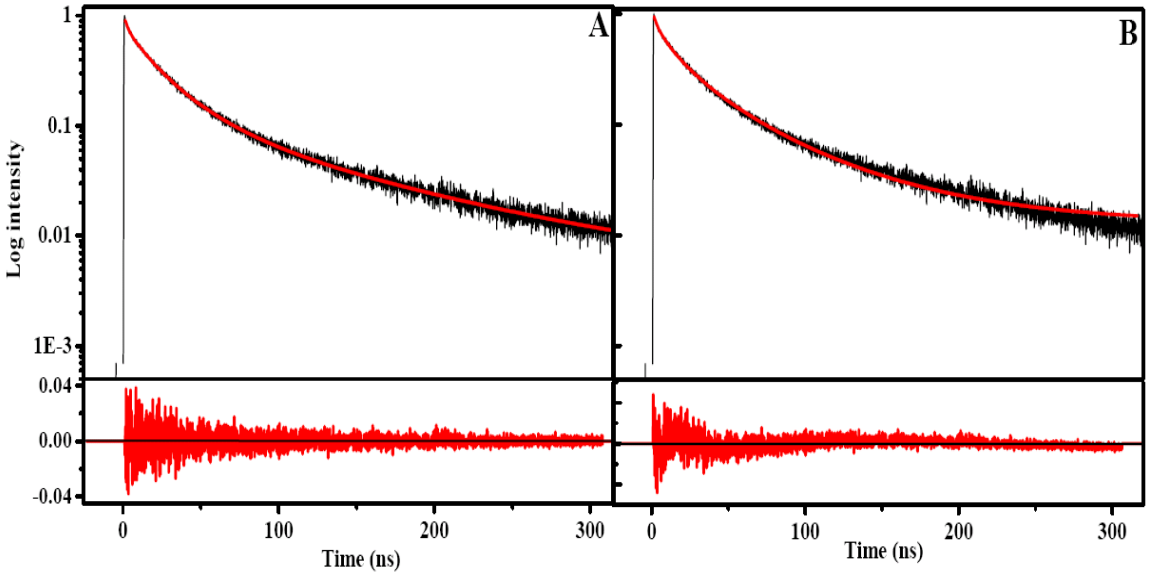

Figure 2.6: The decay kinetic of a CdSe/TOPO sample (4 nm size) fitted with. A) Four-exponential fit function. B) Streched-excponential function. The Red curve in A and B shows the residual of each function.

Again and to explain our choice of fitting function and to probe deeper the data, we fitted our decay kinetics at room temperature with and without convolution of Gaussian pulse (FWHM = 134 ps) proceeding by two steps: first, we used simple exponential fits; we did not try to deconvolute the data to take into account the instrument response function. While in the second step, we fit the data with the convolution of four exponential decays with a Gaussian pulse. The fit lifetime constants and their amplitudes show identical values in the two cases, and the effect of deconvolution does not affect our results. For this reason, we used simple exponential fits for all decay traces in this work.

2.4.2 Time-gated fluorescence:

The registration of luminescence emission spectra at different time decays of the excitation pulse is called time-gated luminescence spectroscopy. Here, the aim of time-gated fluorescence spectroscopy is to make time and spectral resolved measurements simultaneously. The advantage of this study is to allow one to resolve the relative contribution of each component in the emission spectrum. Figure 2.7 presents how time-gated fluorescence principe.

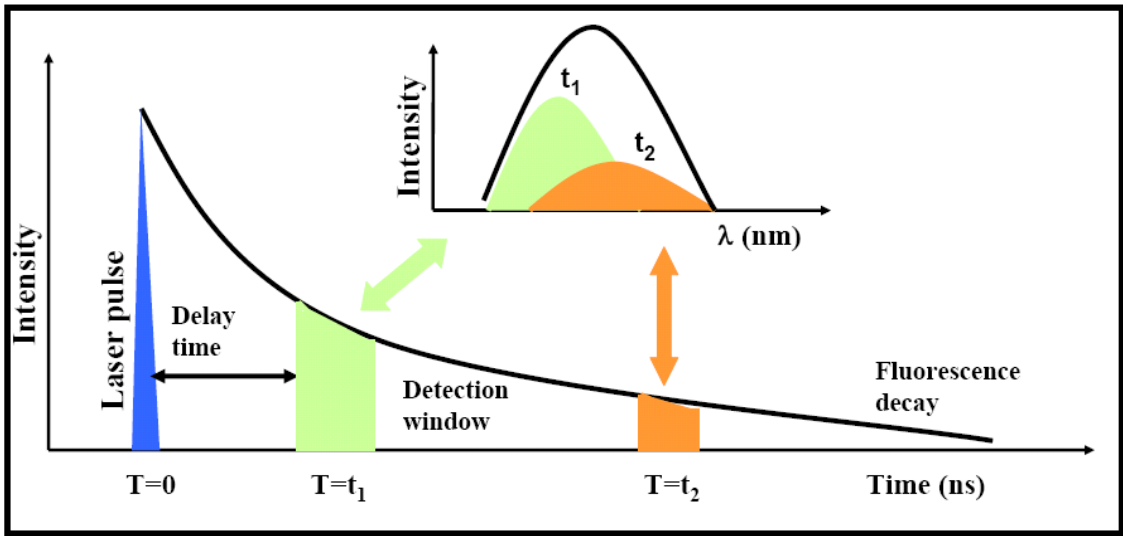

Figure 2.7: Schematic showing how time-gated emission spectra are performed, the inset presents the emission spectra at different delay t_1, and t_2.

TCSPC cards used as a counter of photon numbers for each wavelength from the whole scan between any fixed range of wavelengths, and steeps after the laser pulses. All of these measurements were controlled using a Lab View program (Appendix I) to control the MCP, the monochromator, and collect data. The interface of the Lab View program is presented in appendix II. After data collection, and for any time window for any wanted delay, we use the same lab View program that integrates all photon number from all physics effects that have decay in this chosen window (for all wavelengths detected before). Then resolve these photon numbers as a function of their wavelengths.

2.5 Sample preparation and characterization.

Several chemical methods have been used and were eventually modified in order to produce particles with uniform size, shape, structure, and a strong fluorescence yields in CdSe nanoparticles. The samples were synthesised in-house [86, 87] using wet chemistry routes, which allowed obtaining large quantities of NPs with uniform size, shape [87], and structure [86]. Chemical syntheses allow modifying the particle concentration and environment, which has been particularly useful for the fluorescence experiments and low temperature studies. I will only report on those that were successful for my research purpose and that were employed in the measurement presented in this work.

2.5.1 Colloidal solution of CdSe QDs with a wurtzite structure.

The preparation of CdSe colloidal solution wurtzite structure was based on the method introduced by Murray *et al* [36], and modified by Peng *et al* [88].

0.6 g of steric acide was added to 0.1 g cadmium oxide CdO (Both from Fluka, 99%) in a three-neck flask under stirring and N_2 flow and heated by a mantle to 160 ^oC, whereupon the mixture tuned from a brown to clear color.
5 g trioctyphosphine oxide (TOPO, Alfa, 97%) and 2.5 g hexadecylamine (HAD, Fluka, 99%) were added, and the temperature increased to 300 ^oC. 0.2 g Se powder (Riedel, 99%) was dissolved in 2.5 mL trioctylphosphine (TOP, Fluka, 90%) and swiftly poured into the reaction flask. After Se injection, the solution was kept at about 260 ^oC. The different samples were extracted at increasing times, ranging from 10 s to 10 min.
The injection process starts the nucleation phase, as the precursor reagents thermally decompose. Growth then proceeds by addition of monomers from the solution to the QD nuclei (monomer concentration is below the critical concentration for nucleation, they therefore add to existing particles rather than form new nuclei). Finally, when no unreacted monomers are longer available, growth proceeds by Ostwald ripening. Size and dispersion can be controlled during the reaction: in general, longer reaction times lead to larger particle average size [89].
To isolate the CdSe NCs from the organic subproducts and from unreacted materials, each sample was cleaned twice.
Each time, a 1:1 methanol/acetone mixture was added to the sample and then centrifuged. The CdSe NCs precipitated out and were redisolved in toluene. The different samples shown in this thesis were obtained from the same chemical synthesis except for the capping materials; oleic acid was sometimes used instead of TOPO. The dot diameters range from 2.4 to 5 nm, as estimated from the position of the first absorption peak using the calibration curves of Peng *et al* [90].

2.5.2 Colloidal solution of CdSe QDs with a zinc-blend structure.

This method was developed in-house and details can be found in ref ([86]). A mixture of 0.25 g of CdO (Fluka, 99%), and 6 mL of octadecyline(ODA, Aldrich, 97%) was loaded into a three-neck flask and heated under nitrogen until the reddish CdO powder completely dissolved and the solution became clear and colorless. In another flask, the Se solution was prepared by dissolving 0.2 g of Se powder (Riedel, 99%) in 3 mL of TOP (Fluka, 90%). Then, 3 g of ODA and 2 g of tetradecylphosphonic acid (TDPA, Alfa, 97%) were added to the Se solution. This was heated until the solution became clear. The Se solution was injected quickly into the reaction flask at 240 ^oC. The temperature dropped to 190 ^oC and then raised again to 210 ^oC and remained at this value throughout the course of growth. Again, as we described in the previous synthesis for wurtzite CdSe QDs, the different samples were extracted at increasing times, but at a different growth rate, where in this case the ranging time was from 20 s to 20 min to obtain the same band gap absorption CdSe samples as the wurtzite structure. The treatments of the as-prepared samples were the same methods described previously. The characterization of the

CdSe ZB samples (Transmission electron microscopy (TEM), and X-Ray diffraction) are shown in the figures 2.9B and 2.10.

2.5.3 Colloidal solution of CdSe nano-rod nanocrystal.

To obtain CdSe nanorods (NRs), dimethyl cadmium and Se metal mixture dissolved in tri-n-octyl-phosphine (TOP) has been injected into a hot mixture of tri-n-octyl phosphine oxide (TOPO), hexyl phosphonic acid (HPA) and tetradecyl phosphonic acid (TDPA). The relative growth rates of the different faces could be controlled by suitable variation of the ratio of TOPO and the co-surfactants (TDPA and HPA) and the concentration of the precursors. Two possible NRs can be obtained. Different lengths with nearly same diameters NRs, and same lengths NRs with different widths. The two types of NRs can be controlled be varying the precursor concentration at the growth temperature (300 °C). Figure 2.9B shows an example of CdSe NRs (length of 15.5 nm and 3.4 nm diameter) prepared in-house with the above method.

2.5.4 Colloidal solution of CdSe tetrapods-shaped nanocrystal.

Again, this method of CdSe tetrapods (TPs) preparation was developed in-house and details can be found in ref [87].The Se solution was prepared by dissolving 0.3 g of Se powder in a mixture of 3 ml trioctyl phosphine and 1.0 g octadecyl amine (ODA). The solution was heated under stirring until Se and ODA completely dissolved. A mixture of 0.25 g CdO, 4.0 g TOPO and 1.0 g octadecyl phosphonic acid (ODPA) was heated under Ar until CdO completely decomposed and the solution became clear and colourless. The solution was kept at room temperature overnight. Next, 3 ml of 1-octadecane (ODE) were added and the solution temperature increased to 240°C. The Se solution was injected quickly and the temperature dropped to 190°C. The solution was heated to 240°C again, and remained at this value throughout the course of growth. Figure 2.9C shows an example of CdSe TPs (3.3 nm diameter CdSe dot as a core, and arms of about 9 nm length and 3.4 nm thickness) prepared according to the recent method.

2.5.5 Purification process.

Nanoparticles with the previous different sizes, shapes, and structures appears as a colloidal core of CdSe surrounded by organic ligands (capping material) as we shown in figure 2.7. These particles partially prevent surface reconstruction and defect formation. In our case, the particles can be dissolved in polar solvents (toluene, hexane, chloroform). The purification treatment is based on washing the sample by adding a mixture of methanol and acetone to the solution. The mixture was then centrifuged for about ten minute. The nanoparticles, which precipitated after this

process, are re-dissolved. This treatment can be repeated a couple of times to have clean sample (less ligand), but with lower QY than before.

2.5.6 Preparation of film.

To mount the samples in the helium cryostat for temperature dependence studies, we prepared our samples in two forms. The first form was CdSe embedded in an elastic polymer film (butyl methacrylate-comethy methacrylate) prepared, according to method presented by J. Lee *et al* [91], by dissolving 0.1 g of Azoisobutyronitrile (Fluka, 95%) powder as initiator in a mixture of 5 mL of monomer (Lauryl Methacrylate 96%, Aldrich), 1 mL of trioctylphosphine (Fluka, 97%) and 1.5 mL of Ethylene glycol dimethacrylate (Fluka, 98%). To produce the CdSe doped polymer film, we mix 1mL of the above solution with 0.3 ml of CdSe QDs solution (absorption of 0.5 OD at 400 nm) in toluene, this mixture was heated at 60 ^{o}C for 15 min to create an elastic film with 0.2 OD at 400 nm. Figure 2.8A shows the elastic CdSe polymer film, while in 2.8B we present the fluorescence of pure film (without CdSe QDs) at different temperatures. The fluorescence peak of the film is located in the early visible range (450 nm). Generally, with the relative quantities described above, the fluorescence of the CdSe film is 10 times stronger than the fluorescence of the pure film.

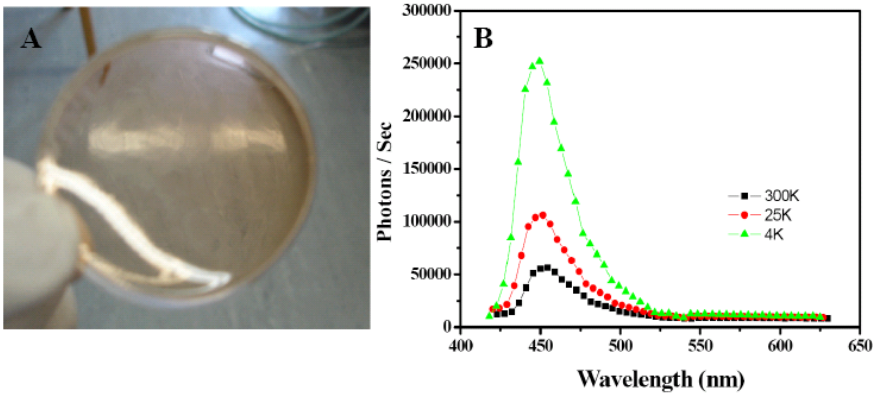

Figure 2.8: (A) The photo of the CdSe polymer film. (B) Pure polymer film fluorescence at different temperature.

The other method to obtain the CdSe QDs in a suitable form for low temperature studies (solid and clear form) was to prepare a solution of CdSe in the same way to the starting solution for the film but without starting the polymerization. This mixture was drop-cast onto a CaF_2 glass slide and left for two days to get completely dry.

2.6 Transmission electron microscopy (TEM).

Transmission electron microscopy investigation of CdSe is an effective method to determine and/or verify the size and the shape uniformity of QDs within a given

sample. Additionally, when a reaction behaves in an odd fashion or produces precursors that emit broadly in the visible spectrum, TEM provides a method for discerning whether or not the QD material was actually produced. One can "see" and take pictures of the material, or rather of its shadow. In TEM, an electron beam is focused on a monolayer of dried out QDs on a copper grid coated with carbon. Electrons pass through the CdSe QDs at a slower rate than through the plain carbon grid, and hence, a shadow is detected by the film when it is exposed for the purpose of taking a photograph. Unfortunately, at the high magnifications (necessary for observation of the 3-10 nm diameter QDs) the resolution is often not very good, but does at least indicate that a certain kind of material was produced, such as dots, rods, or other shapes. Additionally, the pictures taken through TEM provide a good means of asserting the aspect ratio and comparing samples. Scanning the pictures into another digital format can allow for enlargements of certain QDs to look at individual shapes. However, the original picture must be of high resolution and very clearly defined QDs are required for such enlargement to be effective. Our CdSe samples (shape and size) were determined with a (TEM) Philips CM20 microscope, operating at an accelerating voltage of 200 kV. A drop of a very dilute sample solution was deposited on an amorphous carbon-copper grid and left to evaporate at room temperature.

TEM was occasionally used to cross-check the average shape and size of the reaction products of our lab. Figure 2.9 shows an example of the shape and size of these products.

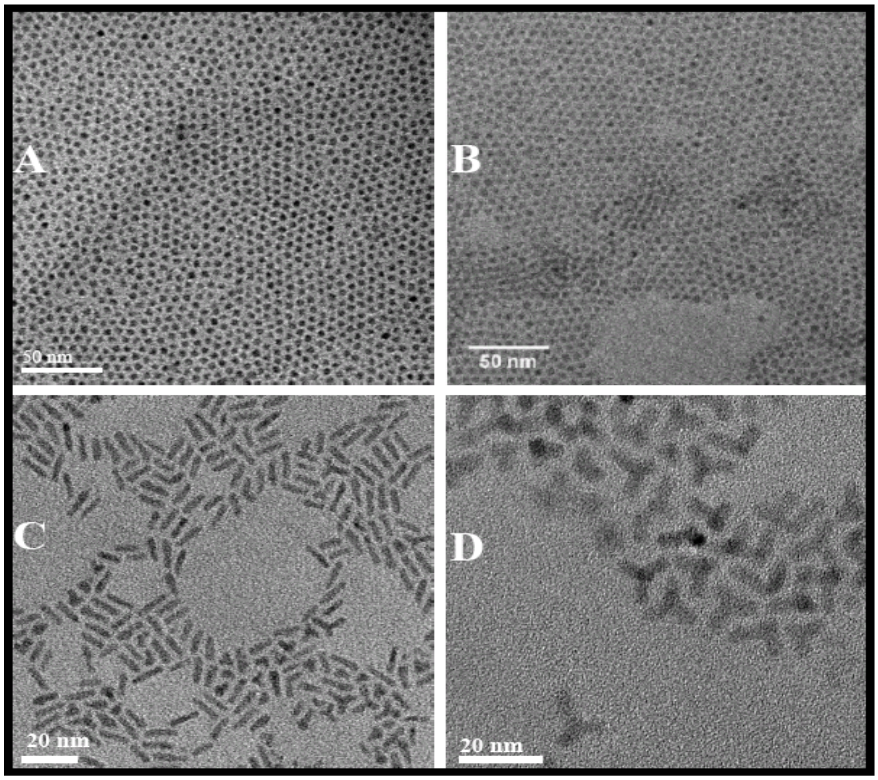

Figure 2.8: Typical TEM of ensembles of CdSe nanocrystals. A) QDs with WZ structure prepared by the method that presented in 2.5.1. B) QDs with ZB structure (2.5.2). C) NRs (2.5.3). D) TPs (2.5.1).

2.7 X-Ray diffraction.

The spacing of adjacent atoms in a crystal structure is typically about 0.3 nm. The wavelengths of X-rays (electromagnetic radiation with wavelengths between roughly 0.01 nm and 10 nm) are therefore of the same order as the atomic spacing in a crystal and can be scattered. W. L. Bragg found an simple geometrical interpretation $n\lambda = 2\,d \sin\theta$ (λ is the wavelength of incident waves which have an angle of incidence θ to a set of lattice planes at distance d, n is an integer), this equation making it easy to relate the angle of diffraction to the interplanar spacing and in conclusion to allow us to make accurate quantification of the results of experiments carried out to determine crystal structure. In typical measurements, the diffractometer projects a beam of X-rays through the crystal. The diffracted beam is collated through a narrow slit and passed through a nickel filter; in order to ensure that only one wavelength of X-rays reaches the counter as shown in figure 2.9.

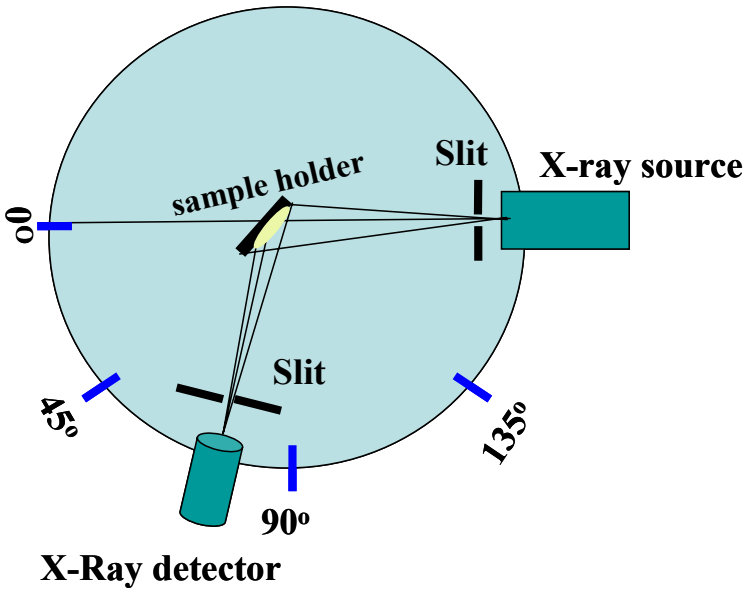

Figure 2.9: Scheme of X-ray diffractometer.

In our work, X-ray diffraction (XRD) measurements were carried out with a Philips X'Pert powder diffractometer operating with a Cu anode. The samples were prepared by precipitation with methanol from the washed toluene solution. The precipitate was let exsiccate on disoriented silicon wafers. When the Bragg conditions for constructive interference are obtained, a "reflection" is produced, and the relative peak height is generally proportional to the number of grains in a preferred orientation. The x-ray spectra generated by this technique provide a structural fingerprint of the unknown crystalline materials.

Figure 2.10 shows an example of the XRD patterns obtained for CdSe dots prepared by the method 5.2.1 (spectrum A), and 5.2.2 (spectrum B). Figure 210A shows three distinct features: the first at 2θ = 25° is due to (111) reflection and the two broad features appearing at 2θ = 42° and 50° are due to (220) and (311) reflection,

respectively. The shoulder at 2θ = 30° is due to the (200) planes. Moreover, the absence of (102) reflection at 2θ = 35° and (103) reflection at 2θ = 46°, typical of the W lattice structure (see Fig. 2.10B), is further confirms to ZB structure.

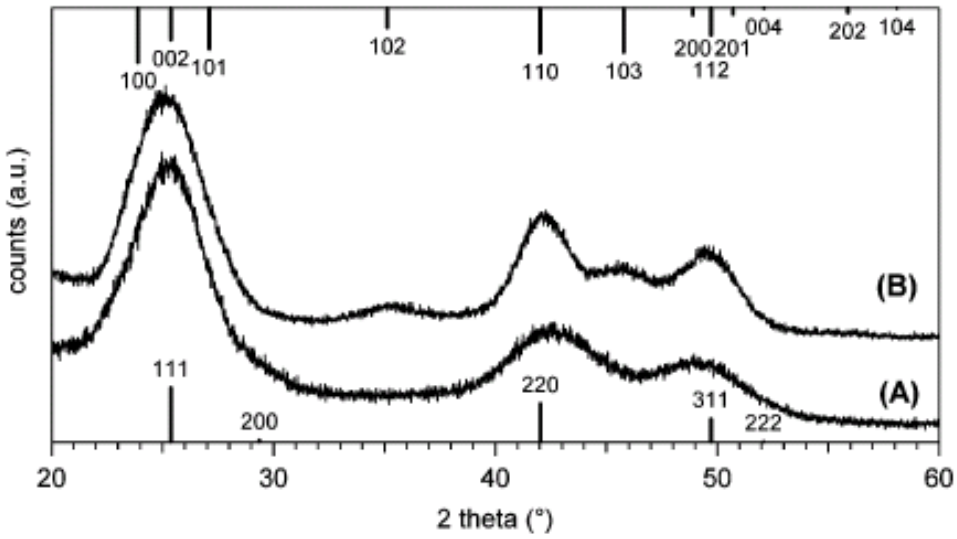

Figure 2.10: XRD pattern of CdSe NCs prepared according to the "zincblend" (A) and "wurtzite (B) preparation techniques. Trace A corresponds to 515 nm band gap absorption, whereas trace B corresponds to a 4 nm average size dot, according to TEM images. The lower (upper) vertical bars represent the position of the diffraction peaks for the bulk zinc blende (wurtzite) lattice structure, and their hight is proportional to their intensity.

Chapter 3

Nanosecond exciton recombination kinetics in colloidal wurtzite CdSe quantum dots.

3.1 Motivation and review of the literature.

Great attention has been paid to the exciton dynamics of quantum dots due to their potential uses in optoelectronic devices [92-94]. CdSe nanocrystals (NCs) are probably the most studied quantum dots (QDs) because of their tuneable band gap in the visible region and ease of preparation. The exciton recombination dynamics of CdSe NCs has been studied extensively for both, single dots [53, 84, 95, 96] and for ensemble of dots in solutions [51, 61, 97-101]. It has been reported that the band edge states responsible for the exciton radiative recombination in CdSe QDs are characterized by a dark exciton (|2>) and a bright exciton state (|1>) split by a few meV (from 6 to 16 meV, depending on size and shape of the QDs) [61, 102] as presented in chapter 1.3. At low temperatures (~ 4 K), the reported radiative lifetime of ~ 1 μsec by far [53, 103] exceeds the value found in bulk CdSe (1.0 ns) [52, 54] .
In the case of "single" CdSe quantum dots, fluorescence decays extending over three orders of magnitude appear in the majority of reports. These experiments established a correlation between the fluorescence count rate and the mono- or multi-exponential character of the decay curves [84, 96, 104], which were commonly fitted by a stretched exponential. A bi-exponential behaviour was found by O. Labeau *et al* [53] at low temperatures (<16 K) explained by a Boltzmann equilibrium between the dark and the bright exciton. Increasing the temperature (140 K), the same authors observed a disappearance of the short component and recovered a mono-exponential decay curve, with a lifetime of ~ 15-30 ns and. Fisher *et al* [95] presented a room temperature power dependence study of single CdSe nanocrystals. Their results show a fast component (< 1 ns) attributed to multiexciton emission, and a long lifetime (~ 20 ns) interpreted as the intrinsic e-h recombination. Their study ignores an additional long component of about 100 ns.

In experiments on ensembles of ZnS-capped CdSe dots [97], multi-exponential behaviour was observed at short times but the long time behaviour was fitted with a mono-exponential, with a lifetime of ~ 1 μ s at T<2K. The work indicates a constant lifetime of 20 ns above 100 K. The data shows unclear dependence from this temperature up to 300 K. The relative ratio between signal and background is no more than two orders.
Using size-selective resonant excitation of the lowest excited state, Bawendi *et al* [52], reported multi-exponential kinetics with a short, temperature insensitive component on the 100 ps time scale and a temperature sensitive microsecond component. The 100 ps component was attributed to an emitting state with short lifetime, while the slow component is red shifted by about 75 cm^{-1} and attributed to surface localized trap states.
Bi-exponential decay kinetics were reported by Javier *et al* [51] with a ~ (1-3) ns short component lying ~ 20 meV below a ~ (20-30) ns long one. The short component was attributed to charged excitons, while the long one to neutral excitons. The data in this work was fitted in linear scale for only one order of signal to background ratio, and with a 120 ns time window.
Another and different interpretation for the lifetime decay in CdSe was reported by Wang *et al* [105]. A bi-exponential decay with a short 2-5 ns and a long 15-25 ns component was detected. They concluded that the long component is surface-related while the short one was the radiative electron-hole recombination in CdSe nanodots.
Finally, Zhang *et al [98]* studied CdS-capped CdSe dots deposited on SiO_2 substrates. They report mono-exponential kinetics with a decay time of ~ 30 ns. They also showed that depending on the SiO_2 thickness separating the dots from the Silicate surface, the lifetime showed variation by as much as a factor of 2 due to the interaction with the SiO_2 surface. This result shows the extreme sensitivity of the spontaneous emission rate to environment effects presumably, even in the absence of charges.

Although there is still some discussion about the interpretations of the decay components in literature, the picture which arises from these observations and supported by numerous calculations [63] indicates that the lowest single exciton state is optically forbidden with a radiative lifetime of hundreds of ns to ~ 1 μs, while the bright exciton lying just few meV above, has a lifetime of about 10-20 ns. Single molecule spectroscopy shows a bi-exponential fluorescence decay at very low temperatures, while at high temperatures a single fluorescence lifetime of about 20 ns, indicates rapid thermal equilibrium between dark and bright state [103]. The dynamics get more complex for single molecules with low quantum yield. In measurements on ensembles of nanoparticles non-exponential decays are always found, revealing faster components due to trapping. At room temperature, slower decay components (>50 ns) have not been discussed in literature. This reported component was measured in many works for single dots [95] and ensemble of dots [52, 106] without any deeper investigation. This component lies in the same lifetime

range as the proposed dark state lifetime at low temperatures, especially in the case of an ensemble of dots. In table I, II, we classify the works results of a various studies, according to dot size, excitation power, capping material, and type of experiment (on single or ensemble of dots).
The general tendency that can be gathered from tables I and II, and from the above discussion is that: In the case of ensemble of dots, it seems that multi-exponential behaviour is due to the inhomogeneous sample quality, which affects groups of dots with different relaxation rates. This is supported by the experiments on single dots discussed above, where multi-exponential kinetics arise when weak emission dots count rates are integrated, while mono-exponential kinetics is recovered when only the highest count rates are integrated.
For a uniform sample, the decay should be mono-exponential at room temperature, as argued by Labeau *et al [53]*, with a lifetime in the 15-30 ns range. The origin of the bi-exponential kinetics with typical 1-5 ns and 15-30 ns lifetime [51], [98] is unclear in the light of the above.

From the tables I and II, we note that the exact interpretation of the different components is still a topic of much discussion. Each study highlights different aspects of the kinetics as independent effect, while more realistically, the combination of a large number of different physical effects plays an intrinsic role in the relaxation process of the CdSe QDs.
While single dot measurements are very interesting for our understanding of their properties, care must be taken, when extrapolating these results to realistic conditions. They provided important insight to different relaxation behaviours and showed that multi-exponential behaviour can occur in single dot, while high QY dots show nearly the behaviour predicted by the theoretical level scheme. But we must not forget that single dot measurement always have to be performed under very special conditions. It is also shown by our results that the properties of NCs can be strongly influenced by the environment and the preparation. For clarifying more NC properties in solution, measurements on ensemble are essential; all the studies presented in this work were concerned with ensemble measurement of QDs in solution. For most "real-life" application of NCs these results are much more relevant than single dot experiments, and the behaviour of ensembles of dots is still under much discussion as it shows from the different lifetime values (table I and II).
In this chapter, I present a systematic study of the CdSe decay lifetime as a function of excitation, dot size, power, surface properties (different capping and quantum yield effect), and detection energy. All of the previous effects were probed in a wide temporal window (up to 1 μs). The study shows four order of magnitude of signal to background ratio, and a multi-exponential (in general four exponentials) fit is the best way to describe the kinetics. We relate each component in the fit function to possible physical effects. The dependence of each component on the different parameters and their effects on the total relaxation dynamics of the CdSe QDs at room temperature is presented.

TABLE 3. I: The literature resume of the ensembles CdSe QDs dynamics.

Reference	λ_{exc}, rep rate, and power	Size range	Capping material	type of fit	Decay times (τ_1, τ_2,..) And Amplitudes (A_1, A_2, …)	Notes
[51]	320 nm, 20 μW	From 1.6 up to 2.8 nm		Bi-exp	τ_1= 1-3 ns τ_2= (20-30) ns $A_1/(A_1+A_2)$= 0.45 up to 0.6 Size dependence	Ensemble of Dots RT
[103]	410 nm, <3 nJ/cm²	1.3, 1.8, and 2.1 nm radius	ZnS and TOPO. Diluted on polymer and then dropped onto glass slide	Multi-exp (Short time), mono (long time)	τ_{short} = 20-30 ns τ_{long} =1 mic sec at low Temp	Ensemble of dots, temp-dependence
[53]	514 nm	1.9 nm radius	ZnS	RT : Multi-exp 16 K: Multi-exp 16 K : bi-exp 140 K:mono-exp	τ (RT, ensemble) ~ 18 ns. τ (16 K ensemble)~ 100 ns. τ (16 K single) ~ 73 ns. τ (140 K single) ~19 ns	(Single and ensemble of Dots) temp- dependence
[98]	400 nm. 16.4 MHz, 6.3 pJ/pulse	2 nm radius	CdSe/CdS on the SiO2 substrate and a layer of PMMA polymer	Mono-exp, temporal window (only 40 ns)	τ =30 ns	Ensemble of dots (Short time window (40 ns))
[107]		3.5 – 5 nm diameter	CdSe on the PMMA solution	Bi-exp	τ_1=2-5 ns τ_2=15-25 ns	QY-dep (τ_1 is the intrinsic lifetime)
[52]	480 and 570 nm	3.2nm diameter	Partially scattering 1mm from CdSe solution	Bi-exp	τ_1=110 ps (Temperature independent) τ_2= long lifetime Temperature dependent)	Ensemble of dots, temperature dependence steady
[99]	400 nm	3 nm radius	ZnS	Stretch exp	τ_{briht} = 15 ns at RT τ_{dark} = 142 ns at 4K	5- 80 K- Ensenmble of QDs
[106]	400 nm	2.5-3 nm radius	ZnS, TOPO, and CD(OH_2)	Multi-exp	τ_1=1.5 ns A_1= 12 % τ_2=12 ns A_2= 37 % τ_3=26 ns A_3= 53 % τ_4=160 ns A_4= 8.5 % For all CdSe capping	Different capping test, different QY test, ensemble of Dots

TABLE 3. II: The literature resume of the single CdSe QD dynamic.

Reference	**λ_{exc}, rep rate, and power**	**Size range**	**Capping material**	**type of fit**	**Decay times (τ_1, τ_2,..) And Amplitudes (A_1, A_2, …)**	**Notes**
[53]	514 nm	1.9 nm radius	ZnS	RT : Multi-exp 16 K: Multi-exp 16 K : bi-exp 140 K : mono-exp	τ (RT, ensemble) ~ 18 ns. τ (16 K ensemble)~ 100 ns. τ (16 K single) ~ 73 ns. τ (140 K single) ~19 ns	(Single and ensemble of Dots) temp-dependence
[84]	414 and 532 nm 5 MHz for 414 nm. and 4.75 MHz for 532 nm	3.1, 3.3, 3.5 nm radius	ZnS (dilute in PMMA and onto a glass)	stretched exp (depend on the rate of fluorescence)	Mono-exp τ =26.5 ns. Bi-exp τ =24.6 ns. Multi-exp τ is less than the previous two values	Single dot experiment (quality sample)
[85]	458 nm, 4.7 MHz, 4-40 mW in ps mode. 60- 600 mW in the fs mode	5 and 5.6 nmdiameter	ZnS (dilut in polymer film then spin casting onto a glass)	stretched exp (depend on the rate of fluorescence)	Mono-exp τ = 19.9 ns. Bi-exp τ = 6.5 ns. Less τ for multi-exp fit	Single dot experiment (quality sample)
[95]	=400 nm, 4.75MHz	From 2.5 up to 5 nm radius	ZnS	Bi-exp at low power	τ = 29 ns τ_{short} < 1 ns τ_{short} increases as a function of power	Single dot experiment R T. A fast component intensity-dep
[104]	410 nm	3.2 nm diameter	ZnS, TOPO, and HD	Stretch exp	τ =25 ns	Single CdSe Dot R T

3.2 Results and discussion.

3.2.1 Size dependence.

To describe the dependence of the relaxation processes on the dot size, three groups of CdSe with different capping were studied. Figure 3.1 shows the absorption and the luminescence spectra of the whole set of CdSe samples used in this work, while table 3.III presents their characteristics.
The lowest possible laser pump power 0.05 μJ/cm^2 is used in these measurements, so that, less than one exciton per particle is formed [108]. Thus, multi photon processes leading to Auger processes or multiexciton formation [109] do not occur during the carrier relaxation dynamics (§ 1.5.2).

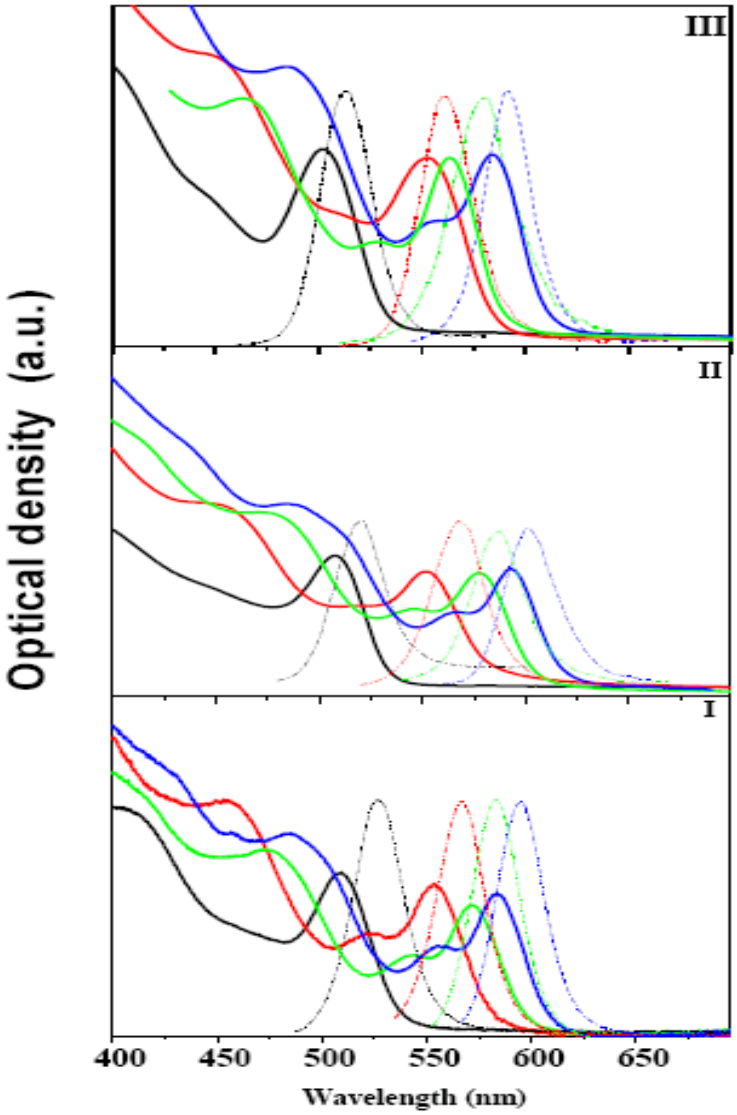

Figure 3.1: Absorption (solid line) and fluorescence (dashed line) spectra of CdSe QDs. Type I house-made CdSe/TOPO. Type II Commercial CdSe/TOPO QDs. Type III Commercial CdSe /ZnS core-shell sample.

Table 3.III: Characterization of Case QDs samples.

Type	Capping	Size (nm)	QY %	Preparation
I	TOPO	2.4 2.7 3.5 4	28 32 34 37	House-made (§ 2.5.1)
II	TOPO	2.4 3.1 3.7 4.2	20 22 24 23	Commercial (Evident Technologies)
III	ZnS	2.4 3.1 3.4 4	24 25 24 28	Commercial (Evident Technologies)

Figure 3.2 shows the decay kinetics for different dot sizes of these three types of samples. Note the excellent signal to background ratio over four orders of magnitude. The kinetics show similar general behaviour in all cases, especially, a slower decay for smaller sizes. The kinetic traces are best fitted with three or four exponentials depending on the yield and the size of the sample. The fitting parameters of the kinetic traces are listed in Table 3. IV

Type I: The larger dots and higher quantum yield (table 3.VI) are best fitted with three exponential. While for the smallest size (2.4 nm), a fourth component is added. The fit results for the large dots show that the first component has an average lifetime of about 8.5 ± 0.8 ns, the second one is 26.8 ± 0.5 ns, while the longest component is about 80 ± 3 ns. The first two components τ_1 and τ_2 become faster as the size of QDs decreases. The smallest sample (2.4 nm) shows an additional fast component (< 1 ns), while τ_2, τ_3, and τ_4 for this CdSe QDs sizes are equivalent to the other decay times described above.

Type II and III. These samples are best fitted by four-exponentials. One can notice that the fastest component with lifetime τ_1< 2 ns appears even for large dots.
Type III (ZnS capped), the first two components show the same pre-exponential values for all sizes. The third and forth components show slightly slower decays as the size decreases.

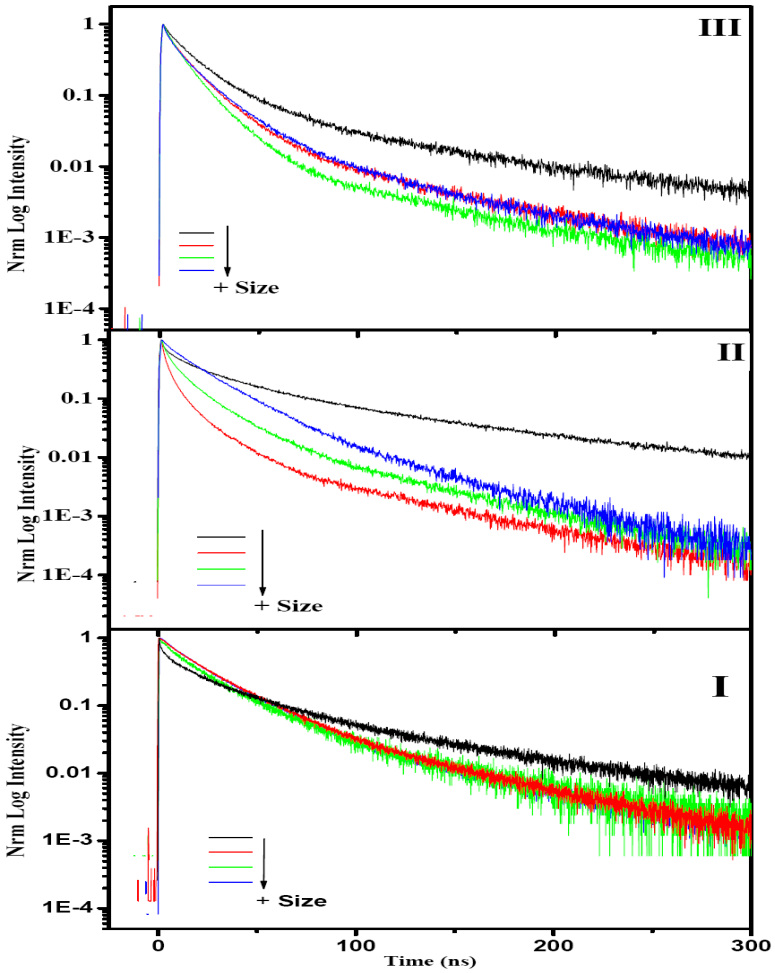

Figure 3.2: Luminescence decay curves of types I, II, and III as a function of size (see table 3.III). At low excitation power (corresponding to less than one exciton /particle). The smallest size sample shows slower decay.

TABLE 3.IV: Fit parameters of the fluorescence decay curves of the four different samples (different sizes and capping) pumped at lowpower (0.05μJ/cm^2).

Dot Diameter (nm)	type	A_1	τ_1 (ns)	A_2	τ_2 (ns)	A_3	τ_3 (ns)	A_4	τ_4 (ns)
2.4	I	0.41	0.85	0.33	5	0.20	33.2	0.06	88
2.4	II	0.40	0.85	0.33	5	0.21	28.5	0.06	84
2.4	III	0.41	1.5	0.29	9	0.25	22.3	0.05	89
2.7	I			0.32	7.7	0.63	26.8	0.05	83
3.1	II	0.39	1.05	0.32	3.2	024	26.8	0.05	78
3.1	III	0.43	1.5	0.27	5.1	0.24	15	0.03	75
3	I			0.30	8.9	0.65	27.3	0.05	80
3.7	II	0.36	1.45	0.31	6.1	0.28	15.8	0.05	76
3.4	III	0.41	1.8	0.29	6.6	0.27	17.2	0.03	73
4	I			0.30	9.1	0.63	26.3	0.07	79
4.2	II	0.33	1.8	0.29	7.3	0.34	14.5	0.04	78
4	III	0.40	1.9	0.28	8.6	0.28	17	0.04	74

3.2.2 Power dependence.

To clarify the power dependence of the exciton kinetics in colloidal CdSe QDs, we carried out a series of lifetime measurements of the colloidal CdSe/TOPO sample with 4 nm diameter (band gap absorption at 583 nm) from type I used above. The fluorescence was detected at 595 nm (emission band maximum) and the laser excitation intensity was varied in the range of 350 nW - 15 mW corresponding to the formation of 1 - 12 e-h pairs produced per dot. These numbers calculated starting from of the average number of photons absorbed per particles, which is given by:

$$\overline{N} = \frac{\sigma \lambda E}{hc}$$

Where λ is the wavelength of light, E is the laser energy per cm^2, h is Planck's constant , c is the velocity of light, and σ is the absorption cross section, At 350 nm it can be expressed as in ref [110] and is strongly dependent on dot sizes: $C_{abs} = (5.501 \times 10^5) a^3 cm^{-1}$, where a is the particle radius in cm. This empirical formula neglects scattering from the QDs. The cross section at 400 nm was obtained by rescaling σ_{350}, with the absorbance at 400. The absorption cross section is insensitive to the solvent refractive index [110]. With a pump power of 15 mW, this lead to more than 13 absorbed photons per particle for a 4-nm dot diameter. These estimates should be taken as an upper limit, since not all the absorbed photons lead to luminescence [109], due to the scattering that is caused by the chemical preparation of the samples [111].

Figure 3.3 presents five decay curves at different excitation power. At low power (< 0.4 mJ/cm^2) corresponding to the formation of less than one exciton per particle [108, 112] the decay time is fitted, as before, by three-exponentials with decay times τ_2 = 9.1 ns, τ_3 = 26.3 ns, and τ_4 = 79 ns. As power increases (0.85 mJ/cm^2), an addition shorter decay (<2 ns) appears (inset of the figure 3.3). The traces are best fitted with tri- or multi-exponential (4 components) depending on the excitation power. The amplitude of this fastest component A_1 increases dramatically as the excitation power increases, while its decay time decreases. The fit results are given in table 3.V.

As far as pre-exponential factor are concerned, table 3.V shows that the τ_3 (~ 26 ns) component is dominant at low power, while τ_2 has an amplitude of two times less but still overall significant. Remarkable decrease in the relative weight of the τ_3 component is observed as the power increases, and it is accompanied by a parallel increase of the relative weight $\mathbf{A_1}$ and $\mathbf{A_2}$. The longest component τ_4 (~ 79 ns) has a weaker weight $\mathbf{A_4}$ of < 7 % of the total weight at low excitation power, and it decreases to 2% at high excitation. All components exhibit less variation in their lifetime's values as the power increases.

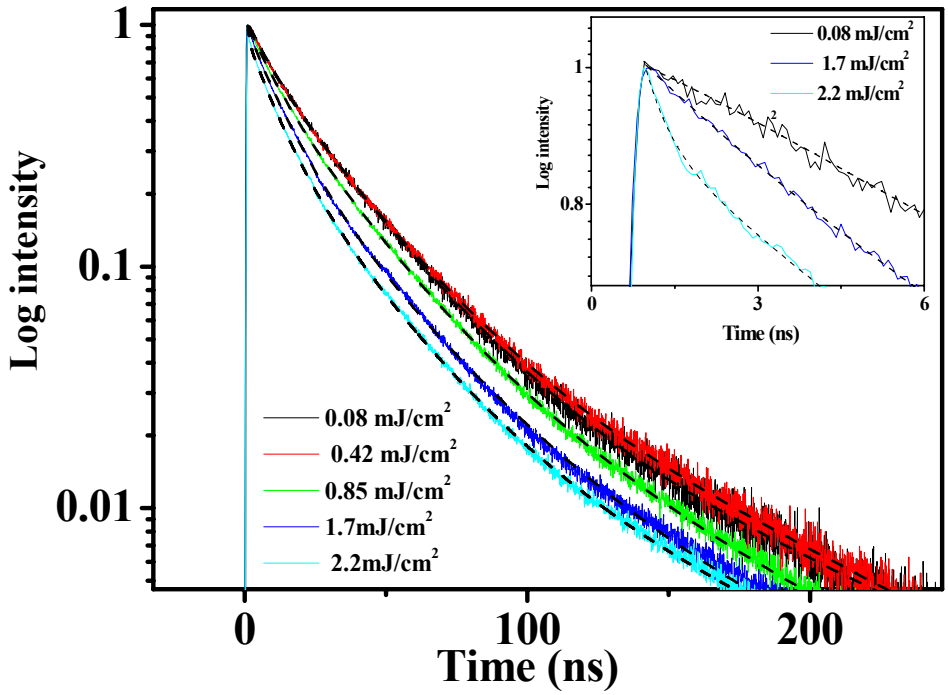

Figure 3.3: Relaxation kinetics of CdSe QDs (type I) (4 nm diameter) as a function of excitation power. The black traces represent the multi-exponential fit. The inset shows the early response of the fluorescence.

TABLE 3.V: Fit parameters of the decay curves at different excitation powers of a 4 nm CdSe (Type I) dot.

Excitation power	A_1	τ_1 (ns)	A_2	τ_2 (ns)	A_3	τ_3 (ns)	A_4	τ_4 (ns)
0.05 μJ/cm²			0.30	9.1	0.63	26.3	0.07	79
0.4 mJ/cm²			0.28	8.5	0.65	27	0.07	79.2
0.85 mJ/cm²	0.12	1.8	0.31	8.8	0.5	27	0.07	80
1.7 mJ/cm²	0.20	0.95	0.55	10	0.22	29	0.03	80
2.2 mJ/cm²	0.30	0.50	0.49	9.3	0.20	25	0.02	81.5

For the samples, where the fastest component appears even at low power (I and II CdSe types or small sample (2.4 nm from I) (See table III)), the effect of power shows similar dependence as above.

In summary: (a) The effect of power appears only on τ_1 which decreases to 0.5 with increasing the power up to 2.2 mJ/cm²

(b) The relative amplitudes of A_1 and A_2 increase with power, while the preexponential factors A_3 and A_4 show opposite dependence.

3.2.3 Wavelength Dependence.

As the CdSe emission spectra are multi-components, and to see if we can isolate different spectral components, we studied the lifetime decay of a 4 nm QDs (type I, QY = 37 %) as a function of the emission wavelength, and for two different laser excitation powers: 0.5 μW and 6 mW, corresponding to 0.08 mJ/cm^2 and 0.85 mJ/cm^2.
At low pump power corresponding to < 1 exciton/particle, we find no dependence of the decay kinetics on the emission wavelength (figure 3.4A).

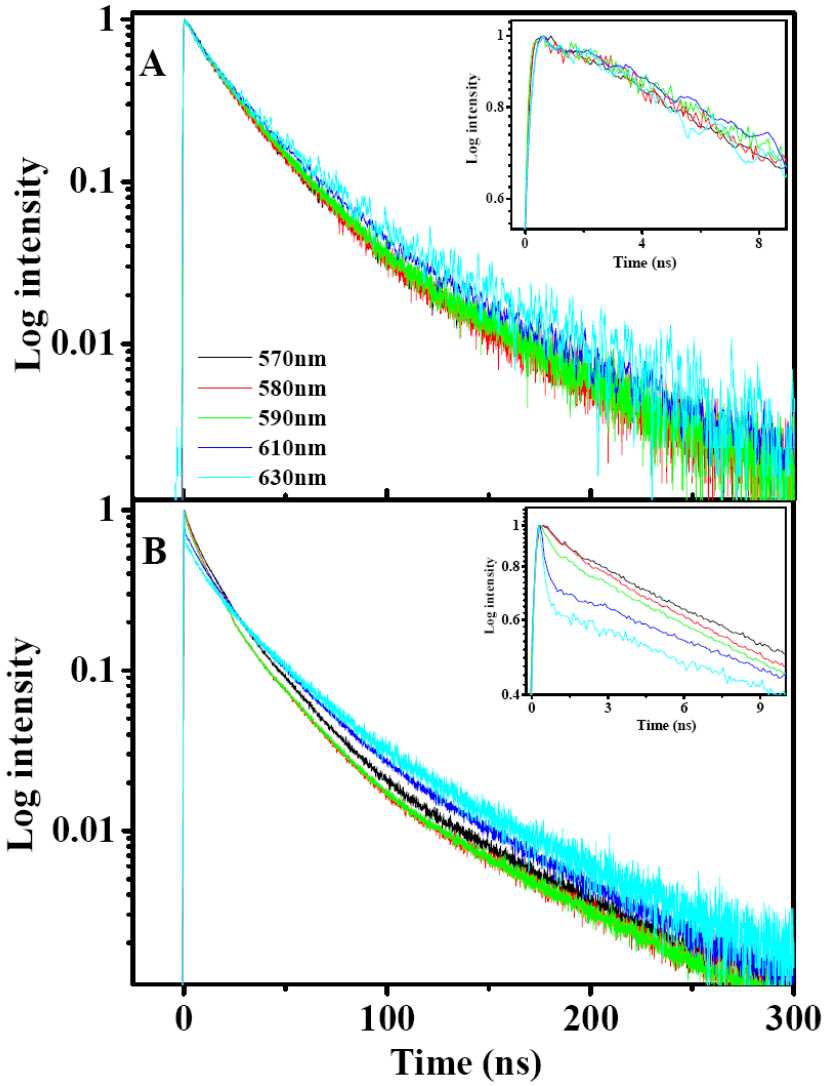

Figure 3.4: A) Decay curves at low excitation power (0.08 mJ/cm^2) and at different emission wavelengths. B) Decay curves at high power excitation (0.85 mJ/cm^2) and at different emission wavelengths.

At high laser pump power (figure 3.4B), where more than 5 excitons per particle are formed, a remarkable dependence of the decay kinetics on the emission wavelength has been detected. The decay at the low energy side (630 nm) shows a more pronounced fast component than at the high-energy side. This is clearly seen in the

fit parameters of the decay (table 3.VI), where it can be seen that the relative weight of the shortest component increases by a factor of 3 from the blue side to the red side of the emission band. This seems to occur mainly at the expense of the second components τ_2. This component (τ_2) shows faster decay but less relative amplitude at lower energy. The third component presents slower lifetime constant at lower energy that at the blue side. Unchanged values (lifetime and prefactors) for the longest component τ_4 were detected.

TABLE 3.VI: Fit parameters of the relaxation processes at different wavelength at high excitation power.

Wavelength (nm)	A_1	τ_1 (ns)	A_2	τ_2 (ns)	A_3	τ_3 (ns)	A_4	τ_4 (ns)
570 nm	0.13	1.8	0.44	11	0.37	25.5	0.06	82
590 nm	0.22	0.7	0.40	9.5	0.34	26.3	0.05	81.5
610 nm	0.26	0.4	0.26	9	0.43	28	0.05	81
630 nm	0.36	0.3	0.22	8	0.35	33	0.07	84

Further, and to resolve the spectral components in the multi-exponential decay curves at low and high excitation power, we measured nanosecond time-gated fluorescence spectra (see chapter 2) of CdSe NDs at 400 ns time delay. At low pump power 0.08 mJ/cm^2, we obtain identical gated fluorescence spectra at all time scale. The time gated fluorescence intensity decreases with time after excitation. For high excitation power, we find a small shift different between time-gated fluorescence bands at early and at late time windows as shown in figure 3.5. We find that the band in time-range of 1-5 ns is red shifted by about 5 nm with respect to the steady state fluorescence.

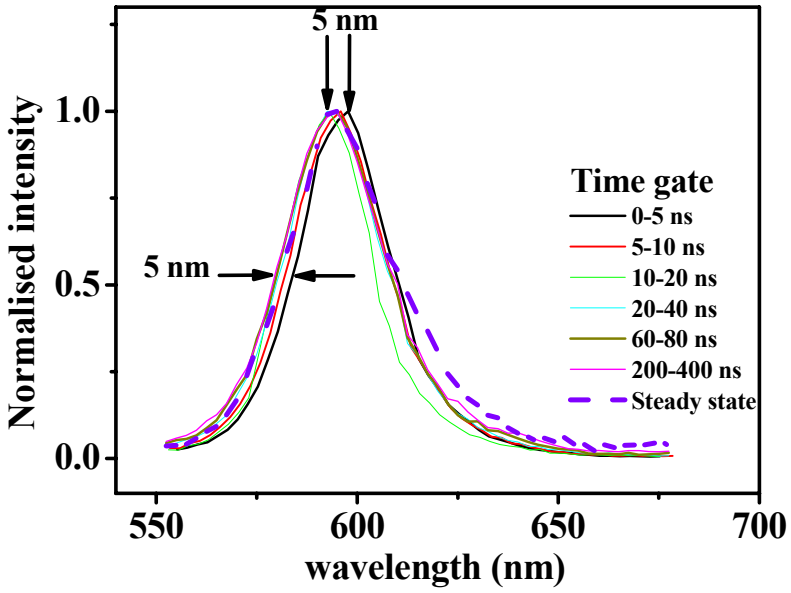

Figure 3.5: Fluorescence bands at high power excitation (0.85 mJ/cm^2) for different time-gate.

From the above results and from the effect of power discussed in 3.2.2, we conclude that the shortest component τ_1 (< 2 ns) has a spectral emission located on the low energy side.

3.2.4 Surface effects.

As discussed in the first chapter of this work, both the radiative and the nonradiative processes play an important role in the relaxation kinetics of the nanocrystals. Moreover, the effect of size that presented recently in paragraph (§ 3.2.1), we found that the small CdSe samples, where the majority of atoms are surface atoms, show different kinetics than the bigger samples. To emphasise the surface effect, which is one of the source for the nonradiative effects (traps, defects,..), we measured the decay dynamics of two different CdSe QDs sizes (2.7 nm and 4.3 nm) capped with oleic acid and HAD after every purification step (See § 2.5.5) using low excitation power (0.08 mJ/cm^2). The purification procedure will remove partly capping around the CdSe QDs and deteriorates the surface quality [111]. Figure 3.6 A and B show the absorption and fluorescence spectra of the two CdSe QDs in toluene solution after purification.

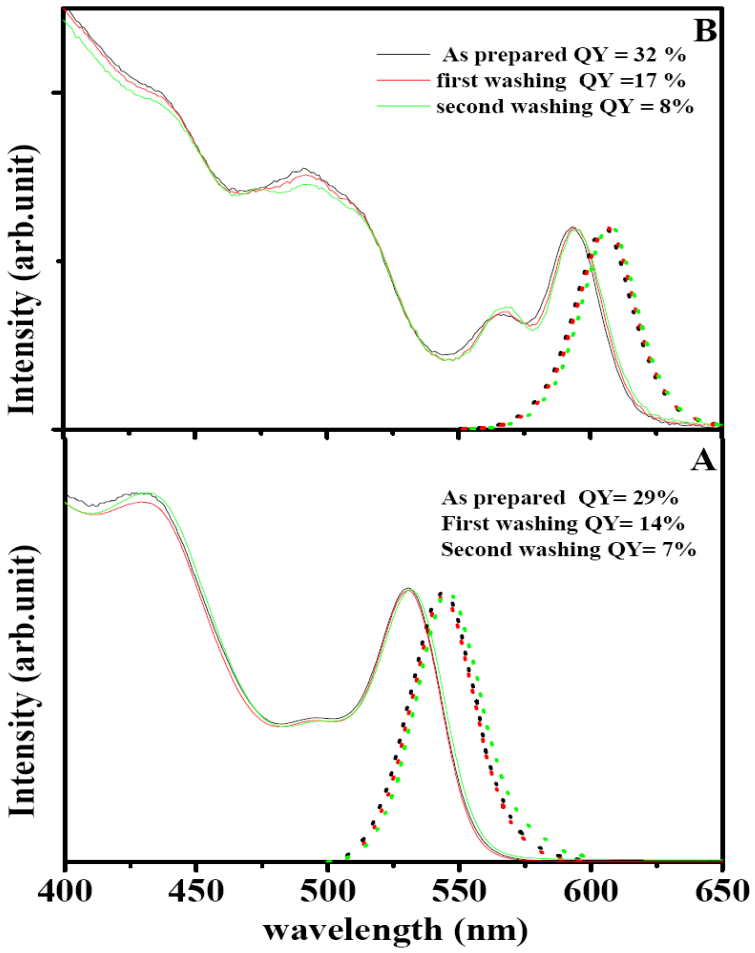

Figure 3.6: The absorption (solid line) and luminescence (dashed line) spectra of CdSe /oleic after two washing with mixture of toluene and methanol for two dot sizes. A) 2.7 nm, B) 4.3 nm.

It was found that the quantum yield of the particles decreases after each purification step, while the absorption and luminescence spectra stay identical as it shows in figure (3.6A, B). In the large CdSe dots (4.3 nm), the QY decreases from 32% for the fresh sample to 17 % after the first step purification, then finally to 8% after the second purification step. The other sample (2.7 nm) exhibits the same dependence after washing (table 3.VII). Figure 3.7A and B shows the decay kinetics of the three CdSe samples (as prepared, first purification, and the second purification) for the two sizes. All these traces are best fitted with four exponential decay components, and fit parameters are given in Table 3.VII. The fastest component (< 2 ns) appears even at very low excitation power. This indicates that this fast component should not be attributed to Auger processes or multiexcitonic effect, because of the weak excitation power.

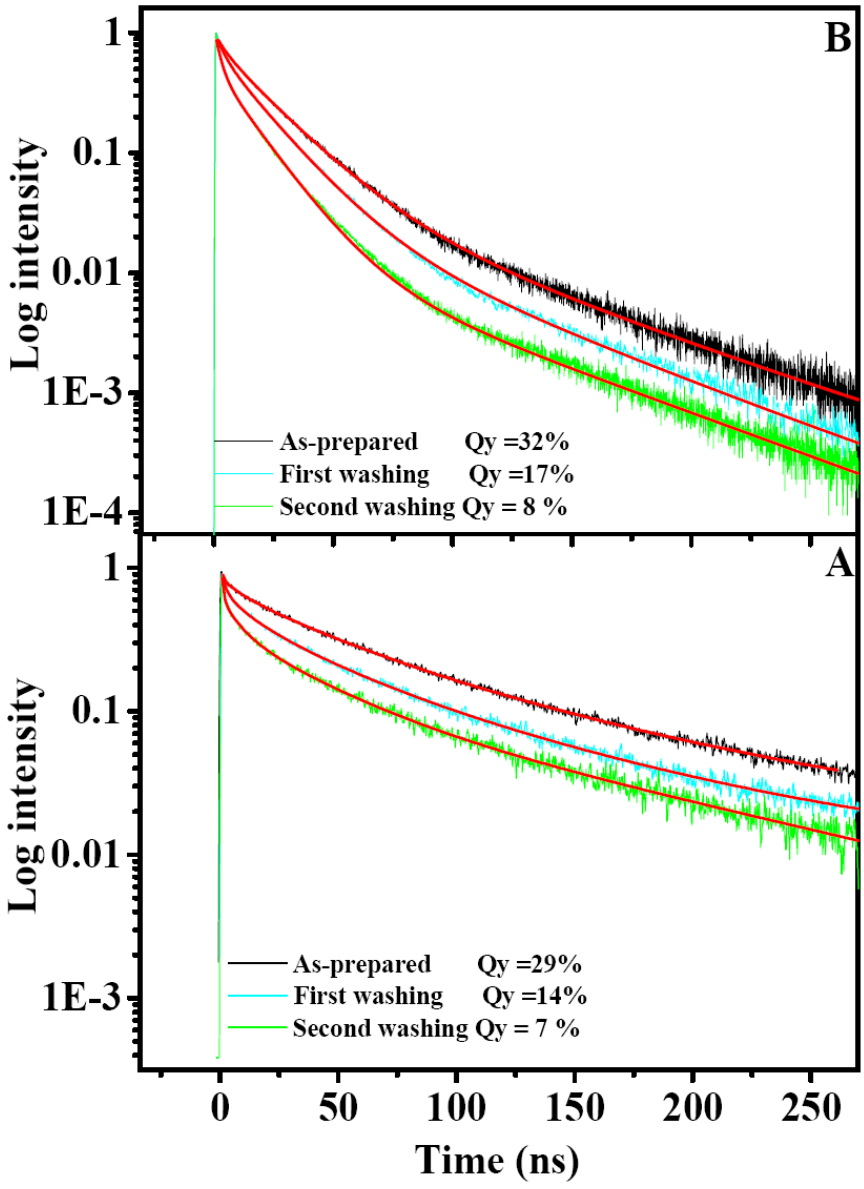

Figure 3.7: Normalized time decay for the CdSe QDs after washing and reprecipitation process. A) CdSe QDs size of 2.7 nm. B) Sample of 4.3 nm.

The components of the decay curves change significantly in the two groups. $\mathbf{A_1}$ and $\mathbf{A_2}$ increasing relatively to $\mathbf{A_3}$ and $\mathbf{A_4}$ as the QY decreases. To prove the real dependence of $\mathbf{A_1}$, $\mathbf{A_2}$, $\mathbf{A_3}$, and $\mathbf{A_4}$ as a function of QY, we fitted the decay kinetics without normalization (table 3.VII). The fit results show larger decreases in the amplitude of the third component $\mathbf{A_3}$ and A_4, while the other components stay unchanged. This result indicates that only a relative increasing for $\mathbf{A_1}$, and $\mathbf{A_2}$ occurs after washing and is due to large decrease of $\mathbf{A_3}$.

TABLE 3. VII: Quantum yield and fit parameters of the decay kinetics of 4.3 nm and 2.7 nm CdSe NCs after every purification step.

QY	A_1	τ_1 (ns)	A_2	τ_2 (ns)	A_3	τ_3 (ns)	A_4	τ_4 (ns)
CdSe (4.3 nm)								
30 %	1733±180	0.8±0.1	2000±145	6.5±0.5	7220±425	21.5±3	477±67	73±5
17 %	1990±198	0.9±0.1	2040±125	5±0.4	4340±325	18.2±2.1	274±34	65±4
8 %	1542±240	0.6±0.1	2383±114	4.2±0.6	1710±123	15.3±+2	118±23	60±4
CdSe (2.7 nm)								
29 %	1816±312	0.9±0.1	1945±165	6.2±0.9	8124±341	31.9±2	754±25	98±4
14 %	1994±322	0.7±0.1	1897±232	5.7±1.2	5452±289	26.9±3	379±145	92±5
7 %	1897±212	0.6±0.2	2013±314	4.1±1.1	2145±189	25.1±2	221±124	89±3

3.3 Discussion and conclusions.

In all measurements, the kinetics of an ensemble of CdSe QDs, in all sizes, powers, and surface treatments shows a consistent behaviour. Different samples under different conditions can be described with three or four-exponential fitting model. In general, our work indicates that the decay curve of CdSe results from many independent processes covering a range of lifetimes between one nanosecond up to hundreds of nanoseconds. In the literature, nanosecond kinetics of CdSe presented recently and resumed in table I and II analyse the relaxation decay as, resulting from only one physical effect due to the e-h recombination (τ ~25 ns at room temperature). At low temperature, this decay comes from the forbidden state relaxation (|2>) with a very long lifetime (> 100 ns). The parameterization to four exponential decay components is rather crude, but works so well for all dots, that we believe it somehow reflects distinct physical processes occurring in all samples. The lifetime constants and the prefactors measured in our work, have a comparable behaviour to that described by Henis *at al* [106]. The authors in this reference indicate the preexponentials without any discussion about the probable physical meaning of these components and their dependence.

In our measerements, we always find a contribution with a decay time of τ_3 ~20 ns, which, according to literature, reflects the room temperature radiative fluorescence

lifetime of the nanodots (§ 1.5.3). This component stays relatively independent upon variations in excitation power and surface cleaning, which supports this interpretation as an intrinisic property of the nanodots [51, 52, 64, 113, 114]. This decay is the result of a dark state (|2>) in rapid thermal equilibrium with the bright fluorescent state (|1>) as we have shown in the theoretical introduction (§ 1.3.1 and figure 1.9) about the lower exciton band-edge states. The energy splitting between them (the bright and dark states) is ranging between 6 and 16 meV for sizes from 4.2 to 2.6 nm [59, 103] and only at very low temperatures (T <10K) the coupling between them would be slowed down sufficiently [51, 52, 103, 115, 116], as we will discus in more detail in the following chapter.

The recombination dynamics of luminescence in colloidal CdSe quantum dots has been studied recently [51, 106, 107, 117-119]. The radiative decay of photoluminescence is generally dominated by a bi-exponential distribution, consisting of a fast component (~ several nanoseconds) and a slow component (~ tens of nanoseconds) at room temperature (table I and II). The origins of these two lifetimes are not conclusive in previous studies. Landes *et al* suggested that both shorter and longer lifetimes of photoluminescence occur from trap states, not directly from the band edge states [118]. Wang *et al* attributed the shorter and longer lifetimes of photoluminescence to the intrinsic recombination of initially populated core states and the involvement of the surface states respectively [105, 119]. On the othwer hand, Javier *et al* pointed out that a photoinduced charged exciton and an intrinsic band-edge exciton is responsible for the shorter and the longer lifetime decay [51]. Obviously, the origin of photoluminescence decays in colloidal CdSe QDs remains an open question.

In all of colloidal CdSe decays the measured in our work, in addition to the 20 ns component, faster contributions (<2 ns and ~5 ns) and a slower processes with a lifetime constant of about 80 ns were found.

The sub-ns decay time in our experiments has two different origins:

(i) For the core-QDs of groups I and II at low power, the smaller particles have a significantly faster component (< 1 ns), while the third component (~ 30 ns) appears slower for these small samples than the others, as seen in table III. This dependence of slower decay in smaller CdSe dots is similar to the experimental works that was done by Crooker *et al* [103], and Labeau *et al.* [53]. This dependence goes in the same tendency of the theoretical calculation of Califano *et al.*[120].

For the fast component, this fast decay is probably due to rapid quenching by various trap states [83]. The size dependence of this component can be investigated as a function of increased surface to volume ratio. For example, in a CdSe crystal with 377 atoms (~ 2.4 nm diameter), half of the atoms actually reside at the surface layer [121], and might play an important role, leading to a faster trapping of the excitation to surface trap states [122], which identifies the traps involved as surface traps [52]. The suggestion of the large surface-to-volume ratio [122] leads to consider that, for the smaller dots, the majority of the atoms are surface atoms, and are strongly affected by any type of surface defects. This suggestion shows different tendency in

the two following cases; (1) in the case of the purification treatment (§ 3.2.4). Where, although the relative increasing of $\mathbf{A_1}$, and $\mathbf{A_2}$ after the purification process, the absolute amplitude value $\mathbf{A_1}$ of the first component $\boldsymbol{\tau_1}$ in the two CdSe QDs sizes (figure 3.6) remains constant after treatments, and the main change is due to the decrease of the amplitude $\mathbf{A_3}$. This dependence points to additional contribution, alter than the surface for the fastest effect (< 2 ns).
(2) In addition to the purification treatment, the appearance and the unchanged value of the fast component in the group III (core /shell QDs) also indicates fast trapping processes. The appearance of this component in "well" protected samples like type III (core/shell) and its unchanged weight point to another origin than the surface.
(ii) On the other hand, an additional ultra-short component also occurs upon an increase of the excitation power, which is due to bi-exciton emission recently studied in our group [109]. The main evidence about the origin of this component comes from the wavelength dependence of the decay at high excitation powers (figure 3.4), and the time-gated fluorescence (figure 3.5). The bi-exciton is expected at the red edge, where we find a much faster decay [109, 112, 123, 124]. The bi-exciton decay has a lifetime of (10-50 ps) [109]. Theoretical and experimental works [123, 125, 126] indicate that in CdSe QDs the bi-exciton should emit 22 meV to the red of the neutral exciton emission, which explains the red shift of the early 2 ns time gated fluorescence band (see figure 3.5) measured at high power of excitation.

Increasing the excitation power should also create more excitons that are charged. This behaviour fits to our experimental results. The amplitude of the component that has a lifetime of 8 ns has more weight (from 30% to 50 %) after increasing the power (table 3.III). In addition, this component (5-8 ns) was previously recorded and attributed to charged excitons [51]. Moreover, this component appears independent of purification processes (table V). Washing of samples is expected to eliminate capping molecules from the surface [111, 120], and thus to create more surface defects as charging centres [120]. For that, we interpret the ~ 8 ns lifetime to result from charged QDs, with charges inside the dots (trions). This explanation of the lifetime value is in good agreement with the calculations of Califano *et al* [120], which show faster radiative lifetime decay than the neutral exciton (for both, positively and negatively charged excitons). This difference is due to the distribution of the lowest band gap electronic state, which is optically allowed, and has a short lifetime (~10 ns) [120]. Therefore, we think that our 5-8 ns component corresponds to charged excitons, even with the same absolute values of $\mathbf{A_2}$.

The slow component we find was not discussed in literature previously. Even though the corresponding prefactors in the exponential fits are never more than some percent, its actual contribution is high because of the large decay-time (the relative contribution is proportional to $\mathbf{A_4}*\boldsymbol{\tau_4}$). The reasons for the large neglect ignoring of this component in literature are; (i) the required signal to background ratio (three magnitude in minimum) to detect the low weight of this component. (ii) The same

range of lifetime constant value of this component (τ_4 ~100 ns) and the time decay of the optically forbidden state (|2>) (~ 150 ns for an ensemble of CdSe QDs [53, 99]) at low temperatures.
Our experiments showed that the long component remains unchanged as a function of size, power, and detection wavelength. Again, similar to the radiative lifetime, it starts to be faster after purification treatments with a low amplitude ($\mathbf{A_4}$ <10%); the magnitude of this component decreases to about 30% of its value when the quantum yield decreases from 30 % to 7 % in the two samples shown above (figure 3.7 and Table 3.V). The change in this component after the purification indicates a surface related origin of this component affected by this treatment (§ 1.3.2).
To further understand the origin of this slow physical process, we investigated the decay measurements on CdSe QDs as a function of temperature in the following chapter.

From this discussion, we draw the following conclusions:
(1) The fluorescence decay is best described by a multi-exponential fit with four components with lifetimes of < 2 ns, ~ 8 ns, ~ 20 ns, and > 80 ns.
(2) Changes of the weight of the shortest component as a function of excitation power and wavelength at which we detect the emission gives strong evidence that the origin of the fastest component, at high excitation powers, is the formation of multi-excitons per particle [109, 112, 124].
(3) A similar fast component (< 2 ns) appears also at low excitation power. This component is related to trapping processes or to the strong confinement effect in the smallest QDs. The independence on purification and the results on core/shell QDs points to contributions with different origin than the surface states.
(4) The 8 ns component in the kinetics of the ensemble of CdSe QDs is due to the dot charging (inside the dots), and increases by the laser power.
(5) The intrinsic lifetime (τ_3 ~ 20-30 ns) is the electron-hole recombination and it shows unchanged behaviour in all of the treatments applied to the CdSe QDs, except in the case of purification and the case of different sizes, where a faster decay were noticed in the case of decreasing the QY due to more nonradiative processes after the sample washing.
(6) The forth component has an amplitude of < 10% under all treatments and prametrs, while its lifetime stays unchanged.

In the next chapter, describing and understanding the response and the origin of the fastest and the slowest components will be one of the gaols of the following chapter.

Chapter 4

Temperature effects on the energy and time-resolved band gap recombination in Wurtzite CdSe nanodots.

4.1 Motivation:

Except for the purification treatments, the other parameters in the previous chapter did not reveal any other dependence of the two-slower components τ_3, τ_4 in the decay time of the colloidal CdSe QDs to the measured parameters. Moreover, as the band edge exciton is expected to be the most important state for the relaxation of the nanocrystal, this state is very sensitive to temperature because of the location and energy distances between states (|2>) and a bright exciton state (|1>) [42].
In the last decade, temperature dependence studies have been investigated (See table 3.I) by Crooker *et al* [103], Labeau *et al* [53], and Nirmal *et al* [127] . In these studies, it was found that as the temperature is raised, the radiative lifetime (~ 100 ns for ensemble of dots) decreases due to thermalization between the triplet and singlet states (§ 1.3a). A three-level model is usually used to describe the temperature dependent decay rates in all experimental works in literature [53, 85, 99, 103]. The signal to background ratio presented in the previous works makes the low weight component (τ_4 >70 and A_4 <10 **%,**) unresolved at room temperature. Decreasing the temperature will resolve a long component (τ_{Dark} ~150 ns) [53, 99, 103]. In the chapter, we were able to resolve this component even at room temperature. The comparable value of τ_4 (measured in our case) and the literature value of the dark state (at low temperatures) make the distinguish between them difficult at low temperature.
The literature explanation about the thermalization between the allowed and forbidden states at high temperature that makes the lifetime constant appear faster at RT, does not explain the multi-exponential (four-components) decay with the unchanged long component τ_4.
The main purpose of this study is to resolve the temperature dependence of the two components τ_3, τ_4, with the necessary required magnitude of signal to background to

resolve them, and to have a better explanation of their origin. The other aim is to compare our multi-exponential behaviours with the previous works. We also investigate the effect of the capping of the CdSe QDs on the low temperatures kinetics.

In order to study the influence of the environment on the properties of CdSe QD, we used CdSe QDs embedded in a polymer film [91] or deposited on the surface of a CaF_2 substrate. The temperature-dependent dynamics of electron-hole recombination were investigated over a broad temperature range (4 to 300 K) in a series of colloidal CdSe nanodots. The three CdSe QDs used in the experiment have comparable sizes (about 4 nm diameter), comparable quantum yield (~ 28 %) measured in toluene solution (see § 2.2.2), and different capping (TOPO-capped CdSe (type **I**), oleic acid-capped CdSe (type **II**), and CdSe/Zns core/shell (type **III**). Figure 4.1 shows the absorption and fluorescence spectra of these three different CdSe types in solution.

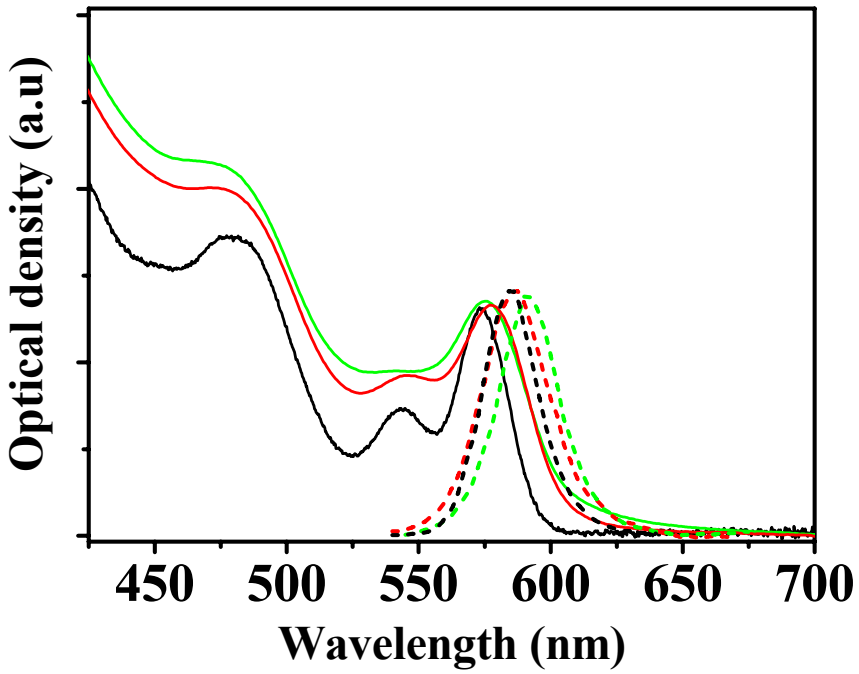

Figure 4.1: Absorption (solid line) and luminescence (dashed line) spectra of ensembles of CdSe nanodots. Type **I** (black), Type **II** (green), and Type **III** (red) in toluene solution.

As presented in the experimental section (§ 2.5.6) great care was taken in preparing an ensemble of dilute, non-interacting nanocrystals. Figure 4.2 shows the absorption and fluorescence spectra of sample (**I**) in three forms: CdSe in toluene solution, in film, and on the CaF_2 substrate. The spectra of the three forms show identical spectra for all CdSe QD environments. The three samples show comparable spectra. Similar behaviour was found for types (**II**), and (**III**). The unchanged spectra point to spectroscopic properties independent of the environments.

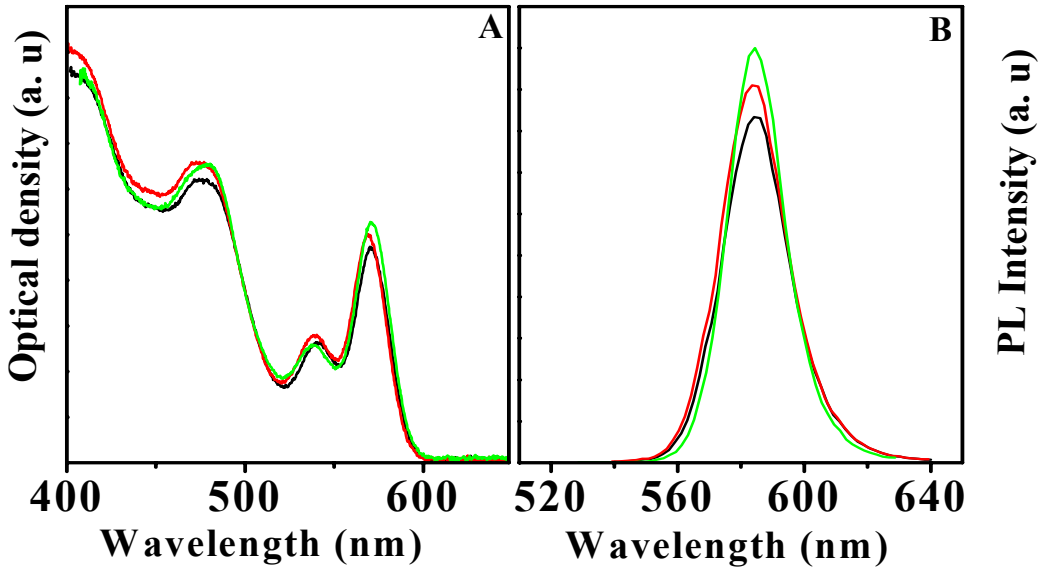

Figure 4.2: Absorption (**A**) and luminescence (**B**) spectra of type **I** QD (4 nm diameter) in toluene solution (black), on the CaF_2 substrate (red), and in polymer film (green).

4.2 Room temperature kinetics.

The kinetics of types I, II, and III CdSe QDs were measured at the maximum of the fluorescence band and are shown in figure 4.3. Differences kinetics in solution than in films was measured. The kinetics of CdSe type I and II (Core samples) present slower relaxation decays in films and on the CaF_2 substrate than in solution. Type III QD (core/shell) presents identical kinetics in all environments.
All traces were best fitted by a four-exponential function and the fit parameters are shown in table 4.I.

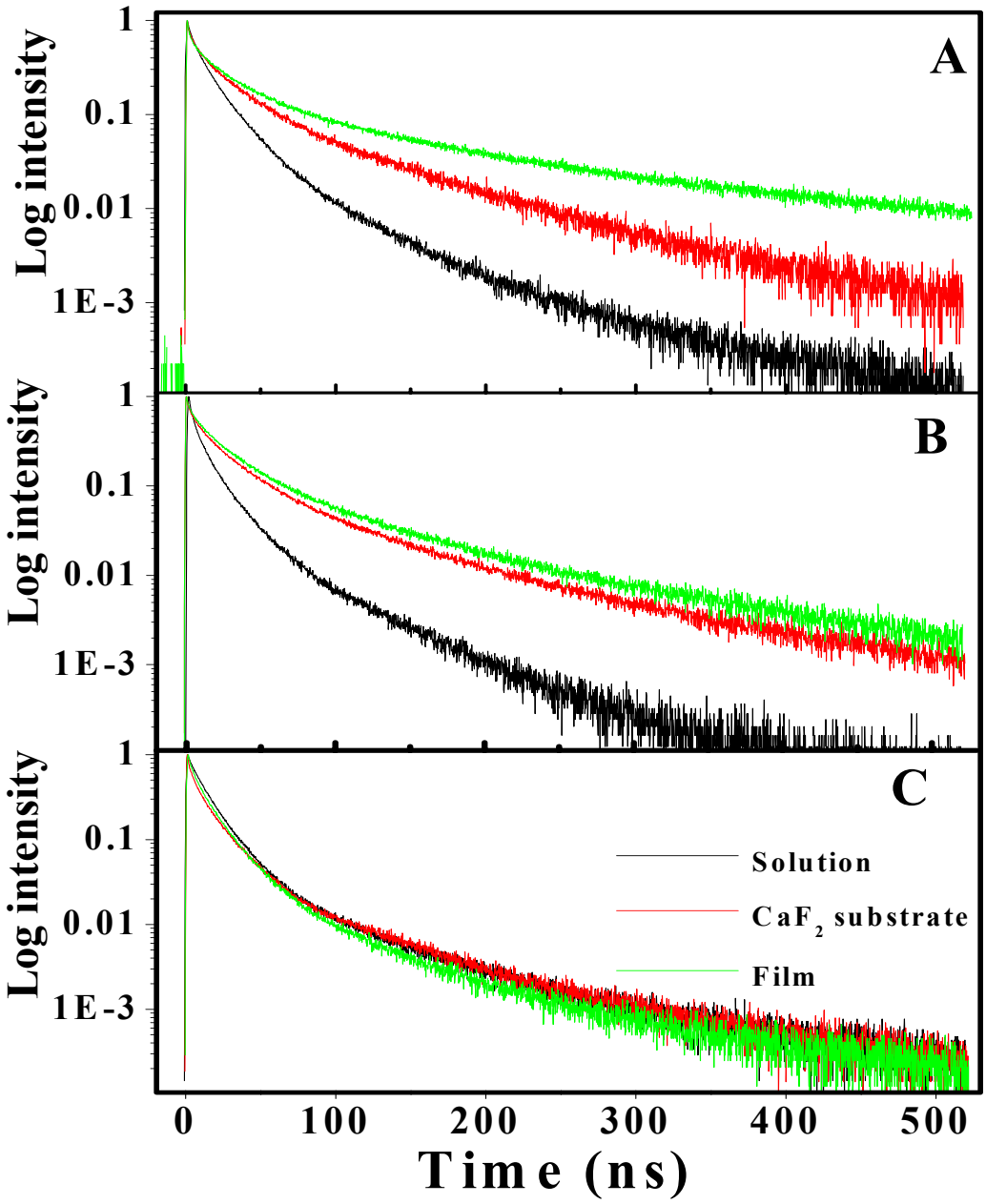

Figure 4.3: Room temperature kinetics traces of same sizes (4 nm diameter) CdSe QDs excited with 0.5 μ W in different environments. A) Type **I**, B) type **II**, and C) type **III**.

The fit results show some interesting trends. All the lifetimes τ_1, τ_2, τ_3, τ_4 (Type **I** and **II**) show larger values in film or on CaF_2 substrate than in solution. The τ_4 component, both in lifetime and in weight, increases similar to τ_3 from solution to substrate to film. The other components (τ_1, τ_2) show slower kinetics in film than on substrate or solution.

For ZnS-capped dots, τ_1 appears slightly faster in film than in the other forms, while the other lifetimes τ_2, τ_3, τ_4 do not change from solution to film case. The prefactors show unchanged values in the weight of all components. Larger values of τ_3, τ_4 in CdSe core form than CdSe/ZnS core-shell QDs in film and CaF_2 substrate form.

TABLE 4.I : Fit parameters of the relaxation processes of the three different samples (CdSe in different forms) at room temperature. The fit errors are no more than 10% in all values.

	A_1	τ_1 (ns)	A_2	τ_2 (ns)	A_3	τ_3 (ns)	A_4	τ_4 (ns)
CdSe (I)								
Solution	0.30	1.4	0.39	6.2	0.27	19	0.04	63
CaF_2 substrate	0.22	1.5	0.28	6.3	0.40	25	0.09	92
Film	0.19	1.7	0.24	6.4	0.47	31	0.10	110
CdSe (II)								
Solution	0.44	1.8	0.30	6.8	0.22	14.5	0.04	70
CaF_2 substrate	0.25	1.8	0.25	7.2	0.40	26	0.10	89
Film	0.20	1.6	0.21	7.1	0.47	27.5	0.12	102
CdSe (III)								
Solution	0.40	1.9	0.28	8.6	0.28	17	0.04	74
CaF_2 substrate	0.38	1.4	0.25	7.1	0.31	17	0.04	77
Film	0.36	1.3	0.24	8.1	0.34	16.5	0.06	73

The time-gated fluorescence does not show significant differences between the three samples in film at different fluorescence time delay. Figure 4.4 shows, as an example, the normalized spectra for TOPO-capped CdSe QD (type I) in film. The difference between the time-gated fluorescence < 60 ns, and the time-gated fluorescence at > 60 ns is a broadening of the bands on the red side for long time gates (). The maximum is unchanged for all delay times.

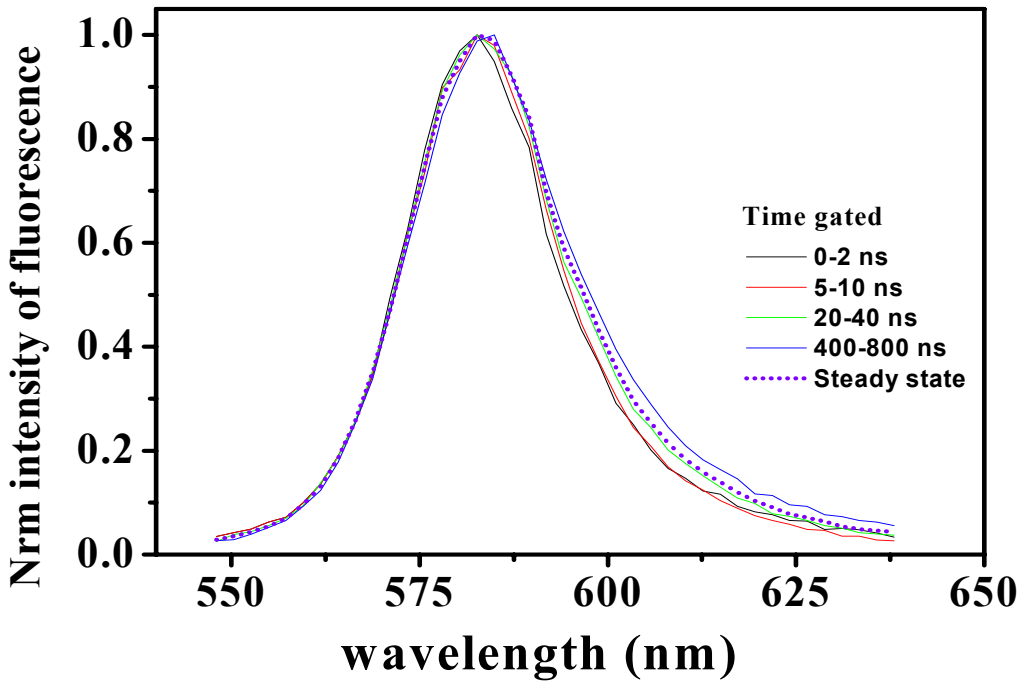

Figure 4.4: Time gated fluorescence of type I CdSe dots in a film.

4.3 Temperature effects.

In this study, the samples were cooled in a range of temperatures between 4 and 300 K, the kinetics was measured under low laser excitation power to avoid multi-excitonic and Auger processes.

The kinetics show different dependence for different samples (CdSe core and core-shell, in film and on the surface of a substrate) and in some cases differ significantly to the literature works [53, 85, 99, 103], [127].

First, I present the study of the spectroscopic properties of the different samples as a function of temperature between 4 K and room temperature. Then, the second part shows the kinetics of these samples and their dependence with temperature. The third part will discuss the processes of one and two photons excitation on the decay kinetics of the CdSe DQs at low and at room temperature to shed more light on the nature of the band-edge exciton.

4.3.1 Temperature effects on the spectral properties.

In general, decreasing the temperature from 300 to ~ 4 K causes: (i) a shift of the emission maximum to higher energies, (ii) a narrowing of the steady state fluorescence band, and (iii) an increase of the fluorescence intensity.

Figure 4.5 presents the evolution of the fluorescence bands of type I CdSe in the polymer film at different temperatures.

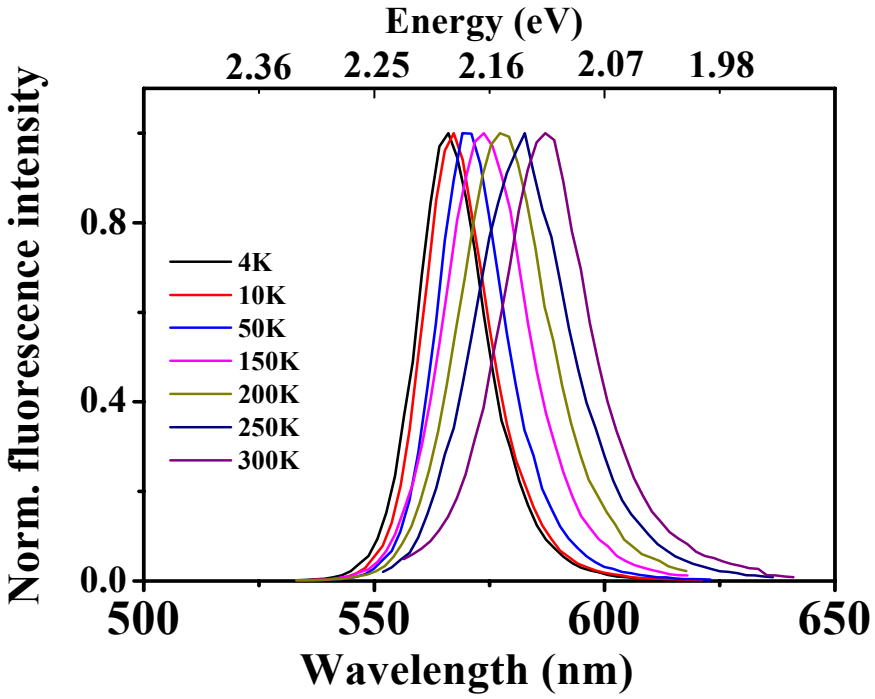

Figure 4.5: Normalised steady–state fluorescence spectra of type I CdSe (4 nm diameter) in polymer film at different temperatures.

In this figure, we note a 21 nm (81 meV) red shift of the maximum upon heating the sample to 300 K, the fluorescence bandwidth decreases from about 25 nm at room temperature to 16.6 nm at 4 K. The relative fluorescence intensity dependence is plotted in figure 4.6C. Figures 4.6 presents the temperature spectroscopic dependence for type I CdSe QD in polymer film and on a CaF_2 substrate. While figure 4.7 presents the same temperature dependence for the case of core-shell QD (type III). In these two figures, and to measure the relative fluorescence increases that due only to the temperature effect, the emission intensity was derived from the integrated area below the steady state emission band after good sample estimation to have the same concentration in the polymer films. The laser spot size (60 μm), intensity (0.5 μ W), and wavelength were also fixed to be the same for all samples. The effects (in the two samples) were divided in two figures for more clarify.

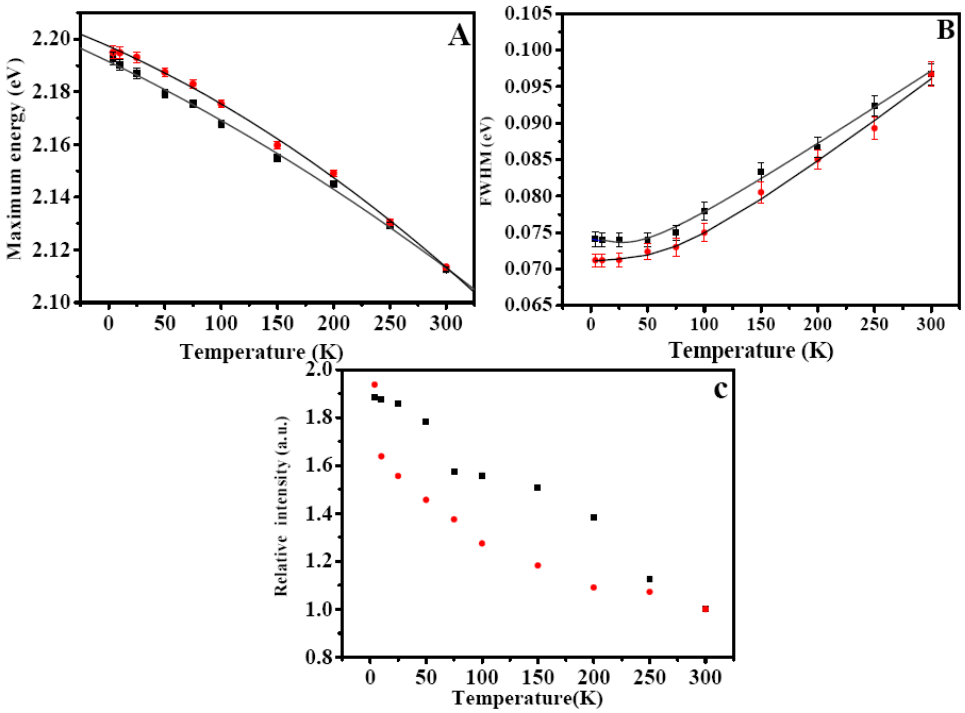

Figure 4.6: Temperature dependence of the optical properties of type (I) CdSe sample (in polymer film (black) and on a CaF_2 substrate (Red). **A)** Position of the fluorescence maximum. **B)** Full width at half maximum. **C)** Relative fluorescence intensity at different temperature.

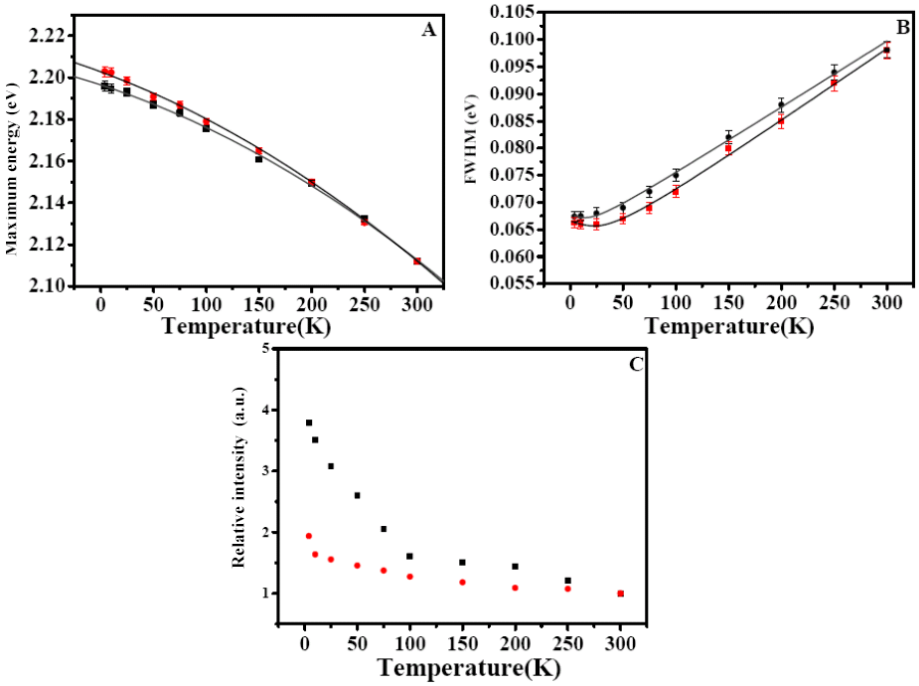

Figure 4.7: Temperature dependence of the optical properties of type (III) CdSe sample (in polymer film (black) and on a CaF_2 substrate (Red). **A)** Position of the fluorescence maximum. **B)** Full width at half maximum. **C)** Relative fluorescence intensity at different temperature.

In general, the variation in the energy gap with temperature is a result of a temperature-dependent electron lattice interaction [128-130]. These previous works introduced the following empirical relation to describe the temperature dependence of the energy gap in bulk:

$$E_g(T) = E_g(0) - \alpha T^2/(T+\beta) \qquad (4.1)$$

Where $\mathbf{E_g(0)}$ is the value of the bulk energy gap at 0 K,$\boldsymbol{\alpha}$ is the temperature coefficient, and $\boldsymbol{\beta}$ is constants is a parameter related to the Debye temperature of the crystal[129-131] (in bulk, $\boldsymbol{\beta}$ ~ 150K, while Debye temperature in bulk ~180 K[131]). Using this relation as a fit function for the temperature dependence of the energy gap in QDs show good agreement with bulk CdSe taking in to account that $E_g(0)$ used in the fit function, is the energy gap of the QDs at zero temperature and is size-dependent. The expression (4.1) fit very well the energy gap variation, as it shows in figures 4.6A, 4.7A, and in table 4.II.

Table 4.II: Fit results of the band-gap temperature dependence in CdSe (I) and (III) QDs in film and on CaF_2 substrate.

CdSe	$E_g(0)$ (eV)	α (x 10^{-4} eV/K)	β (K)
(Type I) Film	2.32±0.12	3.5±0.3	95±40
(Type I) CaF_2	2.2±0.02	3.6±0.5	110±35
(Type III) Film	2.18±0.02	3.7±0.6	139±46
(Type III) CaF_2	2.19±0.07	3.7±0.5	111±25
Bulk	1.75	3.6	150

The fit parameters show comparable values for all fit parameters, and independent of the sample capping or its environment. Due to the larger band gap in the QDs than in bulk, $E_g(0)$ values are bigger for CdSe QDs than in bulk. α appears in agreement to the bulk value with same values for all CdSe types and forms. β indicates to Debye temperature [132] (it will discus in details later in the discussion of this chapter) and has comparable values for the two CdSe types (I, III) , but smaller than the case of bulk (~180 K) [129, 133].

The full width at half maximum (FWHM) of the luminescence band of CdSe core and CdSe/ZnS core-shell (figures 4.6**B** and 4.7**B)** shows pronounced narrowing (about 16 nm in film and 17 nm on CaF_2) at lower temperatures. The reduction of the fluorescence bandwidth between the two forms shows similar behaviour in the two capped-CdSe samples I and II.

In order to have a deeper insight into the processes (exiton-phonon interaction) that involved in the increasing broadening (homogeneous and inhomogeneous broadening), we fitted the experimental data to the relation that describe the temperature dependence of the broadening in bulk semiconductor and can be tested for the QDs [134].

$$\Gamma(T) = \Gamma_{inh} + \sigma T + \Gamma_{LO}(e^{E_{LO}/k_B T} - 1)^{-1} \qquad (4.2)$$

Where Γ_{inh} is the inhomogeneous broadening, which is temperature-independent, and due to fluctuations in the main properties of the nanocrystal like the size and the shape, etc. The other two terms describe the homogeneous broadening, and are due to the exciton-phonon interactions [129, 135, 136]. σ is the exciton-acoustic phonon coupling coefficient, Γ_{LO} represent the exciton-LO-phonon coupling strength, E_{LO} is the LO phonon energy, and k_B is the Boltzmann constant . The fit values for the two types of samples are shown in table 4 II.

Table 4 II: Fit parameters of the full width at half maximum at different temperatures for two types CdSe-capped dots, and in bulk.

		Γ_{inh} (meV)	σ (μeV/K)	Γ_{LO}(meV)	E_{LO}(meV)
Type (I)	Film	43±3	20±3	20±4	24.3
	CaF_2	40±4	22±2	24±4	24.1
Type (III)	Film	51±4	23±4	24±3	24.4
	CaF_2	48±5	24±1	22±5	24.7
Bulk CdSe		-	8	100	26.1

From the above table, the fit values point to larger values (~ 3 times) of exciton-acoustic phonon coupling σ, in all -CdSe dots compared to bulk value. The opposite dependence was found for the exciton-LO-phonon coupling strength Γ_{LO}. E_{LO} have comparable values to the bulk.

We now present the issue of temperature dependence of the fluorescence intensity. From the two figures (4.6C and 4.7C), the fluorescence intensity were normalized to one at room temperature to show the magnitude of the relative luminescence intensity increasing during the cooling. In the case of CdSe/TOPO QDs (figure 4.6**C**), this luminescence intensity increases by about a factor of two as the temperature decreases to 4 K (QY in solution was 28 %). In the case of the CdSe/ZnS core-shell samples (nearly the same QY in solution), this increase is about four times in film form, and two times on the surface of substrate (figure 4.7C).
From the temperature study on the spectroscopic properties of the different capping CdSe QDs in different environments, we have the following points:

(a) The general behaviour (physical effects) of the CdSe QDs is comparable to the CdSe bulk.
(b) The effect of capping and environment appears as a different in the relative emission intensity of the ensemble of dots.
(c) The other effects, the maximum shift and the bandwidth decreasing, show comparable behaviours between the two capping in different environments.
(d) The fit parameters show different fit values between bulk and QDs, these differences point to specific properties in QDs due to size, confinement, and different acoustic or LO- phonon coupling in QDs than in bulk.

4.3.2 Temperature effects of the kinetic properties.

In the following, we present the temperature dependence of the photoluminescence decay of the CdSe core and core-shell nanodots in a polymer film and on a CaF_2 substrate between 4 and 300 K. Our aim is to determine the dependence of exciton lifetimes on temperature, capping, and environments.
Crooker et al [103] show that for temperatures above of 20 K, overall trends may be modelled by thermal activation between dark (|2>) and bright states (|1>) [103]. In our case, the data strongly suggest complicated behaviour than the description of bright and dark states presented in literature [53, 103, 127]. The effect of surface and the sample environments will add additional effects, or totally changes the final behaviour of the relaxation processes. Temperature dependent kinetics of CdSe QDs expect to exhibit, in details, the nature and location of the band-edge exciton (lowest excited states distribution), the surface state contribution due to ligand, and the influence of the polymer surrounding the CdSe QDs on the relaxation behaviour.
Another reason for our investigation is to probe the dependence of the four-components as a function of temperature, especially the τ_3 and τ_4 components that

they do not exhibit any systematic dependence over all the previous treatments (except for purification tratement, chapter 3). In addition, the absence of a large temporal windows (especially at room temperature) and the limit ratio of signal to background in all of the previous literature works, which studied the temperature dependence kinetics of CdSe, make our investigation about the temperature dependence of CdSe QD important to clarify the relaxation effects at different temperatures with better signal to background ratio.

4.3.2.I- CdSe dots in polymer film.

Figure 4.8 shows the decays of CdSe types (I), (II), and (III) in polymer film at different temperature between 4 and 300 K.

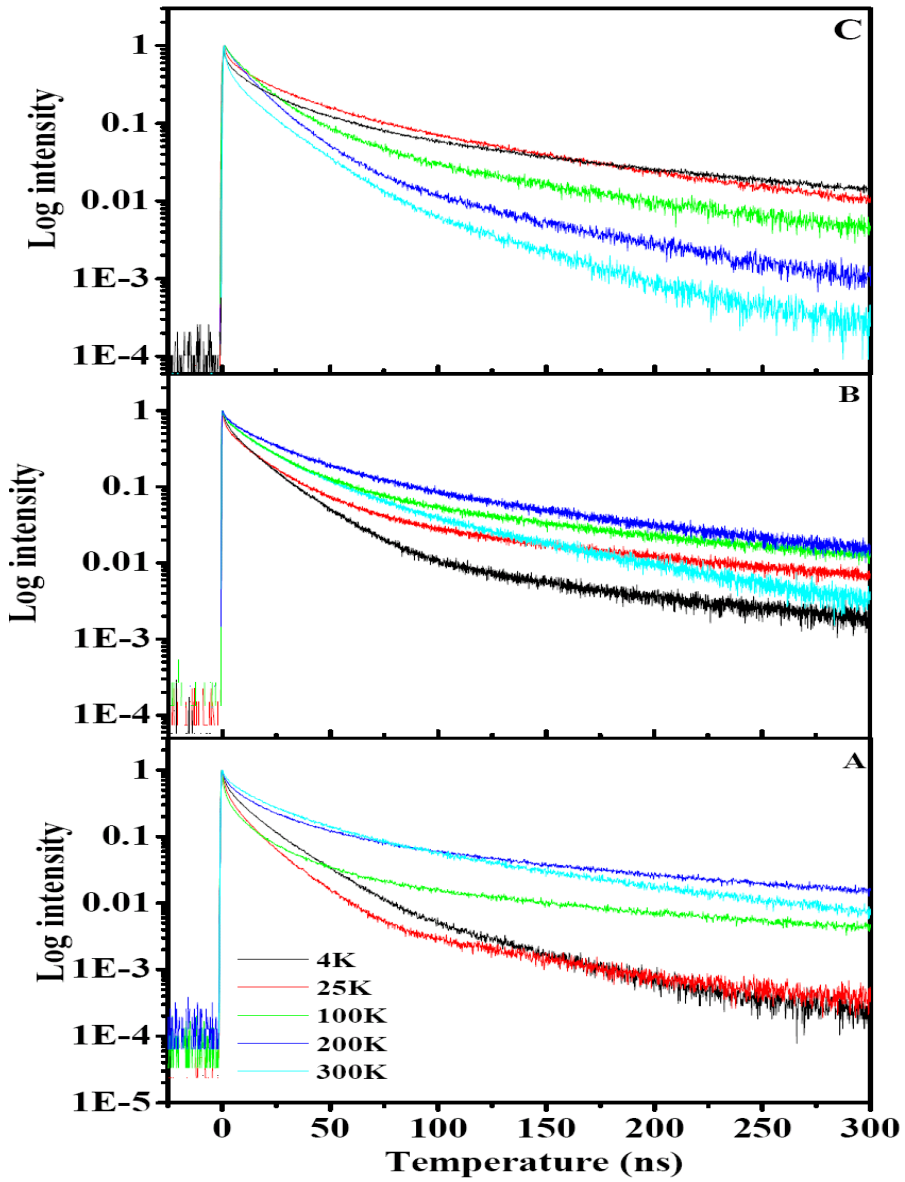

Figure 4.8: Decay curves of CdSe QDs in a polymer film measured at different temperatures. **A)** Type I, **B)** type II, and **C)** type III.

Figure 4.8**A** and **B** show similar trends with temperatures, i.e. slower overall kinetics as the temperature decreases, but then, below 100 K, the decay becomes faster. In Figure 4.8**C** (sample III), the dependence is different. The kinetics become gradually slower upon cooling from 300 to 4 K. Different fit functions (three and four-exponential, low powers, stretched exponential, double stretched exponential, and stretched exponential + mono-exponential) were tested. The best fit was obtained by four-exponential. Figure 4.9 presents the four-exponential fit results for core CdSe types, while figure 4.10 presents the fit results in the case of CdSe core-shell sample.

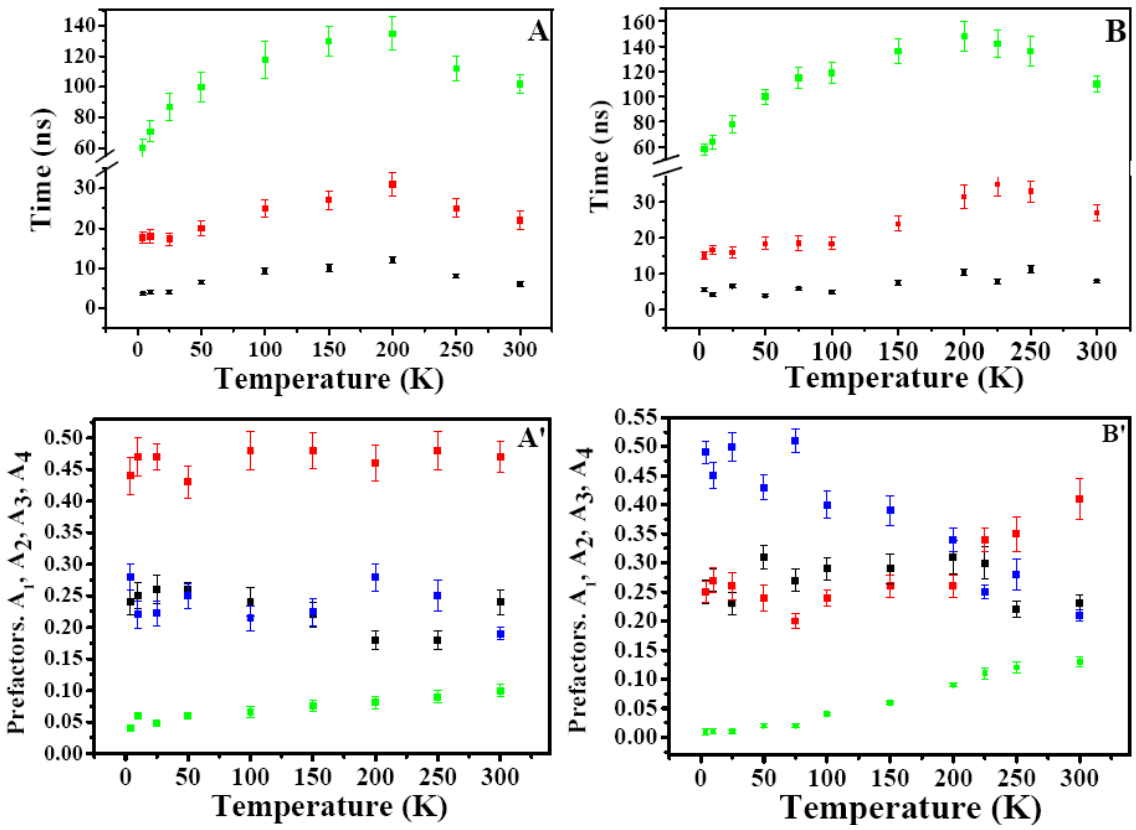

Figure 4.9: Four-exponential fit parameters at different temperatures for type I (A, A´) and type II (B, B´). $\mathbf{A_1}$ (blue); τ_2, $\mathbf{A_2}$ (black); τ_3, $\mathbf{A_3}$ (red); τ_4, $\mathbf{A_4}$ (green).

(i) **Type I and II**: in these two groups, the first decay component lifetime is temperature independent, with a lifetime of τ_1 ~ 1.5 ± 0.3 ns and an amplitude increases from 0.19±0.02 at RT to 0.27± 0.02 in (I), and increases 0.47±0.03 in (II). The three lifetimes τ_2, τ_3, and τ_4 increase between room temperature and 200 K and then gradually fall until the lowest measured temperature (4 K). τ_2 increases from about 6 ns in the two groups at RT to 12 ns at 200 K and then decreases to 4-6 ns at 4 K. τ_3 starts with 22-25 ns at RT, then it rises to 31 ns at 200 K and falls down to 15-17.5 ns. τ_4 starts with 102-110 ns at room temperature then rises to 130-150 ns and finally drops to ~ 60 ns at 4 K.

The prefactors do not reflect the same trends. $\mathbf{A_2}$ seems nearly constant over the whole range of temperatures in the two types. $\mathbf{A_3}$ shows a different trend as a function of capping, which decrease in type II as the temperature decreases and stay unchanged in type I CdSe. Surprisingly, $\mathbf{A_4}$ decreases with temperature.

(ii) Type III: Different to type I and II samples, the lifetimes increase gradually from 300 to 4 K in a pronounced way below 100K.

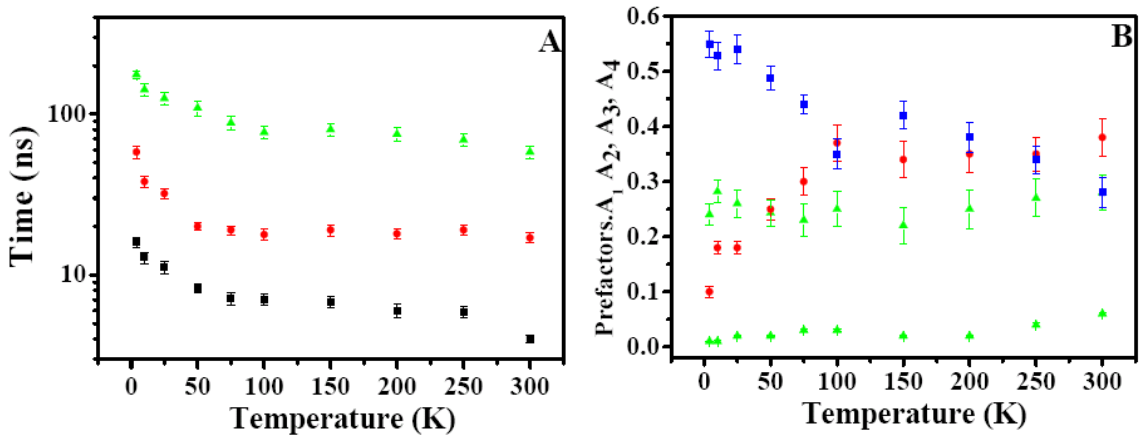

Figure 4.10: Fit result for lifetimes (**A**) and prefactors (**B**) of type III CdSe QDs in film at different temperatures. Again, $\mathbf{A_1}$ (blue); τ_2, $\mathbf{A_2}$ (black); τ_3, $\mathbf{A_3}$ (red); τ_4, $\mathbf{A_4}$ (green).

Again, the value of the shortest lifetime component ($\tau_1 < 2$ ns) is almost constant, while its weight increases to (55±2)% at low temperature. The second component $\boldsymbol{\tau_2}$ rises from 4 ns at RT to 16 ns at 4 K with a constant relative amplitude $\mathbf{A_2}$ of about (30 ± 5) %. $\boldsymbol{\tau_3}$ has a lifetime of ~20 ns at RT, and it rises to ~ 60 ns at 4 K, but remarkably its weight decreases dramatically below 100 K. The longest component $\boldsymbol{\tau_4}$ starts from ~ 70 ns at RT and then increases gradually to 175 ns at 4 K. The amplitude of this component decreases as the temperature decreases.
To resolve the origin of each component in the kinetics, and to compare this dependence at low temperatures to the room temperature results that studied in the previous chapter, we also measured the time-gated fluorescence spectra of the three types of samples. These are shown in figure 4.11, where the spectra are normalized. The intensity drops significantly at long time gates as can be seen from the noise level. Up to 60-80 ns, the time-gated fluorescence of the sample behaves in similar way. Beyond this time, a red shift occurs (especially in type I and II) and a prominent wing appears. This also occurs in type III but in a much weaker way.

In summary to what we found from the previous steady, we have the following:

(a) Different behaviour of the kinetics between CdSe core (I, and II) and CdSe core–shell (III) in polymer film as a function of temperature.

(b) CdSe core-shell samples present comparable behaviour to literature studies [53, 85, 99, 103]. τ_2, τ_3, τ_4 show similar trends with temperature, while the first component τ_1 shows a constant lifetime for all temperatures (figure 4.10).

(c) In type I and II CdSe QDs, τ_1 appears independent of temperature changes, while the τ_2, τ_3, τ_4 components show again similar trends with temperature between 300 and 4 K (figure 4.9). The general dependence of these components appears different to the type III CdSe.

(d) CdSe core dots kinetics shows a maximum of lifetime values of its components at around 200 K and then all these components become faster (figures 4.8 and 4.9). This maximum is absent in type III dots.

(e) In all CdSe types, $\mathbf{A_2}$ remain unchanged with temperature, $\mathbf{A_1}$, $\mathbf{A_3}$ behave differently, the first increases while the other decreases. Finally, $\mathbf{A_4}$ decreases as the temperature decreases.

(f) Time-gated study reveals a red shift of the time-gated fluorescence bands, and a clear wing at this energy side (figure 4.11) above 100 ns delay time. The magnitude of these two behaviours differ from types I and II (core) to type III (core-shell).

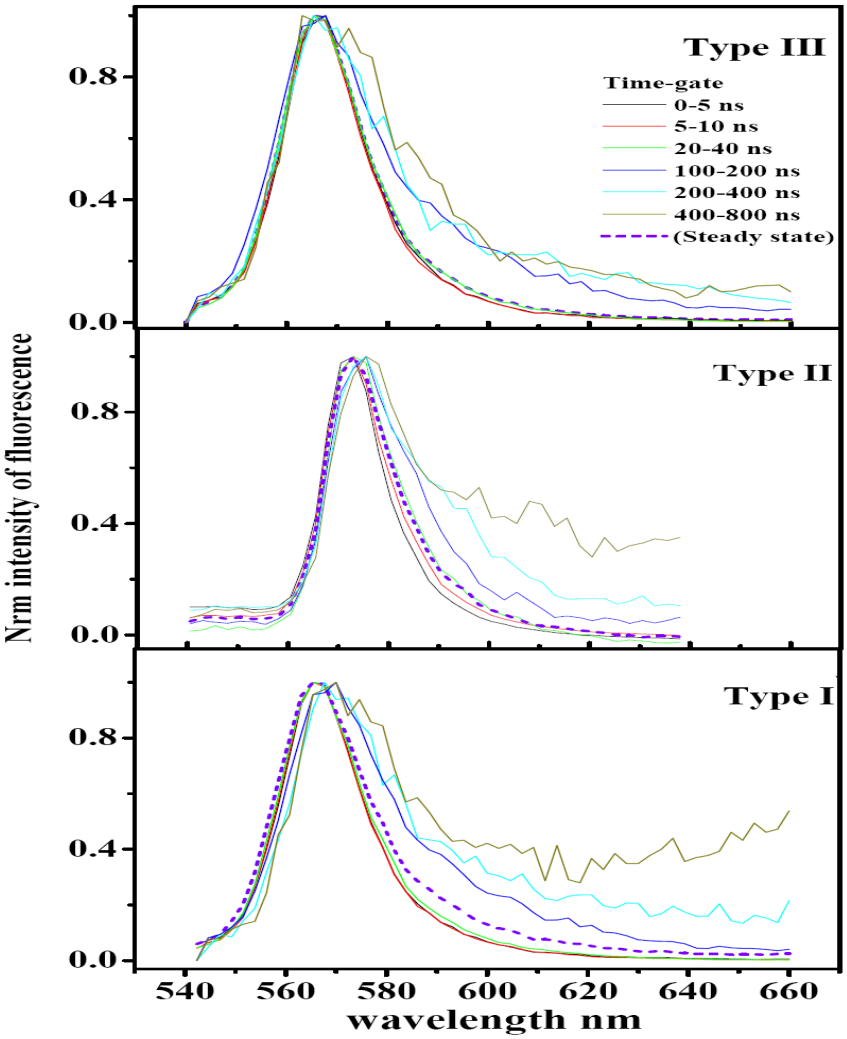

Figure 4.11: Fluorescence spectra at 4 K at different time gates for type I to III CdSe QDs.

4.3.2.II CdSe dots on a CaF_2 substrate:

In this section, I present the results obtained on type I and III dots deposited on a CaF_2 substrate in the same temperature range. Between ~ 100 and 300 K, the kinetics in the two types appears as two independent parts (figure 4.12, 100 K): fast decays with more than two orders of magnitude of signal, and then a slow component takes the rest of the signal.
Below 75 K, The samples show comparable effects to type III dots in a polymer film (see figure 4.8), and to the literature [53, 85, 99, 103]. Because of the remarkable dynamic changes between 4 and 100 K, we presented in figure 4.12 only the decay spectra of types (I) and (III) CdSe in this temperatures range.

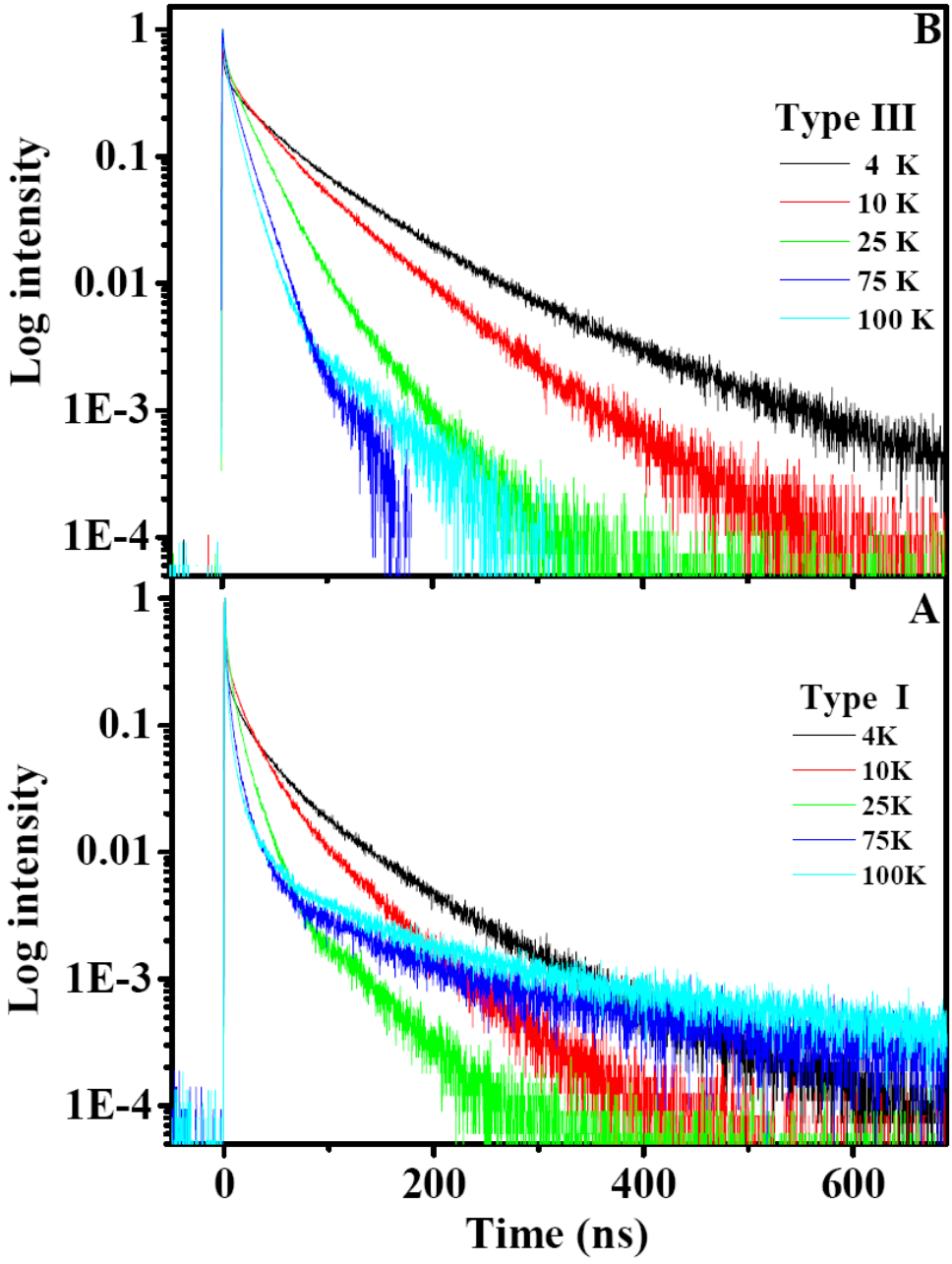

Figure 4.12: The decay curves of CdSe on CaF_2 substrate at different temperatures. A) type (I), B) type (III).

The relaxation decays in figure 4.12A are best fitted with four-exponential decay curves. The fit parameters in the temperature range (from 300 to 4 K) are shown in figure 4.13A, A´ and B, B´. The fastest decay with a lifetime τ_1 of about 1.5 ± 0.3 ns remains unchanged over the whole temperatures range and for both samples with an amplitude increases from 30 % at 300 K to 45 % at 4 K as the temperature decreases.

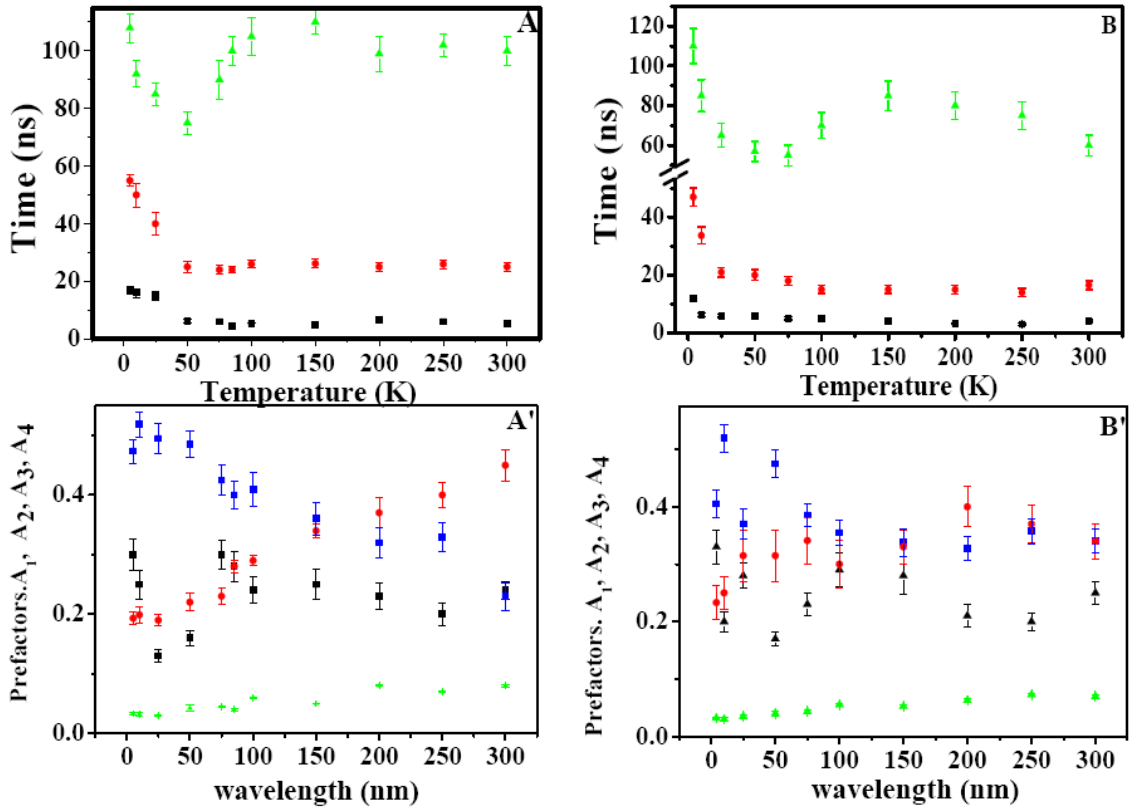

Figure 4.13: Four-exponential fit parameters at different temperatures for type I (A, A´) and type III (B, B´). $\mathbf{A_1}$ (blue); τ_2, $\mathbf{A_2}$ (black); τ_3, $\mathbf{A_3}$ (red); τ_4, $\mathbf{A_4}$ (green).

From figure 4.13A and B, τ_2 and τ_3 in the two types of CdSe QD remain unchanged for temperatures above 50 K; below this value, the two components become slower. τ_4 shows a maximum at 150 K, then decreases until ~ 50 K and below, it becomes slower (~110 ns) at 4 K. In a similar way to what we presented in the case of polymer film, the prefactors behave in complicated way, $\mathbf{A_1}$, $\mathbf{A_2}$, $\mathbf{A_3}$, $\mathbf{A_4}$ have comparable tendency for all temperatures in the two samples (figures 4.13A´ and B´).

Figure 4.14 presents time gated fluorescence spectra of types I and III CdSe QDs at 4 K.

Generally, it shows similar behaviour as in the case of film (figure 4.11). A gradual red shift of the fluorescence band beyond 60-80 ns in type I dots, while no shift in type III. The main difference with the film is the magnitude of shift. We measure 12 nm (39 meV) red shift, while it was 6 nm in the case of samples in film form (figure 4.11). Broad wings appear clearly in the time-gated fluorescence spectra of this group (I) after 100 ns of excitation.

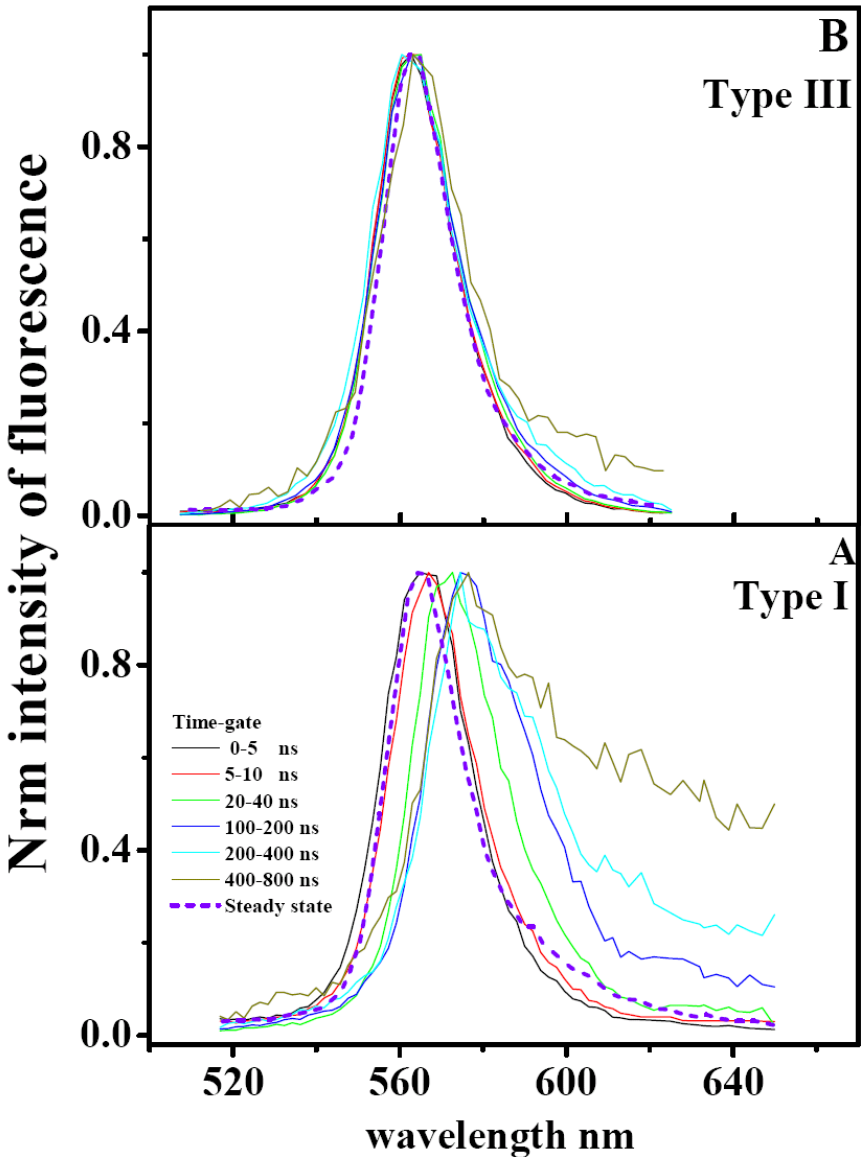

Figure 4.14: Fluorescence bands at 4 K at different time gates, **A)** type I**. B)** type III, on CaF_2 substrate. The colors and gate times are the same as shown figure B for all samples.

For CdSe QDs on a CaF2 substrate we can resume the results by the following points:

a) The general kinetics is qualitatively similar in the two types (I and III) CdSe QD on a CaF_2 substrate at different temperatures.
b) CdSe core-shell sample on a CaF_2 and on a polymer film presents the same kinetics.
c) The τ_2, and τ_3 components show constant lifetime values until 50 K, but below they become slower, while τ_1 stays unchanged for the whole temperature range.

d) The component τ_4 of types I and III shows a maximum around 150 K. This component becomes faster until 50 K and then gradually increases (figure 4.13).
e) Time-gated study resolves slow kinetics (time-delay > 100 ns), in the case of core sample, with a larger red shift (two times more) in the time-gated fluorescence bands, and a clear wing at this energy side (figure 4.14). This behaviour is more clearly in CdSe core than core-shell dot.

4.3.3 Two-Photon excitation.

The main point for using the two-photon excitation technique is that, one and two-photon excitations have different selection rules [137]. In other words, the electronic states which can be reached by one- and two-photon excitation are different.
From the previous models [42, 53, 99, 103], absorption by the lowest band-edge state (|2>) is optically forbidden in the electric dipole approximation[59, 63, 64], because two units of angular momentum are required to go from the ground state $|N_m| = 0$ to the $|N_m| = 2$ sublevel. Therefore, this transition is allowed by two-photon absorption.
The aim of this experiment was to see if we could selectively excite the dark state.
Also, previous studies [53, 95, 99] suggest a population of the bright state from the dark one at room temperature. So one of the purposes of the two-photon excitation is to probe a rise time that reflect this process.
We did the work in three stages: (**1**) We compared the excitation by a laser of 400 nm and tuned to the band gap at RT. (**2**) Compared the 400 nm one-photon excitation with 800 nm two-photon at room temperature and at 4 K. (**3**) Compare the band-gap one-photon excitation with band-gap two-photon excitation at 4 K.
To do that, two different sizes CdSe QDs capped with TOPO were used in these experiments. For experiment (**1**), CdSe dots with 4 nm as diameter corresponds to 585 nm band gap absorption at room temperature, while in (**2)** and **(3**) CdSe sample but with smaller size (3.7 nm diameter corresponds to 577 nm band-gap absorption at room temperature) was used.

1- 400 nm vs 595 nm excitation. The decay kinetics of the CdSe sample excited at 400 nm and at the band gap (595 nm) at RT is shown in figure 4.15. The two decays do not exhibit any difference between the two different types of excitations.

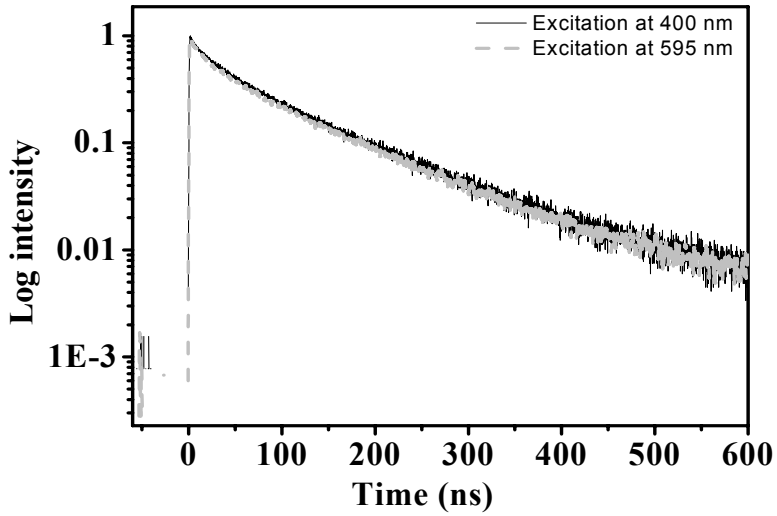

Figure 4.15: CdSe-TOPO QDs sample (4 nm diameter) excited by two lasers wavelengths: at 400 nm and at the band gap absorption (595 nm).

2- One-photon vs two-photon above the band gap. In this part, we detect the decay of CdSe emission after one and two-photon excitation at 400 nm and 800 nm respectively, at room temperature and at 4 K. In both cases (figure 4.16), identical kinetics at these two wavelengths of excitation was found.

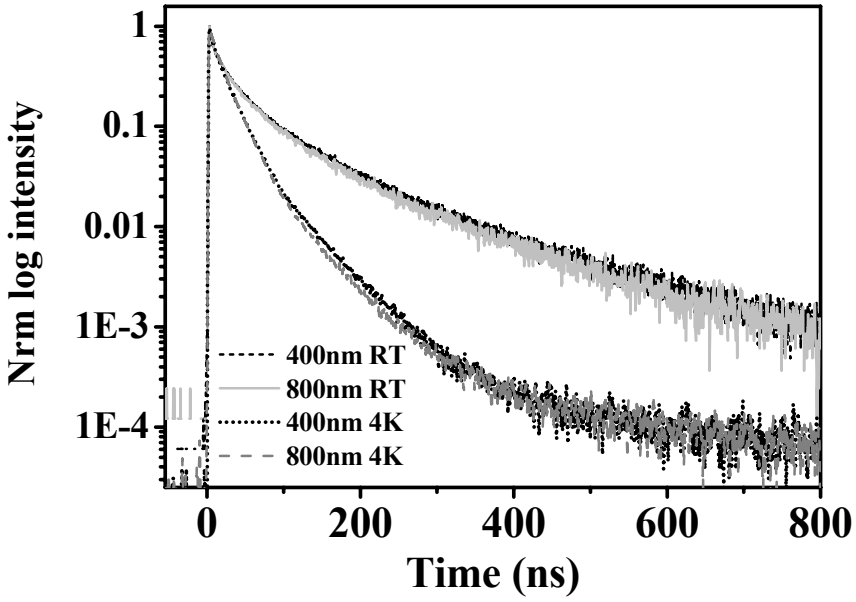

Figure 4.16: Room and low temperature decay kinetics at 400 and 800 nm laser excitation.

- **One-photon vs two-photon excitation of the band gap.** We detect the decay kinetics after excited in resonance with one-photon (band gap excitation at 560 nm), and two-photon (1120 nm) at 4 K.

Figure 4.17 shows the two decay measurements results, which show similar behaviour at the two wavelengths of excitation.

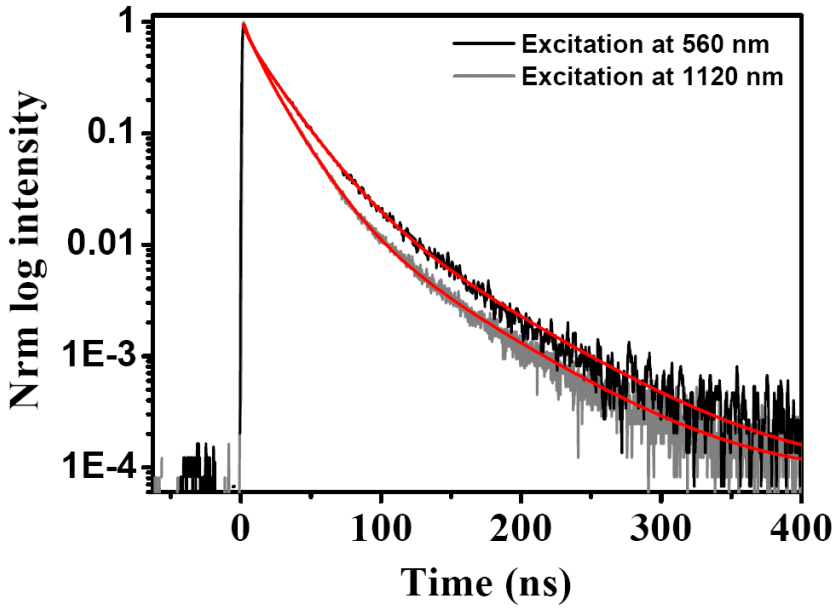

Figure 4.17: Decay kinetics laser excitations of 560 nm, and 1120 nm. The two kinetics are fitted by four exponential (red) fit function.

To better resolve the details of the kinetics at early times after excitation, we repeated the measurements with higher temporal resolution. An instrument time resolution of 65 ps (FWHM) was used to record the decay on a 5 ns time-window. A rise time was expected from this measurement for two-photon excitation. The decay kinetics of CdSe QDs after excitation at the above wavelengths (560 nm and 1120nm) is shown in figure 4.18.

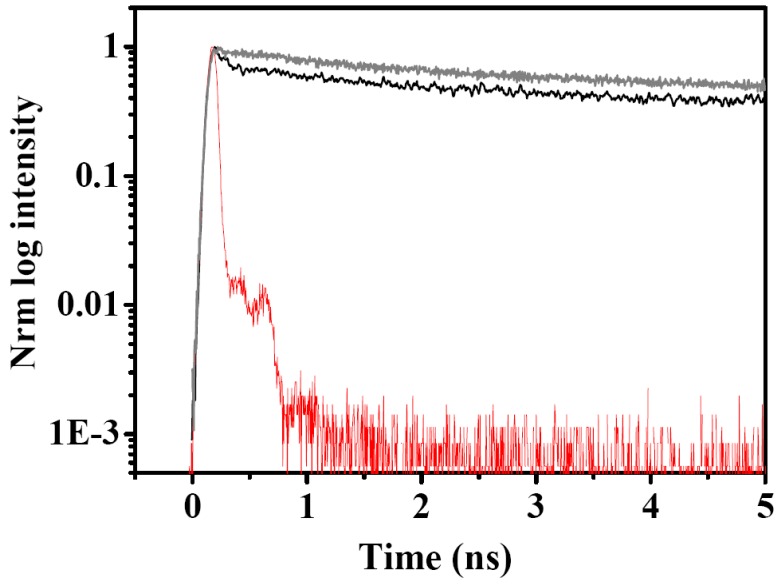

Figure 4.18: Decay kinetics of CdSe QDs after one (gray) and two-photon (black). The temporal resolution of the instrument response function is 65 ps FWHM (red) in this time window.

From the above figure, it is clear that no rise time in the signal and the decay is identical. The short component that appears in figure 4.18 is due to the multi-excitonic decay, occurring because of the 20 mW of laser excitation. With lower excitation power, the signal was difficult to detect.

In conclusion, the result of one- and two-photon excitation for all possible excitation wavelengths at RT and 4 K shows: (**i**) identical decays kinetics in all possible cases detected by one or two-photon excitation. (**ii**) The lower state (|2>) as described in the literature as a dark state with $|N_m| = 2$ does not resolve by our experiment. (**iii**) The expected rise time between the dark and the bright states does not recognized.

4.4 Discussion and conclusion.

4.4.1 Environment effects at room temperature:

The unchanged behaviour of the low-resolution spectroscopy of the different types (I, II, III) of CdSe QDs in different environments (figure 4.2A and B), and the same range of QY values points to unchanged spectroscopic properties of these samples at room temperature [91]. The surprising results were the very different kinetics of these samples revealed in time resolved fluorescence measurement (figure 4.3). The slowest kinetics always occurred in the film form for types I and II, while in type III CdSe core shell sample, the decay was independent on the environment. These differences between CdSe samples, in the presence of the polymer (butyl methacrylate-comethy methacrylate) film form or on the CaF_2 form, can be attributed to chemical changes at the surface of CdSe QDs (I, II). Preparation of the sample in the form of a polymer film in presence of trioctylphosphine and heating of the sample can add more capping to the surface and reduce the traps on the surface. The traps can be considered a state, which decrease the electron-hole overlap of the excited electron hole pair. This treatment makes the whole decay go slower than the case of solution or on the CaF_2 substrate without the additional temperature effect. The above surface changes contribute differently to the case of purification of CdSe surface nanodots in solution, where the intrinsic lifetime τ_3 and the longest component (τ_4 > 80 ns) become faster after purification as we showed in the previous chapter. The τ_1 and τ_2 components become clearly more prominent. This behaviour proves that the purification processes (less ligand and more traps [111]) correlates to faster kinetics, while by add the TOP and heating the mixture increase the lifetime decay of the two longer components in opposite way to the purification. The small changes in the case of CdSe/ZnS core-shell QDs in film and solution are due to the shell layer of protection and less probable chemical modifications in this case. These changes in the CdSe QDs kinetics, and in contrary behaviour, the identical behaviour for the low-resolution spectroscopy point to the important role of the surface and the environment effects on the decay relaxation and not on steady state measurements,

which also appear in the differences between the CdSe core and core/shell as a function of temperature and capping.
Contradictory views presents by other works [121, 138], which consider the surrounding material itself acts as a source of trap states. They show different dependences as a function of the environment of the sample.
Our results with the unchanged absorption and the fluorescence spectra, the purification experiment that presented in the previous chapter, and in addition to the presence of the TOP component in the CdSe samples synthesis and in the method of film preparation, point to different tendency than the consideration of those models. [121, 138]
Another effect appears, as an important parameter in the relaxation behaviour of the nanoparticles, is the effect of the surface charges on the bright exciton lifetime [120, 139]. As an example, in the case of a positively charged dots, the electron is attracted by the surface charge, while the hole moves in the opposite direction. Because of the reduced overlap between electron and hole wave functions, the bright exciton lifetimes was found to increase up to 2 order of magnitude, depending on the location of the surface charge [139]. V. A. Fonoberov *et al* [140] found similar results of excitons in the presence of an ionized acceptor. This type of charging might be another reason for the behaviour of CdSe QDs in the case of the polymer film and on the substrate, where the possibility to have charged particles in these two environments is larger than the case of dots in solution.

4.4.2 Temperature dependent optical properties studies:

The three effects at low temperatures (luminescence maximum shift, width of the fluorescence band, and relative fluorescence intensity) can be due to interactions between electrons and phonons in the crystal and to the decrease of the nonradiative processes at low temperatures [130, 141-143].
In general, different origins contribute to the observed spectral widths of the excitons. The first is the inhomogeneous width due to the size distribution in the nanocrystals [135], the second is the lifetime width due to the recombination with the surface charges or the trapping to the surface states [129], and finally there is broadening due to the interaction of the excitons with longitudinal acoustic (LA) phonons and longitudinal optical (LO) phonons [144] (see also § 1.4). The reduction in the fluorescence band width reflects the quantization of the electronic states in the nanocrystals, thus, there are no electron and hole continuum states for the exciton to be ionized [145]. However, the general trend of the fluorescence bandwidth, presented in our work, at the whole range of temperatures is similar to that presented in many experimental works [135, 143, 146]. The extracted value of σ is much higher than the case of bulk CdSe, which are around 8 μeV/K [129]. This indicates a strong increase of the coupling with acoustic phonons, induced by the reduced dimensionality of the system. And again, this behaviour is in good agreement with both theoretical [144, 147, 148] and experimental [135, 143] studies.

The presence of the some additional dephasing process, as discussed above, which probably induced by the surface defects or trap states, can be explain the bigger experimental σ fit values in our work and in the other experimental works than the theoretical calculations. The further effect of the surface defects and trap states processes is adding important contribution to the homogeneous linewidth in the very small size regime [149]. Another contribution to the increased homogeneous broadening comes from the coupling between the QDs and the matrix [150]. The other fit value, Γ_{LO} ~ 20 meV in all samples form, shows smaller values with respect to the bulk value [151] (~ 100 meV). This reduction in the QDs value is also due to the quantum confinement that affects the phonon energy [135], which depends also on the mechanical boundary conditions[152] (electron-hole interaction in spherical dots is only allows contributions from phonons states with angular momentum $l_p = 0$ and $l_p = 1$), and on the surface phonons [153]. E_{LO} is also consistent with the values obtained from low-temperature Raman spectroscopy on CdSe nanocrystal in polystyrene film [154]. (~ 25.4 meV). Below T =50 K the FWHM shows a linear dependence on T caused by the effective absorption and fluorescence of acoustic phonons coupled to the excitonic state [135]. The main point in this study is the unchanged behaviour between the different types (I, II, III) CdSe QDs in different environments. This behaviour might be due to the nature of the homogeneous broadening, which in main reason is due to the exciton-phonon interaction that appears slightly dependent on the type of capping (TOPO, Oleic acid, and ZnS). In chapter 6, this effect appears hardly effected by the shape of the nanocrystal (especially for rod shape).

The blue shift of the steady state fluorescence at lower temperature can be explained by two reasons: First, a shift in the relative position of the conduction and valence bands due to the temperature-dependent dilatation of the lattice [130]. This dependence is linear at high temperature ($\Delta E_g \propto T(T >> \theta_D)$) and becomes nonlinear for the case of lower temperatures $\Delta E_g \propto T^2(T << \theta_D)$ where E_g is the energy gap in the bulk semiconductor, and correspondingly the dilatation effect on the energy gap is also nonlinear [130, 155] for smaller temperature than θ_D, (β in equation 4.2 ~θ_D). θ_D is Debye temperature, and indicates to the temperature of a crystal's highest normal mode of vibration [132] or, θ_D is corresponds the average phonon temperature [156]:

$$\theta_D = \frac{h\nu_D}{K_B} \tag{4.3}$$

Where ν_D is Debye frequency, and indicates to the maximum number of modes of vibration (allowed phonon frequency) in solid, h is Planck's constant, and K_B is Boltzmann constant.

The second reason is again a shift in the relative position of the conduction and valence band, but as a result of the temperature-dependent electron-lattice interaction[128, 130]. This type of changed interaction between electron and lattice at

low and high temperatures has again the same dependence as above. Comparing the value of energy gap shift in our CdSe QDs, with the temperature dependence of the energy gap of semiconductor bulk described by the relation given in 4.1, show comparable fit values (table 4.II). The smaller value for θ_D in this table indicate to lower phonon temperature in our case than the case of bulk. The fit behaviour and the other fit parameters is not so sensitive to the value of θ_D. The fit values of θ_D show comparable values to our temperature in many experimental works [133, 156]. The dependence of CdSe I indicates that the phonon-mediated gap-shift is similar for nanocrystal and bulk CdSe. Moreover, we can conclude that the crystal lattice of the CdSe nanocrystal shows bulk-like lattice properties already for very small NCs sizes.

In addition, increase of the fluorescence intensity of the nanocrystal is a direct result of the reduced thermal non-radiative processes that affect the emission yield, where, the increasing phonon population (both confined acoustic phonons and LO phonons) supports nonradiative recombination which results in a decrease of fluorescence intensity at higher temperatures. The "quantum yield" of the two-sample types increases in the whole range of temperatures (T < 300).

This behaviour supposes a similar slowing factor in the decay kinetic of CdSe QDs [157]. This behaviour, as we will discus later does not appear in the case of core samples I and II in film. Better argument to the previous QY dependence appears in the case of CdSe/ZnS in film and on a CaF_2 substrate (figures 4.8C, 4.10). This indicates that the lengthening of the lifetime with temperature corresponds to a decrease in the nonradiative relaxation rate.

4.4.3 Temperature dependence kinetics of CdSe QDs:

The kinetics presented in the previous paragraphs (§ 4.2, 4.3.2.I, 4.3.2.II) showed different decays as a function of the capping and environment. Comparing these results with the literature [53, 103, 127] shows that only the CdSe/ZnS core-shell samples (in film and on CaF_2 substrate) show similar results as described in previous works, which were explained in terms of the thermally activated population of the bright and dark state at high and low temperatures. However, even here we observe two distinct differences: (**i**) our data show a multi-exponential decay (no stretched exponential or power law decay in the dynamics). (**ii**) The measured kinetics show an additional process with a long lifetime, which appears at all temperatures. This component complicates the interpretation of τ_3, especially at low temperature where the measured radiative lifetime τ_3 is the lifetime of the dark state ($|2>$) (150 ns for the case of ensemble [53] of dots and ~1 μs for the case of single dot [103]). Less than four orders of signal to background magnitude resolves this component (τ_3 ~150 ns) only at lower temperatures, which might explains the absence of this long component from the literature work. The low weight of the fourth component (A_4) (< 10 %) is might be another reason for ignoring it. This low amplitude A_4 points to an idea about its origin, which is influenced by the environment (solution, film, and CaF_2 substrate).

At room temperature, we found no differences between time –gated fluorescence features at all time-gated windows (figure 4.4), and identical decay at the red and the blue side in all samples and at all forms (film and substrate) at low power of laser excitation. This behaviour is different at lower temperature, where we noticed a 5 nm (figure 4.11 A and B) red shift in type I and II in film after 100 ns, and a 12 nm (figure 4.14 A) red shift for type I on CaF_2. This effect is much less pronounced in core-shell samples, which can be explained by the effect of the ZnS layer. Since the ZnS layer mainly improves the surface quality [158, 159]. The red shift in the time-gated fluorescence bands after ~ 60-80 nm is might by due to the surface trapping states or charging effect.
Generally, chemically synthesized colloidal CdSe QDs have a high photoluminescence QY reaching up to 85 % even at room temperature [160] (no more than 35 % in our synthesis or with the commercially QDs used in this work), indicating that nonradiative decay channels are weak (§ 1.5.2), especially in core-shell samples due to high surface quality [158, 159]. The samples used in our work confirm this tendency about the weak contribution of the nonradiative channels, where no features were resolved at the low energy side of the steady state spectra at low temperature (§ 1.3.2, § 1.5.2). Only time-gated fluorescence bands resolve weak channels with lower energy states than the e-h recombination (§ 1.5.2, Figure 1.12).
Another reason can explain the appearance of the trap states in the time-gated fluorescence, only at low temperature, is the probable different types of single dots in each samples. The ensemble of CdSe dots in all forms (solution, film, and on CaF_2 substrate) could have neutral dots, charged (positive or negative charges) dots, and dark dots [160]. All of these dots contribute differently to the dynamics of the ensemble of CdSe QDs at low temperature with additional surface or trap states, while less differences show up at room temperature due to thermalization between bright and dark states [160] (~ 6-16 meV), and all of the trap and surface states (k_BT (at RT)= 25.8 meV).

The first component $\boldsymbol{\tau_1}$ shows different behaviour than the other components and appears in the following points: (i) $\boldsymbol{\tau_1}$ shows slightly an unchanged lifetime constant for all of the temperature dependence study of CdSe types (**I**), (**II**), and (**III**), while it was clearly sensitive for the other treatments presented in chapter 3. (ii) The amplitude of this component is increasing as the temperature decreases.
The general dependence of all decay times $\boldsymbol{\tau_1}$, $\boldsymbol{\tau_2}$, $\boldsymbol{\tau_3}$, $\boldsymbol{\tau_4}$ in CdSe (I, II) in film, which increase between 300K to 200K and then decrease gradually below this temperature, presents a totally different effect to what was reported in literature, where the radiative life time raises to higher value at lower temperatures. This behaviour indicates that the temperature dependent kinetics of CdSe QDs capped with organic ligand is strongly correlated with the surrounding environment of the QDs. This environment behaviour was found before, even at room temperature, as different between the solution and samples in film form for samples (I, and II). The sample III in film (group III, has a layer of ZnS protects the CdSe crystal) presents environment

independent kinetics (solution, film, and on the substrate) figure 4.3, and comparable kinetics to the literature (slower kinetics at lower temperature) [42, 99, 100, 103]. For that, the temperature dependence of type I and II CdSe QDs in polymer film can be considered as an example of the environment effect on the kinetics of nanoparticles. Where the fine structure of lowest excited state was strongly influenced by the energy states of the polymer film.

Type III (core/shell) CdSe QDs in film and on a substrate as a function of temperature present similar dependence to the experimental [99, 100, 103] and theoretical [42] results. In all of these works, the authors report a single slow lifetime at low temperatures, while we think that this single lifetime is contribution of τ_3, and τ_4 together. Crooker et al [103] indicate similar kinetics in core and core shell CdSe QDs, especially between 90 K and 0.38 K. However, above of 90 K no clear dependence was presented. Sander et al [100] presented similar dependence to what we discussed in CdSe core-shell samples. The same author explains the remarkable changes at ~ 200 K as an influence of the capping molecules, which have a phase transition and cause the detected maximum at 200 K, this effect depends directly on the type of capping ligand [100]. This behaviour correlates very well with our data, which show first maximum (τ_2,τ_3, and τ_4, see figures 4.9 and 4.13) at a 150 K. In addition, the fluorescence quantum yield presents also similar maximum around this temperature (figures 4. 6C and 4.7C).

Below 100 K, Core-shell samples do not show any influences due to film form (figures 4.10) or on a surface of substrate (4.13), and larger values for τ_2,τ_3, and τ_4 were measured. Again, our work resolves τ_3, and τ_4 as two different physical effects, with two distinct lifetimes for all treatments.

Early low temperature studies indicate the resolved long lifetimes to trap states [49, 52]. Following works indicate the temperature dependence of CdSe dynamics to the model of dark and bright states [42, 99, 100, 103], with parameters (shape, crystal structure, and e-h exchange) that play an important role in the exciton fine structure. The way to identify trap states starts from the analysis of steady state emission spectra followed by time, temperature, and intensity-dependent investigation of their dynamics [41]. From the above discussion, we resume that the high quality of CdSe QDs makes it difficult to distinguish the low intensity red traps emission spectra at room temperature. In addition, time resolved spectroscopy presents similar dependence at all wavelengths at room temperature (figure 3.7), due to energy thermalization. In our samples, which all have quite high quantum yield (more than 30%), we never observe trap fluorescence at the far-red side of the steady state emission band at room temperature or at low temperature. As was seen by others upon experiments involving ligand exchange and washing [105, 161].

Cooling the sample reduces all thermalization processes and nonradiative effects. The reduction of these dynamic sources at low temperatures leads to different consequences: (**i**) The samples quantum yield rise as we discussed previously. (**ii**) Very slow trap dynamics appears clearly at low temperature. This trap-fluorescence behaves in a similar way as dark states with long lifetime decay, and become less

probable at lower temperature, which explain the longest lifetime weight in the CdSe decay τ_4. Time resolved spectroscopy at low temperatures shows clearly this contribution at the red side energy (slower decay at the red part than the blue side).
At low temperature, time-resolved spectroscopy in film shows a slower decay at the red side of the emission band than at the blue one in all samples I, II, and III. Steady state fluorescence in this case is the contribution of two luminescence effects with different dynamics: (**1**) The radiative electron-hole recombination band with less broadening width at 4 K than at RT. (**2**) Another slower component (time-gated fluorescence band after 60 ns time delay) band at the red side, which might be due to slow physical processes with lower energy states than the band edge radiative exciton, and less intensity. This second effect goes hand in hand with the decrease of the same component in film form than in solution form at room temperature (figure 4.3), because of the reduced number of traps due to the procedure of film preparation.
In conclusion of the previous discussion, the slowest component in the decay kinetic of CdSe QDs, which appears at all temperatures and after all treatments and application, is might be due to traps? Moreover, the intrinsic lifetime of CdSe QDs (> 100 ns in general) at low temperature in all of the literature that discussed this behaviour is a contribution of two lifetimes. The first one is the radiative e-h recombination lifetime (50-60 ns at low temperatures), while the other component is the traps that contribute this kinetics with long lifetime (~ two times slower than the e-h recombination lifetime), even without clear appearance in the steady state fluorescence due to its low weight (> 0.10 in all studies). This effect will appear more clearly in the case of CdSe nanorods, where the wide surface of the rod particles, comparing to the dot, increases the probability of traps state.

The experiment of one and two photon excitation is another prove to the last conclusion about the origin of the slow component. Where the same energy that used to excite the samples by one or two photons at room and low temperatures present an independent kinetic to this effect. The one or two-photon excitation present similar relaxation decays without any signature of different effects from the dark state. This experiment confirms the origin of the long components as a trap effect than from the spin forbidden |2> state.
The observed time-resolved spectra in film is slightly shift to the red (figure 4.11 A and B), by about 5 nm. We do not think that this could be due to energy transfer, because of the diluted samples we used. The energy difference for the bright |1> state and the dark |2> state is very small due to the size of this sample (4.0 nm). In our case, the significant increase in the decay time occurs at about 200 K (τ_4 =110), and indicates an energy difference of 17 meV (kT=17 meV for 200 K). This value corresponds nicely to the 5 nm (19 meV) shift (between 565 nm and 570 nm) in CdSe in film (I).

Earlier, several luminescence models implying nonexponential decay kinetics were successfully used in the analyses of photo-luminescence decay curves of

semiconductor nanocrystals. The micellar kinetics [162] originally developed to describe luminescence quenching in organic micelles implies a discrete number of traps per crystallites with a random distribution of traps over an ensemble of crystallites and is widely accepted as the relevant model for nonradiative dynamics in nanocrystals.[163-165] Stretched-exponential decay laws imply migration of recombining components in a fractal space and can account for coexistence of local and migration lifetimes. These laws are inherent in a vast number of processes, including the photoluminescence of nanoparticles [166, 167]. The three states model, zero exciton ground level, and two excitonic ground states representing, the dark ($J = \pm 2$) and the bright ($J = \pm 1^L$) excitons, are not completely the temperature dependence presented in this chapter, because of the number of exponential (four-exponential) we used to fit the CdSe QDs kinetics. However, our attempt to apply these models to the analyses of CdSe luminescence decays failed to provide both reasonably good fit to experimental decay kinetics and consistent temperature behaviours of the parameters recovered. They indicate to the complex superposition of different process (radiatively and nonradiatively) affect the decay curve with different dependences. Our work provides quantitative information on the character of the temperature dependence of the photoluminescence decays of CdSe nanocrystal in various environments and different capping form. At present, we have no complete explanation for the temperature dependence decays of CdSe QDs.

Chapter 5

Energy and time-resolved spectroscopy of CdSe nanodots with zinc blende lattice structure.

5-1 Introduction and motivation.

Bulk CdSe exists in two crystalline lattice structures: Wurtzite (W, hexagonal) and zinc blende (ZB, Cubic), shown in figure 5.1. These structures only differ in the stacking sequence of the CdSe hexagonal packed layers. The W structure has an ABABAB stacking sequence along the [168] direction, while the ZB structure has an ABCABC stacking sequence along the [111] direction. The energy difference between these two forms is small. ZB is the stable room temperature phase, but it transforms reversibly to the W structure above a critical temperature of 95±5 ºC [169].

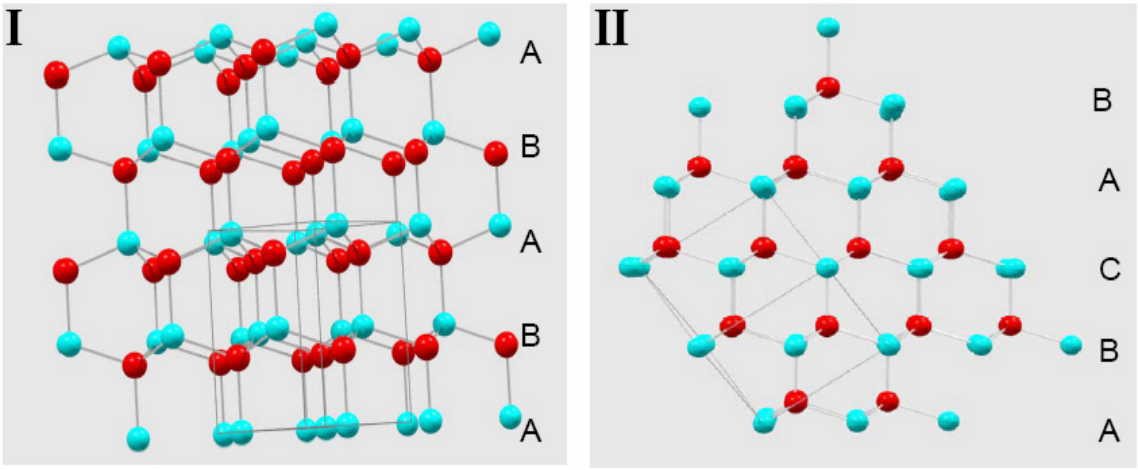

Figure 5.1: The lattice structures of bulk W and ZB CdSe crystals. (I) presents the layer stacking along the (0001) direction in the W structure, while (II) presents the layer stacking along the (111) direction in the ZB structure.

The traditional synthesis of high quality spherical CdSe NCs is usually carried out at temperatures >300 °C (see 2.5.1), and it always yields dots with a W lattice structure, sometimes with a few ZB stacking faults [36]. the seed particles have a ZB structure at the beginning of the growth, but a structural phase transition to the W structure occurs as the particles grow in size [36, 88, 170].
Recently our group presented a method for the synthesis of high quality size-controlled CdSe dots having the ZB lattice structure [86], and the quantum yield was in all cases on the order of 25%. Contrary to the synthesis reported by Rogach *et al* [171], we prepared the ZB samples at high temperature in an organic medium. As Yu *et al* [172], CdTe synthesis, it is based on the use of alkyl phosphonic acid (PA), but here it is added to the Se solution. We also found that the injection temperature is not a crucial parameter in the synthesis. The synthesis details were presented in the experimental section (2.5.2).
The effect of crystal structure on the spectroscopy of CdSe QDs was previously studied theoretically [42, 173]. These models predict that the intrinsic asymmetry of the hexagonal lattice structure of the crystal splits the 4-fold degenerate hole state into two-fold degenerate hole state (see figure 1.3.a). The changes in the band edge exciton structure, which are due to the differences between the two structures (W and ZB), are expected to exhibit different optical properties and kinetics.
The aim of this chapter is to present the structural properties of the ZB CdSe nanoparticles. We then describe their optical properties and relaxation processes. Finally, we will compare their optical properties and dynamics with those of W nanodots, that were studied in chapters 3 and 4, and with theoretical works in literature [42, 173], or with similar experimental studies on CdTe QDs [137].

5.2 Results:

5.2.1 Low-resolution spectroscopy.

In figure 5.2, we presents the UV-Vis absorption spectra for a series of samples prepared in presence of alkyl PA (A) and by the traditional recipe [174, 175] which yields W dots (B) (see § 2.5.1 and § 2.5.2).

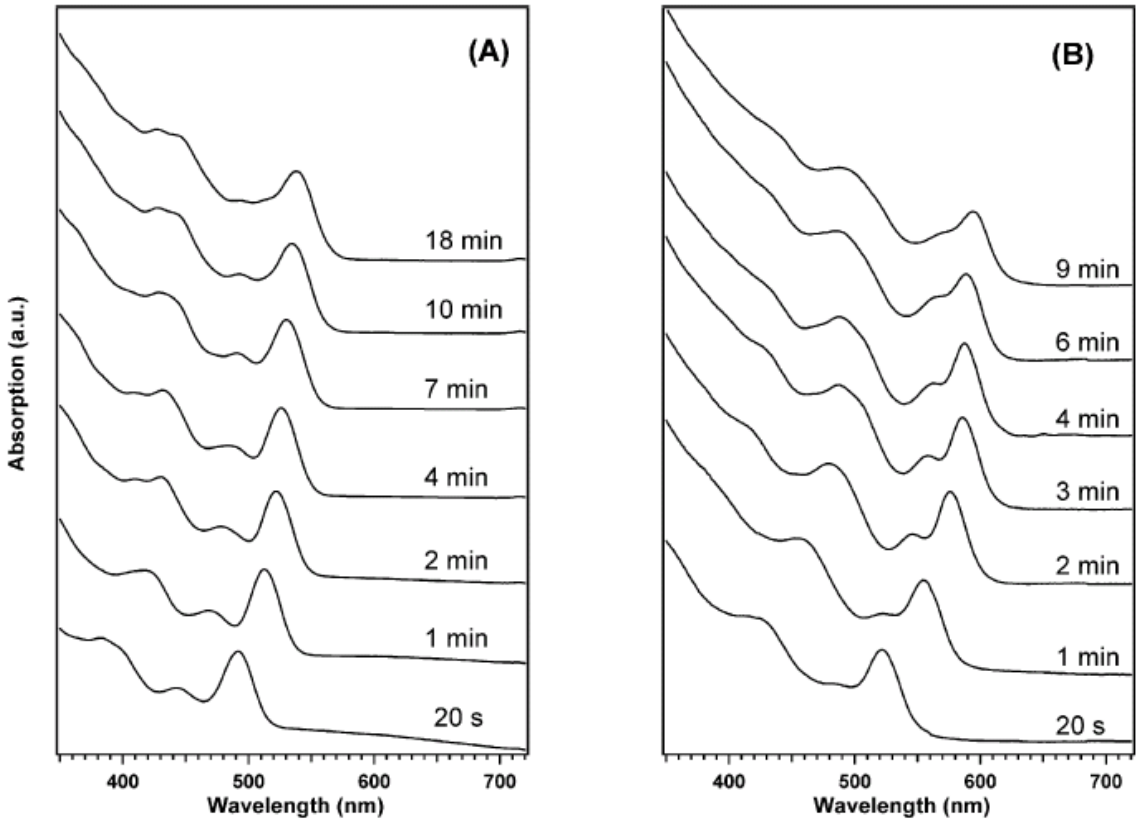

Figure 5.2: Temporal evolution of the growth of CdSe NCs prepared in oleic acid (A) in presence of alkyl PA and (B) according to the recipe of Talapin et al.[174].

Several differences appear between them; first, the growth rate is faster in the recipe of Talapin *et al* [174], where for the same band gap absorption, in the presence of alkyl PA it takes about 20 minute, while it takes 1 minute in the method of Talapin *et al* [174]. The second difference appears more clearly in figure. 5.3A, where two spectra having the same band gap energy are superimposed. In the PA synthesis, particles have a larger energy splitting between the first and second absorption bands, than in the recipe of TOPO one [174, 175]. This applies to the whole range of sizes we obtained in our group, as seen in figure 5.3B, which compares the first-to-second absorption band splitting as a function of band gap absorption with the same plot from ref. [82] for the case of W dots, and from theoretical calculations for CdSe ZB dots [176].

.

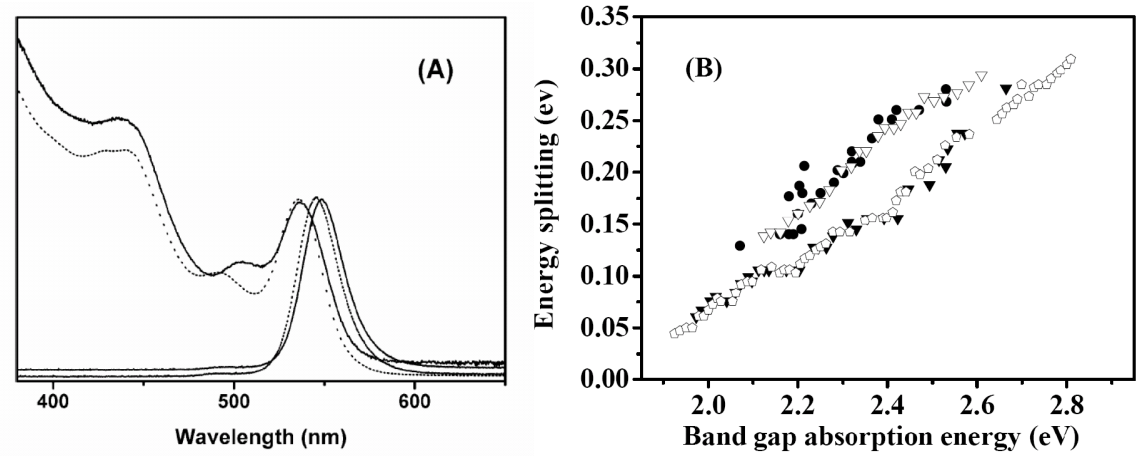

Figure 5.3: (A) absorption and emission spectra of CdSe dots prepared by the recipe of Talapin et al [174, 175] (solid lines) compared with a dot of the same band-gap, prepared in presence of alkyl PA (dashed lines). (**B**) First to second absorption band energy splitting as a function of the band gap absorption energy for CdSe NCs prepared in presence of the alkyl PA (solid circles), and without (solid triangles). The hollow diamonds represent the same plot from ref. [82] for the case of W dots, while the hollow triangles represent the splitting from theoretical calculations on ZB dots [176].

From figure 5.3B, the experimental results in presence of alkyl PA show a different energy splitting than the same values of the samples prepared in the method of Talapin *et al* [164] (house-made) and to that presented in reference [82] for W structure. On the other hand, the results with the PA show good agreement with theoretical calculations [176]. In the latter work, the authors started from the data of W CdSe QDs from ref. ([82]), and then they removed the electron-hole exchange interaction and the crystal field (hexagonal) effects to obtain the possible energy distribution of CdSe QDs with ZB structure.
Figure 5.4 compares the Stokes shift of W CdSe dots with that prepared with alkyl PA, which have ZB structure.

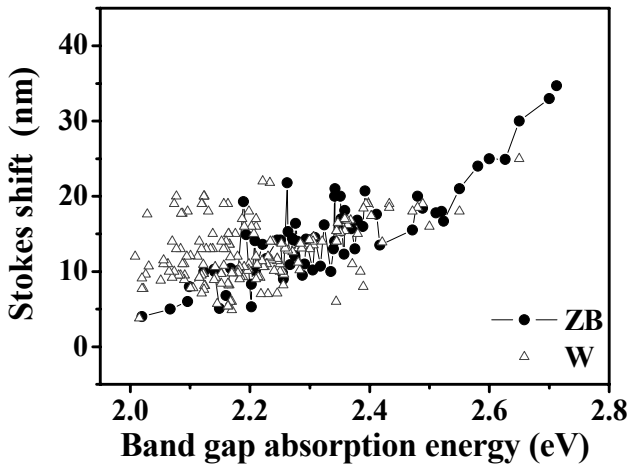

Figure 5.4: Stokes shift values between absorption a fluorescence spectra of all samples prepared using alkyl phosphoric acid (ZB) and TOPO (W).

From figure 5.4, we have the following conclusions:

(a) For the same band gap energy, in the case of both structures, the Stokes shift has comparable value.

(b) Because we can prepare smaller dots with ZB structure only, we see larger range of ZB QDs with bigger Stokes shift than W structure.

In general, the differences in the electronic structure between the two preparations arise from differences in shape, crystal structure, or surface structure [42]. Therefore, we also investigated the morphology and lattice structure of the NCs using TEM as we presented in chapter 2.6. Figures 5.5A and 5.5B respectively show the TEM and High resolution TEM (HRTEM) pictures of CdSe nanocrystals (band gap absorption at 540 nm) prepared with alkyl PA. The images clearly show that the nanocrystals are dot-like with a high uniformity in size and shape. They can also form regular superlattices (figure 5.5A). The HRTEM (figure. 5.5B) reveals the high crystallinity of the dots; different lattice planes could be distinguished.

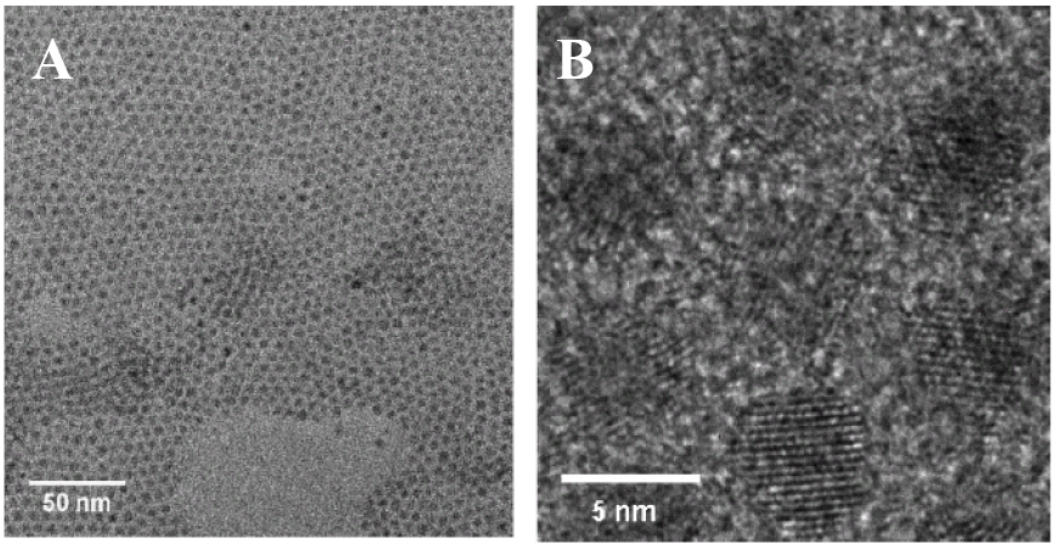

Figure 5.5. TEM (A) and high-resolution TEM (B) images for CdSe nanocrystals (band gap absorption at 540 nm) prepared in presence of alkyl-PA.

Figure 5.6 shows the XRD patterns obtained for dots prepared with (A) and without PA (B). This figure was presented in the experiment of section (2.7) as an example of the aim of X-Ray measurements to prove with certainly the crystal structure. The X-Ray spectra in figure 5.6 confirm the ZB structure of the samples prepared with alkyl PA and the W structure of those prepared without it. Figure 5.6A shows three distinct features: the first at $2\theta = 25°$ is due to (111) reflection and the two broad features appearing at $2\theta = 42°$ and $50°$ are due to (220) and (311) reflection, respectively. The shoulder at $2\theta = 30°$ is due to the (200) planes. Moreover, the absence of (102) reflection at $2\theta = 35°$ and (103) reflection at $2\theta = 46°$, typical of the W lattice structure (see Figure 5.6B), is further confirms to ZB structure.

.

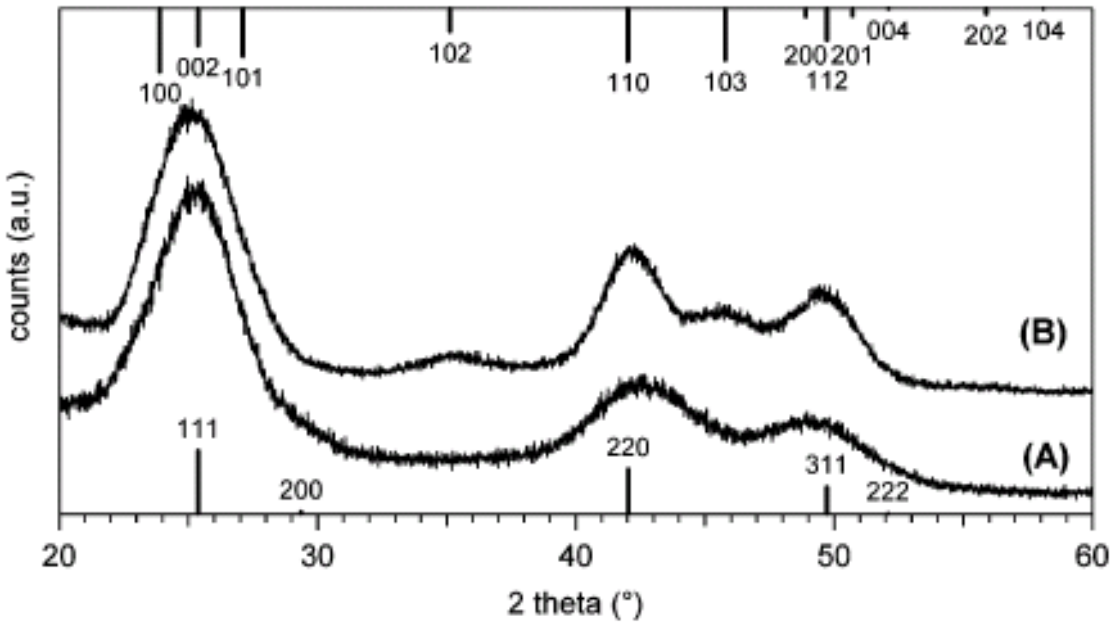

Figure 5.6: XRD pattern of CdSe NCs prepared with (A) and without (B) alkyl PA. The upper vertical bars represent the position of the diffraction peaks for the bulk wurtzite lattice structure and their lengths are proportional to their intensity. The lower bars represent the same for the zinc-blende lattice structure. Trace A corresponds to a ZB dot sample with 515 nm band gap absorption. Trace B corresponds to a W dots with a 4.2 nm (582 nm band gap absorption).

5.2.2 High resolution luminescence and excitation spectra.

Photoluminescence excitation (PLE), and fluorescence line-narrowing (FLN) spectroscopy was used to examine the electronic structure in the band-edge absorption features of CdSe with W structure [59, 61, 113]·[62, 177]. The reasons for these studies were investigated because of a number of puzzles [61]: (i) The photoluminescence of high quality samples is found to be red-shift with respect to the excitation frequency and has very long radiative lifetimes [178] (τ ~1 μs at 10 K) compared to the bulk lifetime (τ ~1 ns). (ii) The very large Stokes shift values of the luminescence with respect to the absorption for excitation far from the band edge [61], whose magnitude reaches ~100 meV in 1.6 nm CdSe crystals [178], while the Stokes shift of the resonant band-edge photoluminescence is only ~ 9 meV for this size. These two effects can be explained if the ground state is an optically forbidden state split from the first optically active state by the electron-hole exchange and the crystal field.

In the case of ZB structure, as discussed in the introduction of this chapter (§ 1.3a), the band edge structure is expected to be different from the case of W Case, while figure 5.4 shows comparable Stokes shift values for the two structures. To explain the remarkable Stokes shift (similar to the case of W structure), and examine the band-edge structure of the CdSe QDs with ZB structure in more detail, and finally to

compare the ZB QDs with literature for the W CdSe QDs, we used the PLE and FLN spectroscopic techniques. We studied a CdSe QDs sample (**I**) with a clear ZB XRD pattern and 570 nm band gap absorption at RT. Later ,and in the second part of this paragraph, we present the same study for two CdSe dots with two different structures, then we compared our results to the work of Norris *et al* [63] and Wind *et al* [62]. The two works used the same technique for W structure.
Figure 5.7A shows absorption and emission spectra of the ZB CdSe sample (**I**) at 4K. The emission spectrum (full luminescence) is obtained by exciting the sample at 400 nm so that emission occurs from the entire sample distribution. No structure is observed within the band-edge absorption and emission features. Figure 5.7B shows FLN and PLE spectra detected from this sample at 4 K, and reveals band-edge structure [178] with higher resolution.

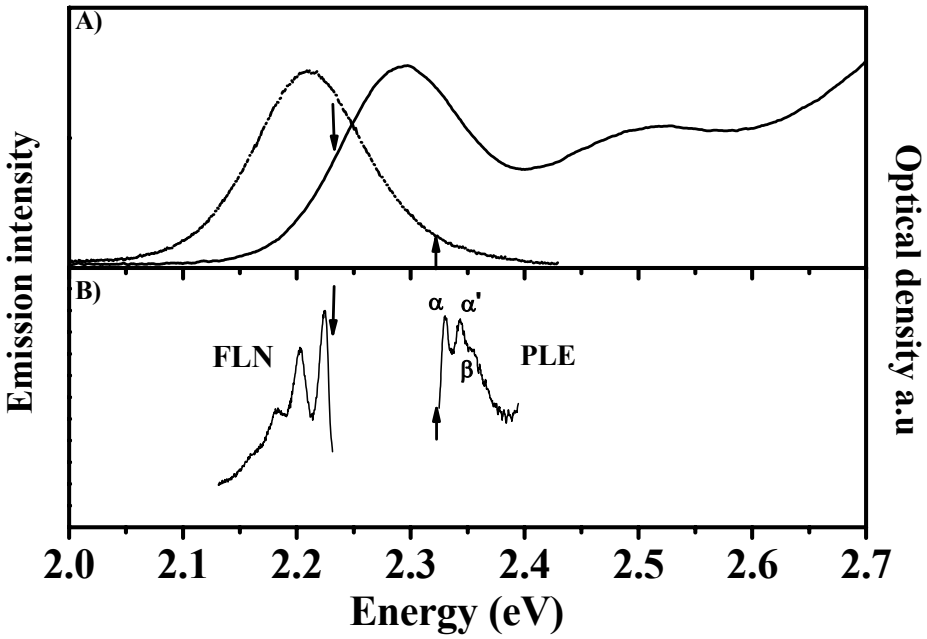

Figure 5.7: (A) Absorption (solid line) and full luminescence (dotted line) spectra for CdSe ZB QD (**I**) at 4 K. (B) FLN and PLE spectra of the same sample. Three features observed in FLN. Both narrow (α, α´), and broad (β) absorption features are resolved in the PLE. The arrows denote the excitation and emission positions used for the PLE and FLN respectively.

For the FLN spectrum, a subset of the sample distribution is optically excited. When the sample is excited on the low-energy side of its first absorption feature (downward arrow in figure 5.7), a longitudinal optical (LO) phonon progression is clearly resolved (comparable to ref. [63] and [62]). In PLE, a narrow feature (**α**), its LO-phonon replica (**α´**) and a broader feature (**β**) are observed.
The highest resolution in PLE is thus obtained when the emission is monitored on the blue edge of the full luminescence [178], probing the smallest dots in the distribution (see figure 5.8)

.

In contrast to PLE, the FLN spectra broaden as the excitation position is moved to higher energy (figure 5.8). The highest resolution in FLN is obtained by exciting the sample on the red edge of the first absorption feature, probing the largest dots in the distribution.

Figure 5.8 shows seven FLN and PLE scans for sample (**I**). For each pair of FLN-PLE results, the FLN excitation energy and PLE emission energy are identical. These energies are represented by arrows and shown with the full luminescence. As the PLE emission position is moved to lower energy (from 1 to 7), the broad underling feature (β) broadens, while only two features are resolved in the FLN at this energy side.

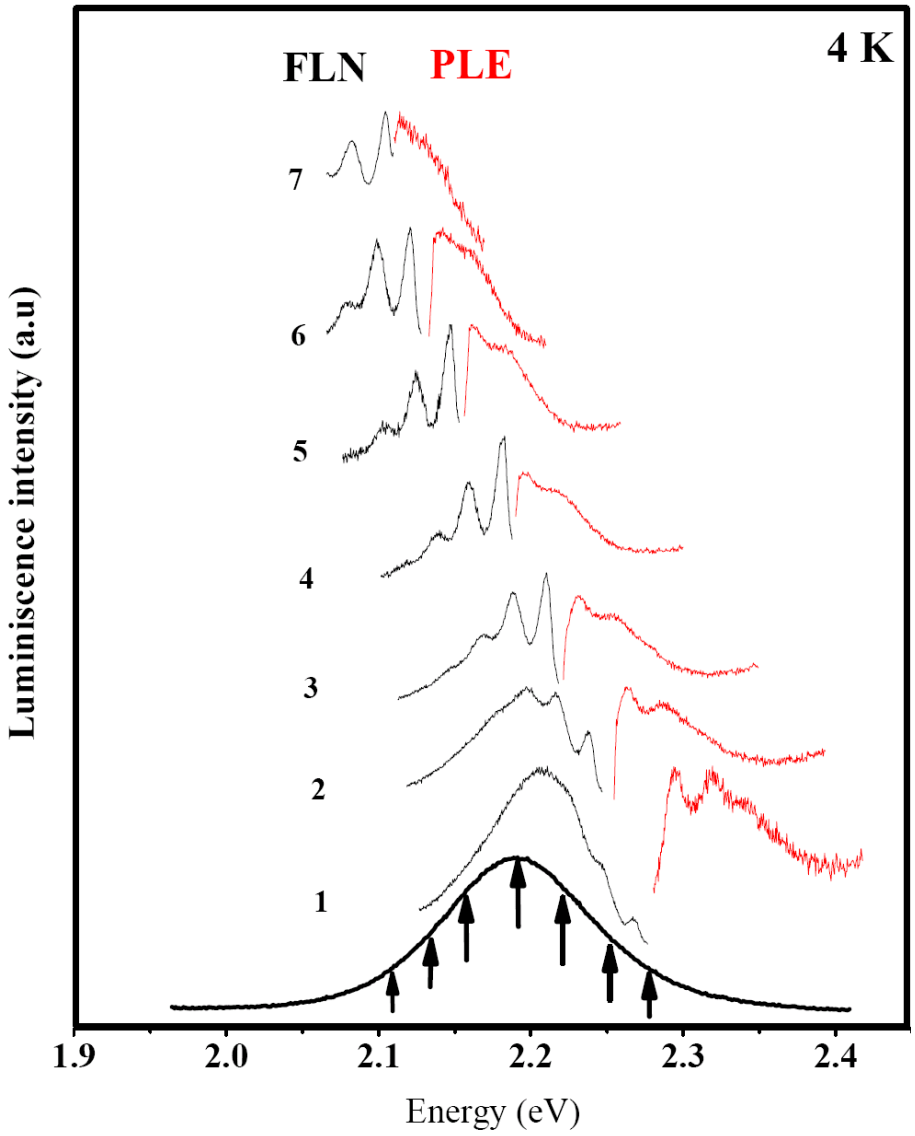

Figure 5.8: Normalized FLN and PLE data for sample (I) (Alkyl PA-prepared) dots for various excitation and emission position. For each FLN-PLE pair, the FLN excitation and PLE emission energy are the same. These energies are designated by arrows on the full luminescence line-shape (bottom).

To resolve in details the differences between the two structures, we compared the PLE and FLN of a CdSe QDs with ZB structure (567 nm band gap absorption and 578 nm fluorescence at RT) with a W QDs of identical band gap energy, under identical conditions (typical resolution of 7 meV FWHM). Figure 5.9A presents the low-resolution absorption and fluorescence spectra of the two CdSe dots, while in figure 5.9B, the W and ZB lattice structure were checked by the XRD.

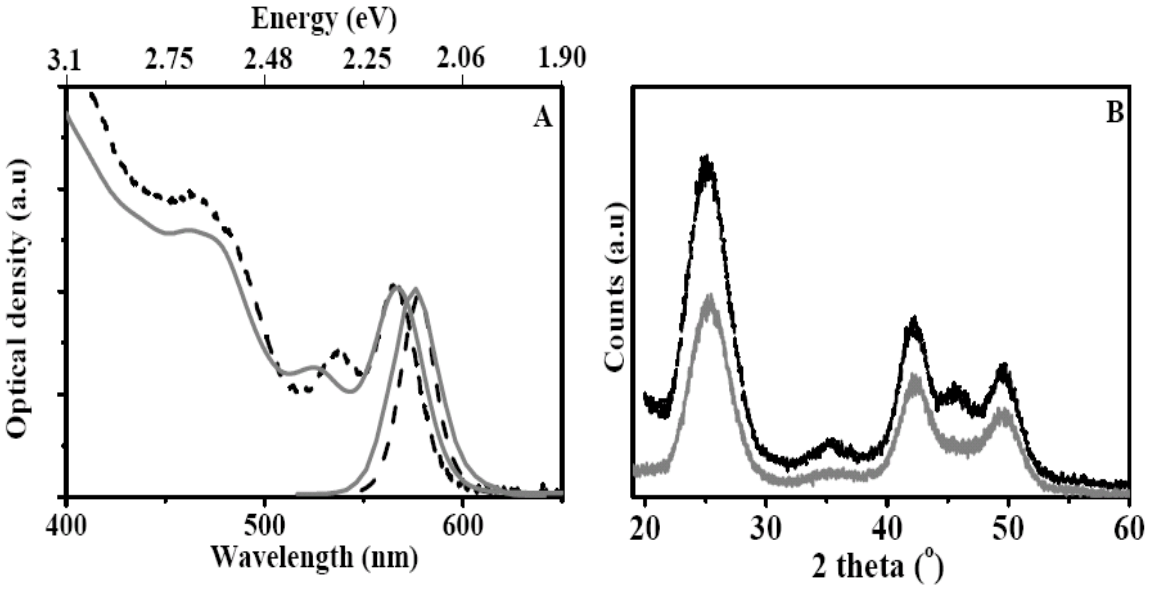

Figure 5.9: A) absorption and emission spectra of CdSe dots (567 nm absorption and 578 emission) with ZB structure (dashed lines) at RT compared with dots of the same band-gap, with W structure (solid lines). **B)** The XRD of the two samples, ZB (Black), and W (Gray).

The absorption and fluorescence spectra (as usual) were blue-shifted (~ 20 nm) at 4 K as shown in the bottom of figure 5.10 (luminescence bands) for the two samples. Figure 5.10A and B present the complete data set for PLE and FLN of the ZB and WZ samples. The laser excitation is indicated by the arrows on the steady state fluorescence band in the bottom of the two figures.

.

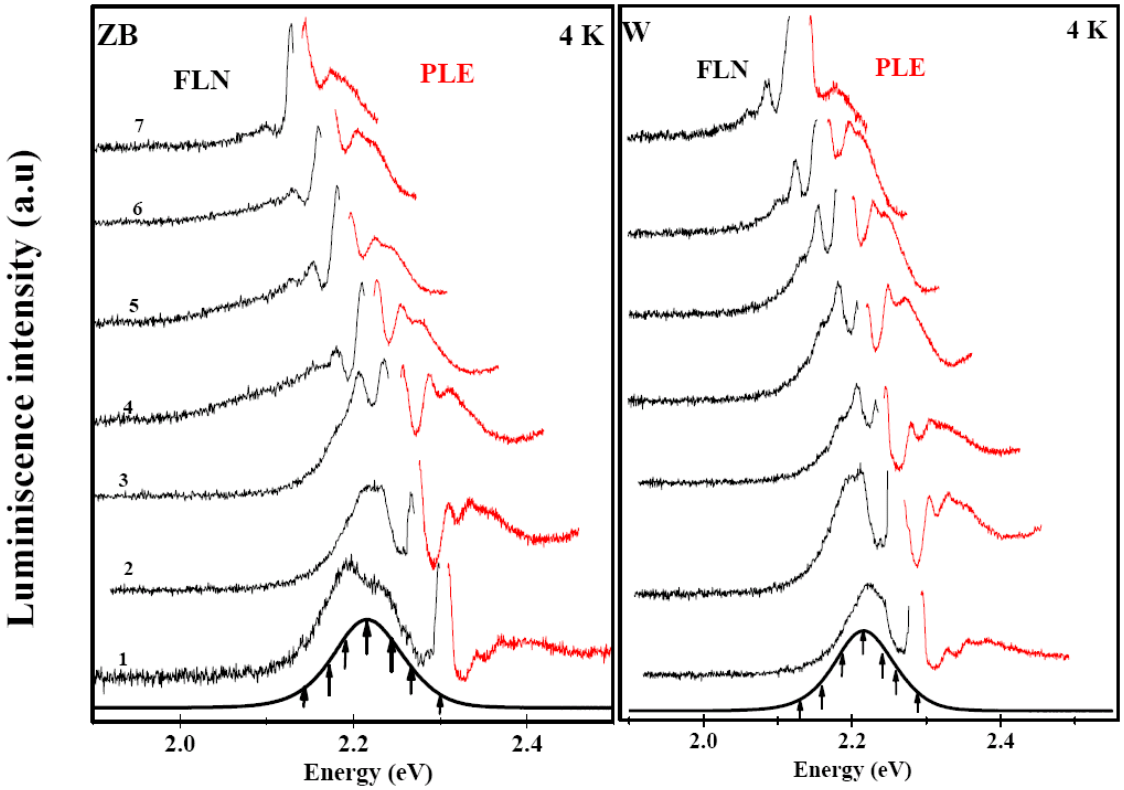

Figure 5.10: Normalized PLE and FLN of the two samples with the different structures for various excitation and emission positions. For each FLN-PLE pair, the FLN excitation and the PLE emission position energies are the same in both figures. These energies are designated by arrows and shown with the full luminescence.

Figure 5.10 demonstrates that the two crystal structures present rather similar band-edge structure. This is confirmed by figure 5.11, where one pair of PLE-FLN spectra (n^{o}-3 in figure 5.10) for W dots is overlapped with a pair for ZB dots.

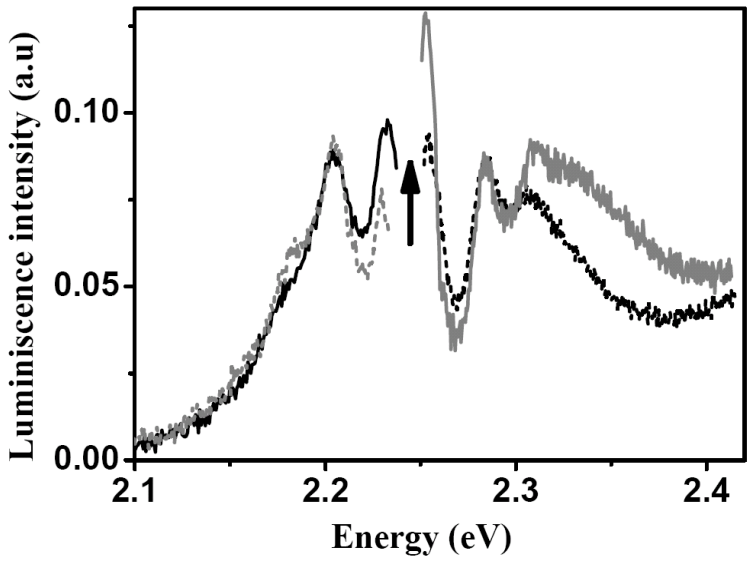

Figure 5.11: PLE and FLN (curves 3 in figure 5.10) of the ZB-dots (black traces) and W dots (grey traces).

To determine the energy position and width of each feature, we fit all the spectra that presented in figure 5.10. The PLE and FLN spectra were best fitted with several Gaussians (the number of Gaussians depends on the excitation and detection energy). The details of the fit are shown in figure 5.12A, and B.

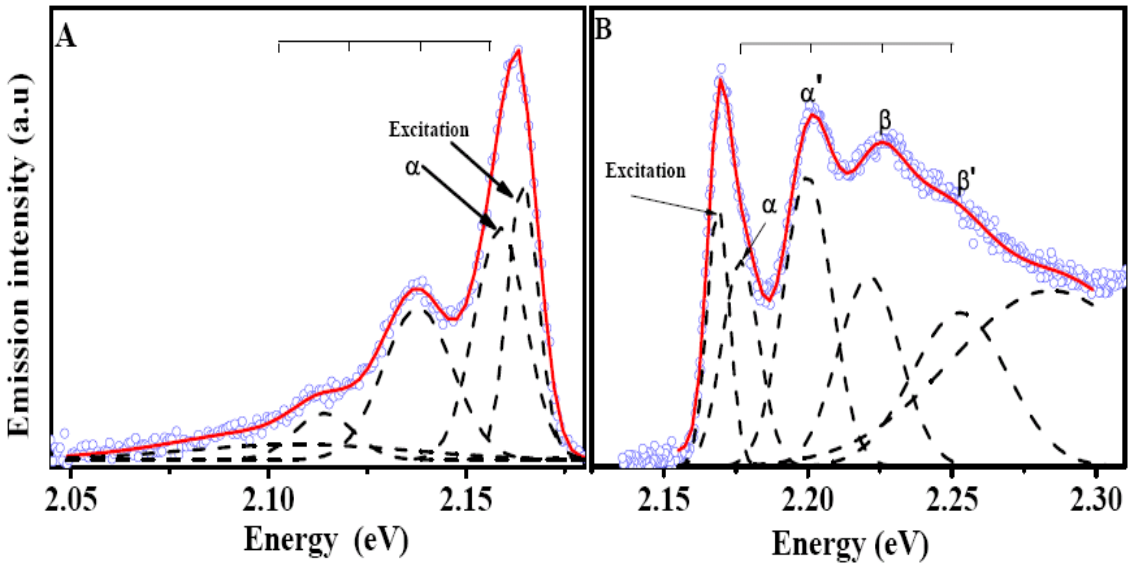

Figure 5.12: FLN (A) and PLE (B) of ZB sample at 2.168 eV for laser excitation and emission positions. Multi gaussian fit for the two spectra.

In the case of the PLE spectrum (figure 5.12 B), the first Gaussian corresponds to the laser excitation (7 meV), measured directly from the scattered light, with a maximum at 2.168 eV. The second Gaussian (α) is related to the zero-phonon line and directly gives the Stokes shift value (~ 11 meV), the width of this Gaussian is twice the width of the excitation peak. The third Gaussian (α′) is the first LO-phonon replica of the state (α), lying about 22 meV from (α), but it has a width of ~20 % larger than the band (α). Note that the phonon energy in bulk CdSe is 25 meV. The next band (β) is fitted by a Gaussian that has 20 % larger width than the Gaussian used to fit (α′), the energy distance between this band and (α′) band is comparable to the LO-phonon energy distance (20 meV). The width of the band (β) and its position suggest that this feature is probably due to more than one state. Another Gaussian was required to fit another band (β′), with ~ 22 meV energy distance from (β) and two times larger in width.

In the case of the FLN spectrum (figure 5.12A), besides the laser band which again was fixed, the second Gaussian (~ twice larger than the exitation) is related to the Stokes shifted zero-phonon line. The other Gaussians fit very well the LO-phonon progression. The same fit, also describes very well the PLE and the FLN spectra of the CdSe QDS with W structure presented in figure 5.10.

The band energy positions from the fits of the spectra in figure 5.10 are given in table 5.I for the PLE of the ZB and W QDs respectively, while in table 5.II we represent the difference between the energy positions of the bands presented in table 5.I.

.

Table 5.I: Parameters of multi-Gaussian fit of the PLE spectra of the ZB and the W sample shown in figure 4.10. The fit errors are 5 % as a maximum fit.

ZB					**W**				
λ_{exc}	α	α´	β	β´	λ_{exc}	α	α´	β	β´
2.135	2.144	2.167	2.186	2.215	**2.135**	2.146	2.168	2.189	2.212
2.175	2.183	2.21	2.227	2.249	**2.17**	2.181	2.207	2.229	2.433
2.19	2.196	2.22	2.24	2.265	**2.19**	2.2	2.222	2.24	2.48
2.213	2.21	2.28	2.26	2.289	**2.213**	2.224	2.247	2.268	2.289
2.224	2.231	2.255	2.276	2.298	**2.224**	2.236	2.26	2.279	2.299
2.27	2.277	2.303	2.322	2.348	**2.27**	2.27	2.3	2.325	2.35
2.3	2.307	2.327	2.355	2.382	**2.3**	2.310	2.336	2.349	2.374

Table 5.II: Energy differences between the ZB and WZ PLE resolved bands presented in table 5.I.

ZB					**W**				
$\alpha-\lambda_{exc}$	$\beta-\lambda_{exc}$	α'-α	β-α	β' -β	$\alpha-\lambda_{exc}$	$\beta-\lambda_{exc}$	α'-α	β-α	β´-β
13	51	19	38	29	11	54	22	43	23
11	52	22	39	22	11	59	26	48	24
11	50	19	39	25	10	50	22	40	24
11	52	20	36	29	11	55	23	44	21
11	47	20	41	22	12	55	24	43	20
11	52	22	41	26	11	55	21	46	25
10	55	17	45	27	10	49	26	39	25

The fit values in the above two tables are very similar for two different structures. The Stokes shift ($\alpha-\lambda_{exc}$) for all excitation energies has comparable values, the (β) band that according to references. [63], [62],[177, 179], and [180], is due to another absorption band, also has comparable values for the all excitation energy values. The other energy splitting between the bands have the same range of values (~ 20-30 meV) and might be due to the LO progression of the zero-phonon line (α).

From this comparison and due to the unchanged results for the case of the CdSe with ZB structure, we can explain the resolved features in ZB sample in the same possible distribution. Our results show no detectable difference in the fine structure of the band gap exciton as a function of the lattice structure.

From the above analysis of the CdSe dots prepared in the presence of alkyl PA [86], we resume the results by the following points:

(a) High quality size-controlled CdSe dots with ZB lattice structure were prepared.
(b) The TEM and X-Ray show a symmetric spherical shape and a clear ZB structure (figure 5.5 and 5.6) respectively.
(c) Low-resolution steady state absorption spectra show a blue shift of the second band of the CdSe QDs with ZB comparing to CdSe QDs with W structures (figure 5.3B).
(d) This shift is in agreement with the theoretical calculation for the CdSe with ZB structure (figure 5.3B).
(e) The Stokes shift measured for the two lattice structures is comparable (figure 5.4).
(f) PLE and FLN spectra reveal a similar fine structure of the lowest exciton state of the CdSe QDs with the two structures (figure 5.11).

5.2.3 Nanosecond recombination kinetics.

As shown in the previous paragraphs, the CdSe QDs, which were prepared in the presence of alkyl PA, have the same Stokes shift, and same band-edge structure as W-CdSe QDs. On the other hand, the theoretical models of Efros *et al* [42, 61], and Schöps *et al* [157] predict different distribution levels of the lower exciton band edge for the two lattice structures (see 1.3a). To clarify the origin of this surprising result, the relaxation kinetics of a ensembles of cubic CdSe quantum dots in toluene solution at room temperature have been studied systematically as a function of size, excitation power, and energy. The experimental techniques in this work are the same used in the case of CdSe W structure (chapter 3) in solution. The temperature effect on the relaxation decay of CdSe QDs in film form was also investigated.
Five different CdSe nanocrystals with a band gap absorption ranging from 514 to 571 nm, and with a QY of about 25 % measured in toluene solution, and with clearly ZB X-ray diffraction, were studied in this work. The lowest possible laser pump power of ($0.05\,\mu J/cm^2$) used to excite the samples. Again, at this power regime, less than one exciton per particle can be formed [108] (§ 3.2.2). Figure 5.13 (**A** and **B**) shows the absorption and luminescence and XRD spectra of the CdSe samples used in this work. Typical cubic structure with two peaks at $2\theta = 42°$ and $50°$ were found in all samples.

.

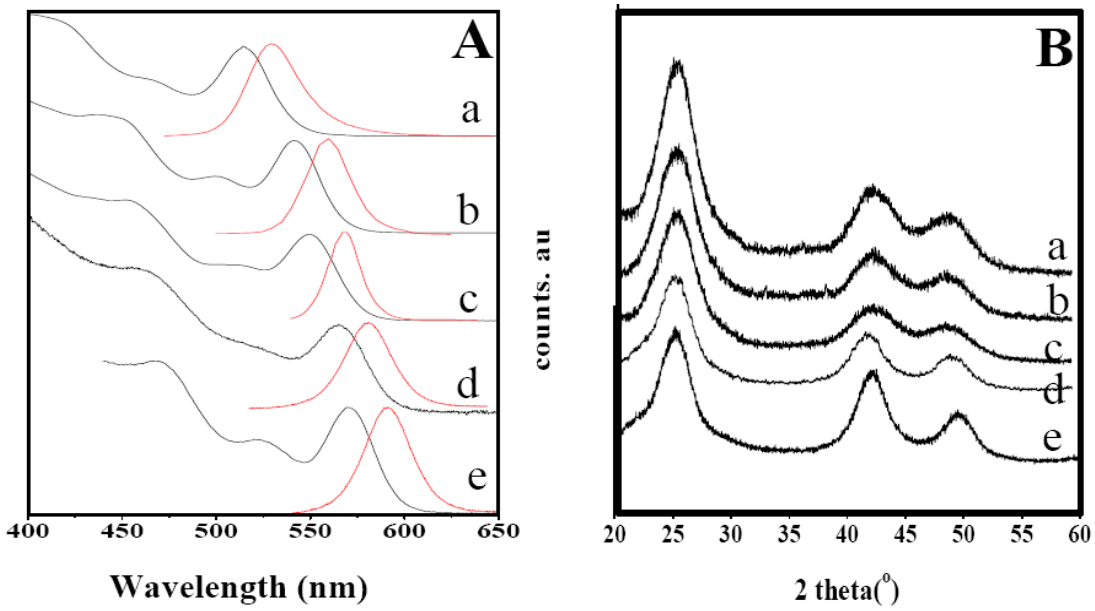

Figure 5. 13: A) The absorption and fluorescence spectra of the CdSe dots used to test the effect of size (from up to down. 514, 541, 550, 565, and 571nm). B). The XRD of the previous samples with clear ZB structure.

Figure 5.14 shows an example of the CdSe decay of sample C (550 nm band gap absorption) in figure 5.13. In general, similar to the case of W CdSe QDs, the kinetic of the ZB CdSe is best fitted by four-exponentials decays. The residuals in this figure highlight the quality of the fit. Typical lifetimes are τ_1 =1.2 ns, τ_2 =6 ns, τ_3 = 26 ns, and τ_4= 77 ns, which all lie in the range of W dots (Table 3.IV).

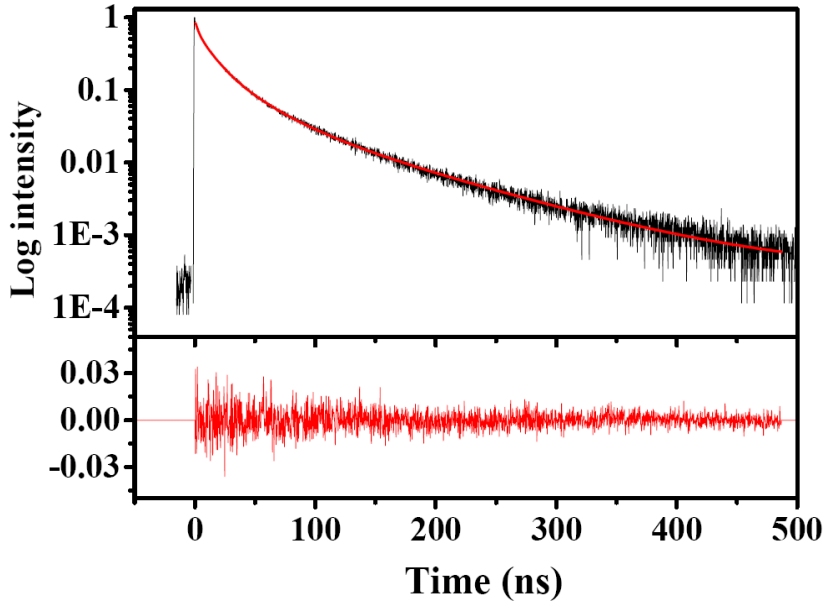

Figure 5.14: Lifetime decay curve of CdSe QDs (550 nm band gap absorption) in toluene solution, at 400 nm laser excitation. A four-exponentials function used to fit the decay kinetics. The residual is shown in the bottom of the figure.

5.2.3.I Size dependence.

Figure 5.15 shows the kinetics of different CdSe QDs sizes with ZB structures presented above in figure 5.13A after 400 nm laser excitation. The parameters of the fit are shown in table 5. III. The smallest sample in the group (sample (a) with 514 nm absorption) has a faster lifetimes τ_1 and τ_2, while slower values for the life time τ_3 and for the long component τ_4 are found.

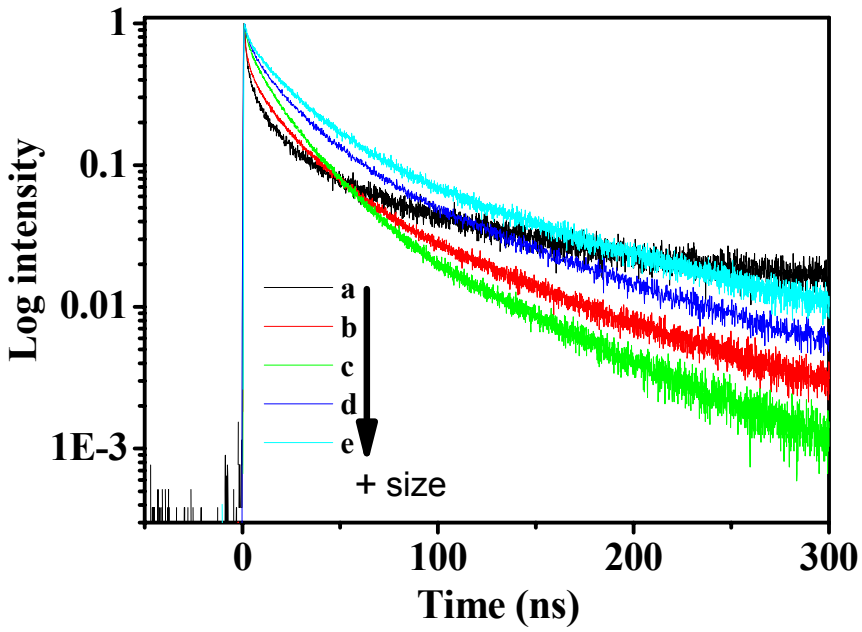

Figure 5.15: Luminescence decay curves of different sizes CdSe QDs with ZB lattice structure in solution at room temperatures.

TABLE 5.III. Fit parameters of the decay kinetics of different ZB dots pumped at low power (0.049 μ J/cm^2). The error in all values is less than 10 %.

Band-gap absorption	**A_1**	**τ_1 (ns)**	**A_2**	**τ_2 (ns)**	**A_3**	**τ_3 (ns)**	**A_4**	**τ_4 (ns)**
a (514 nm)	0.40	1.1	0.30	4	0.21	33	0.09	110
b (541 nm)	0.32	1.2	0.24	5	0.34	28	0.10	77
c (550 nm)	0.29	1.25	0.24	6	0.36	27	0.11	76
d (565 nm)	0.31	1.5	0.23	7	0.4	21	0.06	69
e (571 nm)	0.23	1.4	0.25	6	0.32	20	0.04	67

From the above table, we see that the prefactors $\mathbf{A_1}$, $\mathbf{A_2}$ increase as the size decreases, while the opposite behavior appears for $\mathbf{A_3}$. $\mathbf{A_4}$ does not show any systematic trends as a function of the QDs size.

In conclusion: In a CdSe with ZB lattice structure, the size effect reveals a similar behaviour to that presented for CdSe QDs with W structure (§ 3.2.1).

.

5.2.3.II Power dependence.

We excited sample (**c**) (band gap absorption at 550 nm), with intensities in the range of 350 nWatt up to 15 mWatt corresponds to the formation of 1 to 13 e-h produced per dot (calculated as in § 3.2.2). Again as we showed in the case of W CdSe NDs, increasing the excitation power to 0.28 mJ/cm^2 leads to formation of more e-h pairs per particle. The kinetics still be described by a four-exponential decay. Table 5.IV present the fit results of CdSe QDs with ZB structure in solution at different excitation powers. τ_1 and τ_2 show smaller values, and the amplitudes $\mathbf{A_1}$, $\mathbf{A_2}$ increase with increasing excitation power. The other lifetime components (τ_3 and τ_4) stay unchanged. $\mathbf{A_3}$ decreases as the power increases.

Table 5.IV: Fit parameters of CdSe QDs (C, band gap absorption at 550 nm) after different laser excitation power.

Excitation power	A_1	τ_1 (ns)	A_2	τ_2 (ns)	A_3	τ_3 (ns)	A_4	τ_4 (ns)
0.06 µJ/cm^2	0.29	1.25	0.24	6	0.36	27	0.11	76
0.4 mJ/cm^2	0.30	1.47	0.24	6	0.33	25	0.13	73
0.85 mJ/cm^2	0.34	1.3	0.26	4.7	0.3	24	0.1	69
1.7 mJ/cm^2	0.35	1	0.33	3.4	0.23	24	0.09	68.5
2.2 mJ/cm^2	0.38	0.9	0.34	3.1	0.20	25	0.08	68

The power effect presented in the above table for the CdSe dots with ZB lattice structure, and that presented previously for W QDs (table 3.V), show identical behaviour as a function of the number of exciton created per dots.

5.2.3.III Wavelength dependence.

Similar to the study about the decay kinetics of CdSe dots with W structure at different wavelengths (§ 3.2.3), we detected the relaxation kinetics of sample c with ZB structure (figure 5.13) at different detection wavelengths, in low (less than one exciton per particle) and high (more than 8 excitons) laser excitation power ranges.
At low excitation density (0.1 mJ/cm^2), there are no differences in the relaxation kinetics of ZB CdSe QDs at the red and the blue sides of the fluorescence emission band. Figure 5.16 shows the kinetics of sample (c) at different detection wavelengths and high excitation power. Increase of the excitation to more than 0.5 mJ/cm^2 results in an increase of the weight of the first component $\mathbf{A_1}$ at the low energy side of the steady state emission due to the bi-exciton[109] located at the low energy side as was also observed for W-QDs (§ 3.2.3), the lifetime becomes faster. The other components do not show any pronounced tendency.

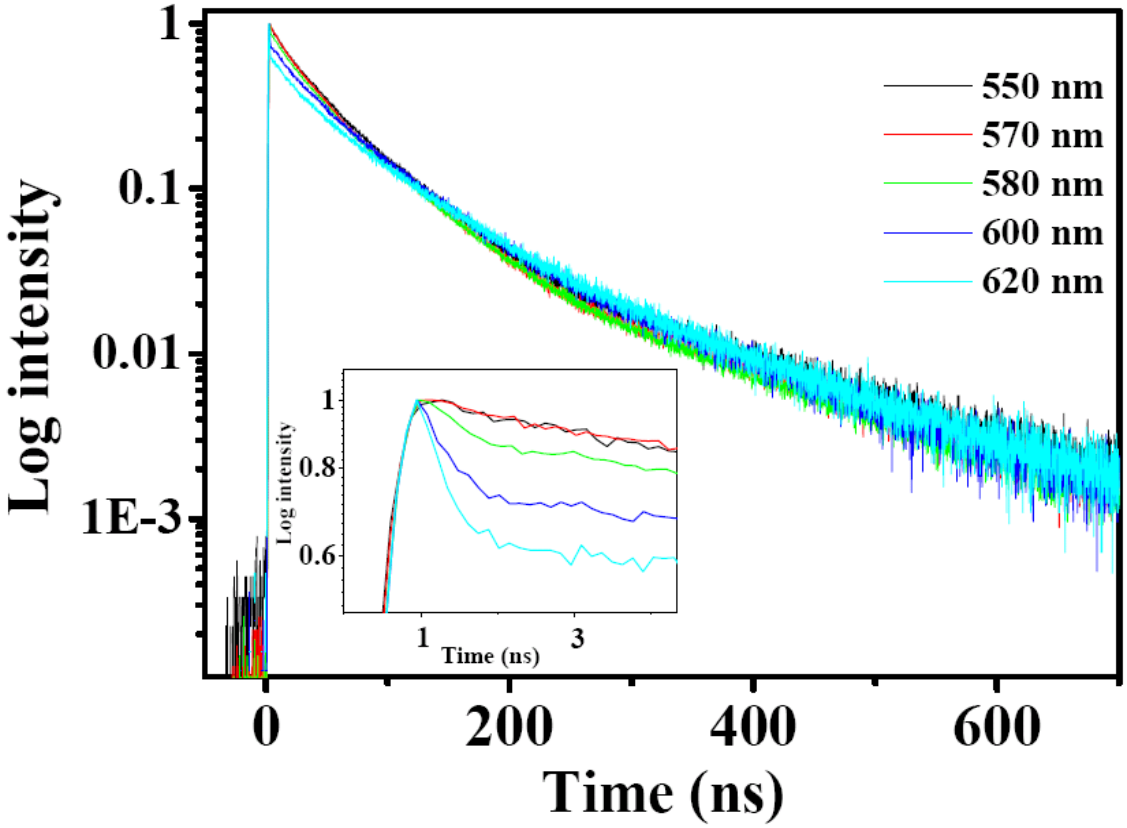

Figure 5.16: luminescence decay curves at high power excitation (0.5 mJ/cm²) of sample (c) at different emission wavelengths. The fast component (τ_1) appears clearly at the red side, as seen in the inset.

5.2.3.V Temperature effects.

In this part, we present temperature-dependent spectral and kinetic studies of the electron-hole recombination over a broad temperature range (from 4 to 300 K) in a series of ZB CdSe QDs. The aim is to compare the temperature dependence of the CdSe QDs with ZB structure, and CdSe QDs with W structure (studied in details in the previous chapter).

The PLE and FLN studies (§ 5.2.2) and room-temperature nanosecond kinetics (§ 5.2.3I, II, III) and the Stokes shift values (§ 5.2.1) did not point to clear differences between the two structures. The final parameter, which can be used as a probe for differences between the two crystals, is the temperature.

Again, the optical properties and the band-edge kinetics were studied. Two samples with different sizes ((b) with 541 nm and (e) with 571 nm room temperature band gap absorption) were tested in this work. The XRD of the two samples is clearly ZB structure (samples (b) and (e) from figure 5.13). The samples were excited at 400 nm with a 0.06 μJ/cm² excitation power (lowest possible power). The emission was detected at the maximum of the fluorescence band for each temperature. In this work, we used the sample in the form of polymer film.

.

5.2.3.IV.1 Temperature effects on the spectroscopy of ZB CdSe QDs.

Similar to what we investigated in the case of W CdSe QDs, the shift of the maximum of the fluorescence peak, the fluorescence bandwidth, and the relative fluorescence intensity were measured as a function of the sample temperature. The two CdSe ZB samples showed similar behaviour in the magnitude of the shift after cooling to 4 K. Figure 5.17 summarizes the evolution of the fluorescence properties as a function of temperature.

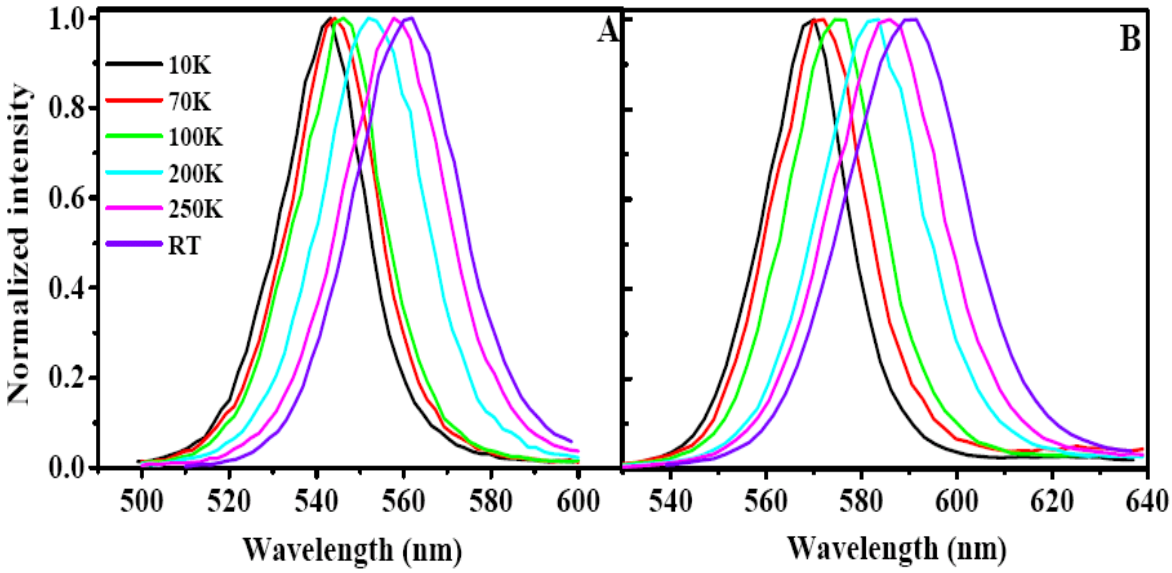

Figure 5.17: Steady–state fluorescence spectra of ZB CdSe in polymer film at different temperatures**. A)**. sample (b) and **B**) Sample (e) in figure 5..13.

We note a 18 nm (74 meV) and 21.4 nm (81 meV) red shift of the maximum for sample (b) and (e) respectively, upon heating the sample to 300 K, while the fluorescence bandwidth increases from about ~ 20 nm at 4K to ~20 nm at room temperature. The relative fluorescence intensity increase does not appear in this figure due to normalization, but is plotted in figure 4.18A and B. Figure 5.18 summarises the temperature effects on the steady state spectra for samples (b) and (e) in polymer film at different temperatures. Again, the emission intensity was derived from the integrated area below the steady state emission band, with the same possible identical conditions for fluorescence intensity measurements (§ 4.3.1).

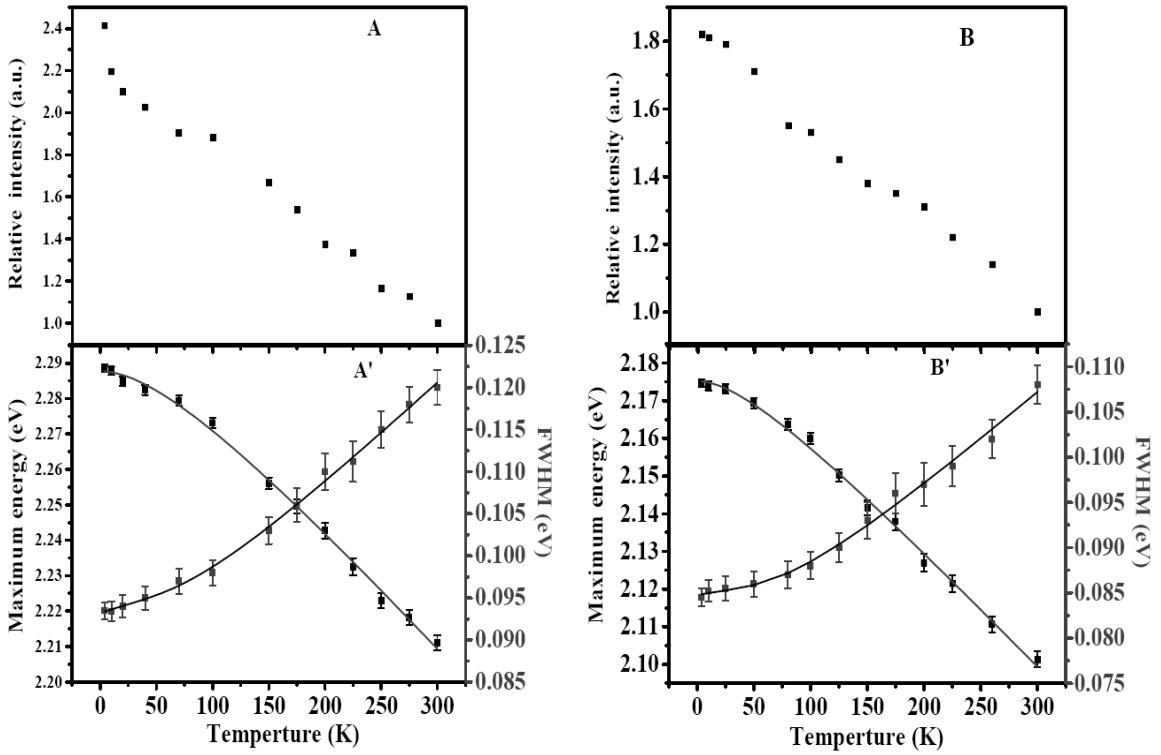

Figure 5.18: Temperature dependence of fluorescence of the ZB CdSe samples.**A**, **A´**for sample b and **B**, **B´** for sample e in polymer film. **A**, **B** Relative intensity normalized to 1 at RT. **A´**, **B´** maximum energy (square) and full width at half maximum (dots). The points in A´ and B´ are fitted using equations (4.1), and (4.2) (see text).

In the large dots (sample e) (figure 5.18B), the relative fluorescence intensity after cooling of the sample to 4 K is ~ 2 times larger than at room temperature. This relative value is larger in the small CdSe dot (sample b) (figure 5.18A). The comparison between the fluorescence intensity at RT and 4 K for the ZB samples and the same measurements for CdSe QDs with W structure (figure 4.6C), shows another comparable behaviour between the two structures in polymer film.

As was explained before (chapter 4), the variation in the energy gap with temperature (5.18A´, B´) is a result of a temperature-dependent electron lattice interaction [128], and is identical to the energy gap of CdSe bulk [130]. Following the same relation (eq. 4.1) used in chapter 4, we fitted the variation in the energy gap in CdSe dots with ZB structure, and the result is shown in figure 5.18. Again, the dependence is linear for high temperature $\Delta E_g \propto T (T >> \theta)$ ($\theta \sim \beta$) is the Debye temperature) and $E_g(0)$ is the energy gap, and non-linear for lower temperature $\Delta E_g \propto T^2 (T < \theta)$.

In table 5.V, we present the fit constants of the two samples (b and e) presented in figure 5.18, and the fit values for W CdSe QDs (~ 575 nm band gap absorption, presented in figure 4.6).

.

Table 5.V: Fit results of the band-gap temperature dependence in ZB CdSe QDs, and similar size (similar to sample e) W QDs. The sample refers to an absorption spectra presented in figure 5.13 for ZB dots and figure 4.2 for W dots.

Sample	$E_g(0)$ (eV)	α ($x10^{-4}$meV/K)	β (K)
b (ZB)	2.28±0.01	3.61±0.06	100±54
e (ZB)	2.17±0.02	3.22±0.05	78±35
W QDs ~ size of (e)	2.32±0.02	3.51±0.06	95±40
Bulk ZB	1.75	3.6	150

The Fit parameters of the above tables show $E_g(0)$ larger values for W CdSe QDs than the same absorption band gap CdSe with ZB structure. α (for the two structures) appears in agreement to the bulk value. β has comparable values for the two CdSe structures.

The width of the emission band (sample b) decreases gradually from 120 meV at room temperature to 95 meV at 4 K. While in sample (e), this width has a value of 107 meV at RT and decreases to 85 at 4 K. We fitted the temperature dependence of the FWHM with eq 4.2. The fit results are shown in figure 5.18 and the fit parameters are given in table 5.VI.

Table 5.VI: Fit results of the FWHM dependence as a function of temperature in ZB CdSe QDs, and similar size (sample e) W QDs in polymer film.

CdSe	Γ_{inh} (meV)	σ (μeV/K)	Γ_{LO}(meV)	E_{LO}(meV)
(b) ZB	80±0.4	28±3	26±5	24.5
(e) ZB	79±0.7	20±4	30±4	25
W QDs ~ size of (e)	43±3	20±3	20±4	24.3
Bulk	-	8	100	26.1

The fit values indicate larger values (~ 3 times) of exciton-acoustic phonon coupling σ, compared to the bulk value (8 μeV/K), and similar to the case of W structure (~20 μeV/K) as shown in table 4.II. The LO-phonon coupling strength Γ_{LO} has smaller values than the bulk (~100 meV), but slightly bigger than the LO-phonon coupling in CdSe QDs with W structure (see table 4.II). E_{LO} shows comparable values for bulk and the other CdSe structures.
From the above results, the effect of temperature on the spectroscopy of ZB CdSe QDs shows an identical dependence to that detected for W CdSe QDs in chapter 4.

5.2.3.IV.2 Temperature dependence of the fluorescence decay time.

The temperature dependent relaxation kinetics of the previous two samples (b) and (e) are detected. The excitation and the detection conditions were the same as described previously in chapter 4. Figure 5.19A and B shows the decays of the two samples between 4 and 300 K.

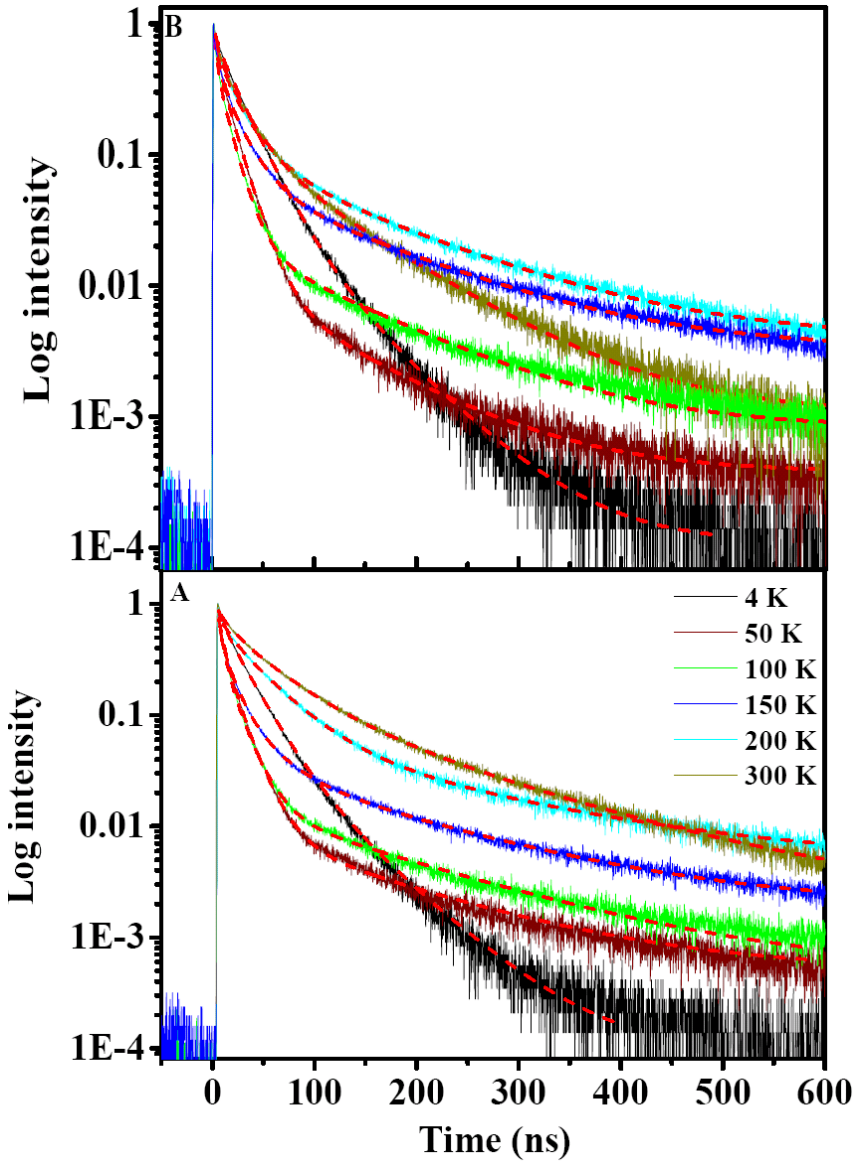

Figure 5.19: Decay curves of ZB CdSe QDs measured at different temperatures for sample b (**A**) and sample e (**B**) in figure 5.13. All decays were best fitted with four-exponential decay function as it shows by the dash red lines.

Similarly to the temperature dependence dynamics of W CdSe QDs (chapter 4, § 4.3.2), the relaxation decays of ZB CdSe QDs at different temperatures are best fit by four-exponentials. The fit parameters (error < 10 %) are plotted in figure 5.20 as a function of temperature.

.

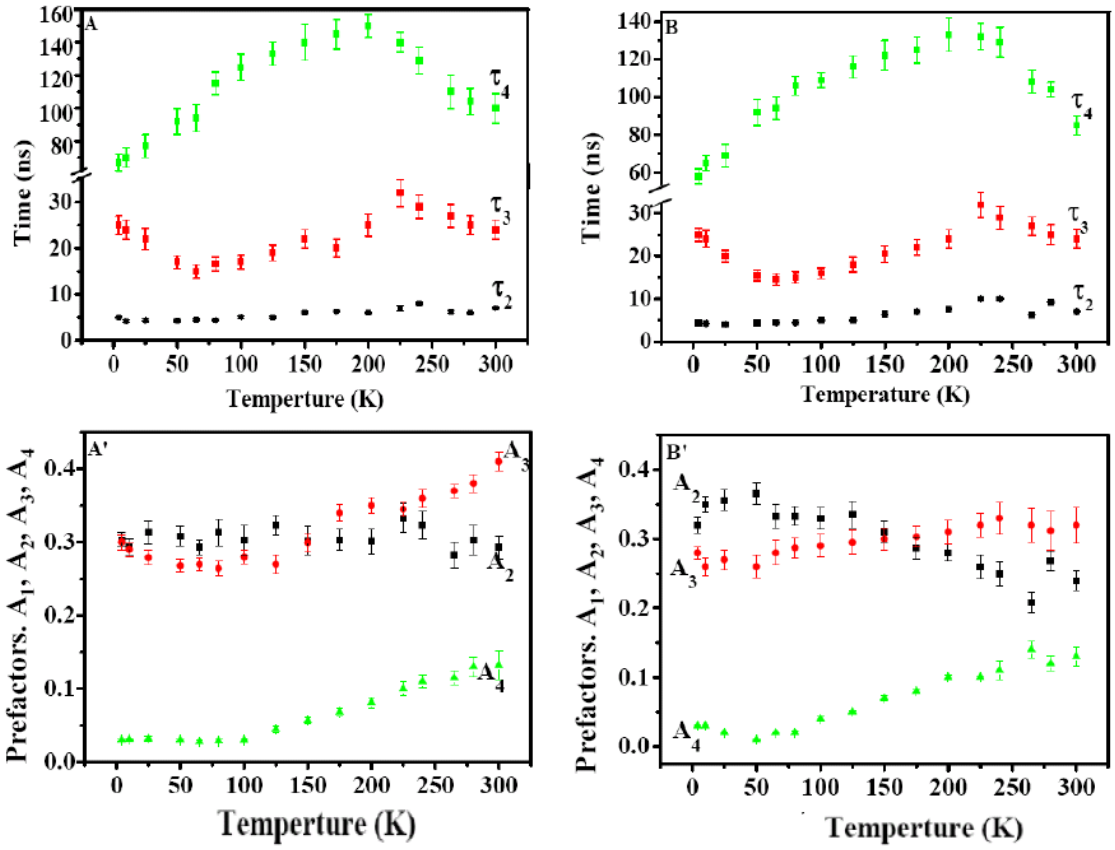

Figure 5.20: A, A´) Lifetime constants of sample (b, 541 nm band gap absorption) and their prefactors at different temperatures**. B), B´)** the same fit parameters for sample (e, 571 nm band gap absorption).

the fastest decay with a lifetime τ_1 of about 1.5 ± 0.3 ns remains unchanged for the whole range of temperatures and samples. Its amplitude increases from (~ 25 and 40) % at 300 K to (~ 35 and 45) % at 4 K as the temperature decreases, τ_1 is not shown in figure 4.14.

The τ_2, τ_3, τ_4 values present comparable behaviour for the two samples, and are very similar to results of CdSe with W structure (see figure 4.9). The components τ_2, τ_3, τ_4 increase between room temperature and about 225 K and then fall gradually until the lowest measured temperature. Only τ_3 increases below 50 K, but its lifetime values stay in the same range as at room temperature.
The prefactors show more variations than the decays lifetimes. They show comparable dependence between the two ZB samples, and those presented before in the case of CdSe QDs with W structure (figure 4.9).
Finally, time-gated fluorescence spectra were measured at 4 K and are shown in figure 5.21.

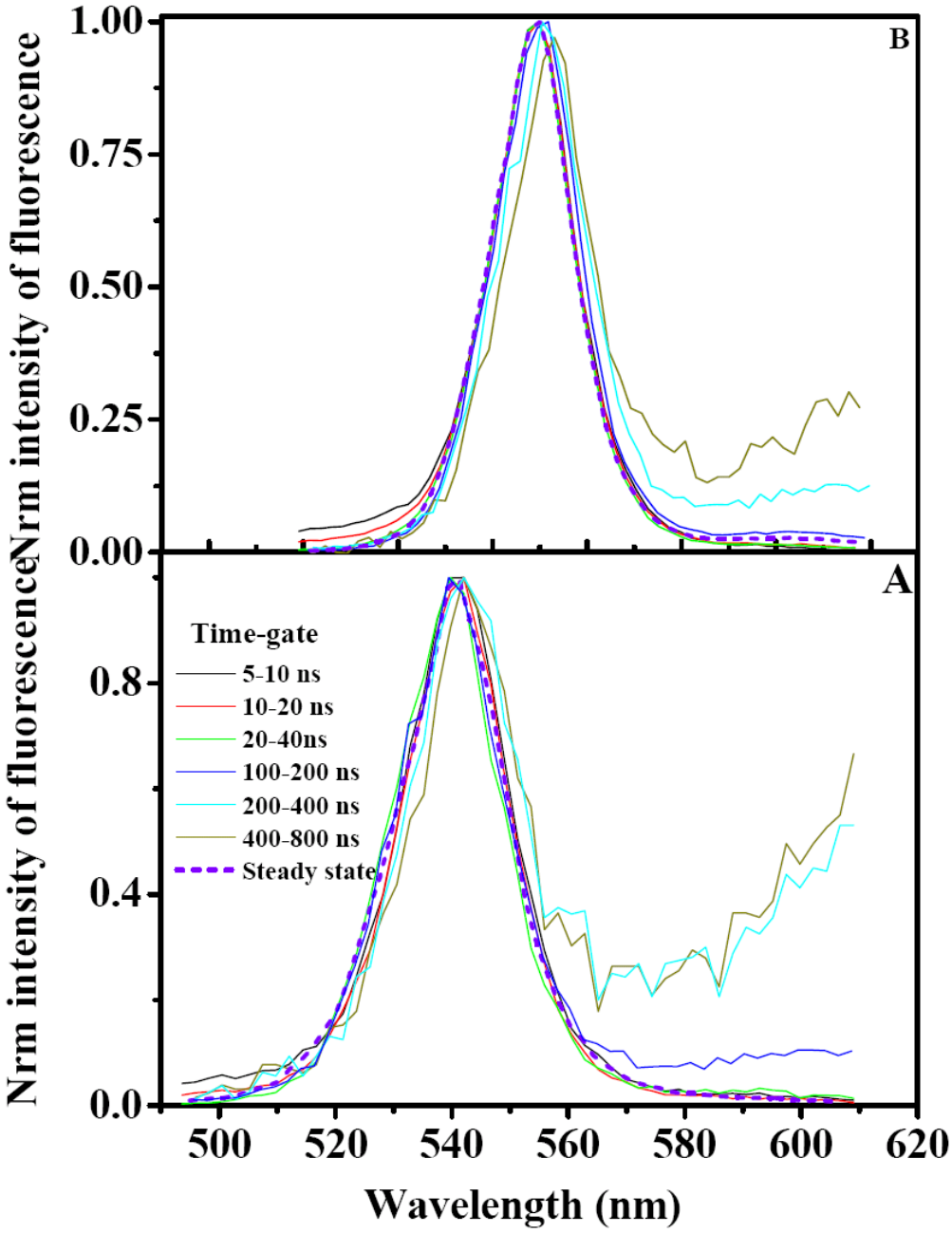

Figure 5.21: Fluorescence bands at 4 K at different time gates. **A)** Sample (b). **B)** Sample (e). The colors and gate times are the same as shown (**A**) for all samples.

Generally, the behaviour is similar to the case of CdSe QDs with W structure (figure 4.11).

Up to 60-80 ns, the transient spectrum of the sample does not change. Beyond this time, a red shift occurs (4 nm) and a new band appears, which is more pronounced in the smaller sample (figure 5.21A). At room temperature, the time-gated fluorescence study shows identical spectra (fluorescence features) over all the range of time.

Finally, and from the above (the nanosecond dynamics and the temperature dependence of the CdSe with ZB structure), we can highlight the following conclusions:

.

(a) The nanosecond kinetics of CdSe QDs with ZB and W structures at room temperature (fit function, lifetime constants, and prefactors) is identical.
(b) The dependence as a function of size, power, and the detection wavelengths are also identical for W and ZB dots.
(c) The dependence of the fluorescence energy, the FWHM, and the relative fluorescence intensity for ZB and W dots as a function of temperature in polymer film show comparable behaviour. This behaviour is similar to that of bulk CdSe with W and ZB lattice structure.
(d) The decay kinetics of ZB CdSe samples as a function of their temperature in film form shows a comparable dependence for the CdSe QDs with W structure in the same environment (chapter 4).
(e) Time-gated fluorescence study in ZB CdSe QDs shows the same tendency that measured for CdSe dots with W structure, with about 5 nm blue shift after 60-80 ns and a clear wings at the red side of the fluorescence band.

5.3 Discussion and conclusion.

To summarise, the results we presented in this chapter contain several important points: (i) Evidence of the structure of the CdSe NCs that are prepared with our new synthesis (see § 2.5.2) and their properties.
(ii) Characterize of the spectroscopy and the kinetics of the ZB QDs at room temperature and their dependence to temperature.
(iii) The comparison between ZB and W structures.

The NCs, presented in this chapter, have a highly spherical shape as we observed in figures (5.6A and 5.6.B). Figure 5.6B (HRTEM) reveals the high crystallinity of the dots, as we can distinguish the different lattice planes. Unfortunately, we cannot identify the crystal phase to recognize the stacking sequence [66, 181].
The XRD of samples (presented in figure (5.15)) establish the ZB structure for these samples, which is clearly different from the W structure (figure 5.7). The other differences is the splitting between the first and second absorption band, which shows larger values than in W CdSe dots (figure 5.3B). This figure compares this value in our samples with the same parameter in calculations of the ZB CdSe done by Wang et al [176]. The results show very good agreement. While the same parameters show differences between our samples and both, the experimental [63] and theoretical first-to-second absorption band splitting differences in the case of W structure (figure 5.3B). This difference between the two structures indicates that the energy splitting between the first and second bands of the low-resolution absorption spectra is strongly influenced by the lattice structure. On the other hand, the Stokes shifts are comparable in the two different structures (figure 5.4), and point towards similar band-gap energy levels.
The band-edge fine structure discussed before showed a similar PLE and FLN in the whole range of excitation and detection energy positions we investigated. Theoretical

consideration [55], [56], [182], [183], [59] predict that the band-edge exciton ($1S_{3/2}$,$1S_e$) is eightfold degenerate (§ 1.3). Due to hexagonal lattice structure of CdSe dots,[55] the non-spherical shape [56] and the electron-hole exchange interaction,[182], [183], [59] the initially eightfold degenerate band-edge exciton is split into five sublevel.[42] In figure 1.9a, the exciton fine structure is illustrated in an energy-level diagram. This model supposes that, narrow (α) and broad (β) absorption features of PLE are assigned to the lowest allowed transition 1^L and to a combination of 1^U, and 0^U respectively.

In the case of ZB structure, the internal crystal field should be absent. The effect of structure in the previous models was discussed in the same theoretical part (1.3). In the case of CdSe QDs, the model is discussed for W structure only [63] because of the less probable CdSe QDs with ZB structure with medium and big sizes. Norris *et al* [63] showed the band-edge fine structure calculation of spherical CdTe QDs that have a ZB lattice structure. The exciton fine structure of the ZB band-edge of spherical CdTe QDs and the size dependence of the exciton band-edge structure in hexagonal spherical CdSe appears in figure 1.9a and d. From these two figures, we see that: in the case of ZB structure with spherical shape (fig 1.9 d), the electron-hole exchange interaction splits the eightfold degenerate band-edge exciton into fivefold degenerate exciton with angular momentum 2 (the lower levels 0^L, $\pm1^L$, and ±2), as well as the threefold degenerate exciton with total angular momentum 1 (upper states 0^U and 1^U). These two states split in the hexagonal QDs structure into five size dependence states(figure 1.9 a), three allowed states (1^L, 0^U, and 1^U) and two forbidden states (0^L, 2).

In general, the PLE of the ZB QDs should have less absorption features (only one allowed absorption state) than the W QDs (three allowed absorption states) [42, 62, 99].

In our case, the PLE does not present any differences between the ZB and W CdSe QDs of identical size. The two groups of PLE shown in figure 5.12 present the same shape and the same relative intensity between absorption features in the two samples. The energy splitting between the resolved absorption features are the same in the two samples as presented in tables 5.I and 5.II. The comparison between the PLE and FLN spectra (for both CdSe QD structures) that we measured, and the works of Norris *at al* [63], Wind *et al* [62], Woggon *et al* [177, 179], and Chamarro *et al* [180] (whose studied in details the fine structure of the lower exciton state in the case of W CdSe dots) show good agreement between the PLE and the FLN spectra, in both the relative intensity of resolved features (figure 6.10), and the energy splitting between them (see tables I and II).

The same authors relate the resolved features to the band-edge energy levels, presented in figure 1.9a. (**α**) was assigned to the lowest allowed transition, 1^L, (**β**) to the combination of 1^U and 0^U**,** and the other features to the LO-phonon coupling. Because of the unpolarized luminescence of the band (**β**) in W CdSe lattice structure, and the polarized luminescence of the band (**α**) [63, 179, 180], it was reported that (**β**)

.

does not correspond to the same recombination channel as (α′), but it relates to another absorption state and not to the LO-phonon replica.
The values of energy position and splitting between the resolved absorption features also agree well with those previous literature works [63, 177, 179] for nearly the same size W QDs. The PLE spectra in the dots with W and ZB structures indicate to insignificant changes in the exciton fine structure between the two lattices. In other words, structure effect is a parameter that does not play the dominant role in the band-edge fine structure. It seems that the crystal field is much less important than shape asymmetries and exchange interaction. Figure 1.9 shows a more pronounced effect as a function of shape (1.9a, b, and c) than the case of different structures (1.9d). The shape changes show different energy values (especially for small sizes), and also different distribution of electronic states (1.9c). While the changes of structure present different energy values.
Another parameter that explains the negligible effect of the W and ZB structures on the splitting of the fine structure of CdSe QDs is the dipole moment. A permanent dipole moment in inevitable in the polar lattice at the wurtzite CdSe NCs but should be absent in zinc blende NCs [184, 185]. Shim *et al* [184] and Blanton *et al* [185] report that CdSe QDs with W structure exhibit large dipole moments (25-100 D). The surprised result is the appearances of a dipole moment in ZnSe NCs [184] that have a ZB lattice. The value of this dipole moment is slightly smaller than for similar size W CdSe QDs. It was shown [184] that the appearance of the measured dipole moment does not arise from charged NCs, but another reasons that might be the origins of the dipole moment, such as the surface states and the shape asymmetry of the NCs [184, 186].

The kinetic of the ZB QDs at room temperature presented in 5.2.3 pointed to similar kinetics as we discussed before in the case of colloidal ensemble of W dots in chapter 3 (figure 5.14). This behavior is expectable after the PLE, FLN studies, especially at RT (thermal equilibrium between states). The effect of QDs sizes, power, and the different detection energy show identical behaviour to that probed for W structure. Again, the ZB structure does not produce any remarkable changes in the relaxation processes of an ensemble of dots after excitation. The bi-exciton process is pronounced at high power and at the low energy side. The charged excitons (second components in the kinetics τ_2 ~ 5 ns) still show more important weighting effects in smaller dots and high power of excitation. The radiative electron-hole recombination is an intrinsic process. The changes in this component appear only at different temperatures, and should be due to the form of the band-edge fine structure which is still an open question. The forth decay time τ_4 is the longest and low-weighting component as the case of W CdSe dots, and appears as a process independent of all of these treatments and even structures. This component has a weight of less than 10%, and it reduces gradually after cooling the samples. In conclusion, the nanosecond kinetics of ZB CdSe QDs at room temperature has the same behavior as

that discussed in the CdSe QDs with W structure. The effect of structure is not relevant parameter in the kinetic behavior.

The final comparison between the two structures is the temperature dependence. The discussion includes two points: the optical properties dependence and the kinetic variations in wide range of temperatures between 4 and 300 K.

The optical properties have a similar dependence to that described in the case of W structure. The band–gap variation equation was the same that describe the bulk CdSe at the same temperatures range. The fit values in the case of ZB structure (table 5.V) are comparable to that studied for W QDs (4.3.1, and the table 5.V).

The bandwidth indicates a strong increase of the coupling with acoustic phonons (the big values of σ) compared to bulk, induced by the reduced dimensionality of the system. This behaviour is in good agreement with both theoretical [144, 147, 148] and experimental [135, 143] studies and with the results presented in the previous chapter. The source of the additional dephasing process, as we discussed for W samples, is probably induced by the surface defects.

The relative fluorescence intensity in the two structures (at different temperatures) does not show any remarkable differences between the ZB CdSe dots and the other W structure.

The kinetics at very different temperatures is best fitted by a four-exponential function (figure 5.20, and with similar results as for W QDs described in chapter 4). The lifetime constants behave in comparable behavior to the previous QDs (W QDs) in polymer film. The time-gated fluorescence spectra point to two global features with about 5 nm difference between them. The first are correlated to the fast processes with a lifetime time of much less than first 100 ns after excitation, while the slow processes still go on for longer times after the first faster decays, and with clear wings in the low energy side. This behavior is studied in details before in the case of W QDs and similar groups were resolved and faster decay was detected in the blue side than at the red one. Smaller ZB (figure 5.21A) dots show relatively more intense wings at the red side and in earlier time than the other size sample (sample e, see figure 5.21B). The more intense wings in the smaller sample indicate to more probable traps in small size QDs, and again is might be due to the increased surface to volume ratio as the case of W CdSe structure.

.

Chapter 6

Nanosecond exciton recombination kinetics in CdSe rods and tetrapods nanocrystals.

6.1 Introduction and motivation.

New fabrication methods have enabled the synthesis of high-quality CdSe nanocrystals with other shapes than the spherical QDs, the examples are CdSe nano rods [66, 187, 188] (NRs) and CdSe tetrapods [87, 170, 189, 190] (TPs). The shape effects of semiconductor nanocrystals have found many applications, such as in lasers [191], biological labels [10], and in solar cells [102].
As we showed in the previous chapters, the optical properties and the kinetics of spherical CdSe QDs have been studied extensively. The band gap and the oscillator strength can be tuned by changing the quantum dot size. However, also the nanocrystal shape has a strong influence on the optical properties. For example, the lack of a large overlap between absorption and emission spectra in CdSe nanorods rods (NRs) can improve the efficiency of light-emitting diodes (LEDs) due to the reduction of reabsorption [65, 187]. The shape effect is expected to produce different kinetics compared to the dynamics of QDs measured and discussed before. The shape can be used as an efficient way to control the electronic structures of the nanocrystal [65, 99]. Moreover, changing the shape is more flexible and provides a larger variety of electronic states than can be obtained simply by changing the size of the system [192].

Semiconductor NRs provide a good opportunity for theoretical studies of the shape-dependent electronic and optical properties [65, 187, 192, 193] due to their simple form. On the other hand, calculations on CdSe TPs presented the most dramatic findings, especially, the localisation of the lowest electronic states CB1 and first hole state VB1 in the central tetrahedron and in the arms of the tetrapods, respectively [192].
As shown in the previous chapters, time–resolved spectroscopy is a powerful technique to probe the relaxation and recombination dynamics in CdSe nanostructures [119]. In this chapter, we report our experimental study on the shape dependence of the time-resolved photoluminescence (PL) of different aspect ratio CdSe NRs and CdSe TPs with different sizes. We present the results of temperature dependent optical properties and kinetics of these particles for a wide range of

.

temperatures between 300 and 4 K. Furthermore, time-gated fluorescence was used to resolve fluorescence features at different time windows over the whole decay spectrum of these particles.

6.2 CdSe Nanorods (NRs)

6.2.1 Low-resolution spectroscopy of CdSe NRs.

We focused our studies on two groups of samples (different lengths, and widths of CdSe §nanorods) controlled by varying the precursor concentration at the growth temperature (300 °C) (the procedures of the NRs synthesis were detailed in the experimental section (§ 2.5.3)).
The first group (I) comprises three nanorod samples with nearly identical diameter and different lengths, while the second group (II) consists of two samples with discrete diameters and identical length. Table 6.I presents their characteristics.
The shape and the aspect ratio of these NRs were measured from the TEM photos figures 6.1 and 6.2. The size distribution, extracted from more than 200 particles for each sample, is less than 5 % for the diameter and about 8 % in length for all samples. Figure 6.1 shows TEM photos of the three NRs of group I, while figure 6.2 presents the two NRs TEM photos of group II.

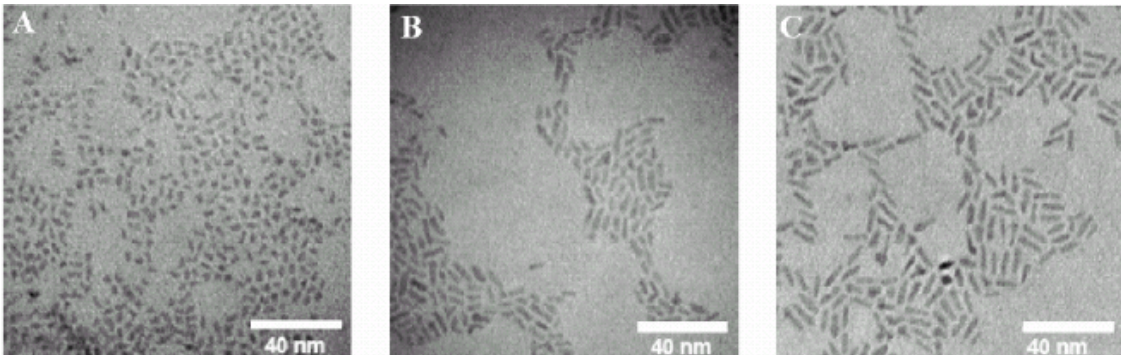

Figure 6.1: TEM images of three CdSe rod samples (group I) with three aspect ratios of (A = 2.1, B = 3.7, and C = 4.2).

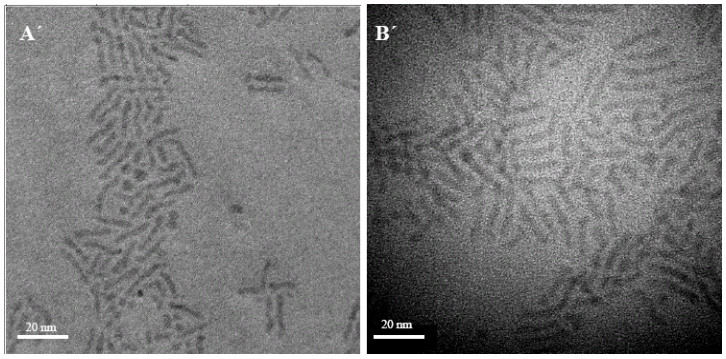

Figure 6.2: TEM images of two CdSe rod samples (II) with two aspect ratios of (A´ = 4, and B´ = 3.2). Two different resolutions for each group of samples.

All samples we used in this work have a quantum yield (in toluene) between 5 and 8 %. On the contrary to the behaviour of CdSe QDs, here smaller rods have better QY than the longer ones (AR =4.2), and less variation in the QY is found for group II. The QY was measured with the method described in the experimental section (§ 2.2.2).

Table 6.I: Characterization of CdSe QDs samples. NRs.

Sample	Diameter (nm)	Length (nm)	Aspect ratio	QY %
Different length (I)				
A	3.2±0.2	6.5 ±0.2	2.1	8
B	3.2±0.2	11.84±0.23	3.7	7
C	3.2±0.2	13.44±0.25	4.2	5
Different diameter (II)				
A´	3.87±0.14	15.5 ± 0.2	4	7.3
B´	4.8±0.1	15.5 ± 0.2	3.2	7

The room temperature absorption and emission spectra of the group I of nanorods crystals are shown in figure 6.3A, while in Figure 6.3B, we present the absorption and emission spectra of CdSe NRs from group II.

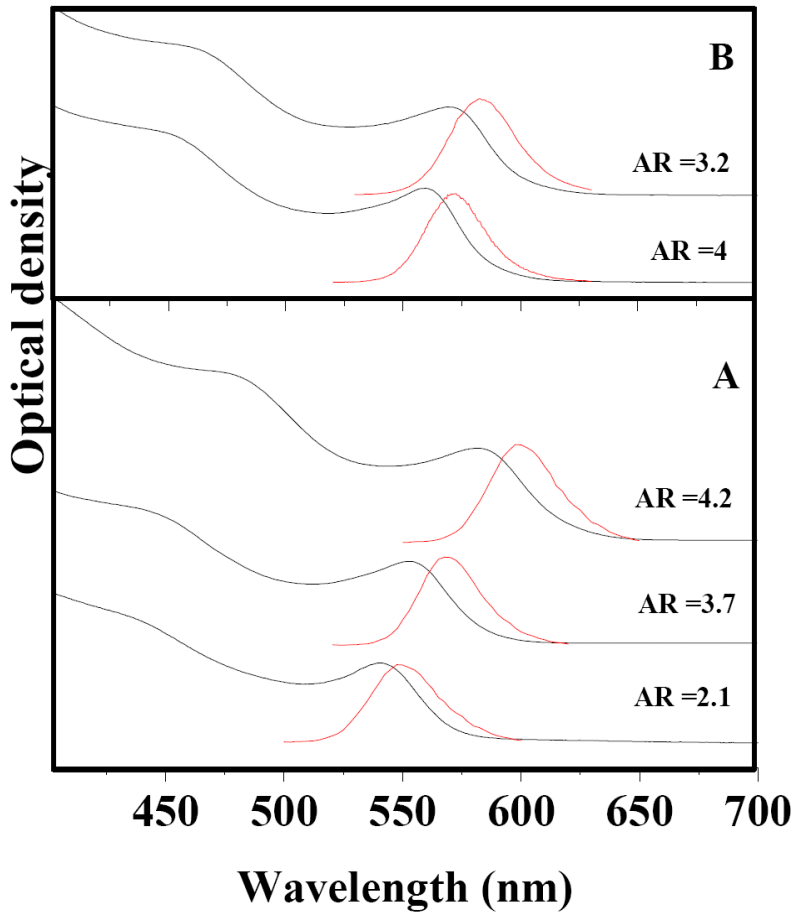

Figure 6.3: Absorption and emission spectra of two groups of NRs. A) Group I. B) group II.

For group I (figure 6.1A), both the absorption and PL spectra show red shifts as the aspect ratio increases. The measurement of group II (Figure 6.3B) show opposite dependence: the absorption and fluorescence spectra are red shifted as the aspect ratio decreases due to the increase in diameter. Stokes shift values observed in the two groups, are presented in table 6.II.

Table 6.II: Stokes shift values for different aspect ratio NRs.

	Different length (I)			**Different diameter (II)**	
Aspect ratio	2.1±0.2	3.7 ±0.2	4.2±0.3	3.2±0.2	4±0.3
Stokes shift (nm)	11.1±0.4	16.2±0.6	19.8±0.7	12.4±0.5	12.4±0.5
Stokes shift (meV)	39 ±1	53±2	65±2	51±2	48±2

The samples of group I have a larger global Stokes shift as the aspect ratio increases. Group II shows similar values of Stokes shift, but with smaller values for comparable aspect ratio with respect to group I.

6.2.2 Temperature effects on the spectral properties of NRs.

Low-resolution optical properties of CdSe QDs as a function of temperature were discussed in chapters 4 and 5 and classified in three behaviours: blue shift of the steady state fluorescence band, decrease of the width of the fluorescence band, and increase of the relative fluorescence intensity at low temperatures. Here we discuss the same parameters to clarify the effect of shape and aspect ratio on the previous physical processes, and their dependence on temperature. Three CdSe NRs samples were tested in this study, two samples (AR = 2.1 and 4.2) from group I and one sample (AR = 4) from group II. NR nanocrystals were prepared in a thin clear film, in similar way to the case of CdSe QDs and as described in the experimental chapter (§ 2.4.59), with low concentration to avoid all re-absorption and energy transfer processes. The same excitation set-up and power values indicated above were used in these measurements. As in the case of CdSe QDs, the low-resolution spectroscopic measurement (absorption and emission spectra) of samples in solution and in film are identical. Figure 6.4 shows the effect of temperature on the position of the maximum of the fluorescence band, on the bandwidth of the fluorescence band, and on the relative increase of luminescence.

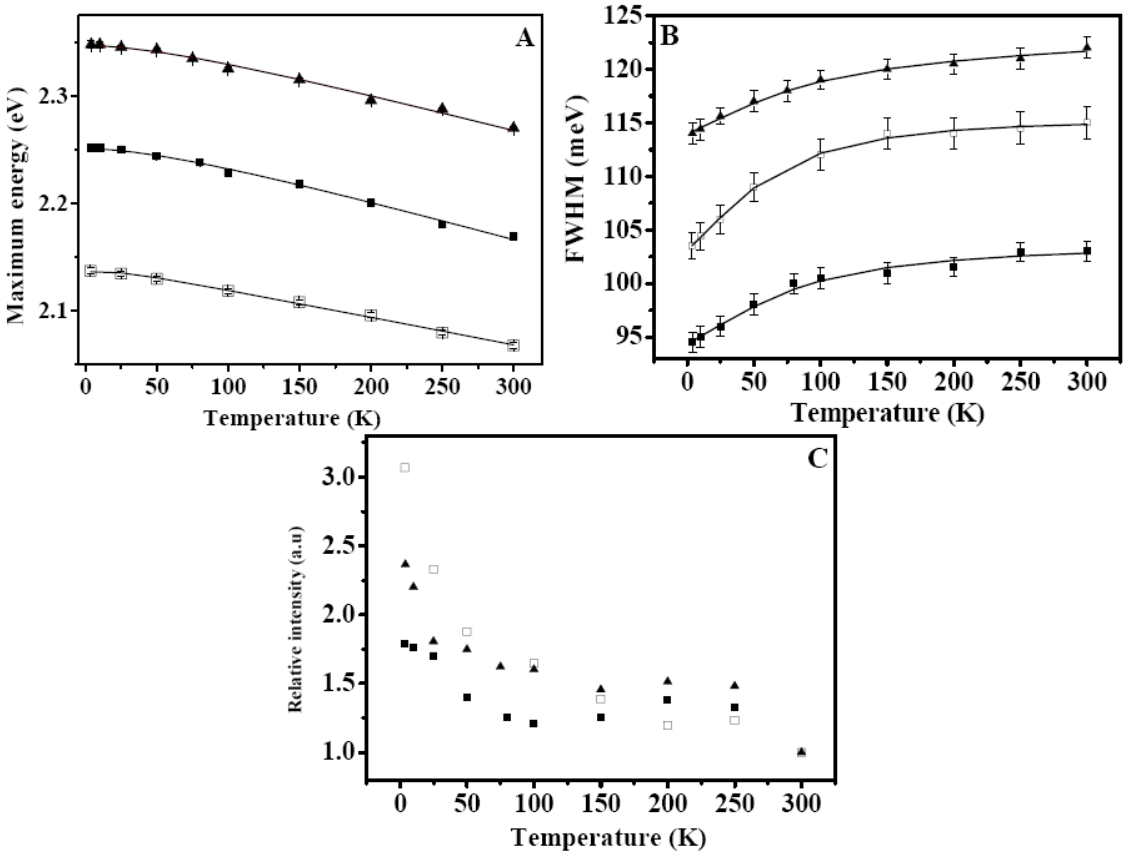

Figure 6.4: Temperature dependence of the optical properties of CdSe NRs samples (AR = 2.1 (solid triangle), AR = 4.2 (open square), and AR = 4 (solid square) in polymer film. **A)** Position of the fluorescence maximum. **B)** Full width at half maximum. **C)** Relative fluorescence intensity at different temperature. The position maximum and bandwidth were fitted using the same expression 4.1 and 4.2 in chapter 4.

In detail, decreasing the temperature from 300 to around 4 K has the following effect:

(1) A blue shift of the fluorescence band maximum. The shift is about 20±2 nm for all rod samples, with respect to the steady state at room temperature. This variation in the energy gap with temperature shows a typical temperature dependence, as observed for the energy gap of CdSe bulk [171] , and similar to what we noticed for QDs (§ 4.3.1 and § 5.2.3 IV). It can be fitted using the same relation for the energy-gap dependence (4.1) [171]. The fit values for the three different aspect ratios are shown in table 6.III.

Table 6.III: Fit results of the band-gap temperature dependence in CdSe NRs.

NRs (AR)	**$E_g(0)$ (eV)**	**α (× 10^{-4} meV/K)**	**β (K)**
2.1 (sample A, I)	2.35 ±0.03	2.8±0.1	88 ± 19
4.2 (sample C, I)	2.13±0.01	3.2±0.1	126 ±23
4 (sample A´, II)	2.12±0.02	3.5±0.2	129 ±30

The results show a smaller energy gap $\mathbf{E_g(0)}$ for the bigger aspect ratio rod. This value is comparable for all aspect ratios (4.2, 4) NRs. α in the above table shows a different dependence than $\mathbf{E_g(0)}$ and does not seem to be directly correlated to the aspect ratio. It is smaller than the bulk value (3.6×10^{-4} meV/K)[129, 156]. A bigger α value is found in the case of the rod of AR = 4. we obtain different values for β for various aspect ratios. The values of β for all aspect ratios, as the case of CdSe QDs, are smaller than the values in bulk CdSe (180 K)[129, 156].

(2) A narrowing of the bands in all of NRs samples is found at lower temperatures, gradual narrowing until 75 K and then a faster decreases in the fluorescence bands width below 50 K (figure 6.4B). This behaviour differs to that reported for the CdSe QDs in paragraph 4.3.1. Fitting of the experimental data to relation 4.2 (which describes the temperature dependence of the broadening, and which was used in the previous two chapters for the QDs) fails to describe the behaviour displayed in the figure 6.7B for all NRs.

Since the behaviour of NRs is distinctly different from QDs, we have to use a different discrioption. Lee *et al* [194] have demonstrated how scattering by ionized impurities, shows up in the temperature dependent line broadening. In this case, a term proportional to e^{-E_A/k_BT} has to be added, where E_A corresponds to the activation energy, necessary for ionization

. The NR curve can well be fitted using the following fit function:

$$\Gamma(T) = \Gamma_{inh} + \sigma T + \Gamma_{LO}\, e^{-E_A/k_BT} \qquad (6.1)$$

where Γ_{inh}, σ, Γ_{LO} correspond to the same parameters in expression 4.2. This expression indicates an underlying broadening process that necessitates an activation energy. However, the physical nature of this process is still not clear at present and does not necessarily involve the creation of ionized impurities.

Results from fitting to the equation 6.1 are shown in table 6.VI. Note that also the temperature dependence of QDs and TPs are well fitted by this function. This is not surprising, because equations 4.2 and 5.1 are identical in the limit of E>>kT, and for QDs and TPs we obtain activation energies, which are close to the LO phonon energy, indicating again the importance of exciton-LO phonon scattering for these systems.

Table 6.VI: Fit results of the bandwidth dependence of CdSe NRs using the relation 6.1.

NRs (AR)	**Γ_{inh} (meV)**	**σ (μeV/K)**	**Γ_{LO} (meV)**	**E_A (meV)**
2.1 (sample A, I)	95±0.3	2.2±0.3	7.8±1.2	3.7±0.7
4.2 (sample C, I)	106±0.7	2.1±1	11±1	4.2±0.6
4 (sample A′, II)	114±3	3.1±0.5	8.5±3	3.2±3

Fit values indicate smaller values of exciton-acoustic phonon coupling σ, compared to bulk value (8 μeV/K) [129], and also to the case of QDs shape (~20 μeV/K) (table4.II).

In similar dwpendence, the LO-phonon coupling strength Γ_{LO} has smaller values than the bulk (~100 meV), and CdSe QDs (see table 4.II). E_A shows an average value of ~ 3.7 meV, indicating predominant broadening by processes with a very low activation barrier.

(3) We further find an increase of the relative fluorescence intensity of the NRs samples. The emission intensity increases gradually below 300 K (figure 6.4C). A remarkable step in the relative fluorescence intensity is found below 50 K in all NRs samples. The ratio of QY gain is 2.4, 1.8, and 3.2 for samples with aspect ratios of 2.1, 4, and 4.2 respectively.

6.2.3 Room temperature kinetics of CdSe NRs.

For time resolved measurement, the optical density of all samples was adjusted to be 0.1 OD at 400 nm to ensure that the number of the absorbed photon in each sample is the same. The excitation and detection set-up are the same used in the case of CdSe QDs (chapter 3). Low laser excitation power was used to excite all samples ($0.1\ \mu J/cm^2$). At this power regime, multi-photon processes, which can lead to Auger processes and multi-exciton formation, do not affect the carrier relaxation dynamics of the samples. The relaxation at all detection wavelengths showed identical decay curves. All kinetics measurements at room temperature were taken at the maximum of the fluorescence band. Figure 6.5 presents a typical decay of an ensemble of CdSe NRs (AR = 4.2 from group I) in toluene at room temperature. Similarly to CdSe QDs, the kinetics decay was best fitted by a four-exponential expression:

$$I(t) = A_1 \exp(\frac{-t}{\tau_1}) + A_2 \exp(\frac{-t}{\tau_2}) + A_3 \exp(\frac{-t}{\tau_3}) + A_4 \exp(\frac{-t}{\tau_4}) \qquad (6.2)$$

The result and the residuals of this fit are shown in figure 6.5.

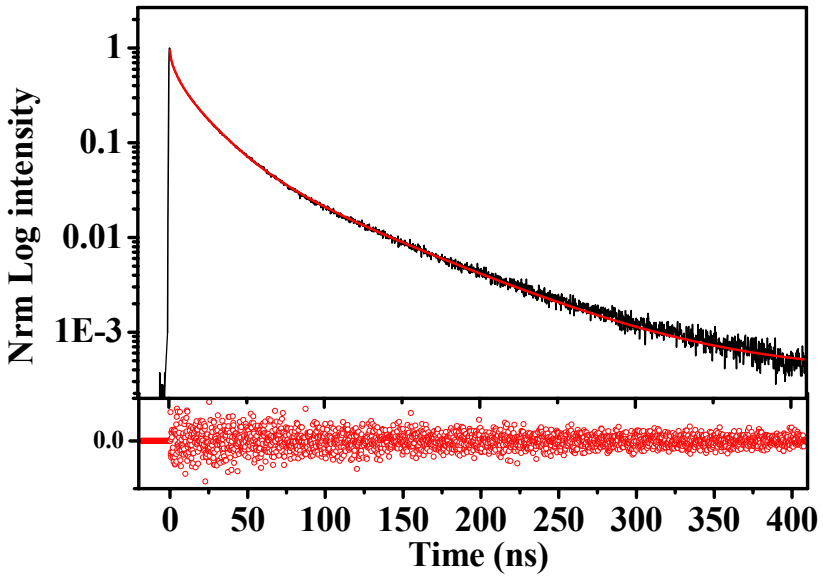

Figure 6.5: A typical PL decay curve (aspect ratio of 4.2 from group I). The straight red line is the four-exponential fit. Red circles in the bottom of the figure present the fit residual.

The fitting indicates that the lifetime constants correspond to : τ_1= 1.25 ± 0.02 ns, τ_2 = 7.2 ± 0.4 ns, τ_3 = 33 ± 1.2 and τ_4 = 90 ± 5 ns. Amplitudes **A_1**, **A_2**, **A_3** are around 30%, and only **A_4** is less than 10%. All fit values presented in this chapter have less than 10 % errors.

To compare the shape effect at room temperature, we measured the relaxation kinetics of two CdSe samples with different shapes (dot and rod), but with comparable band gap absorption spectrum at room temperature in toluene. Figure 6.6 shows two decay curves of a CdSe QD (diameter of 3.7 nm) and a CdSe NR (Diameter of 3.87 and AR of 4 (group II). The dot sample was chosen with W structure to be similar to the NRs lattice structure. The rods sample has a lower quantum yield (~ 7.3 %) than the dots sample (15 %).

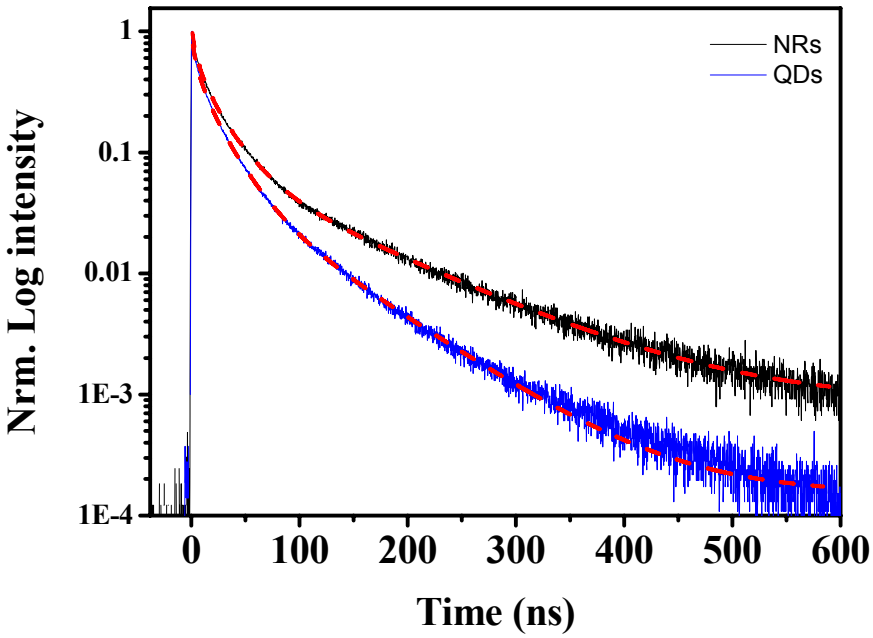

Figure 6.6: PL decay curves of CdSe Dot (Blue), and CdSe NRs (AR = 4 group II) (black) at room temperatures. The two curves were fitted with four-exponentials.

The fit values of the above two sample kinetics, show slightly faster decay for CdSe dots (shorter lifetime constant τ_3 and larger amplitude **A_3**) than for rod sample, even with 50 % less quantum yield in the rod sample. Fit values are shown in table 6.V.

Table 6.V: Fit value of two CdSe nanocrystals with different shapes at room temperature.

Sample	A_1	τ_1 (ns)	A_2	τ_2(ns)	A_3	τ_3 (ns)	A_4	τ_4 (ns)
NR(3.87 nm diameter, AR = 4)	0.33	1.20	0.27	7.5	0.32	30	0.08	95
QD (3.7 nm diameter)	0.27	1.6	0.29	7.2	0.37	24	0.07	75

This behaviour is a general trend. A number of NRs with comparable diameter of CdSe QDs, show slightly faster decays in dots than rods at room temperature.
Except for small dots (~ 2 nm diameter) as we showed in chapter 3, which shows a similar lifetime decay to that measured in the same diameter NRs.
To probe the effect of aspect ratio in the kinetics of the CdSe NRs, we measured the decay of the two NR groups (I) and (II) at room temperature. The four-exponential fit values of the kinetics decays for all aspect ratios are shown in table 6 VI.

Table 6.VI: Fit value of all CdSe NRs at room temperatures. The error in all values is less than 5 %.

AR	A_1	τ_1 (ns)	A_2	τ_2 (ns)	A_3	τ_3 (ns)	A_4	τ_4 (ns)
2.1	0.30	1.25	0.35	6.20	0.29	27	0.06	80
3.7	0..29	1.21	0.31	8	0.31	28	0.09	84
4.2	0.33	1.25	0.30	7.2	0.33	33	0.05	90
3.2	0.31	1.4	0.29	5	0.34	32	0.06	84
4	0.33	1.2	0.27	7.5	0.32	30	0.08	95

The comparison between fit results of the kinetics decay indicates a comparable behaviour of NR samples in group I and II.

6.2.4 Low temperature kinetics of CdSe NRs.

In this section, we probe the temperature dependence kinetics of different aspect ratio NRs over a wide range of temperatures. Samples we used in this work are the same as described in table 6.I and § 6.2.2. In addition, the kinetics of the NRs shows (for all aspect ratio samples) a faster decay in solution than in film. A similar behaviour was also detected in CdSe QDs (§ 4.2). Figure 6.7 shows the decay curves of CdSe NRs (AR = 4.2) in toluene and in film at the same detection wavelength and at room temperature. A faster decay appears in the case of solution than in film. The four-exponential fit values of the NRs sample in film and solution are shown in table 6.VII.

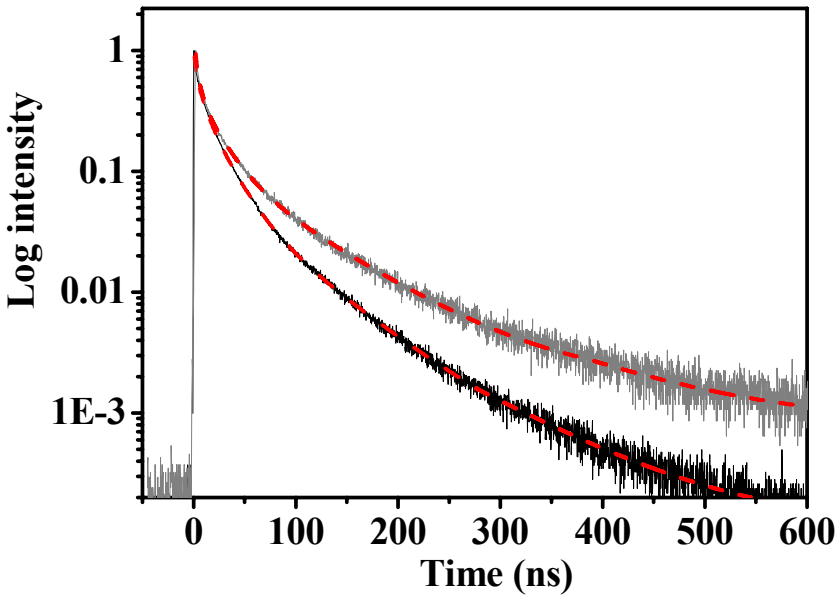

Figure 6.7: Photoluminescence decay curves of CdSe (AR = 4) at room temperature in toluene solution (black) and in film (Gray). The two kinetics are fitted by four exponential (red) fit function.

Table 6.VII: CdSe NRs fit values in two samples environments (solution and film) at room temperatures.

CdSe NRs	A_1	τ_1 (ns)	A_2	τ_2 (ns)	A_3	τ_3 (ns)	A_4	τ_4 (ns)
Solution	0.31	1.25	0.31	7.2	0.30	33	0.08	90
Film	0.31	1.25	0.30	6	0.34	36	0.05	125

In the polymer film, the largest lifetime component τ_4 shows an increase of about 30% compared to its value in solution. The intrinsic lifetime τ_3 in film is about 9% larger than in solution, and its amplitude increases by 13%. The other two components τ_1, τ_2 remain unchanged in the two samples phases.

In the following, we present the temperature dependence of the photoluminescence decay kinetic of all CdSe NRs samples in the range of temperatures investigated above. Figures 6.8 and 6.9 show characteristic PL decay curves at selected temperatures for the two groups of samples I, and II. We present the first 40 ns of kinetics only. All the NRs in this range show faster decay at lower temperatures.

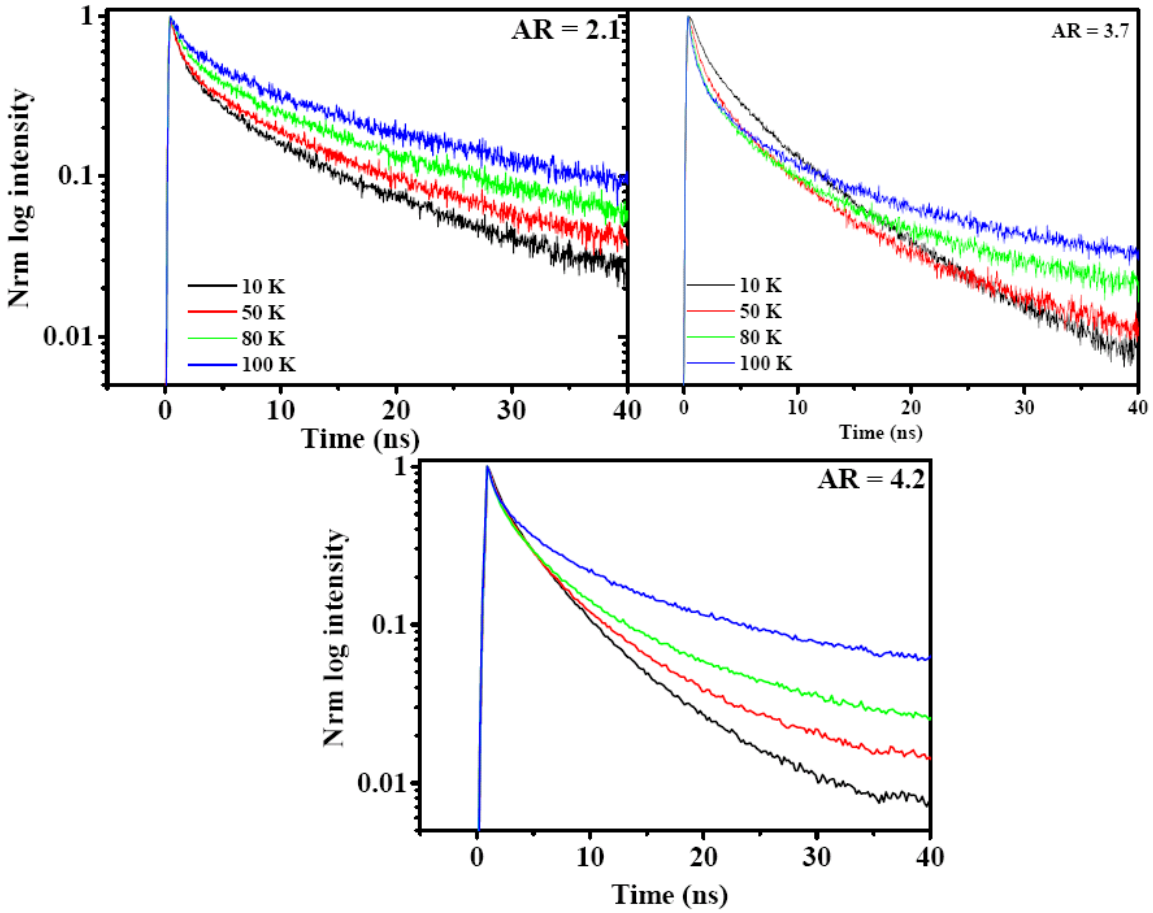

Figure 6.8: Ensemble photoluminescence decay at different temperatures (between 10 and 100K) for the three different aspect ratios samples of group I. only 40 ns time window is detected in this case.

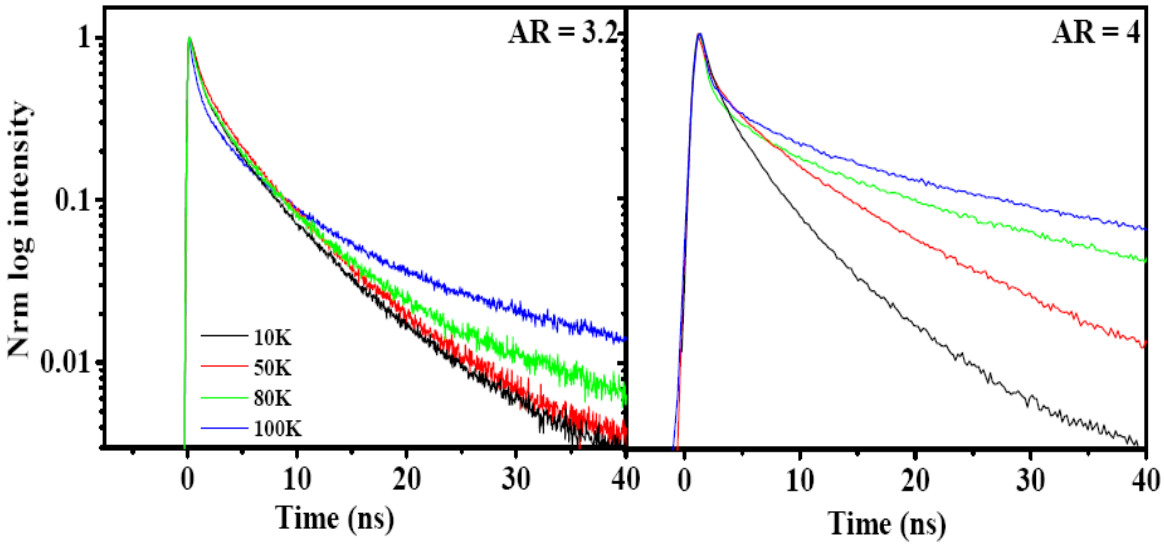

Figure 6.9: Ensemble photoluminescence decay at the same temperatures in figure 6.8 (between 10 and 100K) for the two different aspect ratios samples of group II. 40 ns time window is detected in this case.

The kinetics in the short time window (40 ns) are best fitted with multi-exponential functions (three-components), and the fitted values indicate consistently a faster decay at lower temperatures for all NRs samples. These results appear in good agreement with the work of N. Le Thomas *et al* [99] on the temperature dependence of CdSe NRs.
For a more complete description of the whole kinetics of the CdSe NR crystal, we measured the relaxation processes over a long time window (600 ns). In this time window, the NR samples shows additional characteristic and more variable kinetics than that presented in the last two figures. Figures 6.10A, and B, present the whole decay of CdSe NRs on a long time scale, and for the whole range of temperatures (from RT to 4 K) for two NR samples, with aspect ratios of 4.2 (**C** from group I, see table 6.I) and 4 (**B´** from group II, the same table) respectively.

From the figure 6.10 A and B, the kinetics decay shows two different regimes of kinetic changes: above 200 K, and below this temperature. For the first temperature range (300 K-200 K), the whole decay (all components) slow down with decreasing temperature. Then at lower temperatures, the dynamics is gradually becoming faster until 4 K for the three components we presented in the previous figures 6.8, and 6.9. The rest of the decay shows a slower relaxation at lower temperatures, especially in sample (**C**), where a very slow decay was detected at lower temperatures (lower than 100 K). This long component shows a similar decay in (**B´**) below 80 K. The temperature dependence kinetics in this time range (600 ns) is best fitted with a multi-exponential decay (one more exponential than the decay kinetics in the short window). Figure 6.11 presents the fit results of the samples (**C**) and (**B´**) for the whole range of temperatures. τ_1 appears constant with no more than 10 % changes around its lifetime value (~1.3 ns) at RT. This component does not appear in figures 6.11**I** and **II**. The second component τ_2 decreases below of 100 K. The intrinsic lifetime τ_3 increases from 13 ns in (**C**) and 8 ns in (**B´**) to have 33 ns and 30 ns at 300 K. the longest component τ_4 shows a slower values at lower temperatures. $\mathbf{A_1}$ in these two samples increases from 30 % at RT to about 50 % at low temperatures. $\mathbf{A_2}$ has the same amplitude for the whole range of temperatures. $\mathbf{A_3}$ in the two samples is smaller at lower temperatures. The same dependence appears for the amplitude of the slower component $\mathbf{A_4}$.

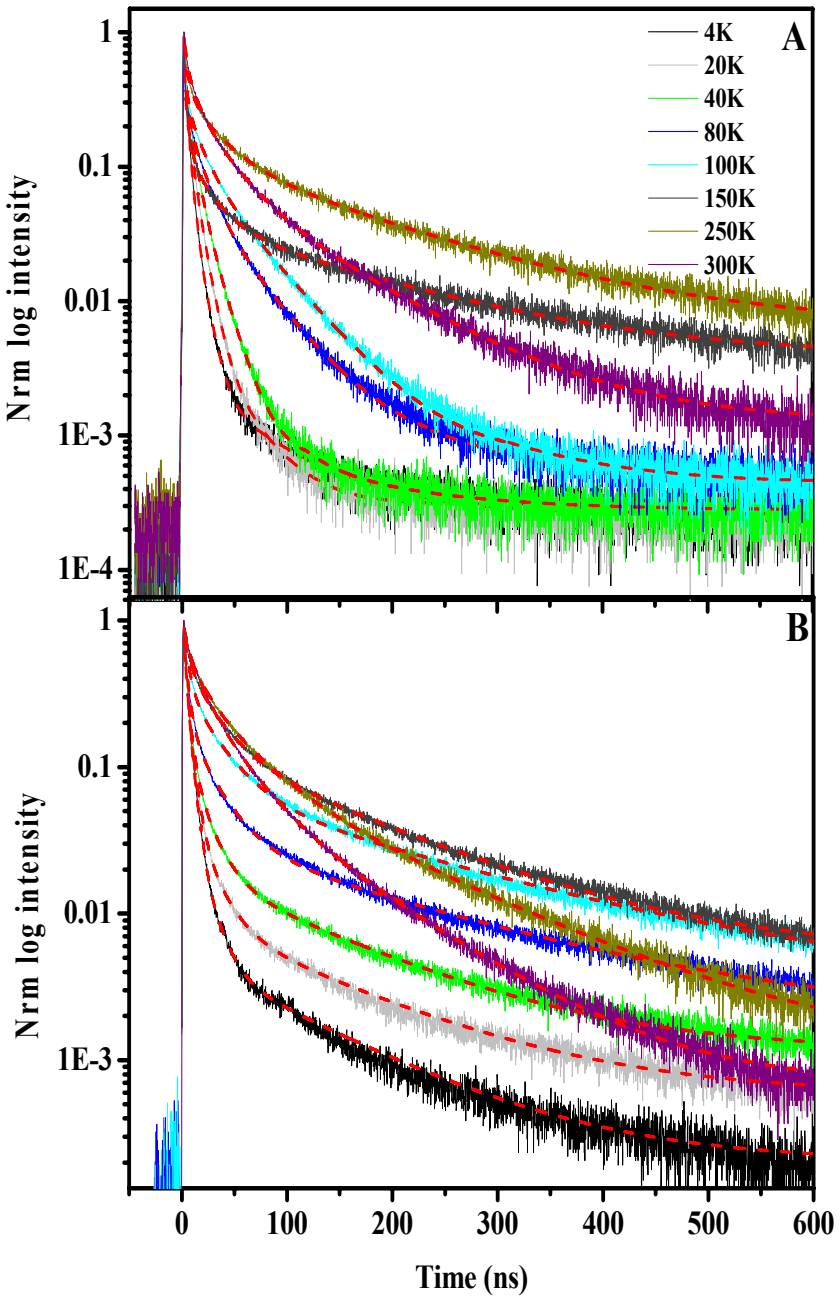

Figure 6.10: Photoluminescence decay at different temperatures (between 4 and 300K) for two different aspect ratios samples(AR= 4.2 and 4) for long time scale. A) sample (**C**) from group I. B), sample (**B´**) from group II. Four-exponential function (red dashed line) was used to fit all decay curves at all temperatures.

The other samples (AR = 2.1, 3.2 (group I), and 3.5 (group II)) present the same general temperature dependence explained previously, and their kinetics can be resumed in the following points: (i) faster decay at low temperatures (for the three first components) and an additional low weight slower component at lower temperatures. (ii) All samples were best fitted by the four-exponential fit function. (iii) The pre-exponential factors show increasing of $\mathbf{A_1}$ and decreasing of $\mathbf{A_3}$ and $\mathbf{A_4}$. $\mathbf{A_2}$ stays unchanged for all temperature range.

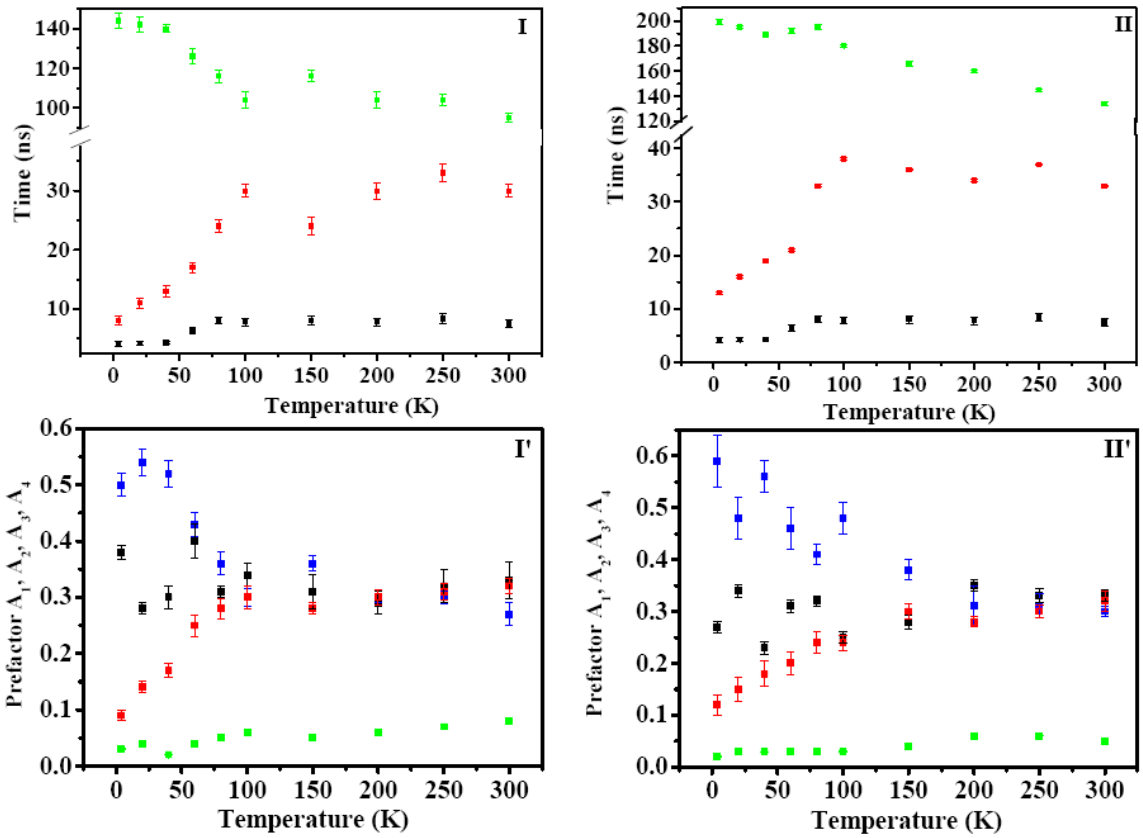

Figure 6.11: Four-exponential fit parameters at different temperatures CdSe NRs samples (**C**) (I, I´) and (**B´**) (II, II´) respectively. $\mathbf{A_1}$ (blue); τ_2, $\mathbf{A_2}$ (black); τ_3, $\mathbf{A_3}$ (red); τ_4, $\mathbf{A_4}$ (green).

As we did before in the chapter 4 and 5 for CdSe QDs, we used the time-gated fluorescence to resolve the fluorescence components at different time windows. Figure 6.12 shows the time-gated fluorescence of four CdSe NR samples from groups I, and II at 4K. In figure 6.12A, and B, we present the time-gated fluorescence of group II samples (A: AR = 3.2 and B: AR =4). While in figure 6.11C, and D, the time gated fluorescence of CdSe NRs of group I are presented (C: AR = 2.1, D: AR =3.7). The third sample of group I (AR =4.2) is shown in figure 6.13 with longer wavelength range than the others. The reason for this individual study is the presence of an additional red fluorescence band appeaiy at low temperature (appears in the same figure 6.13). The other samples do not show a comparable intense fluorescence band at the low energy side.

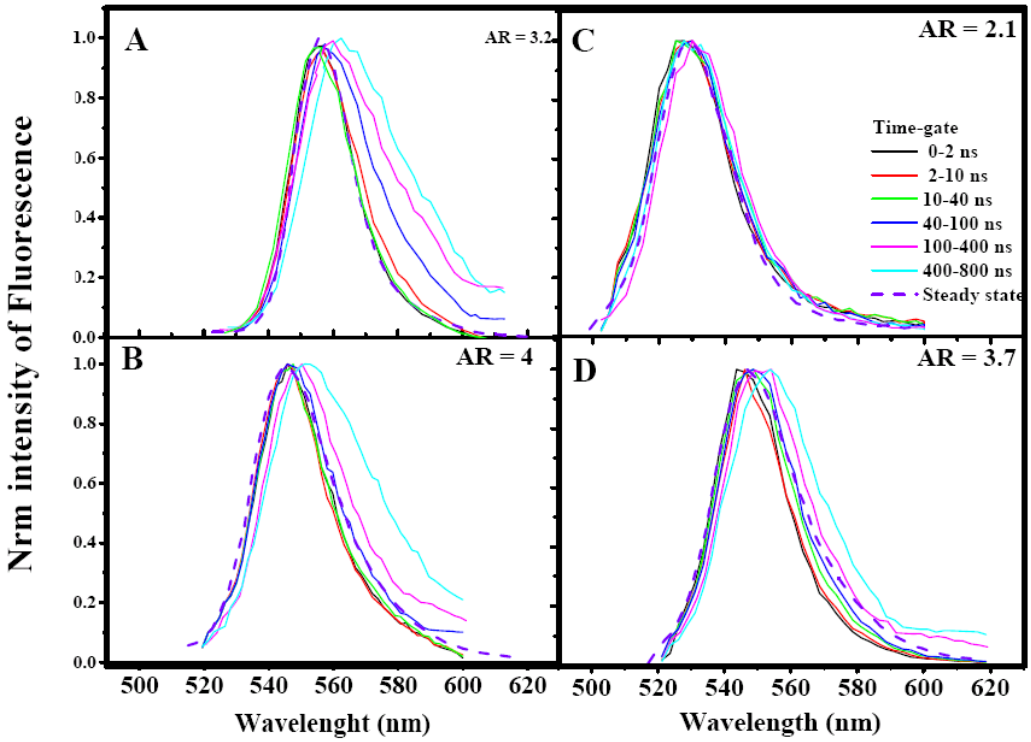

Figure 6.12: Time-gated Fluorescence bands at 4 K. A) and B) for group I (AR = 3.2, 4.5). C) and D), group II (AR = 2.1, 3.7). The colors and gate times are the same in all samples.

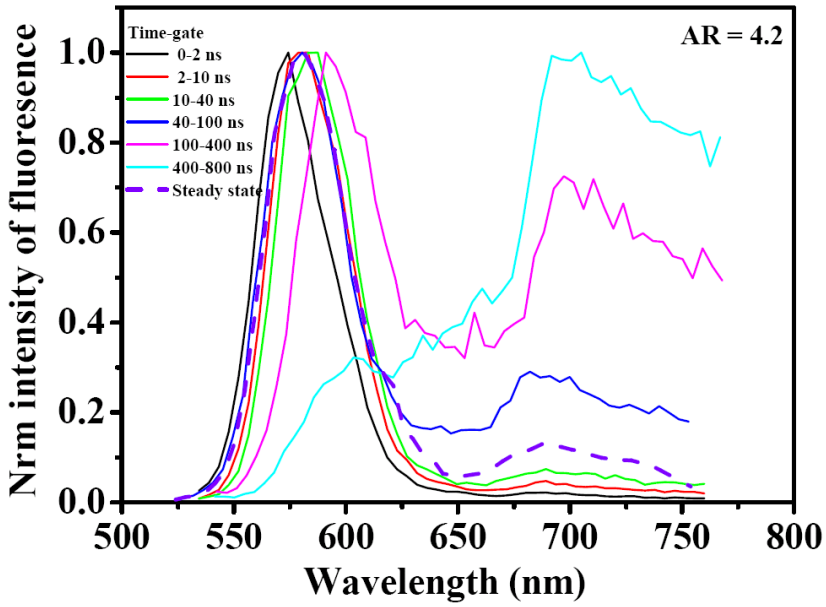

Figure 6.13: Time-gated Fluorescence bands of 4.52 aspect ratio sample at 4 K.

From figure 6.12, the time-gated fluorescence presents the following dependence: up to 60-80 ns, the time-gated fluorescence band of all samples behaves in similar way. Beyond this time, a red shift occurs (especially in bigger AR) and a small wing appears in the same energy side. This effect possesses an aspect ratio dependence as we show below in figure 6.14. The same behaviour is obsereved even more

remarkably in large AR (4.2) (sample **C**) as it shows in figure 6.13. In this NRs sample, the blue shift after a delay time of 100 ns is about 75 meV. The contribution of the red fluorescence wing on the fluorescence band is about 30 % after 40 ns and 70 % after 100 ns.

The size dependent positions of the fluorescence maximum in the time-gated fluorescence spectra were calculated, for the whole ARs NRs presented in figures 6.12 and 6.13, and represented in figure 6.14.

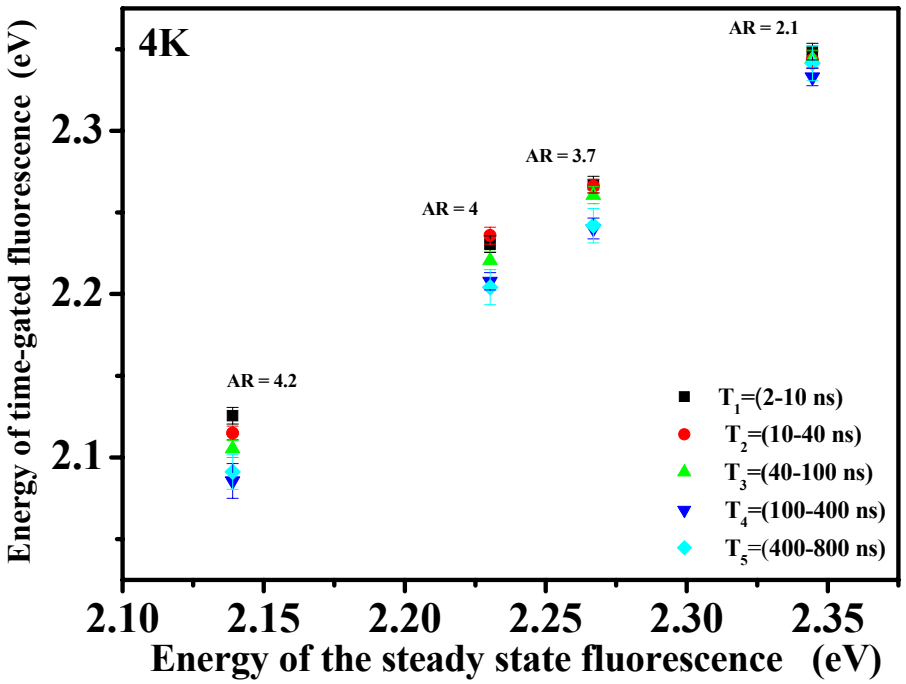

Figure 6.14: The maximum time-gated fluorescence band for each sample in the fixed integration time window. The colors indicate to different time windows.

From figure 6.14, The maximum of the time-gated fluorescence band in smaller aspect ratio sample (AR = 2.1), between the early and final delay time after excitation, is 4 nm (17 meV). This shift increases to 6 nm (22 meV) in the sample of AR = 3.7, and to 12.5 nm (35 meV) for the largest aspect ratio (AR = 4.2).

To confirm the long-lifetime component origin, we probe the relaxation kinetics of the sample of the longest AR (figure 6.13) at two different wavelengths (600 and 725 nm) at 4K. At 600 nm, we detect the contribution of all processes in the relaxation decay.

While at 725 nm, only the fluorescence effects of the additional fluorescence band are the pronounced features. Figure 6.15 shows the two relaxation decays.

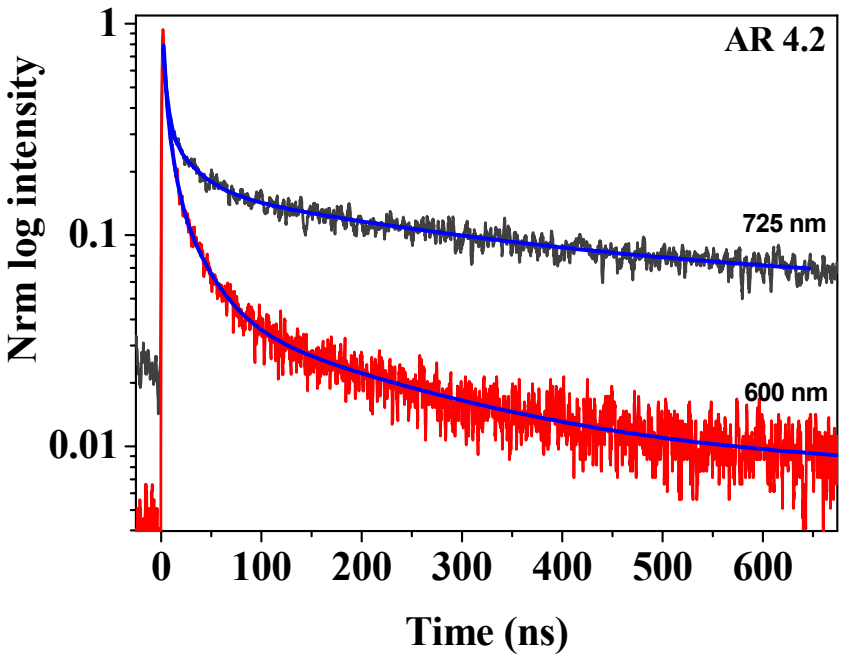

Figure 6.15: The decay curves of CdSe NRs (AR of 4.2) at 4 K at 600 nm (Red) and at 725 nm (Gray) detection. Bi-exponential fit for the blue wavelength detection, and four-exponential in the other wavelength.

The decay kinetics have weaker signal at the red wavelengths than at 600 nm. The traps kinetics (725 nm) is best fitted with two-exponentials, while the kinetics at 600 nm is fitted as usually by four-exponentials decay. Table VIII presents the fit results using the two functions above.

Table VIII: Fit parameters of two energy detections of 4.2 CdSe NRs relaxation processes appear in figure 6.14.

CdSe NRs	A_1	τ_1 (ns)	A_2	τ_2 (ns)	A_3	τ_3 (ns)	A_4	τ_4 (ns)
Red side (600 nm)	0.23	1.20	0.56	6	0.17	25	0.04	191
Traps fluorescence (725 nm)					0.67	8.8	0.33	205

The value of the longest component is the same in the two decays. Only the amplitude of this process is larger in the red side detection. The other component, which is prominent in these two kinetics, is the second component at 600 nm and the first one at 725 nm. This result suggests a similar physical origin of the two long components.

The same measurements were performed using the same CdSe NR samples deposited on a substrate of CaF_2, in a similar way to the case of CdSe QDs (4.3.2.II).

The results of the temperature dependence study show similar dependence to that presented above. For that we presented only the results in the polymer film.

6.2.5 Discussion and conclusions:

-Shape effect.

The cylindrical symmetry of the rods assumes a key-role in the explanation of the optical properties and kinetics of the nanoparticles that appears as the spherical symmetry is broken[187]. It is well known that the broken spherical symmetry of atoms alters the polarization of their light emission [195]. Examples are the Zeeman effect and the Stark effect in atomic spectra. Similarly, it can also be expected that shape anisotropy of nanocrystals should result in optical anisotropy, and in the pecular optical properties [99] of the CdSe NRs.
The CdSe nanord samples that were chosen in this work have systematic properties. The NRs of group I and II were obtained from the same preparation (each group) and have gradually increasing aspect ratios. All the optical and kinetic effects were tested in these samples to present the shape and the aspect ratio effects in a systematic study.
Generally, the dominant parameter that indicates the range of optical changes in the NRs is the aspect ratio of rod. In fact, the length dependence becomes significant only for small aspect ratios (around two) [196]. For bigger AR values, the length becomes less important and the significant effect is due to the width [196]. For rods that have a radius smaller than ~ 5.6 nm (exciton Bohr radius in bulk CdSe), the band mixing is substantial so that the band gap becomes very sensitive on the length. For rods with radius greater than ~ 5.6, the band mixing is less significant, and increasing the length only lowers the band gap [65]. For that and to identify the rod samples, the two parameters must be counted as characteristic parameters for each NR. In group I, the aspect ratio (2.1, 3.7, and 4.2) and the diameter (<< 11.2 nm) of the CdSe NRs make this group to be length dependent. As the length increases, the absorption spectra (see figure 6.3A) and the Stokes shift values (table 6.II) change in pronounced way. This effect is different in the samples of group II, where the length stays constant, but the diameter increases (figure 6.3B and table 6.II).

-Stokes shift.

The Stokes shift values in the samples of the two groups are between 39 meV and 65 meV. The Stokes shift values range is comparable to literature works on nanorods, both experimental [119] and theoretical [187]. The Stokes shift dependence discussed above can be explained by comparing our result with previous works [187], [119]. A critical aspect ratio value (AR_{crit} = 3 for 3.9 nm of rod diameter) was presented in the work of Hu et al [187]. This work shows that above this value, the Stokes shift increases with increasing AR, while below, an opposite dependence appears. The

theoretical model and calculations presented in the same work confirm the idea of a critical aspect ratios value (AR_{crit}). The calculations indicates one AR_{crit} value (1.25 for all rods width), independent from the variation of the rod diameter. X-Y. Wang *et al* [119] observed a comparable experimental aspect ratio critical value (AR_{crit} 2.5), and Stokes shift value rising for longer rods. The diameter of the NRs in this work was 4.5 nm, and no results for other diameters values are presented. In our work, the diameter of our samples was 3.2 nm and no critical value was resolved. All of the measured Stokes shifts (6.II) increases with the length. The rods samples of group II show similar Stokes shift values (~ 50 meV).
From the comparison between the previous literature results and our work, we can point out a few general remarks on the Stokes shift values:

(i) The critical Stokes shift, AR_{crit}, is diameter independent.
(ii) The experimental values of AR_{crit} are bigger than the calculated ones [187] (AR_{crit} 1.2).
(iii) We do not observe a critical aspect ratio. The possible reason for this, is the limited number (3) of our samples that covers the aspect ratio interval from 2 to 4.2, compared to the five samples presented by Wang *et al* [119] , and to the 19 single NR samples presented in the other cited work [187].
(iv) The small difference in A_{crit} between the two works [187], [119] is due to the difference between the single rod experiment [187] (sample on substrate), and colloidal ensemble of rods [119]. In case of single particle, more probable charging and possible polarization are expected, while the case is very different in solution for an ensemble of NRs.
(v) The general Stokes shift values depend significantly on the length of the NRs, we observe a good agreement between our measurements and the literature results presented in the previous two works.

From the small relative difference between the AR_{crit} values (2.5 and 3) in the two rod samples presented in the previous works, we can estimate the AR_{crit} value in our samples. This value must be around 3.5 This value is nearly the aspect ratio of the second rods samples (**B**) from group I (table 6.I). The smaller and bigger NRs in the group I do not show a Stokes shift tendency that confirm the idea of AR_{crit} presented in the previous discussion. Even with 1.4 nm difference in the diameter between the two rods (group II), the Stokes shift stays the same.

- Quantum yield.

The values of the quantum yield in the table 6.II indicate an increase of the quantum yield as the length decreases. This tendency appears similar to what was reported by Mokari *et al* [197]. The authors show a decrease in the QY of CdSe/ZnS NRs as the AR increases. The reason is due to the effect of the thicker layer of ZnS that covers the smaller AR NRs compared to the bigger AR NRs. In our case, as our NRs have a

layer of ligand molecules (TOPO) surrounding the CdSe core, the QY decreases as the samples become longer. This is due to the relative lower number of traps in smaller rods than in longer ones. This explanation is strongly proven by the time-gated fluorescence study at lower temperature. Especially for the smallest and the longest rods in-group I (figure 6.12C and 6.13), where the traps fluorescence features (very slow lifetime decay) appears clearly on the red energy side of the steady state fluorescence. The different diameter rods (group II) do not present any variation in the QY values between them. This behaviour can be explained considering a favourable axis with less probable traps: The number of traps along the diameter axis is less pronounced than the number of trap along the rod axis, due to the particles growing mechanism.

- Environment.

The different kinetics of the same rod size in different sample environments (solution or film) presented in figure 6.6 is discussed in chapter 4 for the case of CdSe QDs, which show slower kinetics in film. This difference between CdSe NRs samples in the presence of the polymer (butyl methacrylate-comethy methacrylate) film form has a similar explanation to the CdSe QDs, which was attributed to chemical changes on the surface.
Preparation of the sample in the form of a polymer film in presence of trioctylphosphine and heating of the sample can add more capping to the surface, and reduce the traps. This treatment makes the whole decay slower than in the case of sample in solution.

- Temperature.

The effect of temperature on the steady state optical properties of the NRs shows a similar general trend as that presented in CdSe QDs, even for the W or ZB lattice structure, discussed in the chapters 4 and 5. The temperature dependence of the PL resonance peak energy changes is independent of the size, shape, or even structure. The same fit function describes the temperature dependence of the maximum band energy. The same behaviour is detected also in CdSe TPs, as we will present later in this chapter. The different values in the fit function parameters reflect only the specific unit-cell properties (defects, stacking fault) of the crystal, without effective variations that change the general tendency.
The other process that causes a decreasing of the full width at half maximum (FWHM) of the luminescence bands in NR samples has a specific different dependence in the rod shape than in the QDs and TPs as we will discuss later. The different fit function used to describe the decreases of the emission band indicates a different specific phonon coupling than in the case of dots. Equation 6.1 was used in the NR case than the CdSe QDs. A possible physical explanation for this behaviour might be the role played by surface charges. Banin *et al* [198] showed evidence for

thermal contributions to the charging process of NCs with an activation energy of 8 meV. Furthermore, it was recently shown that charge migration in elongated NCs can give rise to spectral diffusion and a temperature dependent broadening [199],[200],[201] due to the quantum confined Stark effect.[202] Fluctuating surface charges give rise to electric field fluctuations, whose magnitude depend on the distance from the exciton. The amplitude of this effect is on the order of tens of meV [202], which could quantitatively explain the broadening we observe. In this picture, the temperature dependent broadening is the result of thermally induced charging in combination with spectral diffusion due to charge migration on the surface. Charging effects might be larger in NRs due to less complete surface passivation or reduced quantum confinement in one-dimensional NRs compared to zero-dimensional NDs.[203] Furthermore, in spherical NDs it would not lead to broadening from spectral diffusion, since charge fluctuations occur at a fixed distance from the exciton.[203]

The integrated emission bands in the largest aspect ratio NRs in-group I (Sample **C**, figure 6.7C open squares) show three magnitudes of increase in the relative fluorescence intensity as the temperature goes down from room temperature to 4K. while the other samples present less gain in the relative luminescence intensity. This value might be reflects the magnitude of the nonradiative processes and traps-related effects for two NR size. This is also observed later in the time-gated fluorescence (figures 6.12 and 6.13) by the non-negligible traps contribution in this rod sample.

Time resolved spectroscopy measured for all NR samples at all temperatures between 300 and 4 K was best fitted by four–exponential decays with different dependence compared to the CdSe QDs shape presented in the chapter 4 and 5.
Time-resolved spectroscopy of CdSe NRs were previously presented in two literature works: the first is the work done by Wang *et al.*[119] concerning room-temperature measurements, where the measured radiative lifetime first decreases and then increases around the critical aspect ratio of the nanorods ($AR_{crit} \sim 2.5$). The authors show only two components and less than two order of magnitude of signal to background. The two lifetime components of the bi-exponential fit have time constants of several nanoseconds (3-8 ns) and several tens of nanoseconds (100 ns) correlated to the trap states lifetimes respectively.
The second work, which investigates the effect of shape on the relaxation kinetics of the CdSe nanorod nanocrystal, is that done by Le Thomas *et al* [99]. The authors present a comparison between time-resolved spectroscopy of two different diameter CdSe NRs with CdSe QDs at low temperatures (5, 40, and 80 K). Note that the NRs are much longer (25-35 nm) than the NR samples used in this thesis. In addition, the fit function used (stretched exponential), is different from the multi-exponential fit employed in our case. The third difference, with respect to our work, is the long component lifetime τ_4, which was completely ignored in their work, especially for measurements at room temperature.

The values of τ_3 and τ_4 at different ARs at RT (table 6.IV) show comparable relaxation behaviors for different lengths and width NRs. This behaviour does not agree with the relaxation behavior that was presented by Wang *et al* [119] for 4.5 nm diameter NRs samples [119]. The tendency in the previous work was explained by a transformation in the electronic structure as the aspect ratio increases. In our case this transformation in the electronic states distribution does not recognize because the limit number of NR samples (3).
In general, the transformation were presented in many works in literature [42, 99, 187, 202]. The reason of this behaviour is that in nanorods, the $4P_{X,\,Y}$ and $4P_Z$ components of the valence states are subject to different confinements. There is greater momentum projected onto the long axis of the $4P_Z$ orbit than the $4P_{X,\,Y}$ orbits. Thus, it will have less confinement energy and become the highest valance state with the increase of the aspect ratio. After the $4P_Z$ becomes the highest valance state, the photoluminescence should exhibit complete polarization. This polarization is aspect ratio dependent. Increasing the aspect ratio will decrease the confinement along the long axis and show slower decay as the aspect ratio increases. In our case, the effect of different aspect ratio on the decay kinetics does not resolve a slower decay for longer rods.

The effect of temperature on the kinetics of the NR particles shows peculiar and interesting behaviour. Firstly, the CdSe NR experimental kinetics show opposite temperature dependence (slower decay as the temperature rises) than the CdSe QDs. Secondly, the calculated changes in the fine structure band gap present a transformation on the electronic structure of the band-gap fine structure [42]. Le Thomas et al [99] showed temperature dependent lifetimes of thin and thick NRs. The smallest sample in this work was 5 nm as diameter and 25 nm length (AR = 5). The biggest NR presented was 8 nm diameter and 35 nm length (AR = 4.4). The kinetics of these two samples was very different. For the smaller diameter sample, the lifetime is faster at lower temperatures. The opposite dependence (similar to CdSe QDs) was detected in the bigger diameter sample. The data in the two cases was fitted (similar to what we discussed above at room temperature) with a stretch exponential function ignoring the long component which appears in all samples. No descriptions for the kinetic behaviour for temperatures above 80 K were given.
In our work on the temperature dependence, we show NR samples with thinner (from 3.8 nm to 4.8 nm diameter) and shorter (from 6.5 nm to 15.7 nm) length, but with comparable aspect ratio (AR = 4.2) to those presented in the reference [99] (AR = 4.4). Again, all treatments, fit function, time windows, and the signal to background ratio are different in our study. The classification of our samples compared to reference [99], present the same range of the smaller diameter rods (< 5 nm diameter) [99]. Thus, all of our samples show faster kinetic at low temperatures than RT.

For the kinetics of our NR samples in the first 40 ns time-windows (figures 6.8 and 6.9 group I and II respectively), the intrinsic life time τ_3 becomes faster below 100 K in all NRs samples (different diameters). To explain this effect at these temperatures, the band gap fine structure must be the key. The electronic structure of CdSe QDs has been studied theoretically [42, 55, 61, 99, 176] as we presented in the introduction (1.3.a). The effect of shape (symmetry) of the QDs leads to remarkable transformation in the fine structure (figure 1.9b and c). The fine structure of the band gap of prolate CdSe QDs [29-30] or longer CdSe NRs [99] show that the dark state ± 2 is not the ground state , in contrast to the spherical QDs, due to the interplay between the electronic confinement and the hexagonal crystal symmetry [99]. This contribution makes $S_eS_{1/2}$ to be the ground state in CdSe NRs ($S_eS_{3/2}$ is the ground state of CdSe QDS). By considering the exchange interaction, the ground state will be the dark state 0^L state in the NRs followed by the bright states $\pm 1^L$ and 0^U. Small energy differences between these states lead to a thermal population between them at very low temperatures (15 K) [99]. Because the bright states $\pm 1^L$ and 0^U are energetically below the dark state ± 2, the measured decay at low temperature will be faster than at RT.

As all physical processes have general slower nature at lower temperatures, this experimental behaviour is interesting as temperature dependence.

The time-gated fluorescence study (figure 6.12 and 6.13) shows a comparable effect to that presented in the case of CdSe QDs (figure 4.12). The first 60 ns shows the same features, while for further time delay the time-gated fluorescence features show red shift and pronounced wings on the low energy side. The different effect to the CdSe QDs shape is the increase of energy differences between time-gated fluorescence bands in the longest nanorod samples (figure 6.14). With a more pronounced wing for the biggest AR NR (sample **C** figure 6.13) for more than 100 ns time-delay after excitation. The fluorescence band that appears clearly on the low energy side, while the magnitude of the shift shows an aspect ratio dependence. The more contribution of trap states can be easily correlated with the large surface of longest rods than quantum dots, and the more probable trap states on longer rods than shorter nanorods. Moreover, the decay curves detected at different wavelengths present an idea about the same origin of the additional fluorescence band that resolved on the low energy side in the longest sample in-group I and the wings appears for long time delay in the time-gated measurements in the case of CdSe dots. The similar lifetime constant τ_4 in table VIII proves its origin as a surface traps component. The aspect ratio dependence (figure 6.14),which depends on the length more than the width can prove that on the axe of length, more traps might be produced than the case of growing on the direction of NR width.

6.3 CdSe tetrapods.

6.3.1 Growth and optical properties:

Recently Alivisatos and co-workers [189] demonstrated the high yield synthesis of tetrapod-shaped cadmium telluride (CdTe) nanostructures. What underlies their work is the polytypism of tetrahedrally bonded structures, such as those of the II-VI SCs [204]. Indeed, their lattice has a common crystal plane, which can be used to achieve branching. The [111] plane of the cubic (Zinc Blende, ZB) lattice structure is atomically identical to the ± [0001] plane of the hexagonal (Wurtzite, W) structure. Their synthesis was achieved by performing the initial nucleation in the ZB phase, followed by the growth of the four arms in the W phase. This is possible using organic surfactants, which inhibit growth at the sides of the arms, but not at their end, thereby achieving selective elongation [205]. In a later work, the same authors also demonstrated the synthesis of heterostructures (consisting of CdS, CdSe and CdTe) with both linear and branched topologies [206], but in all cases the core consisted of CdTe. This is possible because CdTe is easily synthesized as a dot with a ZB lattice structure [207].
Recently, we demonstrated the synthesis of high quality CdSe dots with a ZB lattice structure [86] using a procedure based on adding a ligand such as alkyl phosphonic acid (PA) to the tri-octylphosphine (TOP) and the Se solution, prior to its injection into the reaction mixture. This reduces the rate of nucleation and growth and allows the formation of ZB dots. Based on this result, CdSe tetrapods, branched NCs with a ZB core and four W arms were successfully prepared [87]. Their geometric form makes this nanocrystal a good test to the shape effect in the optical and kinetics of CdSe nanoparticles. The synthesis were explained in details in (2.5.4), and in reference [87].
Figure 6.15 shows the TEM pictures of samples taken from the same growth at the middle and towards the end of the synthesis.

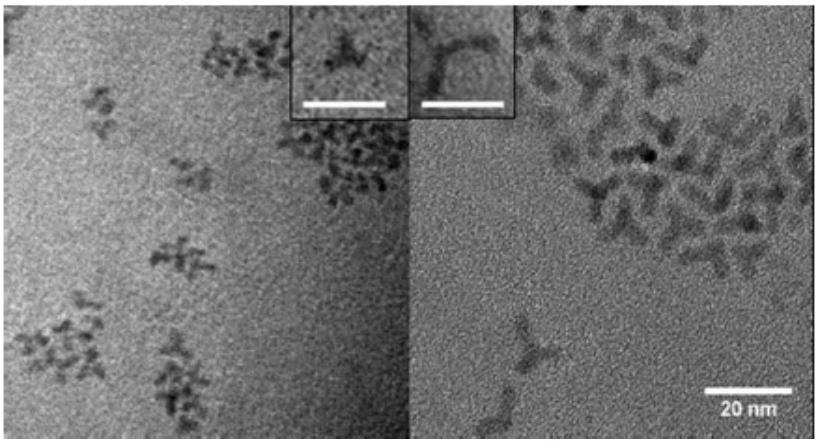

Figure 6.15: TEM pictures of two samples extracted during the growth: (A) after 25 min., (B) after 80 min, corresponding to spectra (iii) and (v) in fig. 2. The scale bar corresponds to 10 nm in the insets.

From Figure 6.15 we find that the arm length increase from 3.0 ± 0.2 nm to 9.0 ± 0.5 nm between the beginning and the end of the growth. Figure 6.16 shows the evolution of the absorption and luminescence spectra during the growth. Note that the absorption spectrum of sample (i), which was recorded right after injection, is similar to that of dots with a ZB structure recently reported [86] and presented in 5.2.1. Indeed, it exhibits the same first-to-second band energy difference, which is larger than in the case of W dots, and is a characteristic spectral feature of CdSe ZB dots [86]. As already mentioned, initiation of the growth with ZB dots is a prerequisite for the synthesis of branched tetrapod NCs [189, 206]. The quantum yield (QY) in all of our CdSe tetrapods samples was of the order of (6-8) %.

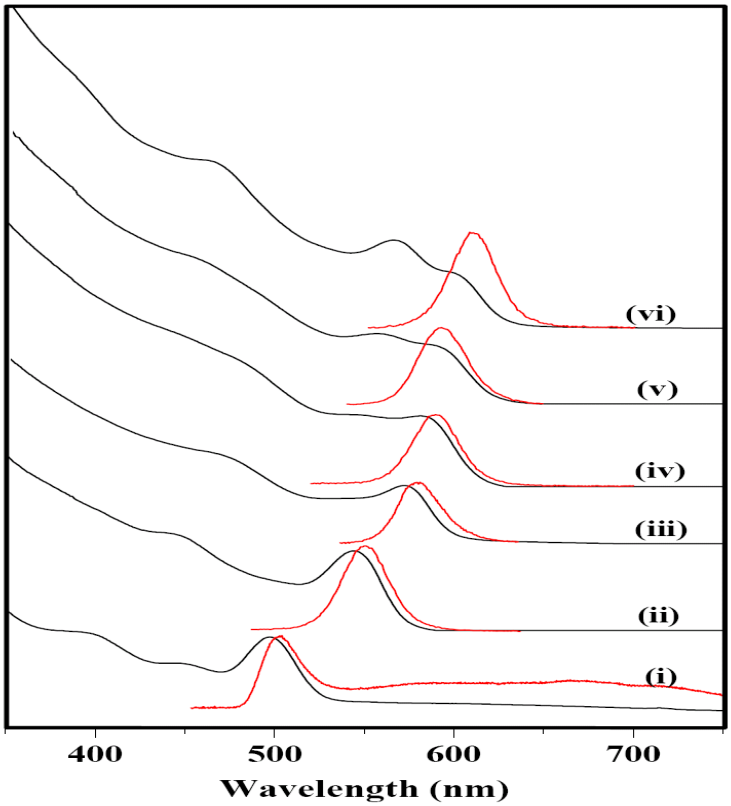

Figure 6.16: Absorption (solid traces) and luminescence (red trace) spectra recorded during the growth. The samples (i-vi) were extracted at the following time intervals: 1 min, 10 min, 25 min, 50 min, 80 min, 2 hours.

The evolution of the absorption spectra reveals that during the growth, the first band shifts to lower energies, and then it slightly stabilizes at a nearly fixed energy (from spectrum iv, onwards). In parallel, the second band increases gradually, eventually becoming more intense than the first band, at the end of the synthesis. Considering that in the course of the synthesis, the arms grow but not the ZB nanodot seeds, we attribute the first band to the absorption by the ZB core of the NC, and the second band is associated to the arms. Figure 6.17 shows the energy splitting between the resolved absorption features in figure 6.16, and the Stokes shift evolution during the growth.

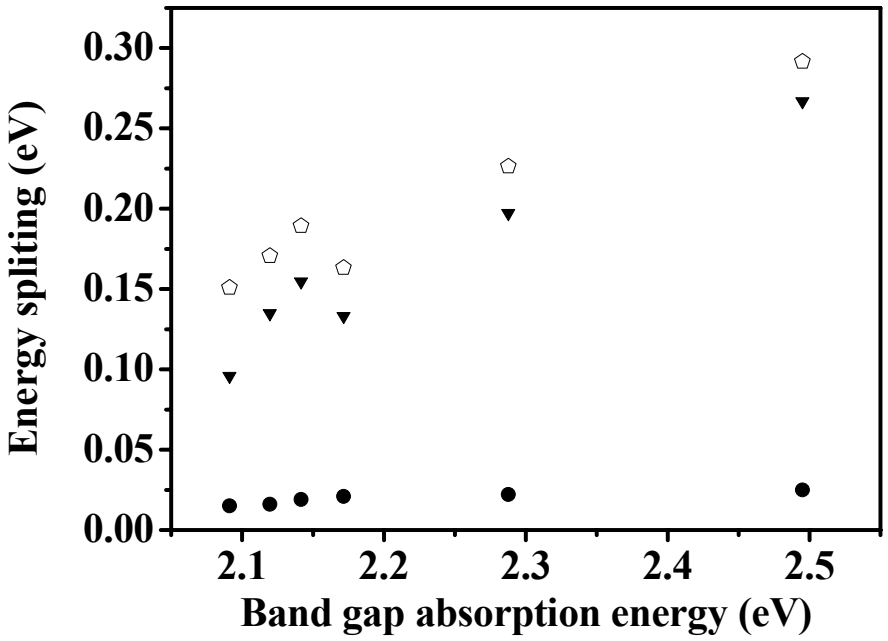

Figure 6.17: First to second absorption band energy splitting (solid triangles), the energy difference between the fluorescence band and the second absorption band energy (hollow diamonds), and Stokes shift (solid circles) as a function of the band gap absorption energy for CdSe tetrapods.

From the above figure, we can resume the following behavior: the Stokes shift is decreased from 25 meV in sample (i) to 16 meV in the biggest tetrapods (vi). From sample (i) to sample (vi), the energy splitting between the first and the second absorption bands decreases from 27 meV to10 meV. This energy splitting showed the same dependence during the CdSe ZB QDs growing (figure 5.3). The energy differences between the higher energy absorption bands are due to the arms and the maximum of the luminescence band (hollow diamonds) presents similar dependence to the splitting between the absorption of the core and the arms bands.
Figure 6.18 shows photoluminescence excitation spectra (PLE) of a large and a small tetrapod recorded at different emission wavelengths and scans the luminescence band. The first two bands are recovered in terms of energy splitting and relative intensities, for the different emission wavelengths used. The energy shift of the PLE spectra is due to the size difference in the inhomogeneous size distribution. Figure 6.18 therefore shows that the first two absorption bands belong to the same entity and are not related to different species. Thus the luminescence spectra (figure 6.16), characterized by a single symmetric band of FWHM in the range of 27-30 nm, reflect a relative homogeneity of the samples in size and shape distribution and shape.

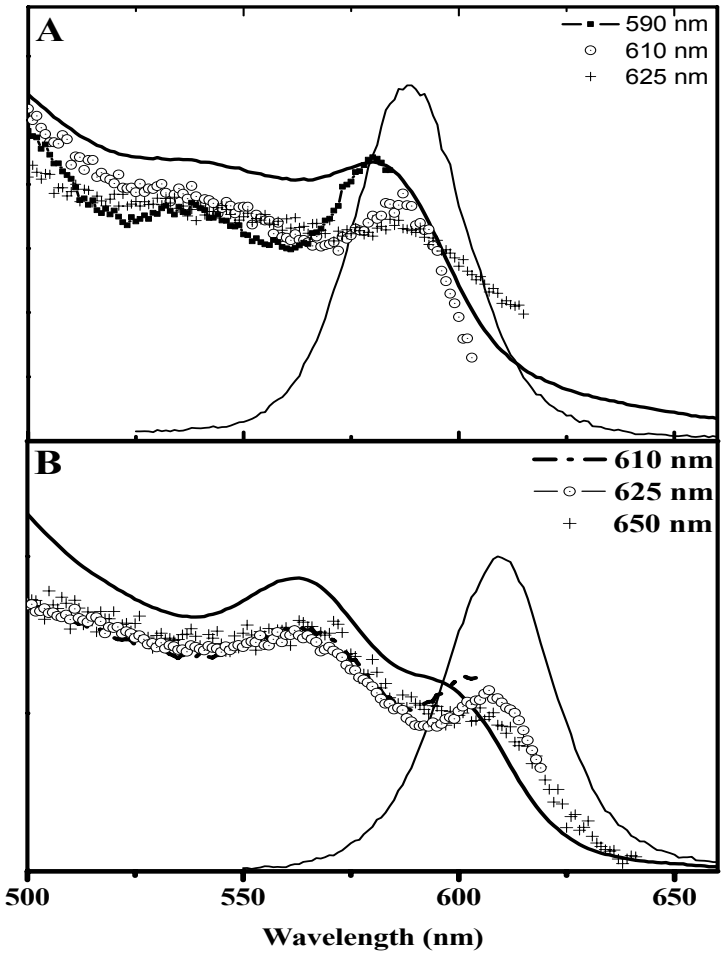

Figure 6.18: Absorption and emission spectra (lines) of tertapods corresponding to A) samples iv and B) sample (vi) in figure 6.16. 1, and their photoluminescence excitation spectra recorded at different emission wavelengths, as shown in the figures.
Nanosecond kinetic CdSe tetrapods.

To present in more details the effect of the tetrapod shape in the relaxation kinetics and in the electronic structure distribution, nanosecond time-resolved studies have been performed as a probe of the previous expected behaviours. The samples we used in this study are these presented above in the previously paragraph (samples iv, v, vi). The samples were studied after similar treatments used in chapters 3, 4, 5. Low power laser excitation (0.1 μJ/cm^2) at 400 nm was used for excitation. The detection was located at the maximum fluorescence band for all samples and temperatures. These CdSe tetrapods nanoparticles were prepared as a solution form (in toluene) for room temperature studies, and in film form for temperature dependence studies. In all studies, the samples concentration was fixed to be 0.1OD at the band gap absorption. Figure 6.19 shows a decay spectrum of a colloidal ensemble of CdSe

tetrapods (sample vi) at room temperature. The kinetics shows more than three order of magnitude of signal to background ratio. This relaxation decay is best fitted with a multi-exponential (four-component) function. The fit values are: τ_1= 2.5± 0.02 ns, τ_2 = 9. ± 0.10 ns, τ_3 = 26.4 ± 4.12 and τ_4 = 79± 10 ns. The amplitudes $\mathbf{A_1}$, $\mathbf{A_2}$, $\mathbf{A_3}$, and $\mathbf{A_4}$ are 0.18, 0.38, 0.37, and 0.07 respectively.

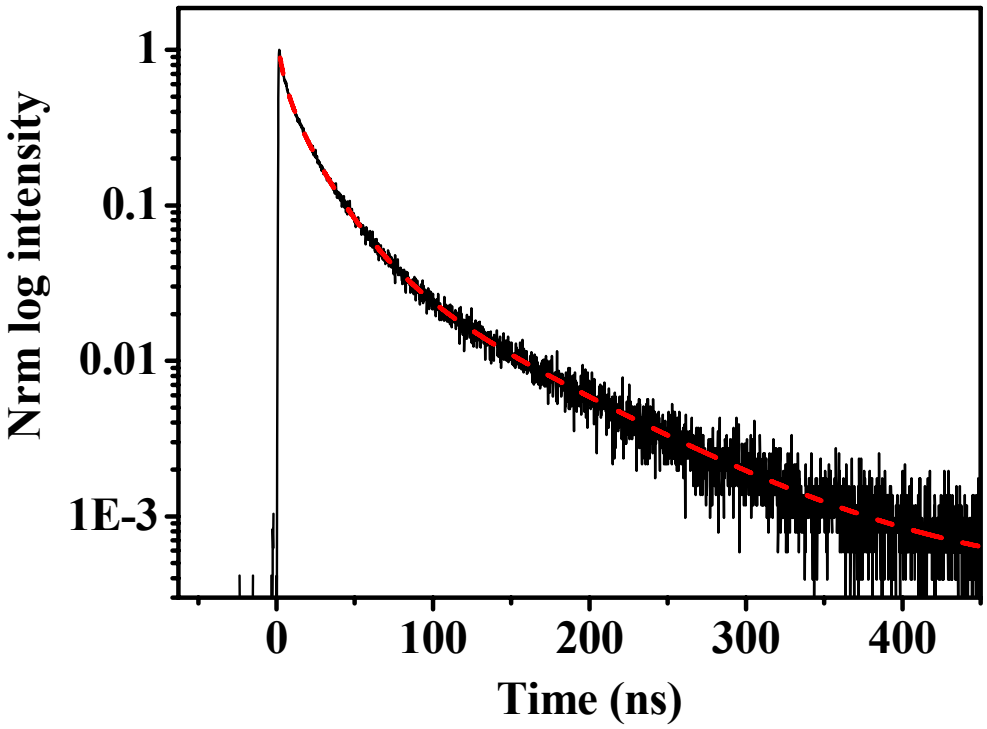

Figure 6.19: Luminescence decay curve of CdSe tetrapods (9.0 nm arm-length) at lower possible excitation power. Four-exponential fit function was used to describe the relaxation behaviour.

Similar to the case of the CdSe NRs shape, the kinetics appears independent of tetrapods size. All tetrapods sizes show identical kinetics with comparable fit values as it shows in figure 6.20.

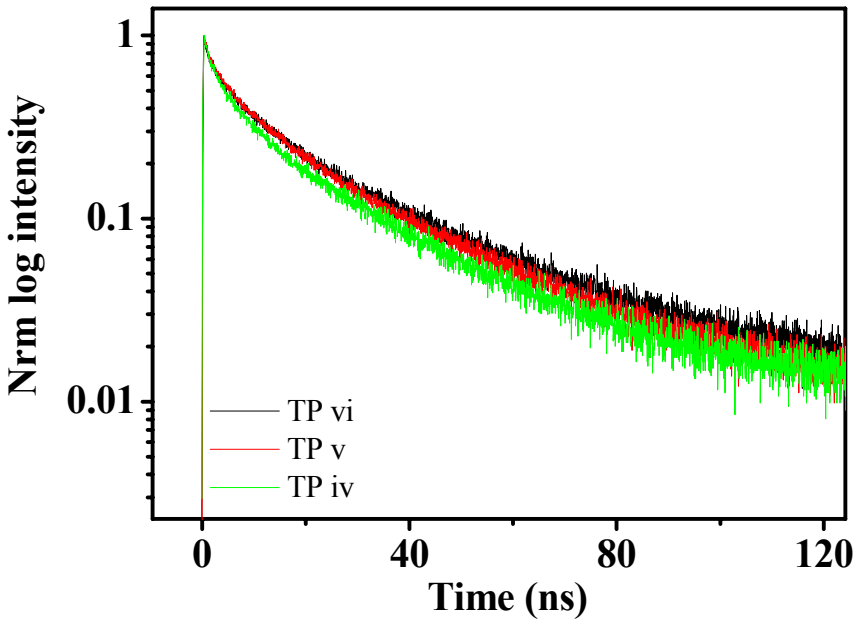

Figure 6.20: Luminescence decay curves of different size CdSe tetrapods.

6.3.2 Temperature dependence of CdSe tetrapods.

The absorption spectrum in CdSe tetrapods has two clear bands with different intensities, and as we shown in the PLE studies, these two band are not related to different species. We attributed the first band to the absorption by the ZB core of the NC, and the second band is associated to the W arms. In this study, we probed the temperature effect on tetrapods samples to see if the high symmetry shape and the different relative size between the core and arms can create any characteristic behaviour. Decreasing the temperature from 300 to ~ 4 K causes optical and kinetics changes in these particles.

The effect of temperature on the absorption spectrum in CdSe tetrapods was studied in this work. The CdSe absorption spectra were measured at room temperature and at 4 K (figure 6.21). From this figure, the samples absorption spectra show blue-shift spectra, and increasing intensity of the bands in each samples. The first absorption band (ZB core) shifts with ~ 24 nm (84 meV) in all samples, while 20 nm (82 meV) is the blue shift in the second absorption band (W arms). The different (in nm) between the two shifts value is due to the energy difference (eV) between the two bands. This study does not resolve any additional features in the absorption spectra due to the low temperature effect. Only the low temperature width of the absorption bands is smaller than the room temperature absorption bands.

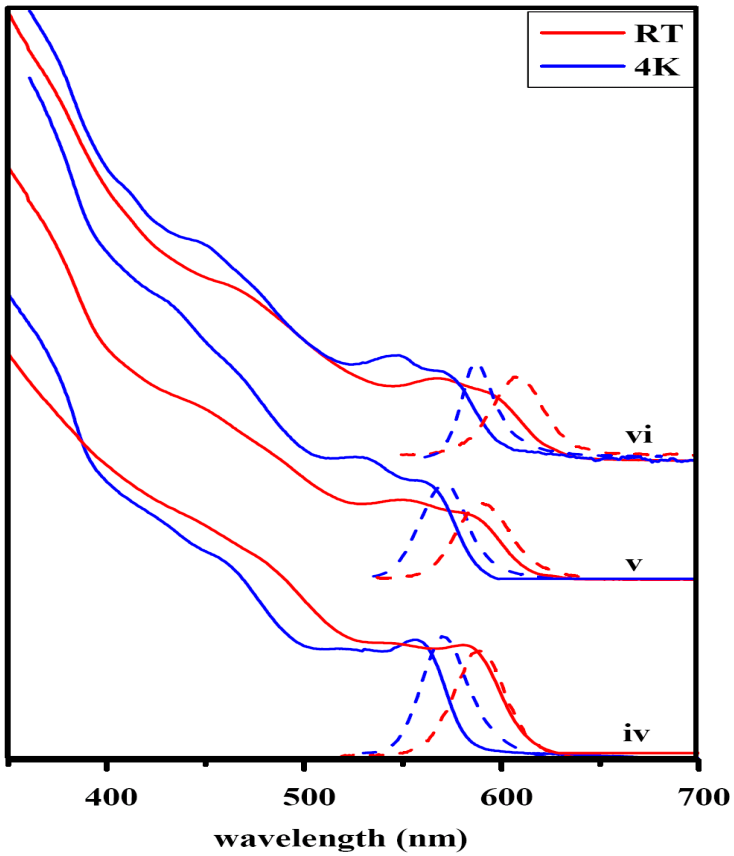

Figure 6.21: Absorption and luminescence spectra of three tetrapods samples at room temperature and at 4K. The dashed line is used for fluorescence bands spectra, while the straight lines were used for absorption spectra.

In the luminescence bands analysis, we observe the same general effects that we reported before for all CdSe shapes and structures (4.3.1, 5.2.4, and 6.2.3I). Figure 6.22A presents an example of all the expected processes in a range of temperature between 300 and 4 K in the biggest tetrapods sample vi. As the CdSe TPs samples are cooled down: (i) A shift of the emission maximum towards higher energy occurs, as we shown in figure 6.22B. (ii) The fluorescence band gets narrower (figure 6.22C). the relative fluorescence intensity increases (figure 6.22D).

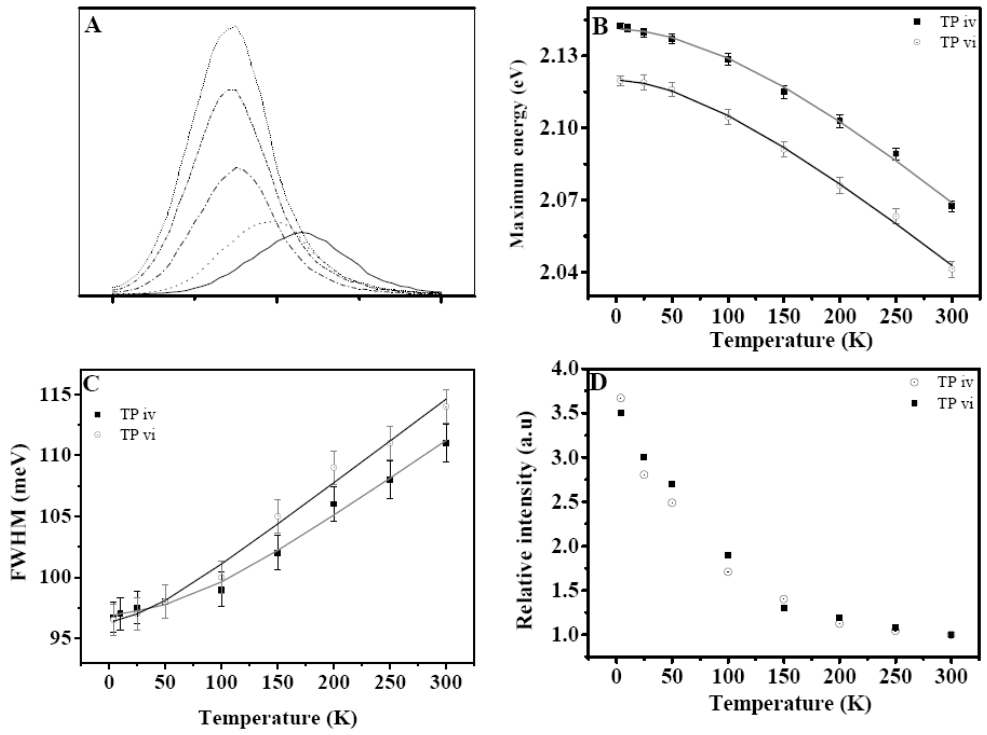

Figure 6.22: Temperature dependence of steady state fluorescence of the TPs CdSe samples (A). (B) Displacement of the maximum fluorescence band in two CdSe TPs (iv, and vi). (C) FWHM of the fluorescence band of the same samples. (D) Relative intensity normalized to 1 at RT. The solid lines are the fit results using the equation 4.1 and 4.2 for B and C (see text) respectively.

The temperature dependent PL resonance peak energy has been fitted to the same empirical expression 4.1 $(E_g(T) = E_g(0) - \alpha T^2/(T+\beta))$ which gives the temperature dependence of the energy gap of bulk semiconductors, and was used before in the case of CdSe QD and NR nanocrystals. Table 6.IX presents the fit values that obtained for iv, and vi TP samples.

Table 6.IX: Fit results of the band-gap temperature dependence in two (iv, vi) CdSe TP samples.

Sample	$E_g(0)$ (eV)	$\alpha \times 10^{-4}$ (meV/K)	β (K)
iv TPs	2.28±0.08	4.1±0.4	188±33
vi TPs	2.12±0.06	4.0±0.3	161±60

The fit parameters show comparable values for the two TP sizes. $\mathbf{E_g(0)}$ values are in the same range of CdSe QDs (table II) and NRs (table 6. VII). α appears in agreement to the bulk value and the other shape of CdSe nanocrystals. β indicates slightly bigger values [132] in the TPs than the other CdSe shapes.

The width of the TPs fluorescence band increases with temperature as the other shapes and structures of CdSe nanoparticles. In order to have a better description of

the phonon scattering processes, involved in the increasing broadening and the effect of shapes, we fitted the experimental data to the same relation (4.2). Which describes the temperature dependence of the broadening in bulk semiconductor ($\Gamma(T) = \Gamma_{inh} + \sigma T + \Gamma_{LO}(e^{E_{LO}/k_B T} - 1)^{-1}$). The fit values of samples iv and vi using the previous expression are shown in table 6.X.

Table 6.X: Fit parameters of the full width at half maximum at different temperatures for two TP samples (iv, vi).

Sample	Γ_{inh} (meV)	σ (μeV/K)	Γ_{LO}(meV)	E_{LO}(meV)
iv CdSe TPs	96±3	30±4	13.5±3.2	25±3
vi CdSe TPs	96±3	50±13	6±1.3	25+2

From the above table, again the fit values indicate to bigger values of exciton-acoustic phonon coupling σ, for the two CdSe TP samples, comparing to bulk value (8 μeV/K). The opposite dependence was found for the exciton-LO-phonon coupling strength Γ_{LO}, where smaller values were measured in CdSe TPs than in bulk (100 meV). E_{LO} have comparable value to the bulk semiconductor one (25 meV).
These results show, in general, similar behaviour to the dots samples (see table 4.II). In the two samples, the acoustic phonon coupling σ is bigger than the bulk. The biggest TP sample vi shows even bigger values than the CdSe QDs. The same dependence was noticed for the LO-phonon coupling strength Γ_{LO} for CdSe QDs and TPs, smaller values than bulk, but smaller for TPs than CdSe QDs (the same table 4. II). E_{LO} appears comparable in the two different shapes. This value in the case of TPs appears different to the case of CdSe NRs as we discussed in the first part of this chapter.
The issue of temperature dependence of the fluorescence intensity appears comparable to the case of other CdSe shapes. From the above figure, the fluorescence intensity was normalized to one at room temperature to shows the magnitude of the relative luminescence intensity increasing during the cooling. The luminescence intensity increases more than three times (for the two CdSe TPs) as the temperature decreases to 4 K (QY in solution was ~ 6 %). There is no specific description on the dependence of the fluorescence intensity, and is due to the CdSe shape.
In conclusion, the temperature dependence of the optical properties of CdSe TPs is dot- like, while it has different trends in the case of rod shape. The relaxation kinetics of the biggest tetrapod sample in the group (vi) used before was detected at different temperatures in polymer film, and shown in figure 6.23.

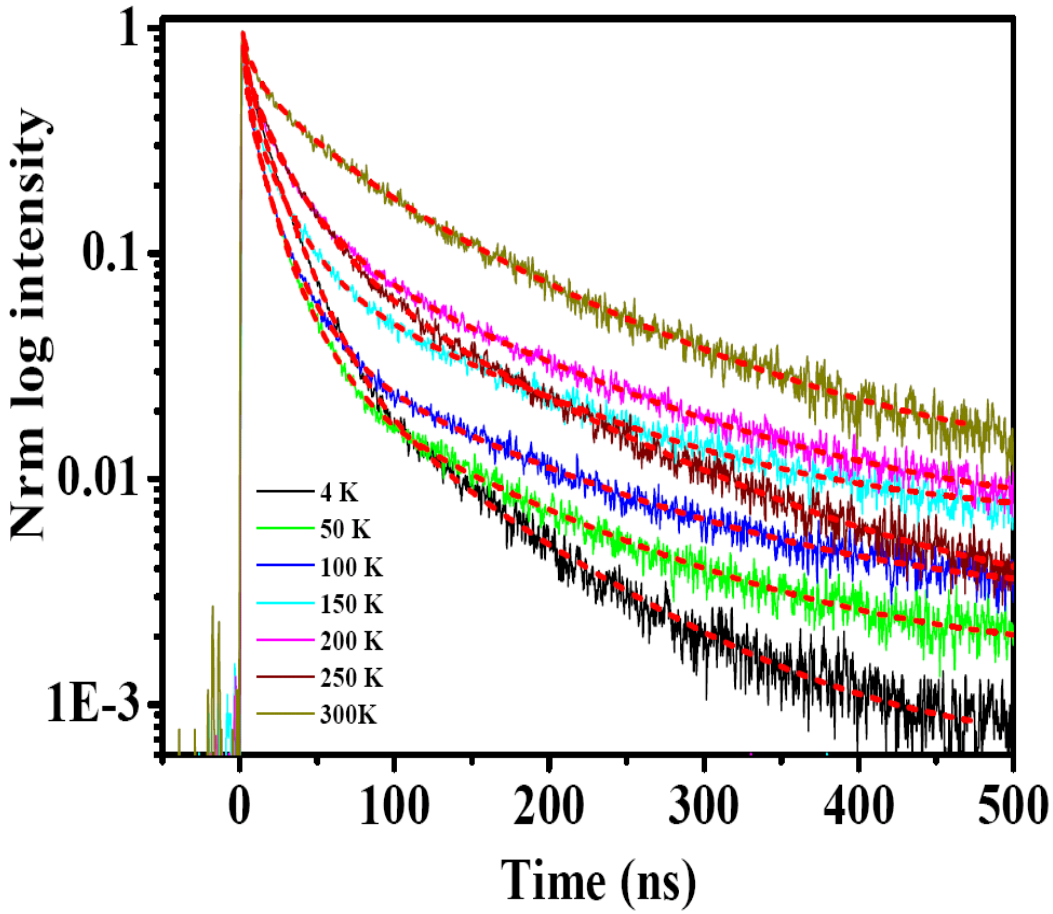

Figure 6.23: Decay curves of CdSe tetrapods (Sample vi ~ 10 nm arm-length) measured at different temperatures. All decays were best fitted with four-exponential function.

The TP sample in figure 6.23 appears more similar to dot-like kinetics than rod in polymer film as a function of its temperature (see figures 4.8A and 4.8B). Faster kinetics at lower temperatures than at room temperature were detected, especially, on the first two magnitudes of the signal. The best fit is obtained by the multi-exponential fit (four-components) for all decay spectra at all temperatures with a fit error of less than 10% for all fit values, reduced χ^2 (~1), and then the best residual between fit and decay curves. The first component lifetime value (τ_1 ~ 1.3 ns) is temperature independent (no differences in its lifetime constant), while its amplitude $\mathbf{A_1}$ increases between 300 and 4 K. The components τ_2 and τ_3 are faster at lower temperatures. $\mathbf{A_2}$ stay in the same range of amplitudes during the temperature decreasing, while $\mathbf{A_3}$ has lower amplitude at 4 K than RT. The long component τ_4 shows a slightly decreasing lifetime value between 300 and about 100 K, and below this temperature, it becomes slower as we decrease the temperature. $\mathbf{A_4}$ is less than 10 % for all cases, with lower values at low temperature than at RT. The fit values at all of the temperature range are shown in figure 6.24A and B.

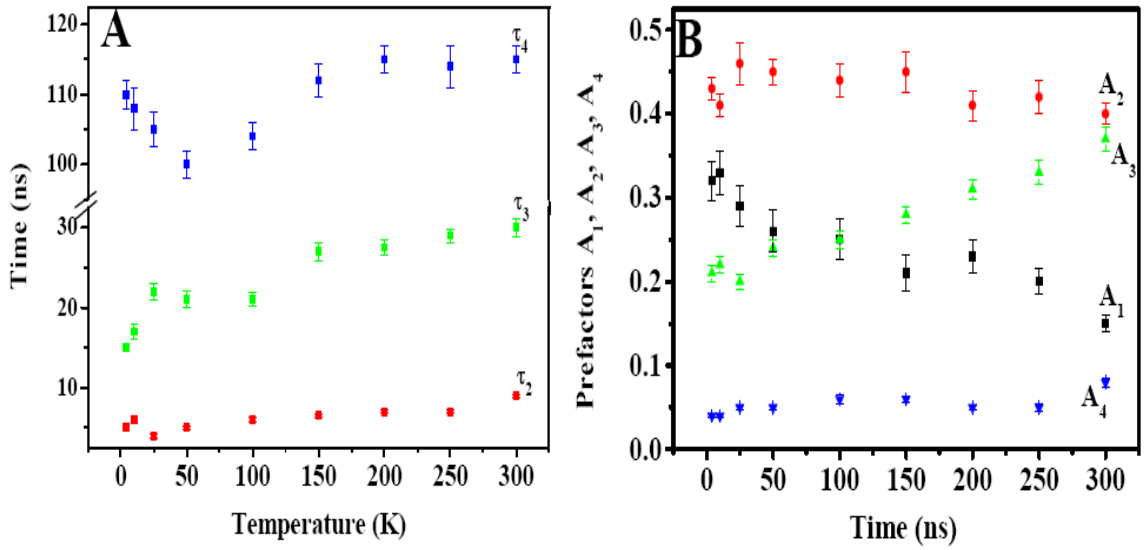

Figure 6.24: The multi-exponential fit parameters at different temperatures. **A)** and **B)** are the lifetime constant of CdSe TPs sample (**vi**) and their prefactors (same color dependence between a and B, except the black square, which indicates to the amplitude of the first component).

We can resume the results on TPs in the following points:

(a) The TEM photos, the absorption spectra evolution (figure 6.16), and the PLE spectra prove the tetrapod shape of the prepared sample and their evolution in size.

(b) After the core growth, a significant and efficient growing in the arms occurs, while the increase in the dot core size is small (figure 6.16, 6.17).

(c) The relaxation decay appears similar to the other CdSe shapes, with similar fit function and comparable lifetime constants and prefactors.

(d) The RT relaxation decay is independent on the effect of the size of the TPs (figure 6.20).

(e) The effect of temperature on the optical properties appears more similar to the dot shape behaviour, with the same fit functions for the cases of fluorescence band shifts and for the bandwidth decreasing of the fluorescence band as a function of sample temperature.

(f) The temperature dependence of the CdSe TPs dynamics in the polymer film is more similar to dot-like dependence, with faster decay at low temperatures than at RT as we were shown in figure 4.8 A and B .

6.3.3 Discussion and conclusions:

The TEM photos presented in figure 6.15 clearly demonstrate the tetrapods form of the CdSe nanocrystals prepared by the method presented in the experimental part (2.5.4). These TEM photos show the different size arms during the growth.

The evolution of the second band in the absorption spectra (figure 6.16) is similar to the NRs absorption band gap red shifts during the length growing (figure 6.1- group

I), this behaviour indicates to increasing on the arms-length more than arms-diameter. The ZB core absorption band increases from 581 nm in the first well shaped tetrapode iv to 592 nm in longest tetrapods arms sample vi in figure 6.16. This core absorption energy shift indicates to comparable size CdSe core (from 4.0 to 4.1 nm). The energy splitting between the two absorption bands (core and arms) presented in figure 6.17 (solid triangle) prove this tendency of arms growing, fine reconstruction in core. These two dependences of the core and the arms point to two growing's (core and arms) in the same time. Significant and efficient growing in arms, while fine increasing in the dot core size.

The central tetrahedron is joint by four W structure nanorods at the $(111), (\bar{1}\bar{1}1), (1\bar{1}\bar{1})$, and $(\bar{1}1\bar{1})$ surfaces [192]. The relative intensity of the absorption bands of the TP samples (vi, v, and vi samples) allows the assignment to contributions of different crystal partst (core and arms) in the absorption spectra. Bigger tetrapods show longer arms absorption intensity.

The Stokes shift (figure 6.17) of TPs at room temperature show nearly identical values (16 meV) as the arms grow. This behaviour is due to the same reasons as discussed above about the significant growing of the rod arms while the core dot size stays unchanged. This behaviour is very different to the case of rods, the Stokes shift increases for longer rods, while in CdSe TPs, this parameter is independent on the TPs size.

The complexity of the TP geometry makes its behaviour distinguished as we noticed. The temperature dependence of its optical properties (maximum band shift and the bandwidth of the fluorescence band) is closer to the dot shape behaviour than the rod shape (figure 6.22, 4.6, and 4.7). This dot-like behaviour also presents a description for the case of dynamics, where these particles are dot-like for the temperature dependence of their kinetics in the polymer film (figures 4.8A, 4.8B).

To explain the dot-like dependence of the TPs, we compared our results with the theoretical calculations presented by Pang *et al* [190] and Li *et al* [192]. The two works show the excited and ground state calculations for the CdSe TPs. In the two works, the electronic states are similar to the dot electronic states energy, especially for the first excited state [190]. Moreover, the lowest electronic state is localised in the central region of tetrapod. Figure 6.25 A, B shows the result of the previous calculations on the first excited state energy, and the wave functions of the electron and hole in the TPs nanoparticles.

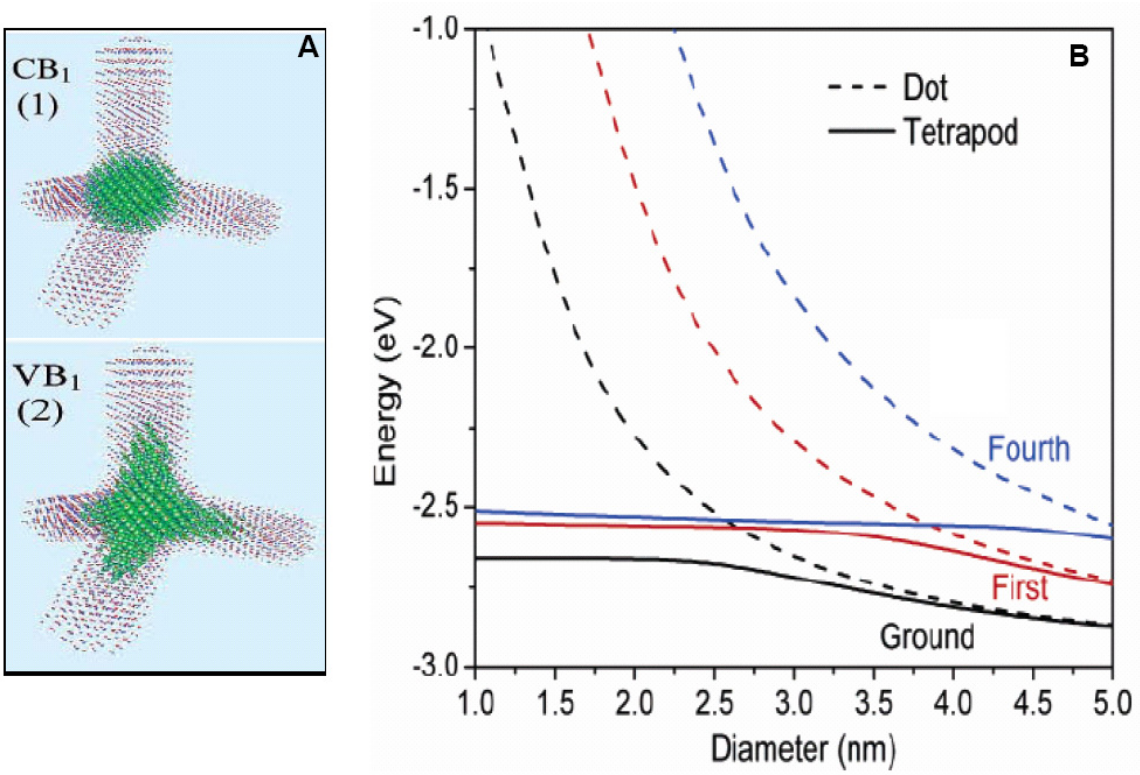

Figure 6.25: A) Wave function charge densities of CdSe tetrapods nanocrystal, with core of 3.9 nm as diameter. CB_1 and VB_1 indicate to the conduction-band and valence-band states (reference [192]). B) Eigenenergy of the CdSe dot states (dashed line) and comparable core diameter of CdSe tetrapods states (solid line) (reference [190]).

From the figure above (6.25A), the calculations (same length and width for the NRs) indicate the localization of the lowest electronic state in the central tetrahedron, while the first hole state enters the arms of the particle. This localization shows ideal overlap between the electron and hole wave functions. Dot-like behavior was expected with this localization of the two wave functions. The other work [190] as it shows in figure 6.25B indicate to the dot-like ground and excited states as a function of the dot diameter [190]. As the dot core diameter increases, the eigenenergy of the tetrapods states becomes closer and closer to that of the dot of the same diameter as the wave function distribution within the tetrapods concentrations more and more inside the core for large enough core size and appears dot-like states [190]. For that the optical properties dependence as dot-like is due to the previous explanation. Note that the two previous works consider that the four arms are ideal (length and diameter) to simplify the problem. The effect of the arms appear in the forth excited state [190]. Below this state, the effect of the rod arms can be ignored. Our temperature dependent studies for the relaxation process show dot-like fine structure for the lower excited kinetics (figure 6. 23).

Concerning the optical properties as a function of temperature (figure 6.22), we can point out that:
(i) The blue shift of the steady state fluorescence at lower temperature, for all CdSe shapes and structures, has the same tendency. The fit values of the CdSe TPs are comparable to the parameters fixed before in chapter 4, 5, and in the first part of this chapter for rod samples. The value of the Debye temperature of CdSe TPs (table 6.IX) is bigger than the other CdSe shapes (table 4.II, 5.V, and 6.VI) and structures (table 5.V).

(ii) The effect of the temperature on the bandwidth of the steady state fluorescence band (figure 6.22C) was fitted by expression 4.2, with the same fit values as for QDs of dot-shape. The biggest TPs sample (Sample vi) shows about two times bigger value of σ (coupling to acoustic phonon) than for CdSe QDs. The presence of the additional dephasing process that appears in the case of TP samples is induced, in addition to the confinement effect [129], by the surface defects or trap states.The further effect of the surface defects and trap states processes is adding important contribution to the homogeneous linewidth in the very small size regime [149]. Again, as we discussed for the case of CdSe QDs, the coupling between the TPs and the matrix [150] adds another contribution to the increased homogeneous broadening [150]. The other fit value, Γ_{LO} ~ (13-6) meV in samples iv and vi, shows smaller values with respect to the bulk value [151] (~ 100 meV), which was also the case for QDs shape (see table 4.II). This reduction in the TPs values indicate a strongly reduced LO phonon coupling for the case of TPs, compared to QDs, whereas the coupling to acoustic phonons is increased (σ). Other effects might act and explain the different dependence in TPs shape. (**i**) the different quantum confinement of the dot core and the NRs arms that affects the phonon energy [135]. (**ii**) the mechanical boundary conditions [152] (electron-hole interaction) which will be different in big system as TPs than the QDs [152], where in spherical dots it only allows contributions from phonons states with angular momentum $l_p = 0$ and $l_p = 1$, and the surface phonons [153]. E_{LO} is also consistent with the values of LO phonon energy in bulk. (**iii**) The low quantum yield in CdSe TPs at room temperature (6-8 %), compared to the other CdSe shapes (~ 35 % for dots, and 8 % in rods), explains the increase of the relative fluorescence intensity in TPs samples for ~4 times as the temperature decreases to 4 K (see figure 6.22D). The other shapes show about 2-fold increase in dot (figure 4.6) and 3 fold in rod (6.7) nanocrystals.

The lifetime decay, as we presented in figure 6.19 at room temperature, shows that the kinetics (lifetime components ($\boldsymbol{\tau_1}$, $\boldsymbol{\tau_2}$, $\boldsymbol{\tau_3}$, $\boldsymbol{\tau_4}$) and the amplitudes ($\mathbf{A_1}$, $\mathbf{A_2}$, $\mathbf{A_3}$, $\mathbf{A_4}$) are comparable to these presented in the case of CdSe QDs and NRs shapes. The identical value for all CdSe tetrapods sizes (figure 6.20) indicates the complexity of this kinetics that does not present mainly the contribution of the confinement regime. This behaviour does not surprise because of eigenenergy scheme in figure 6.25, where the wave function of the electron (conduction band) and the hole

(valence band) show good overlap in the dot core. Thus, the expected relaxation process behaviour will be similar to that in dot or in rod at room temperature. Note that the previous calculations present an ideal case for TPs sample with identical rods (length and diameter), while the real case of ensemble of tetrapods supposes different lengths and widths between each particle arms and between all the nanocrystals that form this ensemble of tetrapods. Deviations from the ideal case will decrease the overlap between the electron and hole wave function. This real inhomogeneity between the components of the TP parts still presents dot-like relaxation kinetics in polymer film at lower temperatures. However, the nature of recombination processes in CdSe nanoparticles is a complex issue, even in simpler system like CdSe QDs, as we presented previously in chapter 3 and 4. Thus, for the case of CdSe tetrapod nanoparticles, it requires much further investigations that simulate further experimental and theoretical works to clarify the real interpretation of its relaxation processes.

Chapter 7

Conclusions

This thesis presents a comprehensive study of the spectroscopic properties of CdSe nanocrystals with special focus on understanding how size, shape, and structure influence fundamental properties like the optical spectra and exciton kinetics. As a model system, we have chosen chemically synthesized CdSe-based nanocrystals, because their properties can very selectively be tuned; they can be prepared with wurtzite and zinc blende lattice structure and in the form of dots, rods, and tetrapods.

In the first part of the work, the excited state dynamics of spherical CdSe quantum dots with wurtzite lattice structure was explored using time resolving fluorescence spectroscopy with a wide temporal window (up to 1 μs), an excellent signal to background ratio (four orders of magnitude), and with a time resolution of 100-400 ps. From our systematic study of the fluorescence spectra and kinetics as a function of quantum dot size, laser excitation power, detection energy, and temperature, we found that the relaxation process is best described by a multi-exponential decay with four discrete lifetimes in the range from less than 2 ns up to several hundreds of ns. These lifetime values were resolved in all sample environments, temperatures, and different treatments. For the first time, a long component with an amplitude of less than 10% was resolved and investigated in detail as a function of the parameters mentioned above. It was shown that trap states are the most probable origin of this component. The other components were assigned to radiative electron-hole recombination (~20 ns) and to the lifetime of charged excitons (trions). The origin of the fastest component was assigned to fast trapping processes. However, the nature of these traps is not completely clear and seems not to be related to surface states.
At higher excitation power, multi-exciton effects with sub ns time decays at the low energy side of the fluorescence spectrum were resolved. Also the type of capping and the environment has strong effects on the kinetic behaviour of the samples at both, low and high temperatures.

In the second part of the work, we investigated CdSe quantum dots with two different lattice structures (wurtzitre and zinc blende), which were expected to exhibit different optical properties and kinetics, due to changes in the exciton fine structure of the zero-dimensional quantum dots. Both low- and high-resolution luminescence as well as excitation spectra and time-resolved spectroscopy at room temperature and cryogenic temperatures were used to characterise the properties of the ZB CdSe nanoparticles. The spectroscopy and the kinetics of CdSe quantum dots with cubic lattice structure revealed similar properties as CdSe quantum dots with hexagonal lattice structure. Thus we conclude that, in CdSe quantum dots with cubic or hexagonal lattice structure, the band edge fine structure is identical and the effect of crystal structure is not the most relevant parameter for the kinetic behavior. The crystal field seems to be much less important than other effects, like e.g. influences from imperfection, shape asymmetries, and exchange interaction.

The third part of this work dealt with influences from different nanocrystal shapes and revealed pronounced spectral and kinetic changes. We have developed methods to synthesise elongated CdSe nanorods as well as branched tetrapods, which consist of a core with zinc blende structure and four-nanorod arms of wurtzite structure.
The spectroscopic characterisation of the CdSe tetrapods allowed an assignment of the two lowest bands in the absorption spectrum to states that are localized at the core and the arms, respectively. Furthermore, we presented a detailed analysis of the temperature dependent luminescence spectra from CdSe nanocrystals with the three different shapes. Our results show a totally different behaviour in the temperature dependence of the photoluminescence bandwidth of nanorods, which indicates a different underlying broadening mechanism, that we tentatively assigned to thermal charging and surface-charge mobility in the nanorods. The tetrapods behave qualitatively like the NDs, indicative of a core-centered lowest exciton state.
The fluorescence decays confirm this result. Tetrapods and quantum dots behave qualitatively similar, while nanorods are very different, showing a faster decay at low temperatures. This can be understood because of the band edge exciton fine structure in nanorod samples, where the lowest state becomes allowed as the spherical symmetry is broken.

Acknowledgements

It is a great relief to see myself going through the graduate student life in Lausanne. The past five years have been full of frustrations, struggles, and excitements. I feel very fortunate to have Prof. M. Chergui as my advisor. I would like to express my gratitude to him, who accepted me in the group in September 2001. Majed has been a constant and passionate scientific guide. His patience and trust have been very important for me to develop my own thoughts, and his attitude towards science and his open-mindedness have greatly influenced my perception about scientific research.

This thesis is the result of a collective effort of many people that collaborated directly with me or prepared the necessary groundwork in the past. Without Dr. Andreas Tortschanoff my days in the lab would have been different, his help with laser systems and electronics was essential. I am grateful to him for his daily input, support, motivation, sharing of his experience, and helping me even with English.
Dr. Frank van Mourik who led me to a broader understanding with his undergraduate class on ultra-fast phenomena, and to his great helping in the laboratory.
In order to produce samples I have investigated, I relied on Dr. Mona Mohammed and Dino Tonti. I wont to thank them for their chemical synthesis, with different shapes and structures of CdSe nanoparticles, and for the help with transmission electron microscopy and X-ray diffraction measurements.
The work described in this thesis would not have been possible without the help of the people in the electronics and mechanic-work shops, and the informatics technical staff. Especially, Michel Kessous has been very helpful during all of my thesis work.

I would like to thank Dr. Mohamad Hammoud and Dr. Ahmad Hayder for their advices and helping. And Damascus University for their financial support.

I am very grateful to my parents, my brothers for their support. I thank my love (my wife), Claire for her encouragement over the last six years of ups and downs in life. Our twines Kaiser-Cesar and Sama-Ciel were born in 10-02-2004. I am so lucky to have them in my life. I wouldn't have gone this far without them.

..

Curriculum vita

Name :	Awos Alsalman
Date/place of birth:	25.03.1973 Damascus
Nationality:	Syrian
Address:	Laboratoire de Spectroscopie Ultrarapide ISIC – FSB Swiss Federal Institute of Technology Lausanne BSP, CH- 1015 Lausanne Tel: 0041-21-693 0452 Fax: 0041-21-693 0422 Email: awos.alsalman@epfl.ch

Education

2003-2007	Thesis on "Spectroscopy and kinetic studies of electron-hole recombination in CdSe nanoparticles: effect of size shape, and lattice structure" under the supervision of Prof. M. Chergui in the group of prof. M. Ghergui.
2002-2003	Equivalence of the Syrian diploma, University of Lausanne
1996-2001	Assistant for an assistantship, Faculty of Mechanical and Electrical Engineering, University of Damascus
1990-1995	Physics studies, University of Damascus
1990	High school diploma, Gymnasium high school, Damascus, Syria

Teaching and working experience

2004-2007	Teaching assistant in laboratory works for students in the second year of physics studies, EPFL
2003	Teaching assistant for the 1st year laboratory for medicine and forensic science students
1996-2001	Assistant for an assistantship, Faculty of Mechanical and Electrical Engineering, University of Damascus

..

Publications Appl. Phys. Lett. **90**, 093104 (2007)

M. Mohamed,, D. Tonti, A. Al Salman, A. Chemseddine M. Chergui "Synthesis of Size-Controlled Zinc-Blende CdSe Nanocrystals" *Journal of Physical chemistry B*, **109**, 10533-10537 (2005)

M. Mohamed,, D. Tonti, A. Al Salman, M. Chergui " Chemical Synthesis and Optical Properties of Size –Selected CdSe Tetrapod-Shaped Nanocrystals" *European Journal of Chemical Physics and Physical Chemistry*, **6**, 2505-2507 (2005)

A. Tortschanoff, A. Al Salman, D. Tonti, M. B. Mohamed, G. van der Zwan, F. van Mourik, and M. Chergui " Femtosecond polarization relaxation in CdSe nanocrystals" 2006: Proc .Intern. conf. Semicond. Phys (ICPS 2006), Vienna, Austria, July, Accepted and to be published (2007)

A. Al Salman, A. Tortschanoff, M. B. Mohamed, D. Tonti, F. van Mourik, M. Chergui "Temperature effects on the spectral properties of colloidal CdSe quantum dots, nanorods, and tetrapods" *Applied physics letters*, 90, 093104-093107 (2007)

A. Al Salman, A. Tortschanoff, M. Mohamed, D. Tonti, M. Chergui "Size- and temperature-dependence of nanosecond exciton recombination dynamics in colloidal ensemble of CdSe nanocrystals" (To be Submitted)

Invited Seminars

A. Al Salman "Development of a Time-resolved SNOM/FRET set-up" Faculty of Mechanical and Electrical Engineering, University of Damascus (Syria), June 2004

A. Al Salman "Nanosecond electron-hole recombination in CdSe Nanocrystals" Group of electrochemical engineering GGEC, Institute des sciences et ingénierie chimiques, EPFL, Lausanne (Switzerland), December 2006

A. Al Salman "Nanosecond electron-hole recombination in CdSe Nanocrystals, different shapes and structures" Faculty of Mechanical and Electrical Engineering, University of Damascus (Syria), January 2007

Scientific meetings, workshops and schools

- Workshop of Ultrafast Science with X-rays and Electrons April 9-12, 2003- Montreux, Switzerland

- Symposium 20 years of nano-optics, Basel, April 6, 2004.

- Workshop of NCCR, EPFL June 17-18, 2004 "Fluorescence Resonance Energy Transfer Scanning Near-field Optical Microscopy: from idea to

applications" **Poster** "Nanoprobes for high resolution near-field spectroscopy"

- SPS Meeting 2004 in Neuchâtel, March 3-4, 2004.
  Poster "Development of a Time-resolved SNOM/FRET Set-up"
- Summerschool on Semiconductor Quantum Dots: Physics and Devices, Monte Verità (Ascona), September 5-10/ 2004.
  Poster "Time-resolved Studies of CdSe QDs Fluorescence"
- EPFL- Photonic day. 21 Septembre 2005, and 24 Novembers 2006
  Poster "Different Shapes and Lattice Structures of CdSe Nanoparticles", "Spectroscopic aND Kinetic Studies of CdSe Nanoparticles, Different Shapes, and Structures"
- Summer School on Ultrafast Reaction Dynamics and Applications Algarve, Portugal, June 2006.
  Poster "Time-resolved Fluorescence Studies of CdSe nanoparticles, Different Shapes, and Structure" (**Poster Prize**)
- The International Conference on the Physics of Semiconductors (ICPS) 24-28 July 2006.
  Poster "Spectroscopic and Kinetic Studies of CdSe Nanoparticles, Different Shapes, and Structures"

..

Appendix I

Lab View program
used to control the time-gated fluorescence measurement.

```
;     SPC400 initialization file

;    SPC parameters have to be included in .ini file only when parameter
;       value is different from default.
;    only baseadr in spc_base section  is required
;    other parameters can have default values
;    the file
[spc_base]

baseadr=  0x300    ;base I/O address   (0 ... 0x3E0,default 0x380)
simulation = 0     ; 0 - hardware mode(default) ,
                   ; >0 - simulation mode (see spc_def.h for possible values)
pci_card_no= 0     ; number of module on PCI bus if PCI version of SPC module
                   ;   0 - 3, default -1 ( ISA module)

[spc_module]   ; SPC hardware parameters

cfd_limit_low= -10.84  ; for SPCx3x -500 .. -20mV ,for SPCx0x 5 .. 80mV
                   ; default 5mV
cfd_limit_high= 00.0  ; 5 ..80 mV, default 80 mV , not for SPC130
cfd_zc_level= -3.78     ; for SPCx3x -96 .. 96mV ,for SPCx0x -10 .. 10mV
                   ; default 0mV
cfd_holdoff= -5.0      ; for SPCx0x 5 .. 20 ns , default 5ns
                   ; for SPCx3x (130,230) doesn't exist
sync_zc_level=   0.0  ; for SPCx3x -96 .. 96mV ,for SPCx0x -10 .. 10mV
                   ; default 0mV
sync_freq_div= 1      ; for SPC130(230) 1,2,4
                   ; for other SPC modules 1,2,4,8,16 , default 4
sync_holdoff= 11.21     ; 4 .. 16 ns , default 4 ns
                   ; for SPC130(230) doesn't exist
sync_threshold= -15.8  ; for SPCx3x -500 .. -20mV ,default -20 mV
                   ; for SPCx0x doesn't exist

tac_range= 250   ; 50 .. 2000 ns , default 50 ns
tac_gain= 1           ; 1 .. 15 ,default 1
tac_offset=0.0        ; 0 .. 100% ,default 0%
tac_limit_low=  0.0   ; 0 .. 100% ,default 10%
tac_limit_high=  99.0 ; 0 .. 100% ,default 80%
```

..

```
adc_resolution= 12    ; for SPC300(330) fixed to 10 or 12
                      ; for SPC401(431) fixed to 12
                      ; for SPC402(432) fixed to 8
                      ; for other SPC modules  6,8,10,12 bits, default 10
ext_latch_delay= 0    ; 0 ..255 , default 0
                      ; for SPC130(230) doesn't exist

collect_time= 10      ; for SPC300(330) 0.01   .. 100000s
                      ; for other SPC modules 0.0001 .. 100000s , default 0.01s

display_time= 1.0     ; for SPC300(330) 0.01   .. 100000s , default 1.0s
                      ; for other SPC modules display timer doesn't exist
repeat_time=  10.0    ; for SPC300(330) 0.01   .. 100000s
                      ; for other SPC modules 0.0001 .. 100000s , default 10.0s
stop_on_time= 1       ; 0,1 , default 1
stop_on_ovfl= 0       ; 0,1 , default 1
dither_range= 256     ; for SPC300(330) 0,32,64,128,256 ,default 0
                      ; for other SPC modules subsequent values have
                      ;       different meaning  0, 1/64, 1/32, 1/16, 1/8
count_incr= 1         ; 1 .. 255 , default 1

mem_bank= 0           ; for SPC400(130,230,430,600,630) 0 , 1 , default 0
                      ; for other SPC modules always 0
dead_time_comp= 1     ; for SPC300(330) always 1
                      ; for other SPC modules 0 , 1 , default 1
scan_control= 0       ; for SPC505(535,506,536) , default 0xf000
                      ;   16-bit hex value to control scanning in SPC505(535)
                      ;    or routing in SPC506(536)
                      ;   bits are defined in spc_def.h file
                      ; for other SPC modules always 0
routing_mode= 0       ; for SPC230 0 , 1 , default 0
                      ; for other SPC modules always 0
tac_enable_hold= 50.0 ; for SPC230 10.0 .. 265.0 ns, default 50.0 ns
                      ; for other SPC modules always 0
mode= 0               ; for SPC7xx      , default 0
                      ;   0 - normal operation (routing in), 1 -  Scan In,
                      ;   2 - block address out, 3 - Scan Out
                      ; for SPC6xx      , default 0
                      ;   0 - normal operation (routing in),
                      ;   2 - FIFO mode 48 bits, 3 - FIFO mode 32 bits
                      ; for SPC130      , default 0
                      ;   0 - normal operation (routing in),
```

```
                ;   2 - FIFO mode
                ; for other SPC modules not used
scan_size_x=1         ; for SPC7xx modules in scanning modes 1 .. 65536, default 1
scan_size_y=1         ; for SPC7xx modules in scanning modes 1 .. 65536, default 1
scan_rout_x=1         ; for SPC7xx modules in scanning modes 1 .. 128, default 1
scan_rout_y=1         ; for SPC7xx modules in scanning modes 1 .. 128, default 1
                ; INT(log2(scan_size_x)) + INT(log2(scan_size_y)) +
                ; INT(log2(scan_rout_x)) + INT(log2(scan_rout_y)) <=
                ;                   max number of scanning bits
                ; max number of scanning bits depends on current adc_resolution:
                ;       10                  -           12
                ;       12                  -           10
                ;       14                  -           8
                ;       16                  -           6
scan_polarity=0       ; for SPC7xx modules in scanning modes, default 0
                ; bit 0 - polarity of HSYNC, bit 1 - polarity of VSYNC,
                ; bit 2 - pixel clock polarity
                ; bit = 0 - falling edge(active low)
                ; bit = 1 - rising  edge(active high)
scan_flyback=0        ; for SPC7xx modules in Scan Out mode, default 0
                ; bits 7-0  Flyback X in number of pixels
                ; bits 15-8 Flyback Y in number of lines
scan_borders=0        ; for SPC7xx modules in Scan In mode, default 0
                ; bits 7-0  Upper boarder, bits 15-8 Left boarder
pixel_time= 200e-9    ; pixel time in sec for SPC7xx modules in Scan In mode,
                ;  50e-9 .. 1.0 , default 200e-9
pixel_clock= 0        ; source of pixel clock for SPC7xx modules in Scan In mode
                ;  0 - internal, 1 - external, default 0
line_compression= 1     ; line compression factor for SPC7xx modules in Scan In
mode,
                ;  1,2,4,8,16,32,64,128, default 1
trigger = 0           ;  external trigger condition for SPC6xx,7xx,130 modules
                ;       none(0)(default),active low(1),active high(2)
ext_pixclk_div= 1     ; divider of external pixel clock for SPC7xx modules
                ;   in Scan In mode  1 .. 0x3ff, default 1
rate_count_time= 1.0  ; rate counting time in sec  default 1.0 sec
                ;       for SPC130 can be : 1.0s, 250ms, 100ms, 50ms
macro_time_clk= 0     ; macro time clock definition for SPC130 in FIFO mode
                ;  0 - 50ns (default), 1 - SYNC freq., 2 - 1/2 SYNC freq.,
                ;  3 - 1/4 SYNC freq., 4 - 1/8 SYNC freq.
add_select= 0         ; selects ADD signal source: 0 - internal (ADD only) (default),
              ;                   1 – external
```

..

Appendix II

Interface of the Lab View program
used to convert the time decay measurements to spectral form.

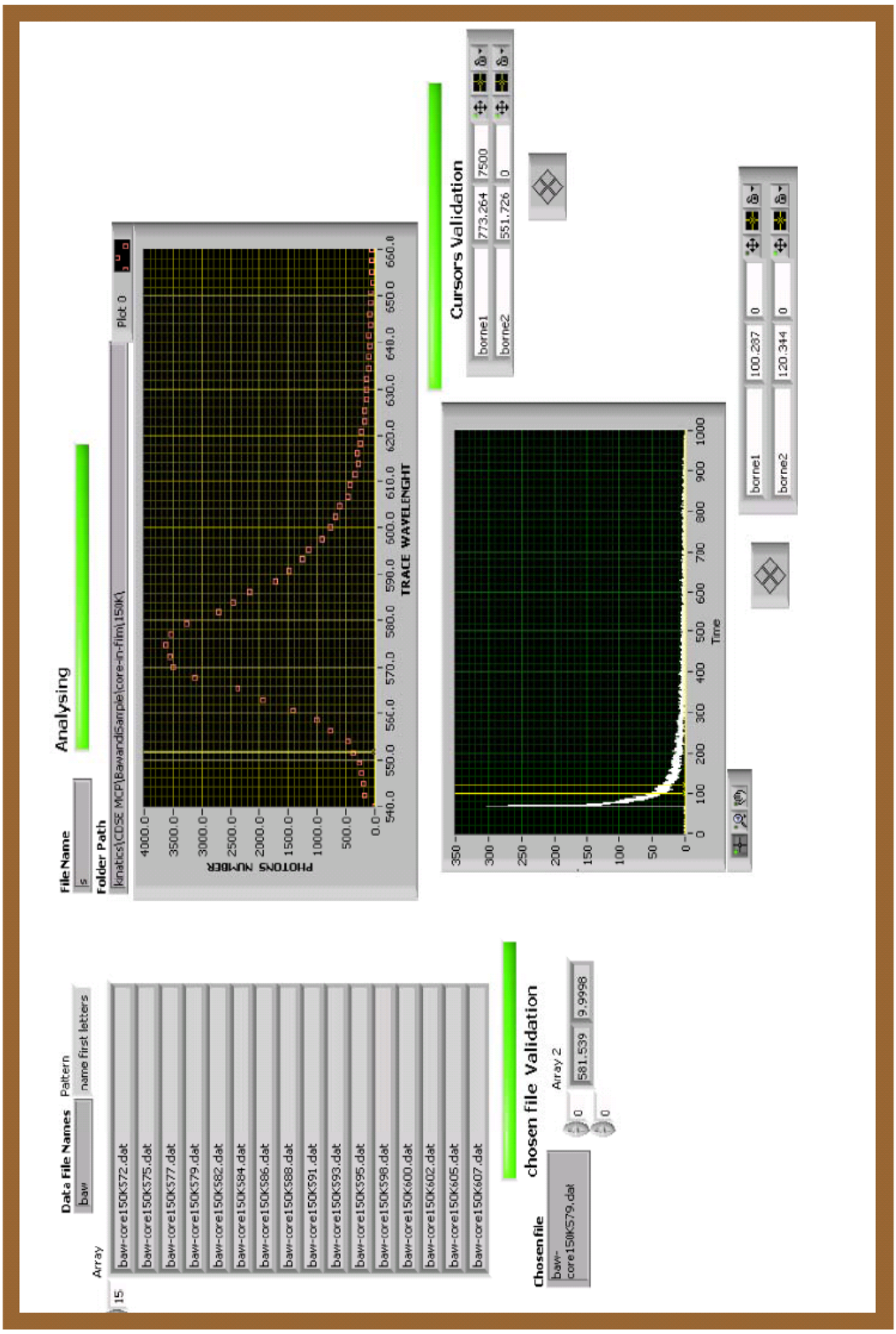

Bibliography

1. Henglein, A., et al., *Photochemistry of Colloidal Semiconductors .30. Reactions and Fluorescence of Agi and Agi - Ag2s Colloids.* Berichte Der Bunsen-Gesellschaft-Physical Chemistry Chemical Physics, 1989. **93**(5): p. 593-600.
2. Weller, H., *Quantized Semiconductor Particles - a Novel State of Matter for Materials Science.* Advanced Materials, 1993. **5**(2): p. 88-95.
3. Schlamp, M.C., X.G. Peng, and A.P. Alivisatos, *Improved efficiencies in light emitting diodes made with CdSe(CdS) core/shell type nanocrystals and a semiconducting polymer.* Journal of Applied Physics, 1997. **82**(11): p. 5837-5842.
4. Coe, S., et al., *Electroluminescence from single monolayers of nanocrystals in molecular organic devices.* Nature, 2002. **420**(6917): p. 800-803.
5. Greenham, N.C., X.G. Peng, and A.P. Alivisatos, *Charge separation and transport in conjugated-polymer/semiconductor-nanocrystal composites studied by photoluminescence quenching and photoconductivity.* Physical Review B, 1996. **54**(24): p. 17628-17637.
6. Huynh, W.U., et al., *Controlling the morphology of nanocrystal polymer composites for solar cells.* Advanced Functional Materials, 2003. **13**(1): p. 73-79.
7. Klimov, V.I., *Optical nonlinearities and ultrafast carrier dynamics in semiconductor nanocrystals.* Journal of Physical Chemistry B, 2000. **104**(26): p. 6112-6123.
8. N. Suzuki, Y.T., T. Kojima *Holographic recording in TiO2 nanoparticle-dispersed methacrylate photopolymer films.* Applied Physics Letters, 2002. **81**: p. 4121.
9. Walters, R.J., et al., *Silicon optical nanocrystal memory.* Applied Physics Letters, 2004. **85**(13): p. 2622-2624.
10. Bruchez, M., et al., *Semiconductor nanocrystals as fluorescent biological labels.* Science, 1998. **281**(5385): p. 2013-2016.
11. Dickson, R.M., et al., *Three-dimensional imaging of single molecules solvated in pores of poly(acrylamide) gels.* Science, 1996. **274**(5289): p. 966-969.

..

12. Alivisatos, A.P., *Semiconductor clusters, nanocrystals, and quantum dots.* Science, 1996. **271**(5251): p. 933-937.
13. Niemeyer, C.M., *Nanoparticles, proteins, and nucleic acids: Biotechnology meets materials science.* Angewandte Chemie-International Edition, 2001. **40**(22): p. 4128-4158.
14. Niemeyer, C.M., B. Ceyhan, and P. Hazarika, *Oligofunctional DNA-gold nanoparticle conjugates.* Angewandte Chemie-International Edition, 2003. **42**(46): p. 5766-5770.
15. Li, L.S., et al., *Preparation and organized assembly of nanoparticulate TiO2-stearate alternating Langmuir-Blodgett films.* Journal of Colloid and Interface Science, 1997. **192**(2): p. 275-280.
16. C. F. J. Flipse, C.B.R., Groot, Eur. Phys, 1999. **9**: p. 479.
17. Bahnemann, D.W., C. Kormann, and M.R. Hoffmann, *Preparation and Characterization of Quantum Size Zinc-Oxide - a Detailed Spectroscopic Study.* Journal of Physical Chemistry, 1987. **91**(14): p. 3789-3798.
18. Daniel, M.C. and D. Astruc, *Gold nanoparticles: Assembly, supramolecular chemistry, quantum-size-related properties, and applications toward biology, catalysis, and nanotechnology.* Chemical Reviews, 2004. **104**(1): p. 293-346.
19. Yin, Y.D., et al., *Synthesis and characterization of stable aqueous dispersions of silver nanoparticles through the Tollens process.* Journal of Materials Chemistry, 2002. **12**(3): p. 522-527.
20. Kim, K.S., et al., *One-phase preparation of palladium nanoparticles using thiol-functionalized ionic liquid.* Korean Journal of Chemical Engineering, 2005. **22**(5): p. 717-720.
21. Li, X., et al., *Preparation of luminescent silicon nanoparticles by photothermal aerosol synthesis followed by acid etching.* Phase Transitions, 2004. **77**(1-2): p. 131-137.
22. Peng, Z.A. and X.G. Peng, *Mechanisms of the shape evolution of CdSe nanocrystals.* Journal of the American Chemical Society, 2001. **123**(7): p. 1389-1395.
23. Wang, W.Z., I. Germanenko, and M.S. El-Shall, *Room-temperature synthesis and characterization of nanocrystalline CdS, ZnS, and CdxZn1-xS.* Chemistry of Materials, 2002. **14**(7): p. 3028-3033.

24. Rogach, A.L., et al., *Synthesis and characterization of thiol-stabilized CdTe nanocrystals.* Berichte Der Bunsen-Gesellschaft-Physical Chemistry Chemical Physics, 1996. **100**(11): p. 1772-1778.
25. Murray, C.B., C.R. Kagan, and M.G. Bawendi, *Synthesis and characterization of monodisperse nanocrystals and close-packed nanocrystal assemblies.* Annual Review of Materials Science, 2000. **30**: p. 545-610.
26. R L. Wells, W.L.G., *Pathways to Nanocrystalline III-V (13–15) Compound Semiconductors* J. Cluster Science 1997. **8**: p. 217.
27. Micic, O.I. and A.J. Nozik, *Synthesis and characterization of binary and ternary III-V quantum dots.* Journal of Luminescence, 1996. **70**: p. 95-107.
28. Uchida, H., C.J. Curtis, and A.J. Nozik, *Gaas Nanocrystals Prepared in Quinoline.* Journal of Physical Chemistry, 1991. **95**(14): p. 5382-5384.
29. Malik, M.A., et al., *Gallium arsenide nanoparticles: synthesis and characterisation.* Journal of Materials Chemistry, 2003. **13**(10): p. 2591-2595.
30. Micic, O.I., et al., *Synthesis and Characterization of Inp Quantum Dots.* Journal of Physical Chemistry, 1994. **98**(19): p. 4966-4969.
31. Schneider, T., et al., *Synthesis and characterization of PbS nanoparticles in block copolymer micelles.* Berichte Der Bunsen-Gesellschaft-Physical Chemistry Chemical Physics, 1997. **101**(11): p. 1654-1656.
32. Hagfeldt, A. and M. Gratzel, *Light-Induced Redox Reactions in Nanocrystalline Systems.* Chemical Reviews, 1995. **95**(1): p. 49-68.
33. Brus, L., *Quantum crystallites and nonlinear optics.* Applied Physics A, 1991. **53**: p. 465.
34. Wang, Y., *Nonlinear optical properties of nanometer-sized semiconductor clusters* Acc. Chem. Res, 1991. **24** (5): p. 133
35. Lewis, L.N., *Chemical catalysis by colloids and clusters* Chem. Rev 1993. **93, 2693** p. 2693.
36. Murray, C.B., D.J. Norris, and M.G. Bawendi, *Synthesis and Characterization of Nearly Monodisperse CdE (E = S, Se, Te) Semiconductor Nanocrystallites.* Journal of the American Chemical Society, 1993. **115**(19): p. 8706-8715.
37. Herron, N., *Small Semiconductor Particles - Preparation and Characterization.* Acs Symposium Series, 1991. **455**: p. 582-601.
38. Brus, L.E., *Electron Electron and Electron-Hole Interactions in Small Semiconductor Crystallites - the Size Dependence of the Lowest Excited Electronic State.* Journal of Chemical Physics, 1984. **80**(9): p. 4403-4409.

39. Brus, L., *Electronic Wave-Functions in Semiconductor Clusters - Experiment and Theory.* Journal of Physical Chemistry, 1986. **90**(12): p. 2555-2560.
40. Knoxy, R.S., *Theory of exciton; Solid State Physics, Supplement 5.* Acadmic Press, New York, 1963.
41. Woggon, U., *Optical properties of semiconductor quantum dots*. Vol. 136. 1996: Springer
42. Efros, A.L. and M. Rosen, *The electronic structure of semiconductor nanocrystals.* Annual Review of Materials Science, 2000. **30**: p. 475-521.
43. Kamat, P.V., *Interfacial Charge-Transfer Processes in Colloidal Semiconductor Systems.* Progress in Reaction Kinetics, 1994. **19**(3): p. 277-316.
44. Ekimov, A.I., et al., *Absorption and Intensity-Dependent Photoluminescence Measurements on Cdse Quantum Dots - Assignment of the 1st Electronic-Transitions.* Journal of the Optical Society of America B-Optical Physics, 1993. **10**(1): p. 100-107.
45. Efros, A.L., Sov. Phys. Semicond 1982. **16**: p. 772.
46. Ekimov, A.I., et al., *Donor-Like Exciton in Zero-Dimension Semiconductor Structures.* Solid State Communications, 1989. **69**(5): p. 565-568.
47. Klimov, V.I., *Handbook of Nanostructured Materials and Nanotechnology.* Academic press, New York 2000. **4**.
48. Li, L.S., et al., *Band gap variation of size- and shape-controlled colloidal CdSe quantum rods.* Nano Letters, 2001. **1**(7): p. 349-351.
49. Brus, L.E., A.L. Efros, and T. Itoh, *Special issue on spectroscopy of isolated and assembled semiconductor nanocrystals - Introduction.* Journal of Luminescence, 1996. **70**: p. R7-R8.
50. Leatherdale, C.A. and M.G. Bawendi, *Observation of solvatochromism in CdSe colloidal quantum dots.* Physical Review B, 2001. **6316**(16): p. art. no.-165315.
51. Javier, A., et al., *Nanosecond exciton recombination dynamics in colloidal CdSe quantum dots under ambient conditions.* Applied Physics Letters, 2003. **83**(7): p. 1423-1425.
52. Bawendi, M.G., et al., *Luminescence Properties of Cdse Quantum Crystallites - Resonance between Interior and Surface Localized States.* Journal of Chemical Physics, 1992. **96**(2): p. 946-954.
53. Labeau, O., P. Tamarat, and B. Lounis, *Temperature dependence of the luminescence lifetime of single CdSe/ZnS quantum dots.* Physical Review Letters, 2003. **90**(25): p. -.

54. Bawendi, M.G., *Chemistry and Physics of Semiconductor Nanoclusters.* Abstracts of Papers of the American Chemical Society, 1994. **208**: p. 4-Inor.
55. Efros, A.L., *Luminescence Polarization of Cdse Microcrystals.* Physical Review B, 1992. **46**(12): p. 7448-7458.
56. Efros, A.L. and A.V. Rodina, *Band-Edge Absorption and Luminescence of Nonspherical Nanometer-Size Crystals.* Physical Review B, 1993. **47**(15): p. 10005-10007.
57. Takagahara, T., *Effects of Dielectric Confinement and Electron-Hole Exchange Interaction on Excitonic States in Semiconductor Quantum Dots.* Physical Review B, 1993. **47**(8): p. 4569-4585.
58. Romestain, R. and G. Fishman, *Excitonic Wave-Function, Correlation-Energy, Exchange Energy, and Oscillator Strength in a Cubic Quantum-Dot.* Physical Review B, 1994. **49**(3): p. 1774-1781.
59. Nirmal, M., et al., *Observation of the Dark Exciton in Cdse Quantum Dots.* Physical Review Letters, 1995. **75**(20): p. 3728-3731.
60. G. L. Bir, G.E.P., *Symmetry and Strain- Induced Effects in Semiconductors.* 1975. **Wiley. New York**
61. Efros, A.L., et al., *Band-edge exciton in quantum dots of semiconductors with a degenerate valence band: Dark and bright exciton states.* Physical Review B, 1996. **54**(7): p. 4843-4856.
62. Wind, O., F. Gindele, and U. Woggon, *Excited state luminescence and fine structure in CdSe quantum dots.* Journal of Luminescence, 1997. **72-4**: p. 300-301.
63. Norris, D.J., et al., *Size dependence of exciton fine structure in CdSe quantum dots.* Physical Review B, 1996. **53**(24): p. 16347-16354.
64. Norris, D.J. and M.G. Bawendi, *Structure in the Lowest Absorption Feature of Cdse Quantum Dots.* Journal of Chemical Physics, 1995. **103**(13): p. 5260-5268.
65. Hu, J.T., et al., *Semiempirical pseudopotential calculation of electronic states of CdSe quantum rods.* Journal of Physical Chemistry B, 2002. **106**(10): p. 2447-2452.
66. Peng, X., et al., *Shape control of CdSe nanocrystals.* Nature (London), 2000. **404**(6773): p. 59-61.
67. Hines, M.A. and P. Guyot-Sionnest, *Bright UV-blue luminescent colloidal ZnSe nanocrystals.* Journal of Physical Chemistry B, 1998. **102**(19): p. 3655-3657.

68. Koch, H.H.a.S.W., *Quantum theory of the optical and electronic properties of semiconductor*. 1990, Singapour: World Scientific.
69. Gribkovskii, V.P., et al., *Optical-Absorption near Excitonic Resonance of Mocvd-Grown Znse Single-Crystals.* Physica Status Solidi B-Basic Research, 1990. **158**(1): p. 359-366.
70. Masumoto, Y., et al., *Breakdown of the phonon bottleneck effect in self-assembled quantum dots.* Japanese Journal of Applied Physics Part 1-Regular Papers Short Notes & Review Papers, 2001. **40**(3B): p. 1947-1950.
71. U. Bockelmann, T.E., *Electron relaxation in quantum dots by means of Auger processes.* Phys. Rev. B 1992. **46**: p. 15574.
72. Yu, P.Y. and M. Cardona, *Fundamentals of Semiconductors*. 1996, Berlin: Springer.
73. V. N. Abakumopv, V.I.P., and I. N. Yassevich, *nonradiative recombination in semiconductores*. 1991, North-Holland, Amsterdam.
74. Marcinkevicius, S. and R. Leon, *Photoexcited carrier transfer in InGaAs quantum dot structures: Dependence on the dot density.* Applied Physics Letters, 2000. **76**(17): p. 2406-2408.
75. Bockelmann, U. and G. Bastard, *Phonon-Scattering and Energy Relaxation in 2-Dimensional, One-Dimensional, and Zero-Dimensional Electron Gases.* Physical Review B, 1990. **42**(14): p. 8947-8951.
76. Inoshita, T. and H. Sakaki, *Electron Relaxation in a Quantum Dot - Significance of Multiphonon Processes.* Physical Review B, 1992. **46**(11): p. 7260-7263.
77. Heitz, R., et al., *Energy relaxation by multiphonon processes in InAs/GaAs quantum dots.* Physical Review B, 1997. **56**(16): p. 10435-10445.
78. Li, X.Q., H. Nakayama, and Y. Arakawa, *Phonon bottleneck in quantum dots: Role of lifetime of the confined optical phonons.* Physical Review B, 1999. **59**(7): p. 5069-5073.
79. Efros, A.L., V.A. Kharchenko, and M. Rosen, *Breaking the Phonon Bottleneck in Nanometer Quantum Dots - Role of Auger-Like Processes.* Solid State Communications, 1995. **93**(4): p. 281-284.
80. Atkines, P.w., *Physical chemestry.* Oxford University Press. 5 editions. 1994., 1994.
81. Fletcher, R.F.K.a.A.N., *Fluorescence quantum yields of some rhodamine dyes* Journal of Luminescence, 1982. **27**: p. 455.

82. Norris, D.J. and M.G. Bawendi, *Measurement and assignment of the size-dependent optical spectrum in CdSe quantum dots.* Physical Review B, 1996. **53**(24): p. 16338-16346.
83. Lakowicz, J.R., *Principles of Fluorescence Spectroscopy* 1999, New York: ed: K.A.P. Publishers.
84. Fisher, B.R., et al., *Emission intensity dependence and single-exponential behavior in single colloidal quantum dot fluorescence lifetimes.* Journal of Physical Chemistry B, 2004. **108**(1): p. 143-148.
85. Schlegel, G., et al., *Fluorescence decay time of single semiconductor nanocrystals.* Physical Review Letters, 2002. **88**(13): p. -.
86. Mohamed, M., et al., *Synthesis of High Quality Zinc-Blende CdSe Nanocrystals.* Journal of Physical Chemistry B, 2005. **109**: p. 1533-1537.
87. Mohamed, M.B., et al., *Chemical synthesis and optical properties of size-selected CdSe tetrapod-shaped nanocrystals.* Chem phys chem, 2005. **6**(12): p. 2505-2507.
88. Peng, Z.A. and X.G. Peng, *Nearly monodisperse and shape-controlled CdSe nanocrystals via alternative routes: Nucleation and growth.* Journal of the American Chemical Society, 2002. **124**(13): p. 3343-3353.
89. Klimov, V.I., *Semiconductor and Metal nanocrystals - Synthesis and Electronic and Optical Properties*. 2004, New York: V.Ied. M. Dekker.
90. Peng, X.G., *Mechanisms for the shape-control and shape-evolution of colloidal semiconductor nanocrystals.* Advanced Materials, 2003. **15**(5): p. 459-463.
91. Lee, J., et al., *Full color emission from II-VI semiconductor quantum dot-polymer composites.* Advanced Materials, 2000. **12**(15): p. 1102.
92. Heath, J.R., *The Chemistry of Size and Order on the Nanometer-Scale.* Science, 1995. **270**(5240): p. 1315-1316.
93. Alivisatos, E.C.S.L.M.A.P., Philosophical Transactions of the Royal Society of London. A 2003. **361**: p. 241.
94. Colvin, V.L., K.L. Cunningham, and A.P. Alivisatos, *Electric-Field Modulation Studies of Optical-Absorption in Cdse Nanocrystals - Dipolar Character of the Excited-State.* Journal of Chemical Physics, 1994. **101**(8): p. 7122-7138.
95. Fisher, B., et al., *Room-temperature ordered photon emission from multiexciton states in single CdSe core-shell nanocrystals.* Physical Review Letters, 2005. **94**(8): p. -.

96. Schlegel, G., et al., *Fluorescence decay time of single semiconductor nanocrystals.* Physical Review Letters, 2002. **88**(13): p. art. no.-137401.

97. Crooker, S.A., et al., *Ultrafast coherent terahertz spectroscopy in high magnetic fields and directed energy flows in quantum dot assemblies.* Acta Physica Polonica A, 2003. **104**(2): p. 113-122.

98. Zhang, J.Y., X.Y. Wang, and M. Xiao, *Modification of spontaneous emission from CdSe/CdS quantum dots in the presence of a semiconductor interface.* Optics Letters, 2002. **27**(14): p. 1253-1255.

99. Le Thomas, N., et al., *Exciton fine structure in single CdSe nanorods.* Physical Review Letters, 2005. **94**(1): p. -.

100. Sander F. Wuister, A.v.H., C M Donegá, A Meijerink, *Temperature Antiquenching of the Luminescence from Capped CdSe Quantum Dots* Angew Chem Int Ed, 2004. **43**: p. 3029.

101. Jones, M., et al., *Photoenhancement of Luminescence in Colloidal CdSe Quantum Dot Solutions.* Journal of Physical Chemistry B, 2003. **107**(41): p. 11346-11352.

102. Huynh, W.U., J.J. Dittmer, and A.P. Alivisatos, *Hybrid nanorod-polymer solar cells.* Science, 2002. **295**(5564): p. 2425-2427.

103. Crooker, S.A., et al., *Multiple temperature regimes of radiative decay in CdSe nanocrystal quantum dots: Intrinsic limits to the dark-exciton lifetime.* Applied Physics Letters, 2003. **82**(17): p. 2793-2795.

104. Ebenstein, Y., T. Mokari, and U. Banin, *Fluorescence quantum yield of CdSe/ZnS nanocrystals investigated by correlated atomic-force and single-particle fluorescence microscopy.* Applied Physics Letters, 2002. **80**(21): p. 4033-4035.

105. Wang, X.Y., et al., *Surface-related emission in highly luminescent CdSe quantum dots.* Nano Letters, 2003. **3**(8): p. 1103-1106.

106. Hines, M.A. and P. GuyotSionnest, *Synthesis and characterization of strongly luminescing ZnS-Capped CdSe nanocrystals.* Journal of Physical Chemistry, 1996. **100**(2): p. 468-471.

107. Wang, X., et al., *Surface-Related Emission in Highly Luminescent CdSe Quantum Dots.* Nano Letters, 2003. **3**(8): p. 1103-1106.

108. Klimov, V.I., et al., *Quantization of multiparticle Auger rates in semiconductor quantum dots.* Science, 2000. **287**(5455): p. 1011-1013.

109. Bonati, C., et al., *Spectral and dynamical characterization of multiexcitons in colloidal CdSe semiconductor quantum dots.* Physical Review B, 2005. **71**(20): p. 205317.

110. Leatherdale, C.A., et al., *On the absorption cross section of CdSe nanocrystal quantum dots.* Journal of Physical Chemistry B, 2002. **106**(31): p. 7619-7622.
111. Tonti, D., F. van Mourik, and M. Chergui, *On the excitation wavelength dependence of the luminescence yield of colloidal CdSe quantum dots.* Nano Letters, 2004. **4**(12): p. 2483-2487.
112. Achermann, M., J.A. Hollingsworth, and V.I. Klimov, *Multiexcitons confined within a subexcitonic volume: Spectroscopic and dynamical signatures of neutral and charged biexcitons in ultrasmall semiconductor nanocrystals.* Physical Review B, 2003. **68**(24): p. 245302.
113. Norris, D.J., et al., *Size-Dependent Optical Spectroscopy of Ii-Vi Semiconductor Nanocrystallites (Quantum Dots).* Zeitschrift Fur Physik D-Atoms Molecules and Clusters, 1993. **26**(1-4): p. 355-357.
114. Nirmal, M., C.B. Murray, and M.G. Bawendi, *Fluorescence-Line Narrowing in Cdse Quantum Dots - Surface Localization of the Photogenerated Exciton.* Physical Review B, 1994. **50**(4): p. 2293-2300.
115. Crooker, S.A., et al., *Spectrally resolved dynamics of energy transfer in quantum-dot assemblies: Towards engineered energy flows in artificial materials.* Physical Review Letters, 2002. **89**(18): p. art. no.-186802.
116. Battaglia, D., B. Blackman, and X. Peng, *Coupled and Decoupled Dual Quantum Systems in One Semiconductor Nanocrystal.* Journal of the American Chemical Society, 2005. **127**(31): p. 10889-10897.
117. Chen, X.B., et al., *Coherency strain effects on the optical response of core/shell heteronanostructures.* Nano Letters, 2003. **3**(6): p. 799-803.
118. Landes, C., et al., *Photoluminescence of CdSe nanoparticles in the presence of a hole acceptor: n-butylamine.* Journal of Physical Chemistry B, 2001. **105**(15): p. 2981-2986.
119. X-Y Wang, J.-Y.Z., A. Nazzal, M. Darragh, and Min Xiao *Electronic structure transformation from a quantum-dot to a quantum-wire system: Photoluminescence decay and polarization of colloidal CdSe quantum rods.* applied Physics Letters, 2002. **81**: p. 4829.
120. Califano, M., A. Franceschetti, and A. Zunger, *Temperature Dependence of Excitonic Radiative Decay in CdSe Quantum Dots: The Role of Surface Hole Traps.* Nano Letters, 2005. **5**(12): p. 2360-2364.
121. Leung, K. and K.B. Whaley, *Surface relaxation in CdSe nanocrystals.* Journal of Chemical Physics, 1999. **110**(22): p. 11012-11022.

122. Manna, L., et al., *Epitaxial growth and photochemical annealing of graded CdS/ZnS shells on colloidal CdSe nanorods.* Journal of the American Chemical Society, 2002. **124**(24): p. 7136-7145.
123. Patton, B., W. Langbein, and U. Woggon, *Trion, biexciton, and exciton dynamics in single self-assembled CdSe quantum dots.* Physical Review B, 2003. **68**(12): p. art. no.-125316.
124. Caruge, J.M., et al., *Transient photoluminescence and simultaneous amplified spontaneous emission from multiexciton states in CdSe quantum dots.* Physical Review B, 2004. **70**(8): p. -.
125. Franceschetti, A. and A. Zunger, *Optical transitions in charged CdSe quantum dots.* Physical Review B, 2000. **62**(24): p. R16287-R16290.
126. Gindele, F., et al., *Excitons, biexcitons, and phonons in ultrathin CdSe/ZnSe quantum structures.* Physical Review B, 1999. **60**(12): p. 8773-8782.
127. Nirmal, M. and L. Brus, *Luminescence photophysics in semiconductor nanocrystals.* Accounts of Chemical Research, 1999. **32**(5): p. 407-414.
128. Zheng, J.P. and H.S. Kwok, *Temperature-Dependence of the Optical-Properties of Semiconductor Microcrystals.* Journal of the Optical Society of America B-Optical Physics, 1992. **9**(11): p. 2047-2053.
129. Valerini, D., et al., *Temperature dependence of the photoluminescence properties of colloidal CdSe/ZnS core/shell quantum dots embedded in a polystyrene matrix.* Physical Review B, 2005. **71**(23): p. 235409.
130. Varshni, Y.P., *Temperature dependence of the energy gap in semiconductors.* Physica B, 1967. **34**: p. 149.
131. Hellwege., K.H. and Landolt-Börnstein, *Numerical Data and Functional Relationship in Sience and Technology*. Vol. 17. 1982, Berlin: Springer-Verlag.
132. kittel, C., *Introduction to solid state physics*, ed. s. edition. 1996: Wiley.
133. Klochikhin, A., et al., *Temperature dependence of photoluminescence bands in Zn1-xCdxSe/ZnSe quantum wells with planar CdSe islands.* Physical Review B, 2004. **69**(8): p. 085308.
134. Zhang, J.Y., et al., *Lattice contraction in free-standing CdSe nanocrystals.* Applied Physics Letters, 2002. **81**(11): p. 2076-2078.
135. Gindele, F., et al., *Temperature-dependent line widths of single excitons and biexcitons.* Journal of Luminescence, 2000. **87-9**: p. 381-383.
136. Woggon, U., et al., *Homogeneous Linewidth of Confined Electron-Hole-Pair States in Ii-Vi-Quantum Dots.* Physical Review B, 1993. **47**(7): p. 3684-3689.

137. Pengguang Wu, H.L., Thomas M. Nordlund, Rudolf Rigler, *Multistate modeling of the time and temperature dependence of fluorescence from 2-aminopurine in a DNA decamer* International Society for Optical Engineering 1990. **1204**: p. 262.
138. Issac, A., C. von Borczyskowski, and F. Cichos, *Correlation between photoluminescence intermittency of CdSe quantum dots and self-trapped states in dielectric media.* Physical Review B, 2005. **71**(16): p. -.
139. Wang, L.W., *Calculating the influence of external charges on the photoluminescence of a CdSe quantum dot.* Journal of Physical Chemistry B, 2001. **105**(12): p. 2360-2364.
140. Fonoberov, V.A. and A.A. Balandin, *Origin of ultraviolet photoluminescence in ZnO quantum dots: Confined excitons versus surface-bound impurity exciton complexes*

Applied Physics Letters, 2004. **85**: p. 5971.

141. Kwok, J.P.Z.a.H.-S., *Temperature dependence of the optical properties of semiconductor microcrystals.* Journal of the Optical Society of America B, 1992. **9**: p. 2047.
142. Zhao, H., S. Wachter, and H. Kalt, *Effect of quantum confinement on exciton-phonon interactions.* Physical Review B, 2002. **66**(8): p. -.
143. Zhang, L.G., et al., *Exciton-phonon scattering in CdSe/ZnSe quantum dots.* Chinese Physics Letters, 2002. **19**(4): p. 578-580.
144. Nomura, S. and T. Kobayashi, *Exciton Lo-Phonon Couplings in Spherical Semiconductor Microcrystallites.* Physical Review B, 1992. **45**(3): p. 1305-1316.
145. S. Nomura, T.K., *Exciton- lo -.* Physical Revieu B, 1992. **45**(3): p. 1305.
146. Schoenlein, R.W., et al., *Investigation of Femtosecond Electronic Dephasing in Cdse Nanocrystals Using Quantum-Beat-Suppressed Photon-Echoes.* Physical Review Letters, 1993. **70**(7): p. 1014-1017.
147. Takagahara, T., *Electron-Phonon Interactions and Excitonic Dephasing in Semiconductor Nanocrystals.* Physical Review Letters, 1993. **71**(21): p. 3577-3580.
148. Schmitt-Rink, S., D.A.B. Miller, and D.S. Chemla, *Theory of the Linear and Nonlinear Optical-Properties of Semiconductor Microcrystallites.* Physical Review B, 1987. **35**(15): p. 8113-8125.
149. Takagahara, T., *Electron-phonon interactions in semiconductor nanocrystals.* Journal of Luminescence, 1996. **70**: p. 129-143.

150. Cerullo, G., S. De Silvestri, and U. Banin, *Size-dependent dynamics of coherent acoustic phonons in nanocrystal quantum dots.* Physical Review B, 1999. **60**(3): p. 1928-1932.

151. Voigt, J., F. Spiegelberg, and M. Senoner, *Band Parameters of Cds and Cdse Single-Crystals Determined from Optical Exciton Spectra.* Physica Status Solidi B-Basic Research, 1979. **91**(1): p. 189-199.

152. Chamberlain, M.P., C. Trallerogíner, and M. Cardona, *Theory of One-Phonon Raman-Scattering in Semiconductor Microcrystallites.* Physical Review B, 1995. **51**(3): p. 1680-1693.

153. Hwang, Y.N., S.H. Park, and D. Kim, *Size-dependent surface phonon mode of CdSe quantum dots.* Physical Review B, 1999. **59**(11): p. 7285-7288.

154. Alivisatos, A.P., et al., *Electron-Vibration Coupling in Semiconductor Clusters Studied by Resonance Raman-Spectroscopy.* Journal of Chemical Physics, 1989. **90**(7): p. 3463-3468.

155. S. Surendran, J.P., K. Jurek, E. Bernstein, P. Maly. , Maly. Material Science and Engenering B 2003. **104**: p. 54.

156. Joshi, A., et al., *Temperature dependence of the band gap of colloidal CdSe/ZnS core/shell nanocrystals embedded into an ultraviolet curable resin.* Applied Physics Letters, 2006. **89**(13): p. 131907.

157. Schops, O., et al., *Recombination dynamics of CdTe/CdS core-shell nanocrystals.* Journal of Physical Chemistry B, 2006. **110**(5): p. 2074-2079.

158. Talapin, D.V., et al., *CdSe/CdS/ZnS and CdSe/ZnSe/ZnS core-shell-shell nanocrystals.* Journal of Physical Chemistry B, 2004. **108**(49): p. 18826-18831.

159. Baranov, A.V., et al., *Effect of ZnS shell thickness on the phonon spectra in CdSe quantum dots.* Physical Review B: Condensed Matter and Materials Physics, 2003. **68**(16): p. 165306/1-165306/7.

160. Qu, L.H. and X.G. Peng, *Control of photoluminescence properties of CdSe nanocrystals in growth.* Journal of the American Chemical Society, 2002. **124**(9): p. 2049-2055.

161. Kalyuzhny, G. and R.W. Murray, *Ligand Effects on Optical Properties of CdSe Nanocrystals.* Journal of Physical Chemistry B, 2005. **109**(15): p. 7012-7021.

162. Gehlen, M.H. and F.C. Deschryver, *Time-Resolved Fluorescence Quenching in Micellar Assemblies.* Chemical Reviews, 1993. **93**(1): p. 199-221.

163. Masumoto, Y., et al., *Band-Gap Renormalization and Optical Gain Formation in Highly Excited Cdse.* Journal of Crystal Growth, 1992. **117**(1-4): p. 732-737.

164. Brus, L., *Luminescence of Silicon Materials - Chains, Sheets, Nanocrystals, Nanowires, Microcrystals, and Porous Silicon.* Journal of Physical Chemistry, 1994. **98**(14): p. 3575-3581.
165. Gaponenko, S.V., et al., *Permanent spectral hole-burning in semiconductor quantum dots.* Journal of Applied Physics, 1996. **79**(9): p. 7139-7142.
166. Oneil, M., J. Marohn, and G. Mclendon, *Dynamics of Electron-Hole Pair Recombination in Semiconductor Clusters.* Journal of Physical Chemistry, 1990. **94**(10): p. 4356-4363.
167. Gaponenko, S.V., *Optical processes in semiconductor nanocrystallites (quantum dots).* Semiconductors, 1996. **30**(4): p. 315-336.
168. Abdallah, W.e.A. and A.E. Nelson, *Characterization of MoSe2(0001) and ion-sputtered MoSe2 by XPS.* Journal of Materials Science, 2005. **40**(9/10): p. 2679-2681.
169. Fedorov, V.A., V.A. Ganshin, and Y.N. Korkishko, *Determination of the point of the zincblende-to-wurtzite structural phase transition in cadmium selenide crystals.* Physica Status Solidi A: Applied Research, 1991. **126**(1): p. K5-K7.
170. Manna, L., E.C. Scher, and A.P. Alivisatos, *Synthesis of soluble and processable rod-, arrow-, teardrop-, and tetrapod-shaped CdSe nanocrystals.* Journal of the American Chemical Society, 2000. **122**(51): p. 12700-12706.
171. Rogach, A.L., et al., *Synthesis and characterization of a size series of extremely small thiol-stabilized CdSe nanocrystals.* Journal of Physical Chemistry B, 1999. **103**(16): p. 3065-3069.
172. Yu, W.W., et al., *Experimental determination of the extinction coefficient of CdTe, CdSe and CdS nanocrystals (vol 15, pg 2854, 2003).* Chemistry of Materials, 2004. **16**(3): p. 560-560.
173. Grünberg, H.H.v., *Energy levels of CdSe quantum dots: Wurtzite versus zinc-blende structure.* Phys. Rev. B, 1997. **55**: p. 2293.
174. Talapin, D.V., et al., *Highly luminescent monodisperse CdSe and CdSe/ZnS nanocrystals synthesized in a hexadecylamine-trioctylphosphine oxide-trioctylphospine mixture.* Nano Letters, 2001. **1**(4): p. 207-211.
175. Talapin, D.V., et al., *Synthesis and surface modification of amino-stabilized CdSe, CdTe and InP nanocrystals.* Colloids and Surfaces a-Physicochemical and Engineering Aspects, 2002. **202**(2-3): p. 145-154.
176. Wang, L.W. and A. Zunger, *High-energy excitonic transitions in CdSe quantum dots.* Journal of Physical Chemistry B, 1998. **102**(34): p. 6449-6454.

177. Woggon, U., et al., *Optical transitions in CdSe quantum dots: From discrete levels to broad gain spectra.* Journal of Luminescence, 1996. **70**: p. 269-280.

178. Bawendi, M.G., et al., *Electronic-Structure and Photoexcited-Carrier Dynamics in Nanometer-Size Cdse Clusters.* Physical Review Letters, 1990. **65**(13): p. 1623-1626.

179. Woggon, U., et al., *Exchange interaction and phonon confinement in CdSe quantum dots.* Physical Review B, 1996. **54**(3): p. 1506-1509.

180. Chamarro, M., et al., *Enhancement of electron-hole exchange interaction in CdSe nanocrystals: A quantum confinement effect.* Physical Review B, 1996. **53**(3): p. 1336-1342.

181. Du, H., et al., *Optical properties of colloidal PbSe nanocrystals.* Nano Letters, 2002. **2**(11): p. 1321-1324.

182. Takagahara, T., *Nonlocal Theory of the Size and Temperature-Dependence of the Radiative Decay-Rate of Excitons in Semiconductor Quantum Dots.* Physical Review B, 1993. **47**(24): p. 16639-16642.

183. Chamarro, M., et al., *Enhancement of Exciton Exchange Interaction by Quantum Confinement in Cdse Nanocrystals.* Japanese Journal of Applied Physics Part 2-Letters, 1994. **34**: p. 12-14.

184. Shim, M. and P. Guyot-Sionnest, *Permanent dipole moment and charges in colloidal semiconductor quantum dots.* Journal of Chemical Physics, 1999. **111**(15): p. 6955-6964.

185. Blanton, S.A., et al., *Dielectric dispersion measurements of CdSe nanocrystal colloids: Observation of a permanent dipole moment.* Physical Review Letters, 1997. **79**(5): p. 865-868.

186. Rabani, E., et al., *Electronic properties of CdSe nanocrystals in the absence and presence of a dielectric medium.* Journal of Chemical Physics, 1999. **110**(11): p. 5355-5369.

187. Hu, J.T., et al., *Linearly polarized emission from colloidal semiconductor quantum rods.* Science, 2001. **292**(5524): p. 2060-2063.

188. Li, L.-s.H., J.; Yang, W.; Alivisatos, A. P., *Band Gap Variation of Size- and Shape-Controlled Colloidal CdSe Quantum Rods* Nano Lett, 2001. **1**: p. 349.

189. Manna, L., et al., *Controlled growth of tetrapod-branched inorganic nanocrystals.* Nature Materials, 2003. **2**(6): p. 382-385.

190. Pang, Q., et al., *CdSe nano-tetrapods: Controllable synthesis, structure analysis, and electronic and optical properties.* Chemistry of Materials, 2005. **17**(21): p. 5263-5267.
191. Kazes, M., et al., *Lasing from semiconductor quantum rods in a cylindrical microcavity.* Advanced Materials, 2002. **14**(4): p. 317.
192. Li, J.B. and L.W. Wang, *Shape effects on electronic states of nanocrystals.* Nano Letters, 2003. **3**(10): p. 1357-1363.
193. Li, J.W., L.-w., *High Energy Excitations in CdSe Quantum Rods* Nano Lett, 2003. **3**(1): p. 101.
194. Lee, J., E.S. Koteles, and M.O. Vassell, *Luminescence Linewidths of Excitons in Gaas Quantum-Wells Below 150-K.* Physical Review B, 1986. **33**(8): p. 5512-5516.
195. Herzberg, G., *Atomic Spectra and Atomic Structure*. 1945, New York: Dover Publications.
196. Katz, D., et al., *Size-dependent tunneling and optical spectroscopy of CdSe quantum rods.* Physical Review Letters, 2002. **89**(8): p. art. no.-086801.
197. Mokari, T. and U. Banin, *Synthesis and properties of CdSe/ZnS core/shell nanorods.* Chemistry of Materials, 2003. **15**(20): p. 3955-3960.
198. Banin, U., et al., *Evidence for a thermal contribution to emission intermittency in single CdSe/CdS core/shell nanocrystals.* Journal of Chemical Physics, 1999. **110**(2): p. 1195-1201.
199. Zhang, K., et al., *Continuous distribution of emission states from single CdSe/ZnS quantum dots.* Nano Letters, 2006. **6**(4): p. 843-847.
200. Müller, J., et al., *Monitoring surface charge movement in single elongated semiconductor nanocrystals.* Physical Review Letters, 2004. **93**(16): p. 167402/1-167402/4.
201. Rothenberg, E., et al., *Electric field induced switching of the fluorescence of single semiconductor quantum rods.* Nano Letters, 2005. **5**(8): p. 1581-1586.
202. Empedocles, S.A. and M.G. Bawendi, *Quantum-confined stark effect in single CdSe nanocrystallite quantum dots.* Science, 1997. **278**(5346): p. 2114-2117.
203. Wang, S., et al., *Fluorescence blinking statistics from CdSe core and core/shell nanorods.* Journal of Physical Chemistry B, 2006. **110**(46): p. 23221-23227.
204. Yeh, C.Y., et al., *Predictions and Systematizations of the Zincblende Wurtzite Structural Energies in Binary Octet Compounds.* Physical Review B, 1992. **45**(20): p. 12130-12133.

..

205. Manna, L., E.C. Scher, and A.P. Alivisatos, *Shape control of colloidal semiconductor nanocrystals.* Journal of Cluster Science, 2002. **13**(4): p. 521-532.

206. Milliron, D.J., et al., *Colloidal nanocrystal heterostructures with linear and branched topology.* Nature, 2004. **430**(6996): p. 190-195.

207. Yu, W.W., Y.A. Wang, and X. Peng, *Formation and Stability of Size-, Shape-, and Structure-Controlled CdTe Nanocrystals: Ligand Effects on Monomers and Nanocrystals.* Chemistry of Materials, 2003. **15**(22): p. 4300-4308.